Collège Doctoral du Languedoc-Roussillon

THÈSE

Pour obtenir le grade de

Docteur

Délivrée par l'**Université Montpellier II**
en Cotutelle avec **Macquarie University**

Préparée au sein de l'école doctorale **I2S***
Et de l'unité de recherche **UMR 5024**

Spécialité: **Astrophysique Stellaire**

Présentée par Dimitri Douchin

Estimation de la Fraction Binaire de Nébuleuses Planétaires

Soutenue le 26/09/2014 devant le jury composé de :

Mme Orsola De Marco	Professeur Ass.	Macquarie Univ.	Directeur de thèse
M. Gérard Jasniewicz	Astronome	Univ. Montpellier II	Directeur de thèse
Mme Griet Van De Steene	Astronome	Royal Observatory	Rapporteur
M. Ryszard Szczerba	Professeur	Copernicus Astron. Institute	Rapporteur
Mme Agnès Lèbre	Astronome	Univ. Montpellier II	Examinateur
M. Quentin Parker	Professeur	Macquarie Univ.	Examinateur

UNIVERSITÉ MONTPELLIER 2
SCIENCES ET TECHNIQUES

La vaste majorité des nébuleuses planétaires présente des formes non-sphériques inattendues. Nous testons si la présence d'un compagnon orbitant leurs noyaux, une explication possible pour les morphologies observées, constitue un canal privilégié pour la formation de ces nébuleuses.

* **I2S :** École doctorale Information Structures Systèmes

Estimating the Binary Fraction of Central Stars of Planetary Nebulae

By

Dimitri Douchin

A phd thesis submitted to Macquarie University
in Cotutelle with
Université de Montpellier 2
Department of Physics And Astronomy
November 2014

Examiner's Copy

Typeset in LaTeX 2ε.

Except where acknowledged in the customary manner, the material presented in this thesis is, to the best of my knowledge, original and has not been submitted in whole or part for a degree in any university.

Dimitri Douchin

Crossing a sea

"When I speak of crossing a sea I am talking of both a body of water and various situations in your life. Be it a hundred miles of choppy water or a turbulent time in your life, the spirit of the conqueror is the same. There come many times in life when a person must set sail and chart out his own path, even if his companions remain safely ashore.

At this time you should learn your route, know your vessel, and watch for the best season. Learn the dangers and face the fears. Ride the wind as long as you can, but if the wind stops and conditions become unfavorable, be ready to take the oar in hand and force your way to the port.

To be successful in life one must have the same spirit. Many obstacles will arise and many opponents will come against you, but do not be detoured. Make up your mind, be decisive, trust your intuition and follow your spirit. Trust the experience of others, but do not let them cause you to doubt your intuition.

In martial arts and in strategy, this analogy is important. Know your opponent like a sea captain knows the ford. Learn his strengths and weaknesses. Know the best plan of attack and never relent. Do not be distracted. Do not be dissuaded. Have a resolute spirit in everything you do.

Attack the opponent's weak points. Always seek the position of advantage and never stop until you win. Once you have achieved your goal you may rest."

– Miyamoto Musachi, *The Book Of Five Rings*

Acknowledgements

I would like to thank my supervisor Orsola De Marco for the time and energy she has dedicated to this project, first on her own and then with me at her side. I am grateful for the constant support you have given me all along this project. Thank you also for being the friend you are.

I thank my Cotutelle supervisor Gérard Jasniewicz with all my heart for his kind supervision and his expertise. I look forward to our future adventures on Maya territory.

I would also like thank my secondary supervisor Quentin Parker for his support and more generally for leading the MQAAASTRO Research Centre the way he does to make it what it is today: a well-renown, creative, dynamic pole for research in PN science. I wish to the MQAAASTRO Centre that it continues to prosper the way I have seen it grow in my little lifespan here.

I would like to address special thanks to David Frew without whom this project could not have been completed. His amazing knowledge of the local sample of PNe has been an example. Thank you for your support and directions, and for having shared with me your sense of scientific integrity as well as your sense of humanity.

I would like to thank the MQAAASTRO PhD & post-doc team: Christina Martina Baldwin, Rozenne Boissay, Tiffany Day, Danica Dravskovic, Elaina Hyde, Sophia Id Salah, Rajika Kuruwita, Geraline Marien, Corinne McDonnell, Stacey Rouge Newbolt-Bright, Isabella Isuśka Spaleniak, Carlos Bacigalupo, Joao Bento, Pandey Birendra, Ivan Bojičić, Nick Cvetojevic, Ashkbiz Danehkar,

Kyle DePew, Tobias Feger, Pablo Galaviz, Brint Jones Gardner, Greg Goldstein, Roberto the Billhook Iaconi, Andrew Lehmann, Daniel Maccer MacDonald, Niyas MC Madappattu, Arik Jones Mitschang, Colin Navin, Nem Nemanovic, Glenn Rees, Aaron Rizzutto, Jan Staff, Travis Stenborg, James Tocknell and Shane Vickers,

and academics Mike Ireland, Richard McDermid, Lee Spitler, Mark Wardle and Daniel Zucker.

I also thank the LUPM PhD & post-doc team: Rana Ezzeddine, Johanna Itam, Louis Amard, Nicolas Fabas, Pierre Ghesquière, Anthony Hervé, Julien Lambert,

and academics: Agnès Lèbre, Ana Palacios, Dahbia Talbi, Éric Josselin, Fabrice Martins, Nicolas Mauron, Bertrand Plez, Denis Puy, Henri Reboul, Olivier Richard and Yohann Scribano.

I thank the administrative staff of both universities, in particular Carol McNaught and Carole Prévot.

Thank you to all the colleagues I have had the chance to meet during my multiple travels to observatories and conferences: Liz Guzman, Di Harmer, Shazrene Mohamed, Carolina Moura Carneiro, Adrien Pa'pondieu Guérou, Jeff Clayton, Todd Hillwig, George Jacoby, Dave Jones, Eric Lagadec, Brent Miszalski and Noam Soker. A star shines for Olivier Chesneau.

Thank you to my eternal inspirations in astronomy Hervé Dole, Mathieu Langer and Phil Yock.

I thank my examiners for taking the time to assess this thesis.

Thank you to Sa Bom Nim Anne Mouland-Claassens, Kwang Jang Nim Ron Claassens and all the team of the Empower Dojang, Sensei Dean Whittle and all the team of Ninjutsu Sydney, Jean-Yves Cassan and all the team of Montpellier Dojo and Celsinho Lopes Dos Santos and all the team of Renascer De Minas.

Thank you Caroline Pany Boulom for making every day of my life extraordinary.

Abstract

Planetary nebulae are the end-products of intermediate-mass stars evolution, following a phase of spherical expansion of their atmospheres at the end of their lives. Observationally, it has been estimated that 80% of them have non-spherical shapes. Such a high fraction is puzzling and has occupied the planetary nebula community for more than 30 years. One scenario that would allow to justify the observed shapes is that a comparable fraction of the progenitors of central stars of planetary nebula (CSPN) are not single, but possess a companion. The shape of the nebulae would then be the result of an interaction with this companion. The high fraction of non-spherical planetary nebulae would thus imply a high fraction of binary central stars of planetary nebula, making binarity a preferred channel for planetary nebula formation. After presenting the current state of knowledge regarding planetary nebula formation and shaping and reviewing the diverse efforts to find binaries in planetary nebulae, I present my work to detect a near-infrared excess that would be the signature of the presence of cool companions. The first part of the project consists in the analysis of data and photometry acquired and conducted by myself. The second part details an attempt to make use of archived datasets: the Sloan Digital Sky Survey Data Release 7 optical survey and the extended database assembled by Frew (2008). I also present results from a radial velocity analysis of VLT/UVES spectra for 14 objects aiming to the detection of spectroscopic companions. Finally I give details of the analysis of optical photometry data from our observations associated to the detection of companions around centrals star of planetary nebula using the photometric variability technique. The main result of this thesis is from the near-infrared excess studies which I combine with previously-published data. I conclude that if the detected red and NIR flux excess is indicative of

a stellar companion then the binary fraction is larger than what we may expect based on the main-sequence progenitor population binary fraction and therefore conclude that binarity is a preferential channel for the formation of planetary nebula. I finish by underlining the need for a sample size of $\sim$ 150 objects to decrease the uncertainty on the planetary nebula population binary fraction and increase the statistical significance of this result.

Résumé

Les nébuleuses planétaires (NP) sont le produit de l'évolution d'étoiles de masses intermédiaires après l'expansion sphérique à la fin de leurs vies. Il a été estimé observationnellement que 80% des NP ont des formes non-sphériques. Une fraction si élevée est déroutante et a mobilisé la communauté de recherche sur les NP pendant plus de trente ans. Un scénario qui permettrait de justifier les formes observées serait que les étoiles progénitrices de noyaux de NP (NNP) ne sont pas simples, mais possèdent un compagnon. Les formes des nébuleuses seraient ainsi le résultat de l'interaction avec le compagnon. La fraction si élevée de NP non-sphériques impliquerait donc une fraction élevée de NNP binaires, faisant de la parité stellaire un canal de formation privilégié pour les NP. Après avoir présenté l'état de connaissance actuelle concernant la formation et la mise en forme des NP, je présente mes travaux visant à détecter un excès infrarouge qui serait la signature de la présence d'un compagnon orbitant le NNP. La première partie de ce projet consiste en l'analyse de données et photométrie acquises par moi-mme. Dans la deuxième partie je présente une tentative d'utilisation de jeux de données d'archives : la campagne optique Sloan Digital Sky Survey Data Release 7 et la version étendue de la base de donnée assemblée par Frew (2008). Je présente aussi les résultats d'une analyse de vitesses radiales de spectres VLT/UVES pour 14 objets dans le but de détecter des compagnons spectroscopiques. Finalement j'expose les détails d'une analyse de photométrie de données optiques dans le but de détecter des compagnons orbitant autour de NNP en utilisant la technique de variabilité photométrique. Le résultat principal de cette thèse réside dans les analyses d'excès infrarouge proche que je combine avec des données publiées précédemment. Je conclus que si la fraction détectée d'excès infrarouge proche est attribuée à la présence

de compagnons stellaires, alors la fraction binaire de NNP est plus grande que celle attendue en se basant sur la population binaire de progéniteurs de la séquence principale et ainsi conclus que la multiplicité stellaire est un canal de formation privilégié pour les NP. Je clos en soulignant la nécessité d'un échantillon d'étude d'environ 150 objets pour réduire l'incertitude sur la fraction binaire de NNP et appuyer les conclusions statistiques de ce résultat.

Contents

List of Figures

List of Tables

Introduction

Planetary nebulae (PN) are some of the most visually captivating astronomical objects. Their formation as the evolution product of Sun-like stars is now fairly well established (Iben, 1991, 1993, 1995; Weinberger & Kerber, 1997; Kwok, 1994, 2005), as evolutionary models have been refined to fit the increasing number of PN observations for the past 30 years. Still, one question strongly resists the efforts of the PN research community: how can the observed PN have non-spherical shapes if they come from approximately spherical stars? The presence of a stellar magnetic field during the PN ejection was considered a satisfactory explanation until it was realised that the magnetic fields do not survive throughout the star's late stages of evolution. Meanwhile the idea that a companion surrounding the central star of the PN (CSPN) could also shape the nebula started to grow.

In this introduction, we present our current understanding of PN formation and raise the problem of the PN shaping mechanisms. We explain why PN shaping from stellar magnetic fields seems to be insufficient by itself and how companions around the central star can create the variety of shapes that is observed. We formulate the Binary Hypothesis and it is shown how measuring the binary fraction of CSPN can help to support or invalidate this hypothesis. At the end we open onto the description of our work by summarising from the literature available to date the different estimates of the CSPN binary fraction determined thanks to a set of various, complementary methods.

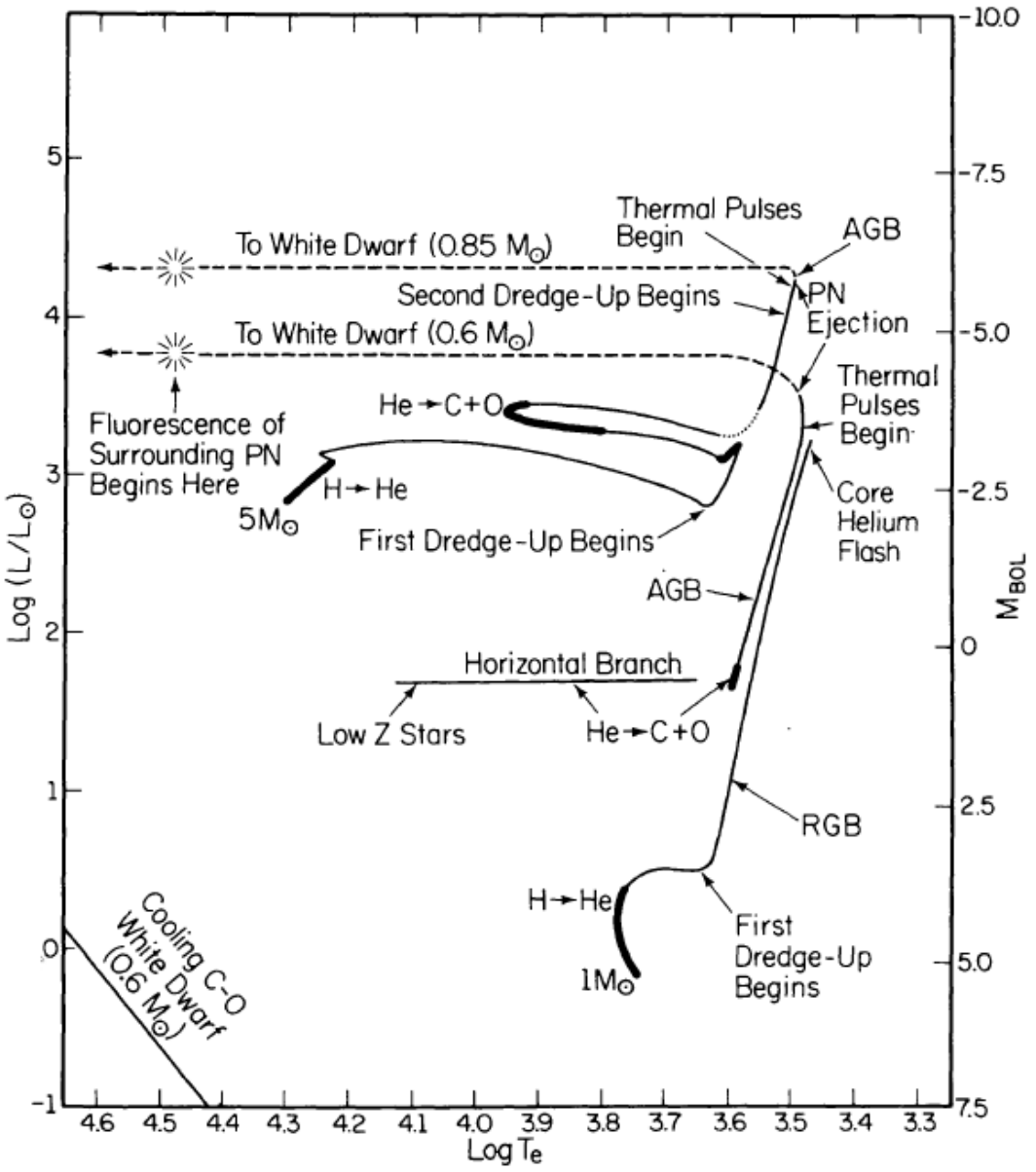

FIGURE 1: The Hertzsprung-Russell diagram depicting the phases of stellar evolution for a 1 $M_\odot$ and a 5 $M_\odot$ stars. From Iben (1991).

0.1 Current paradigm of PN formation

In the current scheme of stellar evolution, PN are the products of the evolution of Sun-like stars. At the end of their lives, stars with masses between ~ 0.8 and ~ 8 $M_\odot$ will leave the main sequence (MS) on the Hertzsprung-Russell (HR) diagram and begin their ascent on the Red Giant Branch (RGB; the evolution can be followed on Figure 0.1).

At this moment, the main nuclear reaction that was happening in the stellar core, the fusion of hydrogen via proton-proton reaction and CNO cycle, slows down due to a shortage of hydrogen. The pressure and temperature inside the core increase. The star has left the main sequence. During this phase, the core composed of inert helium ashes contracts as no nuclear reactions balance the star's gravitational force. At this stage, the helium core is surrounded by a hydrogen burning shell. When the core contracts and releases gravitational energy, this shell heats up as well and the rate of thermonuclear hydrogen burning increases. This sudden increase in energy production does work on the star's atmosphere which expands in response. In the expanding and cooling outer layers, molecules form and the opacity of the medium increases. Convection now transports the excess energy out and the star brightens; the ascent on the RGB has started. The cooling down of the envelope associated with a decrease in the star's effective temperature results in a reddening in the star's spectral type from its main-sequence spectral type down to an early M-type. This is why the RGB is "red". The external layers of the star expand from a radius of $\sim$ 1 $R_\odot$ to $\sim$ 100 $R_\odot$. The star's luminosity class changes from main-sequence to giant (the luminosity increases by a factor $\sim$ 1,000 for a solar-mass main-sequence star). As the envelope expands and cools down, convection becomes the major mechanism of transport of energy, the convective layer extends deeper in the envelope until it reaches layers in which carbon fusion has taken place. The convection mechanism lifts up gas that has undergone nuclear processing elements to the stellar surface and the star's metallicity changes for the first time since its main-sequence life. This process is called the First Dredge-Up. During the RGB phase, the star will migrate upward in the HR diagram. As the star expands, the envelope becomes gravitationally less bound and winds start to slowly deplete the stellar envelope mass. The collapse of the helium core continues until the inner temperature reaches $\sim$ 10^8 K.

At this stage the evolution of the star will depend on its mass. If the star is less massive than 1.8 $M_\odot$ (Herwig, 2005), its core reaches this temperature in a dense, electron-degenerate medium. The triple-α process that fuses helium into carbon starts and releases energy that is used only to heat-up the degenerate core. As the nuclear

rate of the triple α reaction is strongly dependant on temperature ($\propto T^{40}$) and the core is heated-up, the fusion of helium creates a nuclear runaway called the helium flash. The flash happens in the core but is not visible outside the star. Instead, the energy released by the flash is used to lift the degeneracy in the core. Several episodes of helium flash may be necessary before the core reaches a stable state of helium burning. The helium fusion phase heats-up the core that, in its non-degenerate state, expands, slowing down or stopping the hydrogen-burning shell and therefore induces a contraction of the envelope. Once the star is in equilibrium, it spends about $\sim 10\%$ of its main-sequence lifetime burning helium into carbon in the core (Herwig, 2005) on the horizontal branch (HB), or helium MS. Stars with masses between 1.8 and 8 $M_\odot$ will not go through a core helium flash. For these objects, the core ignites helium quiescently. Once the helium fuses in a stable regime, these stars evolve to the red side of the HB in the HR diagram, also known as "red clump".

Once helium is exhausted, a stage similar to the RGB phase begins, known as the Asymptotic Giant Branch (AGB) phase. Once again, as core helium is exhausted, no nuclear reaction takes place in the core and hydrostatic equilibrium is broken. The core contracts and in reaction the external layers are pushed away by the helium burning and hydrogen burning shells surrounding the C-O core. This constitutes the first part of the AGB phase (early-AGB). The star ascends the AGB branch parallel to the Hayashi track once again.

At the base of the AGB, similarly to the RGB phase and the exhaustion of hydrogen in the core, convective mixing processes take place and carbon and nitrogen are brought-up to the surface in convective loops. This second episode of altering the star's metallicity is the second dredge-up. After helium has been exhausted, the main source of energy in the AGB star is the hydrogen burning shell. Helium formed from the fusion of hydrogen will sink in the core and build-up an additional shell of highly compressed, degenerate helium. When this helium shell mass increases, the helium shell suffers a flash, expanding the envelope and by so slowing down the fusion of hydrogen in the hydrogen burning shell. Once this new episode of helium burning stops, the star will once again collapse onto itself, the contraction will allow the continuation

of hydrogen-burning. This alternation of helium and hydrogen burning phases lasting about 100,000 years is called the thermally-pulsating AGB (TP-AGB) and characterises the second phase of the AGB star evolution, the thermally pulsating AGB. The AGB star undergoes an alternation of $\sim$ 10 to $\sim$ 20 helium shell flashes. The star loses between 50% and 90% of its mass as it evolves, mostly during the TP-AGB. A late last pulse may create a hydrogen-deficient star and offer an explanation for born-again objects (Werner & Herwig, 2006).

During each thermal pulse, the star's outer layers change from radiative to convective and at the end of each helium burning phase, carbon synthesised in the helium burning shells is transported to the stellar surface. The series of all these episodes of enrichment of the stellar metallicity by convection constitutes the third dredge-up. The star's chemistry is also altered by the production of heavy elements through slow neutron capture processes (s-process) happening mostly between the hydrogen and a helium intershell layer (Herwig, 2005).

Stars with masses between $\sim$ 4 and $\sim$ 8 $M_{\odot}$ are the progenitors of Type I PN[1]. In these stars a process called Hot-Bottom Burning (HBB) takes place during the AGB phase. The hydrogen-burning shell and the convective layers are in overlapping regions. The more massive the core and envelope the more the hydrogen-burning shell and the convective layers are in contact. As a result the products of hydrogen-burning are continuously convectively mixed and brought to the surface, which results both in a more luminous star and altered abundances. During HBB, carbon is converted into nitrogen. As a consequence, the envelope displays high helium and nitrogen abundances and a lower C/O, as well as other nucleosynthesis signatures such as lithium production (Herwig, 2005).

At the end of the AGB, the envelope is less gravitationally bound to the core and

[1]The PN typology has been introduced by Peimbert (1978). It originally contained four types of PN classified in decreasing heavy element abundances as follows: Type I, He and N rich ; Type II, intermediate population ; Type III, high Galactic velocity and Type IV, halo stars. Nowadays, it is little used by the community apart from this type of objects that keep the name "Type I PN". A modern attempt of conciliating PN types with common PN parameters has been made by Phillips (2005).

an intense mass-loss phase starts called the "superwind". In spite of much work on the topic (Salpeter, 1974; Knapp & Morris, 1985; Wachter et al., 2002; García-Segura et al., 2005; Lagadec & Zijlstra, 2008), the mechanism that triggers the superwind is not well-understood. In the current understanding, the superwind is described in a two-step process: first, pulsations in the star lead to formation of dust due to shocks in the expanding envelope, leading to slow winds with a typical speed of $\sim$ 10 km s^{-1} for a mass-loss rate of $\sim 10^{-7}$ M$_{\odot}$ y^{-1}. Second, radiation pressure pushes outward the newly created dust while the gas is carried along by friction with dust. The mass-loss rate suddenly increases to as much as $\sim 10^{-4}$ M$_{\odot}$ y^{-1} (Delfosse et al., 1997). This model – dubbed the interactive stellar wind when it has been introduced (Kwok et al., 1978), has then been enriched to become the generalised interactive stellar wind (Icke et al., 1989; Soker & Livio, 1989; Mellema & Frank, 1995; García-Segura et al., 1999).

This strong wind affects dramatically the star's structure as it quickly ejects its envelope. As the stellar envelope is being depleted, the star's effective temperature increases as the photosphere sinks deeper in the star. When the envelope reaches a critical mass of $\sim 10^{-3}$ - 10^{-4} M$_{\odot}$, the mass-loss rate decreases to $\sim 10^{-8}$ M$_{\odot}$ y^{-1} and velocities rise to 200-2,000 km s^{-1} (Perinotto, 1989). At this stage, the star has become a post-AGB star. The core itself has a constant mass which dictates the nuclear reaction rate in the shell around it, therefore the star shows a constant luminosity. During the post-AGB phase, the star will heat up and move to the left on a horizontal path in the HR diagram, in a timescale between a few decades to a few times 10,000 years depending on core mass. As it heats up, the star may excite some of the circumstellar ejected material via shock-ionisation or reflection. The excited ejecta will start glowing before the PN phase, and is thus called a pre-PN.

When the effective temperature of the star reaches $\sim$ 30,000K (Frankowski, 2003), the star – reduced to what was originally its core – is hot enough to start the photo-ionisation of the hydrogen, helium and some of the heavier elements present in the ejected envelope.

The atmosphere is now a nebula shining primarily by forbidden line emission. The star's core residue is a CSPN. The nebula itself exists only for a few tens of thousand

years before it disappears after its expansion (at a typical velocity of a few times 10 km s^{-1}) and interaction with the surrounding interstellar medium (ISM). When the CSPN exhausts its last hydrogen or helium-burning shell, it starts dimming to become a white dwarf (WD).

0.2 From spherical to asymmetric, the problem of shapes

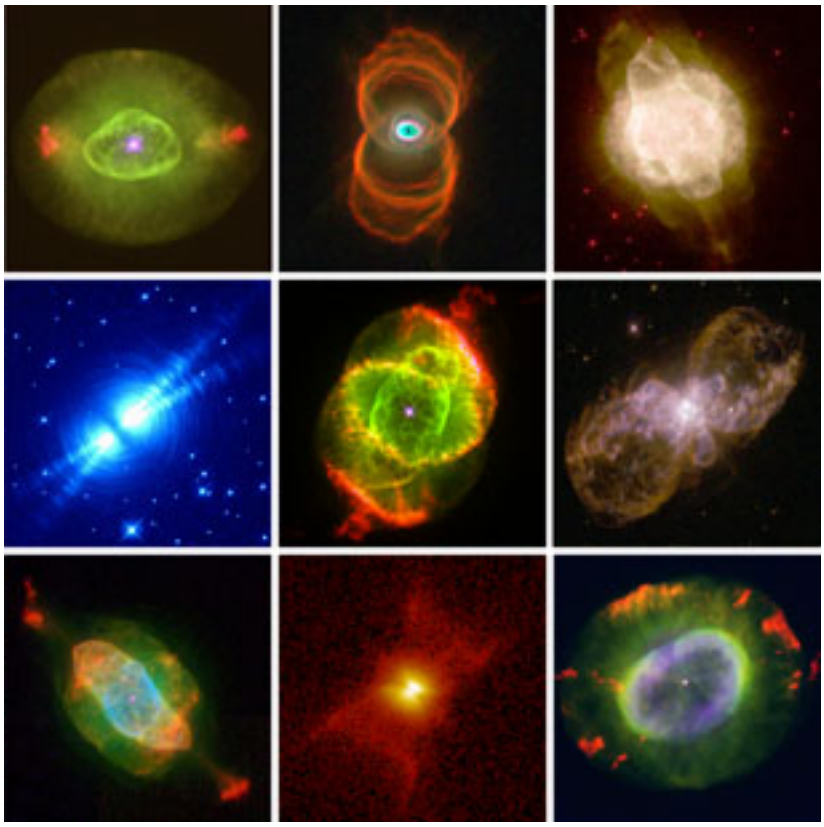

Figure 2: Most spectacular PN observed with the Wide Field Planetary Camera 2 onboard the Hubble Space Telescope. Most of them show exotic features, such as jets, lobes, knots and bow-shocks. Credit: Bruce Balick. Source: http://www.astro.washington.edu/users/balick/WFPC2/

One of the major problems that the PN research community has been facing for about thirty years is the explanation for the observed shapes of PN. Indeed, whereas one might expect a spherical nebula after the spherical expansion and quasi-spherical

mass-loss of the star, only $\sim$ 20% (Parker et al., 2006; Jacoby et al., 2010) of PN are spherical. The other 80% are elliptical, bipolar or irregular in shape, show lobes or present special features like point symmetry, jets, bow-shocks or an off-centered central star (see Figure 2).

There is no known simple argument that explains such a high fraction of non-spherical PN yet. Several mechanisms may be able to perturb the spherical distribution of the nebula and account for the observed morphologies: the influence of the magnetic field during the AGB superwind phase could create an axisymmetry in the ejecta. However as described in the next section this mechanism cannot operate alone. Another mechanism, the existence of an interacting companion - stellar or substellar - around the central star, is viable to explain the observed shapes.

A description of these two channels is presented in the following sections.

0.2.1 Stellar magnetic fields and rotation as primary shaping agent

Historically, the first explanation of the existence of non-spherical PN relied on the apparition of an equatorial density enhancement in the AGB mass-loss. With this assumption in place hydrodynamic simulations were carried out that could reproduce elliptical and bipolar PN (Icke, 1988; Icke et al., 1989; Mellema et al., 1991; Icke et al., 1992; Frank & Mellema, 1994; Dwarkadas et al., 1996). However, in all these studies, the equatorial density enhancement was built-in the model and not the result of the simulation itself. To respond to the need for explaining the presence of the density enhancement as a result of standard evolution of late-stage Sun-like stars, García-Segura et al. (1999) carried out a 2D magnetohydrodynamical simulation that included an AGB superwind in a rotating, magnetic star from which they could derive equatorially confined winds leading to any of the observed PN morphologies. They concluded that the majority of PN could come from single stars that had the appropriate rotation and magnetic fields. Matt et al. (2000) showed that an equatorial enhancement and then a disk can be obtained if the star has a simple dipole magnetic field of only a few Gauss

at the surface of the star. At the same time, the observational discovery of magnetic fields in proto-PN (Etoka & Diamond, 2004) and PN (Jordan et al., 2005) as well as the modeling of this problem (Pascoli, 1997; García-Segura et al., 1999; Blackman et al., 2001) have supported the shaping of the nebula thanks to the action of the magnetic field on the outflow during the superwind episode.

Later, two papers came to argue that magnetic field could probably not be the main shaping agent of PN. Soker (2006) relied on angular momentum and energy considerations to show that during the AGB wind phase, the feedback between rotation and magnetic field prevented the existence of a large scale magnetic field for long enough to allow the shaping of the nebula. They claimed that local magnetic loops in star spots could survive but could only exert a secondary role in shaping the circumstellar winds. This argument was supported by Nordhaus et al. (2007) who showed that the magnetic field could survive only if the envelope dynamo was resupplied by tapping angular momentum from the anisotropic-convection layer in a similar manner than in the Sun (Ruediger, 1989; Ruediger & Hollerbach, 2004). Otherwise maintaining the magnetic field would drain too rapidly the differential rotation from the envelope via turbulent dissipation and Poynting flux (Blackman, 2004) and the magnetic field would quench itself. The models of García-Segura et al. (1999), successful at reproducing the varied shapes of PN from the action of magnetic field and rotation - did not include feedback of the gas onto the field. The magnetic field was assumed to be constant.

Both Soker (2006) and Nordhaus et al. (2007) studied how the presence of a companion to the AGB star could act to resupply the field. Since then, the debate has been rekindled to understand to what extent the presence of a companion, magnetic fields and rotation were coupled to yield the observed shapes of PN, leading to the idea that magnetic fields and rotation could act as secondary shaping agents (see Section 0.2.3). Detections of magnetic fields in post-AGB stars are still being sought using polarisation observations (e.g. Vlemmings & van Langevelde (2005), Vlemmings (2012), Vlemmings (2014), Lèbre et al. (2014)). In spite of such efforts, it remains undetermined how common magnetic fields are in evolved stars and how the field structure and intensity is

linked with the mass-loss process. Observationally, Jordan et al. (2012) conducted a new survey to detect more magnetic fields in CSPN. They found none, and announced that their previous detections were spurious due to calibration errors. Independantly, Leone et al. (2014) carried out another polarimetry survey and found no detectable magnetic field in their CSPN sample.

0.2.2 Binaries as shaping agents

Magnetic fields are not by themselves a viable mechanism for explaining the rupture of the star's spherical symmetry leading to the various PN shapes. In the stellar realm, the most natural way to break a star's symmetry is the presence of a companion.

The companion can influence the shaping of the nebula in different ways. We follow the classification of Soker (1997) that is based on how the companion can supplement angular momentum to the mass-losing star, and is thus associated with binary separation. For more details on the processes described in this section, the reader is invited to consult the references therein. There are four classes of interactions:

- *Very wide binaries:* These are the systems for which the orbital period is much longer than the lifetime of the PN ($\sim 10^5$ years) corresponding to a separation $\gtrsim$ 5000 AU. The companion has no impact on the shaping. The only feature that can be formed is a bubble inside the nebula similar to those stemming from inhomogeneous mass-loss and instabilities inside the nebula. The bubbles can be formed only if the companion is a red giant.

- *Wide binaries:* They are the systems whose orbital periods are comparable to the lifetime of the PN, corresponding to separations of 100 to 1,000 AU approximately. The nebula is shaped by the motion of the mass-losing star wobbling around the system's centre of mass due to the presence of the companion. The interaction results in a PN that shows a slight deviation from axisymmetry and an off-centre CSPN. If the system separation is of a few times $\sim$ 100 AU, the nebula will be axisymmetric but if jets are present they will be bent in the same direction.

- *Close binaries that avoid common envelopes:* These are the systems where gravitational interactions shape the PN without the companion being engulfed in the ejected material, or at least during most of the primary's mass-loss phase. Tides will play an important role in the shaping: the primary will be spun-up as the companion separation shrinks enhancing the mass-loss. If the orbital eccentricity of the system is high, mass-loss variations during the companion's orbit will shift the nebula with respect to the system's centre of mass. Binaries with a period of a few $\sim$ 100 years and possessing jets and a disk will start precessing and create a point-symmetric nebula. Quadrupolar PN made of two pairs of lobes might come from precessing binary systems with periods of a few $\times \sim$ 10 years. Accretion is another shaping mechanism. A companion accreting the primary's winds will create an equatorially enhanced mass-loss leading to a bipolar nebula. This mechanism applies to the shaping of type I PN. High nebular expansion velocities ($\gtrsim$ 100 km s^{-1}) imply that the companion is a WD and the system is a symbiotic. Systems with separations between $\sim$ 20 and $\sim$ 50 AU will undergo little accretion generating modest density contrasts in the mass-loss and create an elliptical PN.

- *Close binaries that form common envelopes:* These are the systems where the companion is close enough to be engulfed by the AGB envelope. It will spiral inward through the primary's outer envelope, releasing its orbital energy to unbind the envelope from the system (in case the companion does not have enough orbital energy, it will end by merging with the primary's core). This interaction class includes binary systems whose initial separation is smaller than one AGB radius or systems that have separations $\gtrsim$2-3 stellar radii and are captured tidally. Observed post common-envelope systems are surrounded by elliptical or bipolar and may have jets. The common envelope can also excite non-radial pulsations in the primary's atmosphere evolving into axisymmetric mass-loss. If the secondary is low-mass (even substellar) and its core merges with the AGB's core, ansae and

jets are likely to form. Close systems undergo intense angular momentum transfer and the influence of substellar companions may not be negligible. They will create similar but less pronounced features. Their mass is insufficient to put the system into corotation so they are likely to enter a common envelope, thus the main parameters for the system's evolution is its separation and the primary's radius. Substellar companions possess less gravitational energy and are more likely to collide with the primary's core before the envelope is released, therefore it is expected that most elliptical PN will not have a companion surrounding their central star. A disk and two jets can form whose migration during the nebula's expansion will form ansae. Another mechanism for jet formation is the ejection of a low-mass envelope by a close companion along the axis of symmetry during the late AGB phase.

Observationally, companions have been detected surrounding post-AGB stars. Van Winckel (1999); van Winckel (2003) presents a sample of $\sim$ 30 close-binary, naked post-AGB stars detected from radial velocity measurements. After a 20 year light variation and velocity variation survey in 24 proto-PN, Hrivnak (2012) concludes that all of them show flux variations ascribable to pulsations. No photometric signature of a binary is observed. This is even more compelling noticing that no proto-PN has a round morphology.

We have seen that companions can act as a reservoir of angular momentum that is tapped during the primary's mass-loss to give its shape to the PN. They can also resupply the primary's dynamo, generating magnetic fields.

0.2.3 Magnetic fields as a secondary shaping agent

As explained in Section 0.2.1, the magnetic field present during the AGB superwind phase does not appear to be a viable shaping mechanism of its own as it quenches itself Soker (2006); Nordhaus et al. (2007). Nonetheless, a companion is so efficient at redistributing angular momentum to the envelope that it can resupply the envelope differential rotation and reseed the primary's internal dynamo, allowing the magnetic

field to survive. When the magnetic field can shape the PN because it is sustained by the presence of an orbiting companion, it is qualified as secondary shaping agent. In this case the models of shaping using the influence of the magnetic field on the ejecta can apply.

Before concluding that magnetic fields cannot, by themselves, account for the varied PN shapes, Soker (2006) summarises the different assumptions and models of interaction between the primary's magnetic field and the envelope:

- the magnetic field is important on the AGB stellar surface. This mechanism fails with a stellar field only, but can work if a companion is spinning the envelope. In this case, the magnetic field plays only a secondary role compared to the companion's influence. Models using this mechanism suffer from an unrealistic angular velocity gradient inside the envelope creating a strong magnetic field that would in turn enforce a uniform rotation (as seen in Section 0.2.1).

- The magnetic field is weak at the stellar surface, but plays a dynamical role at large distances from the surface. Here as well a companion spinning the envelope would allow this process, but the magnetic shaping would be minor compared to the shaping from the companion. Models using this process cannot explain point-symmetric PN that result from precession.

- There is only a local magnetic field at the surface creating cool spots and filaments. In these regions dust is formed and undergoes radiation pressure from the inner layers, enhancing the mass-loss. This mechanism operates even with very slow AGB surface rotation and accounts for moderately elliptical PN. The role of the magnetic field is to trigger a higher concentration of cool spots near the equator and affect the geometry of the mass-loss. It is not a dynamical role as such.

- The magnetic field creates jets from an accretion disk surrounding the primary or the companion. The jets shape the ejecta. This mechanism is different to the ones above. In this case the energy source is gravitational: the accreted gas

is converted into magnetic energy. The magnetic field is not amplified by the companion but by the accretion around either the primary or the secondary. It shapes only a small fraction of the mass of the ejecta, if it does at all.

These processes might take place and come to complement the prevalent shaping of the PN exerted by the companion.

0.3 The Binary Hypothesis

As binaries seem so efficient at shaping the nebula the hypothesis that non-spherical PN come from binary interactions is natural. The Binary Hypothesis (De Marco, 2009) states that non-spherical PN have been exclusively or preferentially shaped by a companion orbiting the central star, through the interaction between the mass lost during the AGB phase and the companion(s) or via a mediating magnetic field. The main parameters influencing the morphological features of the PN are the binary system's separation, total stellar mass and the mass ratio. Since $\sim 80\%$ of PN are not spherical, this would imply that most CSPN have been influenced by a companion. Even accounting for a number of mergers or the action of planets acting as companions we may expect that a large fraction of PN may still harbour a binary. This is different from the current paradigm of PN formation described in Section 0.1, whereby PN are the product of all single and binary stars within ~ 1 and ~ 8 $M_{\odot}$.

Assuming that $\sim 50\%$ of all PN progenitors are binary stars or multiple systems (see Section 0.5) and that only about half will ever interact (i.e. enter common envelope or suffer some other kind of weak interaction, see Section 0.2.2 and Figure 4) and of those, about half again will interact on the AGB then only 10-15% of eligible progenitors under the current PN-forming paradigm would actually make a PN. In the strict version of the Binary Hypothesis, non-spherical PN, i.e. $\sim 80\%$ of the PN population come from binary interactions. This implies that $\sim 80\%$ of PN derive from $\sim 10-15\%$ of eligible main-sequence stars. This also implies that a large fraction of 1-8 $M_{\odot}$ stars make an invisible or under-luminous PN Soker & Subag (2005).

0.4 The binary fraction of CSPN to test the Binary Hypothesis

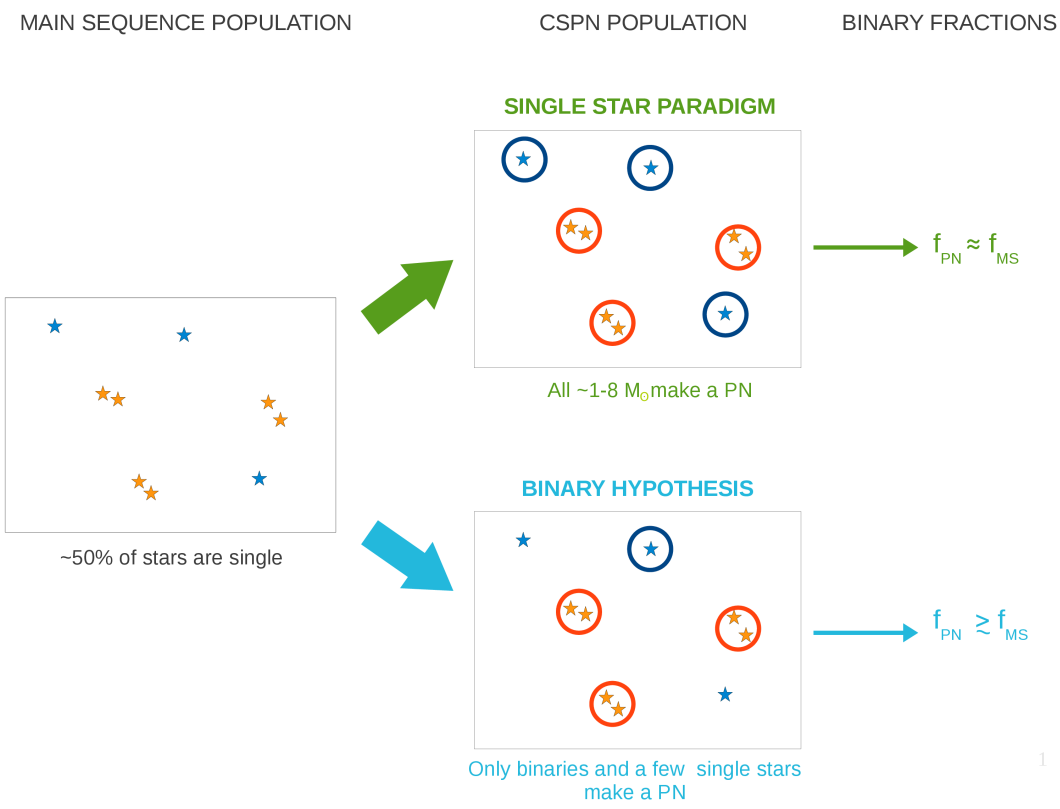

FIGURE 3: Testing the binary hypothesis using a comparison of the binary fraction of CSPN (f_{PN}) and the main-sequence one (f_{MS}).

For the past 30 years great progress has been made to link PN shapes and stellar multiplicity, as detailed in Section 0.2.2. Still no definitive result has been able to support the Binary Hypothesis conclusively from the analysis of CSPN multiplicity. In this study, we adopt the following different strategy: if in the Binary Hypothesis PN come mostly from binaries, then determining the fraction of binary CSPN can afford a first test of the Binary Hypothesis. By comparing the frequency of binaries in the PN progenitor population (the main-sequence population within appropriate mass limits) with the CSPN population, we can start to assess the efficiency of the binary channel for forming PN. *If the binary fraction is higher in the CSPN population than predicted from*

the main-sequence progenitor population, then PN are indeed more favorably formed in multiple systems. On the other hand, a CSPN population whose binary fraction is that predicted by the main-sequence progenitor population would support the current scenario whereby all eligible stars, be they single or binary, make a PN. Figure 3 summarises how these two scenarios lead to the binary fraction being a diagnostic for testing the Binary Hypothesis.

The success of this work relies on the comparison between the main-sequence binary fraction with the CSPN one. To carry out our study, we start by presenting the main-sequence binary population, after what previous predictions and estimations of the CSPN binary fraction are reviewed.

0.5 The main-sequence binary fraction and the period distribution

Several studies have been carried out to determine the main-sequence binary fraction. Abt & Levy (1976) carried out a radial velocity survey of 135 main-sequence stars with spectral types F3 to G2. They determined observed frequencies of single : double : triple : quadruple systems of 42 : 46 : 9 : 2 percent and estimated a median period of 14 years for the single-peaked period distribution. Following the same method but using a volume-limited sample instead of a magnitude-limited sample (to avoid biases favoring double-line spectroscopic binaries that are brighter at a given spectral type and have short periods), Duquennoy & Mayor (1991) published a stellar multiplicity study of the nearby Solar-type Galactic population using the CORAVEL spectrometer for 291 stars, from which they built a sample for the analysis of stellar multiplicity made of 164 primaries within the spectral range F7 to G9. They determined that the period distribution can be well represented by a Gaussian with a central period of 180 years, and a fraction of binary G-type dwarfs of about $\sim 60\%$ (Tokovinin 2008 estimate a binary fraction of 62% for their work). Raghavan et al. (2010) collected data on a

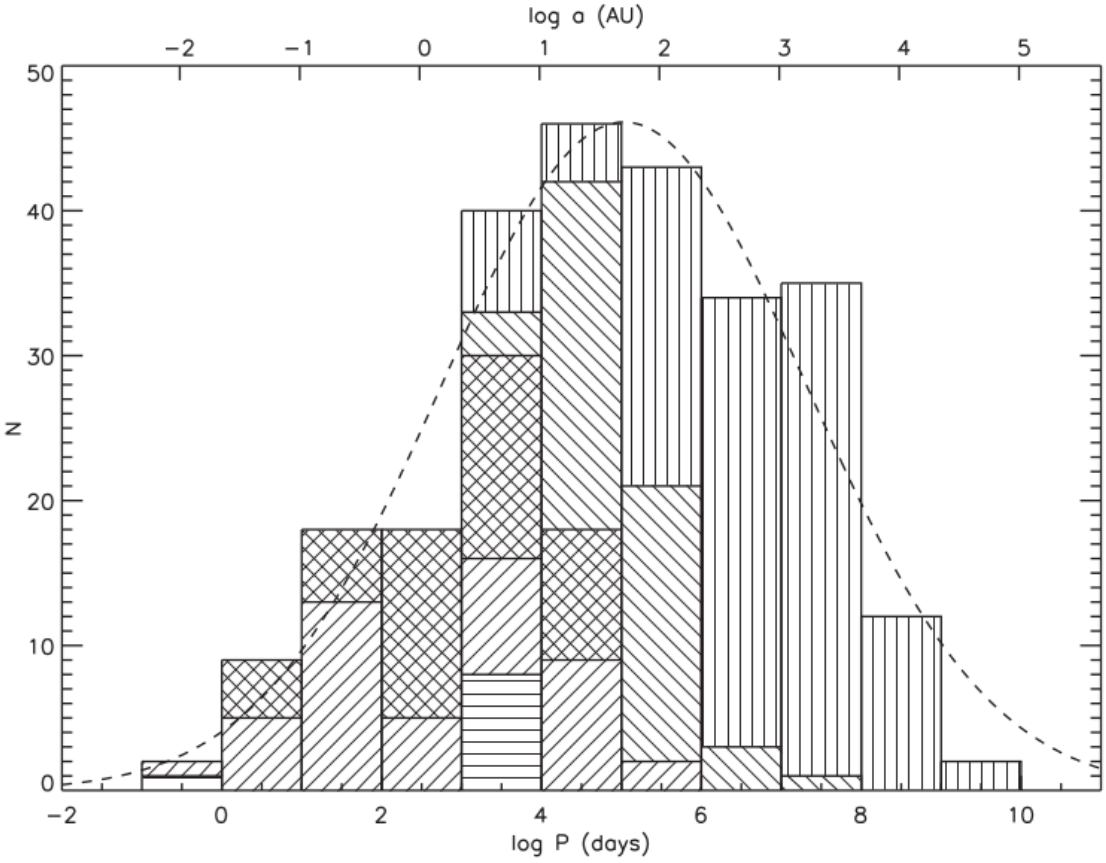

Figure 4: Main-sequence period distribution. The distribution, built from 259 confirmed binaries, is well fitted by a Gaussian centred on log P=5.03 with a width of σ=2.28. The semi-major axes shown in AU at the top corresponds to the periods for a system with a total mass of 1.5 M, the average value for all the pairs. From Raghavan et al. (2010).

sample of 454 $\sim$ F6-K3 main-sequence stars within 25pc to the Sun. Combining long-baseline interferometry for very close companions, speckle interferometry, multi-epoch imaging and radial velocity monitoring, they deduced multiplicity fractions of 54$\pm$2 : 34$\pm$2 : 9$\pm$2 : 3$\pm$1 for the single : binary : triple : higher-order populations. They find a log normal period distribution peaking at $\sim$ 300 years shown in Figure 4. These studies are in good agreement: $\sim$ 50% of Galactic main-sequence stars are single. In our work we will refer to the numbers of Raghavan et al. (2010) as they benefited from more recent observations and from a larger sample size.

Multiplicity varies according to stellar mass: almost all massive stars stand in pairs whereas companions are more rare for cool dwarfs (Raghavan et al. 2010 and references

therein). It is necessary to make sure that these multiplicity studies reflect the actual population of PN progenitors and that they are not biased towards or against binarity because of their spectral type distribution. The numbers obtained by Raghavan et al. (2010) are a statistical combination of a "hot" sub-sample made of F6-G2 stars and a "cool" sub-sample made of G2-K3 dwarfs. The median mass for PN progenitors is 1.2 $M_{\odot}$ (Moe & De Marco, 2006). The hot sample is centered on an F9V spectral type whose mass is comprised between 1.1 and 1.2 $M_{\odot}$ (De Marco et al. (2013), hereafter DM13). We thus used the hot sample statistics to reflect our PN progenitor population for which the multiplicity fraction is of $50 \pm 4\%$.

A note on mergers: among the common envelope binaries described in 0.2.2, a fraction of them will not survive a the common-envelope episode and will result in a merger. According to the population synthesis of Han et al. (1995), $\sim$13% of current CSPN are the result of such merged systems. We do take into account in our statistics the common-envelope systems that do not survive the primary's RGB phase (see Section 6.3), however how the common-envelope AGB phase happens is not well known and those systems that merge during the AGB cannot be excluded as previously. Therefore, our MS population does include those stars that will merge on the AGB. These merged systems will appear as single when we observe themand are therefore included in the pool for single stars, that accounts additionnally for PN that might have undergone substellar interaction as well. For this reason, the binary fraction we estimate is a lower value and our approach is conservative.

0.6 Predictions and determinations of the binary fraction of CSPN

The idea of obtaining the binary fraction of CSPN is not new, both theoretically and observationally. In the two next sections I review past efforts aiming at determining this number.

0.6.1 Theoretical approaches

Population synthesis studies have focused on determining the CSPN binary fraction by evolving a zero-age main-sequence binary population represented by a given period distribution, after a choice of prescriptions for stellar evolution and binary interactions. Yungelson et al. (1993) evolved a population of binaries and found that 20% of the resulting CSPN were single while 66% were CO white dwarfs orbited by main-sequence companions. One third of their PN are formed in close-binaries and the other PN in wider binaries. Similarly, Han et al. (1995) used a population of binaries with a period distribution peaking at $\sim$ 100 years and determined that 34-43% of binary CSPN are influenced by binary interactions. A third of these CSPN resulted from merged systems, another third from post common-envelope systems and the last third from wider binary interactions.

Moe & De Marco (2006) used population synthesis to determine the total number of Galactic PN if all 1-8 $M_{\odot}$ stars make a PN. They found 46,000±13,000 Galactic PN at odds with the 8,000±2,000 determined from observationally based estimates (Jacoby, 1980; Peimbert, 1990, 1993). This mismatch between observation and synthetic population estimation could be brought into agreement if only a fraction of all PN progenitors made a PN. The Binary Hypothesis offers a framework for such a scenario (this comparison is discussed more in details in De Marco 2009).

0.6.2 Previous efforts to estimate the CSPN binary fraction from observations

A suite of different techniques is available to detect binaries at different separations. Here I review previous studies aiming to detect binary CSPN to estimate the binary fraction.

The long-period binary fraction

The only systematic study for finding resolved binary CSPN is the one of Ciardullo et al. (1999). They used the Hubble Space Telescope (HST) to search companions in

113 nearby, low surface-brightness PN. By design they could only detect long-period binaries, in this case those resolved by the HST (with a resolution limit of $\sim 0.05''$) . They found 10 probable associations and 6 additional possible associations, yielding a long-period binary fraction of 9-14%.

The close-binary fraction from photometric variability surveys

Photometric variability is a well-known, reliable technique for finding binaries. The variation is caused by irradiation from the bright hot CSPN onto the companion, ellipsoidal deformation of the stellar envelope or envelopes due to tides and eclipses when the system is viewed edge-on with respect to the orbital plane. Two studies have contributed in building a representative sample of short-period binaries. Bond (2000), supported by the precedent efforts of Bond (1979), Bond (1990), Bond et al. (1992) and Bond (1995) lists 16 known close-binary PN with periods ranging from 3 hours to 16 days and estimate a close binary fraction of $\sim 10\%$. De Marco et al. (2008) reviewed this fraction to 10-15%. Miszalski et al. (2009) used the microlensing OGLE-III[2] survey to look for periodic variable CSPN and found 21, more than doubling the short-period binary sample size. They deduced a post common-envelope binary fraction of 12-21% in good agreement with the previous findings.

The radial velocity surveys

Radial velocity surveys aiming at finding the Doppler signature of a companion have also been carried out. Méndez (1989) obtained high-resolution spectrograms of 28 objects and found that 18% were variable but stellar wind as a source of variability could not be excluded for some objects. Sorensen & Pollacco (2003) led a similar study by acquiring intermediate resolution spectra of 45 PN. They found that 40% of their CSPN were showing velocity variations consistent with binarity. De Marco et al. (2004) studied 11 CSPN and found a high variability fraction of 91%. Last Afšar & Bond (2005) observed 19 CSPN and deduced a variability fraction of 37-50% with their intermediate resolution setup. All these surveys suffer from the fact that the discovered

[2]Optical Gravitational Lensing Experiment, http://ogle.astrouw.edu.pl

variables are not periodic. De Marco et al. (2007) re-observed and analysed 4 echelle spectrograms of the sample of De Marco et al. (2004) and found that all studied objects were variable, although no periods were determined. However, winds or pulsations did not explain the variability either. Although this method is sensitive to short-period binaries up to separations of a few $\sim$ 100 days and seems ideal to cover the gap in separation between short and long-period binaries, its feasibility is not clear as a high signal-to-noise ratio (SNR) is required, the interpretation of the results is delicate and a long time coverage might be necessary to detect the long-period binaries. Recently, Van Winckel et al. (2014) detected two radial velocity binaries with periods between 1.5 and 3 years. One of them – BD+33 2642 – is from the sample of De Marco et al. (2004, 2007) and consistent with those results. This may show that a population of binaries with periods longer than a few days does indeed exist, but is very hard to detect.

The intermediate period binary fraction from IR excess surveys

Another method is available to access these intermediate-period binaries. By comparing the expected colours of a CSPN in the near-infrared (NIR) with its observed, dereddened ones, it is possible to detect the NIR flux excess coming from a companion in unresolved CSPN binaries. The first systematic study available in the literature is the one of Frew & Parker (2007). They tested for NIR excess in the seven close-binaries and eight visual binaries known at the time within the 1 kpc volume-limited sample of Frew (2008) and validated the technique by concluding that all of them would have come out as strong binary candidates due to their NIR excess if they had been binary systems yet undetected. They then applied the search for NIR excess to the rest of the 1 kpc sample and found 4 new detections within the 19 remaining objects. They concluded that 52-58% of all CSPN were found in binaries. Their statistics are drawn from all techniques and do not apply to NIR excess search only, nor can we say that their binary fraction from the NIR excess technique is 4/19 as they excluded successful detections that were known from other techniques.

The other study available in the literature is the one of De Marco et al. (2013).

They found a total binary fraction of 67-78%. This thesis is a continuation of their work: it uses the same technique and takes into account their NIR findings in the final statistics. How the technique works will be explained more in details in the next chapter. The main additions from this work to the calculations and results of De Marco et al. (2013) are

- more observed PN, building a larger selection sample
- new NIR excess detections
- a systematic testing of the photometric parameters
- additional cross-checks between objects observed in common
- a statistic determination of the uncertainty on the binary fraction

These improvements will be highlighted in the different analyses offered in this work, as well as in the final counts and statistics.

Summary

In this introduction, I have presented the current understanding of PN formation and raised the problem of PN shaping thanks to both magnetic fields and the presence of a companion to the CSPN. The Binary Hypothesis has been stated as well as how to use the binary fraction of CSPN to test it. Finally, efforts for estimating the main-sequence and CSPN binary fraction have been detailed.

All the methods described in the last section have proven to be efficient for detecting binaries with a bright primary ($V \lesssim 15$). However detecting the faint population of Galactic CSPN necessary for completion of the sample is difficult, as the observations and analyses become more demanding in time and means, and the results may be difficult to interpret.

These methods - except for the detection of visual binaries - have been fully or partially exploited in this thesis to detect new binary CSPN. Emphasis has been put on detecting binaries with the NIR excess technique. These studies will be shown in

Chapters 1, 2 and 3. The photometric variability technique has been tentatively used to exploit the by-product images of our observations in the optical and are presented in Chapter 4. The radial velocity technique has been employed to look for companions in 14 VLT/UVES CSPN spectra. Their analysis is described in Chapter 5.

In the next chapter I present our NIR-excess detection algorithm.

Chapter 1

The NIR excess technique

The NIR excess detection technique consists in comparing the intrinsic NIR colours of a CSPN, as a function of temperature and assuming that the star is single, with the observed ones. If the CSPN is redder than the colours expected for a single CSPN, it is possible that the NIR emission comes from the thermal emission of a cool companion. The obvious difficulty of this technique is that our CSPN are bright and can outshine the faint companions by large factors.

In this chapter, previous efforts of using this technique are reviewed as well as the limitations they suffered from. I then present our method and its advantages and drawbacks, notably the necessity of high quality photometric data. I finish by presenting the volume-limited sample of Frew (2008) from which we have drawn the target list for our observations.

1.1 Previous efforts and limitations

A certain number of independent studies have discovered binary CSPN thanks to the NIR excess technique. Zuckerman et al. (1991) have led a $K-$band survey (for characteristics of the different optical and NIR filters used in the studies presented in this document, see Table 1.1) on 30 CSPN. They found that 50% of them displayed a K-band excess. The excess was attributed either to a cool companion, ionised gas or hot dust. They announced having little doubt regarding the stellar nature of their three

binary detections: an M2V-M8V companion orbiting around UU Sge, the CSPN of A 63 (UU Sge was already known to be an eclipsing binary), an M5V-M6V companion around the CSPN of EGB 6 (the flux excess is of more than 1.5 magnitudes) and one around NGC 6853 (for this object the companion was resolved but blended with the CSPN on their images). Much later, as mentioned in Section 0.6.2, Frew & Parker (2007) proceeded to a systematic search for NIR excess using the Deep Near Infrared Survey[1] (DENIS) and the 2 Micron All Sky Survey (2MASS, Skrutskie et al. 2006) survey for the 33 CSPN magnitudes within the 1 kpc volume-limited sample of Frew (2008) and found 4 NIR excesses at J, H or K for the CSPN of Ton 320 (whose NIR excess was already known from a similar study of the WD population led by Holberg & Magargal 2005), Lo 16, EGB 9 and HbDs 1. Bilíková et al. (2012) have found 2 CSPN showing IR excess due to companions among a set of 72 WD and CSPN observed with the Spitzer Infrared Array Camera (IRAC) and the Multi-band Imager Photometer for Spitzer (MIPS). They reconstructed the spectral energy distributions (SEDs) for A 66 and NGC 650, using additional data from the HST WFPC $F555W$ and $F814W$-bands to deduce the V and I-band magnitudes of the companions. They pointed out that their low-detection rate (2/72) of NIR excesses due to stellar companions arose from their low sensitivity to faint companions (half of them are expected to be cooler than M3V, Farihi et al. 2005, see Chapter 6) due to a combination of bright CSPN and a large measurement uncertainty. Finally De Marco et al. (2013) carried out a survey of 27 CSPN and detected 4 and 7 excesses in the I and J-band, respectively. Their method and results are detailed later in this document.

From this review, a series of requirements and difficulties intrinsic to the technique arise:

- excess detections have taken place when the signal (colour difference) was large enough. The large uncertainties of most current archival data prevent the detection of faint companions, i.e. a large fraction of them.

- When an excess is found, the origin of the excess is uncertain: it can translate

[1]Information available at http://cds.u-strasbg.fr/denis.html

Filter	Central λ (nm)	FWHM (nm)	Filter	Central λ (nm)
U	365	66	u	355.1
B	445	94	g	468.6
V	551	88	r	616.5
R	658	138	i	748.1
I	806	149	z	893.1
J	1220	213		
H	1630	307		
K	2190	390		

Table 1.1: Johnson-Cousin and SDSS filter systems. From Bessell (1979) and the SDSS DR7 website[3].

to the presence of a companion or hot dust or gas. Previous knowledge on the targets is often required to interpret the nature of the signal.

- all I, J, H and K bands allow NIR excess detections. What is the optimal band-pass that gives a high signal for binary detection while minimising the chances of false alarm due to dust disks or shells. We know that the I band is unaffected by all but the hottest kind of dust, but it is also less sensitive to a companion.

- Optical photometry or knowledge about the target's reddening is necessary to calculate the star's observed intrinsic colours.

- The vast majority of the companions are faint, late spectral type main-sequence stars, whereas our CSPN are very bright. In addition to the difficulties for observing these faint companions, this adds a bias to our detections.

The difficulties raised here are intrinsic to the method. The only way to bypass these limitations is to develop a well-defined, robust, precision strategy.

[3]See http://www.sdss2.org/dr7/instruments/imager/index.html

1.2 The NIR excess detection method

Our method is a fine-tuned process that aims at using the technique described in the above section while avoiding or minimising the hurdles addressed therein. To look for a flux excess in a target we compare the dereddened colours of our CSPN from the best available magnitude sources, ideally our own observations (see Chapter 2) or online optical and NIR surveys with satisfactory photometric quality (see Chapter 3) to that of the intrinsic colours of a model CSPN with the same temperature.

1.2.1 Selection of the interstellar-reddening determination method

The first selection to be made is the estimator for interstellar extinction. A variety of tools is available for CSPN: measuring the nebular Balmer decrement (Tylenda et al., 1992), using Galactic dust maps from which interstellar extinction originates (the most up-to-date are from Schlafly & Finkbeiner 2011) or using a parametrised extinction law (Cardelli et al. 1989, hereafter CCM, Fitzpatrick 1999). The B and V-band magnitudes are not affected by the presence of a companion cooler than about early K spectral type (see Section 1.2.3) so we used the B and V-band CSPN magnitudes combined with an R_V=3.1 CCM extinction-law and a comparison with single stellar colours from pre-calculated stellar atmospheres to determine the dereddening of our CSPN. We cross-checked our reddening measurements using the other listed methods in the different analyses presented in the next chapters: nebular reddening in the analysis of De Marco et al. (2013), an extinction-law combined with U and B-band magnitudes in Section 2.2.4 and the dust maps from Schlafly & Finkbeiner (2011) in Section 3.2.2.

1.2.2 Selection of the ideal spectral range

The second choice regarding the method architecture lies in estimating the dereddened colour of our targets in the NIR. From the previous NIR excess attempts we conclude that the K-band is very sensitive to any cold component, either cool companions or dust, and this is prone to confusion. The I-band is safer in this regard but has a higher detection threshold for companions. The J-band is the ideal spectral band to detect

the coolest companions without being too contaminated by hot dust. In our case, dust is not problematic: while it is indeed true that a a very hot disk could create a small J excess, only ∼20% of CSPN are surrounded by disks (Clayton et al., 2014) and only a fraction of these have temperatures high enough to contribute in the J band (Bilíková et al., 2012). In addition, the J-H colour of a disk and a companion are different and it is possible to discriminate one from the other. It cannot be excluded for systems with a companion that the disk also contributes to the excess, potentially altering the spectral type detected for the companion, but the chance of a disk giving a significant NIR excess without any companion orbiting the CSPN is very small.

The need for two observing runs (one in the optical and one in the NIR) for a given set of targets make the colour determination a time and effort-consuming process, thus we chose to use the I-band magnitudes obtained during our optical observing run and use the available online surveys (namely DENIS, 2MASS and the UKIRT Infrared Deep Sky Survey (UKIDSS, Lawrence et al. 2012) to obtain our J-band magnitudes. $V-I$ and $V-J$ colours are ideal colours for our study because they offer a long spectral baseline and the V-band is mostly unaffected by the presence of a companion.

1.2.3 Calculation of the NIR excess and estimation of the companion spectral type

The last step is the comparison between the dereddened colours for our targets and the ones of the model CSPN with the same effective temperature. In this section we assume that the calibrated magnitudes of our targets and their associated errors are in hand. We call them B, V, I and J. The description of how these magnitudes are determined as well as the statistics carried out to obtain the errors will be detailed in each analysis for NIR excess search (Chapters 2 and 3).

The model stellar atmospheres have been obtained from TMAW[4], the web interface for TMAP (Werner & Dreizler, 1999; Werner et al., 2003) and TheoSSA[5] (Rauch & Deetjen, 2003). The predicted colours of single CSPN are presented in Table B1 of De

[4]Form available at http://astro.uni-tuebingen.de/~TMAW/

[5]Form available at http://dc.zah.uni-heidelberg.de/theossa/q/web/form

Marco et al. (2013) for a temperature range of 20 to 170kK, log g=6, 7, 8 and solar and H-deficient metallicities. Blackbody colours are also given. They also presented main-sequence spectral types, absolute V magnitudes, optical and NIR colours and stellar masses (their Table C1). Let the CSPN single star theoretical colours be called $(B-V)_m$, $(V-I)_m$ and $(V-J)_m$. TMAP is reliable in view of the different analyses have been successfully performed in the past years (e.g. Rauch et al. 2013, Rauch et al. 2014). Yet other model atmospheres are available and could have been used, such as the Kurucz (1979) models and Tlutsy (Lanz & Hubeny, 2003). In our timeframe, we have not carried out a test to observe the differences in colour between the different models. It is however very likely that whether obtained from Tlusty or Kurucz, the obtained model colours would not have been different to ours, in view of the weak sensitivity of colours to temperature and log g for hot stars which make the majority of our targets (T $>$ 80 kK, see De Marco et al. (2013)). The error due to a given choice of stellar models is negliglible compared to the error induced when, for example, our star's colours are compared to that of a black-body, and this error itself is almost negligible in our case. Therefore we are confident that the choice of our model atmospheres does not influence our NIR excess detections, and that such detections would have been made with any choice of model atmosphere for hot stars.

Dereddened magnitudes (Section 1.2.1) V_0, I_0 and J_0 are obtained from the calibrated magnitudes and their associated errors σ_{V0}, σ_{I0} and σ_{J0}. The I and J-band excesses - which are nothing more than colour differences - are defined as $\Delta(V-I) = (V_0-I_0)-(V-I)_m$ and $\Delta(V-J) = (V_0-J_0)-(V-J)_m$. The error on the colour difference is defined as $\sigma^2_{\Delta(V-I)} = \sigma^2_{V0}+\sigma^2_{I0}+\sigma^2_T$ and $\sigma^2_{\Delta(V-J)} = \sigma^2_{V0}+\sigma^2_{J0}+\sigma^2_T$, where σ_T, the error due to the uncertainty on the object temperature determination. Hot stars colours are mostly insensitive to temperature (De Marco et al., 2013), so that the uncertainty due to temperature is almost always less than 0.02 magnitudes. For all stars, we adopted a value of log g=7, which again adds an uncertainty lesser than $\sim$ 0.02 magnitudes, although this error has not been taken into account in our calculation. If the colour difference $\Delta(V-I)$ ($\Delta(V-J)$) lies within the error bar $\sigma_{\Delta(V-I)}$ ($\sigma_{\Delta(V-J)}$), no excess is detected. If it is larger than the error then we call it a detection.

In case of a detection, the putative companion's I-band magnitude is deconvolved from the combined value and the spectral type of the companion is determined by using the distance to the system. If no binary is detected (i.e. $\Delta(V-I)$ or $\Delta(V-J)$ is smaller than the respective errors), the error on the colour difference is added to the colour difference itself and converted into an upper limit for the companion's mass.

To assess the feasibility of this procedure, De Marco et al. (2013) computed a grid of binaries with different primary absolute V magnitudes, M_V, and secondary masses (and spectral types) and predicted the observable NIR excess (Figure 1.1). Most of our targets are on the cooling track (Frew & Parker, 2007), and even more so given our selection of evolved PN (see Section 1.3.3). We therefore used the colours of central stars on the cooling track (Figure 1.1, bottom panels) and not those for stars on the giant branch (Figure 1.1, top panels). As seen on these plots, stars on the giant branch outshine the companions so that only companions brighter than $\sim$ M0 can be detected in the I band and $\sim$ M3 in the J-band. When the CSPN are on the cooling track, the expected flux excess for most of our systems (late-type main-sequence companion) is of the order of a few hundredth to a few tenths of magnitudes. This tells us that the photometric precision we require is of the order of one-to-few percent. This precision is attainable only using the best data with a careful treatment and clarifies why previous studies detected so few companions. The only means to obtain such good quality data is a dedicated observing campaign to acquire B, V and I-band images of our targets in photometric conditions in grey or dark time. The proposal of the 2.3m run is presented in Appendix D to shed light on details regarding the observing run itself.

Contamination by bright companions is taken into account in our method. The hotter the companion the more it will affect bluer bands. As can be seen in the colour predictions of Figure 1.1, as the primary becomes intrinsically fainter or the companion brighter, a given NIR excess will correspond to two sets of spectral subtypes: a cooler one without contamination or a hotter one with contamination. Our algorithm picks the correct companion's spectral type thanks to the knowledge of the distance, and therefore the absolute V magnitude of our primary. From Figure 1.1 we can see that such contamination starts occurring for K0V-K5V companions. For spectral types

hotter than this limit, the star will display colours too red for its temperature and will be dereddened too much, artificially decreasing the red signal from the companion itself. In most cases, it is the reddening comparison with nebular-derived values that lets us know which companion to choose.

We have seen that our method requires excellent photometric and calibration precision the ability to avoid false detection by using the $V - J$ as well as $V - I$ colours alongside several methods to improve the quality of the reddening estimates. The two points that have not been addressed yet are the necessity of additional knowledge on the targets and the issue of biases. Both come with the selection of the targets from an adequate sample.

1.3 The sample of Frew (2008)

Frew (2008) determined distances to Galactic PN using his new Hα brightness - radius relation, now updated by Frew et al. (2014a). He also gathered all available information from the literature to characterise as accurately as possible the local sample of PN. As we have seen in Section 1.2, determining the companion spectral type for our detections implies the knowledge of the system's distance. Moreover, not only do we want to detect new binaries but we also want to know how many have avoided detection. The new volume-limited sample of Frew (2008) provides us with an excellent starting sample.

1.3.1 A new distance scale

Counting 56 PN within 1 kpc and $\sim$ 210 within 2 kpc, the database of Frew (2008) is the most accurate volume-limited sample to date in PN research. For some of these objects, parallax have been measured and used to calibrate a new Hα surface brightness - radius relation determined thanks to the measurement of the Hα integrated flux in 400 evolved nebulae. It is these distances we have been using in our study.

Additionally, systematically measured, up-to-date values for PN diameters, morphological classifications, ionized masses, expansion velocities, kinematic ages, chemical abundances and central star properties are listed in Frew's (2008) database. The

supplementary knowledge of these properties will eventually enable us to observe trends with respect to morphologies in our population of detected binaries (see Section 6.4). Among the existing morphological classifications, we used the 'ERBIAS' classifier (E: elliptical, R: round, B: bipolar, I: irregular, A: asymmetric and S: quasi-stellar (point source)), derived from that of Corradi & Schwarz (1995) and used in the MASH catalogue (Parker et al., 2006). This choice is due to the fact that round PN benefit from a class of their own, and statistical tests such as the one presented in Section 6.4 can be carried out. Furthermore, it is the system adopted in the Macquarie University GPN Database[6](Bojičić et al. 2014, in preparation) and adopting it allows us a systematic query of all our targets. Effective temperatures for each star were also extracted from this database: they come from atmosphere fits, averaging results if there were more than one available. If a model was not available, we calculated a Zanstra temperature (Pottasch, 1984) for this object using the most up-to-date V-band magnitudes (including our new V photometry) in combination with the integrated nebular Hα and/or the He II λ4686 fluxes. The integrated Hα fluxes were taken from Frew (2008) or Frew et al. (2013), and the He II fluxes were determined from the λ4686/λ6563 ratios measured from spectroscopy, if available. Since the Zanstra method only provides a lower limit to the stellar temperature for optically thin nebulae, we have used additional information, where appropriate, to determine the most suitable value for the temperature. We note however that for CSPN with $T_{eff}\gtrsim$70,000K the colours are not very sensitive to temperature.

1.3.2 The advantage of completeness

The main bias that most surveys suffer from is that they are magnitude-limited, which implies that intrinsically bright stars located farther away are preferentially observed. This would bias our detected companion distribution towards higher masses as we would detect preferentially the bright ones not outshone by their host. By using a nearly complete, volume-limited sample we are likely to recover a mass-ratio distribution

[6] http://web.science.mq.edu.au/kosmos/gpne/dbMainPage.php, access must be granted.

reasonably close to the real local one as well as a robust evaluation of our detection limit. Furthermore the goal of this study is not only to detect the maximum number of binaries but to estimate the CSPN binary fraction for a sample representative of the Galactic population. By using a complete 2 kpc volume-limited sample, we can draw the best possible, least biased statistical representation of the local Solar environment.

The contamination by mimics in PN catalogues has drastically reduced since the effort of Parker et al. (2006), Miszalski et al. (2008), Frew & Parker (2010), Frew & Parker (2011) and Boissay et al. (2012). Following the classification of Parker et al. (2006) inspired by the one of Kohoutek (1983), we call a mimic an object that presents similarities to a PN and is misclassified as such. This can occur if the object is classified on morphological criteria or using PN-like spectral features such as certain line-ratios. The most common occurences of these contaminations in PN catalogues are made of a variety of objects: emission-line stars including symbiotics, Be and B[e] stars, Wolf-Rayet stars, pre-main sequence emission stars such as T Tauri and Herbig-Haro objects and cataclymic variables. Additional frequent contaminants are H II regions, reflection nebulae, supernova remnants, and galaxies whose morphologies are akin to PN ones. Mimic types and examples for each class are presented extensively in Frew (2008) and I invite the reader looking for more information to refer to this work. Vice versa true PN that were referenced only in H II region and reflection-nebula catalogues were carefully added.

The combination of a solid detection procedure associated to a non-biased sample is key to make this study both unique and promising.

1.3.3 Target selection

In spite of our aspiration towards completeness not all CSPN are easily observable and can grant us the photometric quality that we require. As in any survey aiming at CSPN flux integration the presence of the PN around the central star is problematic. Nebular subtraction methods exist but their application require narrow-band images in at least one of the prominent nebular lines e.g. [O III] $\lambda\lambda$ 4959,5007 Å; [NII] $\lambda\lambda$ 6548,6584 Å and Hα (Jacoby & Kaler, 1989). Therefore we selected mostly faint,

evolved, extended PN (diameter>25″) for our statistical sample. This might lead us to observe preferentially lower mass CSPN where the PN survives longer after having been ejected, however the extent of such bias is hard to quantify on a small sample. It is also possible that this strategy tends to lead to the observation of more round PNe. It is not the case in our study, as will be shown in Section 6.4. and brighter ones only when we suffered from a scarcity of targets. Most of our observed targets have apparent V magnitudes between ~ 15 and ~ 20. Beyond this value the exposure times take a substantial fraction of observing time and a dedicated observing run for these faint-end objects is more appropriate. PN in the Galactic plane were a second choice to avoid photometry in crowded fields. Albeit the sample being complete to ~ 2 kpc, we did select targets as far as 3 kpc to benefit from some completeness when nothing else was available. We also selected primarily CSPN with $M_V > 5$ to avoid luminous objects showing photometric variability due to turbulent winds in the star's atmosphere and to minimise the contrast with faint companions. It is noticeable that this selection effect biases our study towards low-mass CSPN.

To avoid any biases favoring or impeding the detection of companion, our observed targets were selected in a blind fashion, where no a priori knowledge regarding the existence of a companion was used. The design of our method intrinsically rejects binaries resolved from the ground, but those will be taken into account in our statistics later on.

1.4 Verification of the method and algorithm

Before applying the method that has just been described to unknown objects the algorithm has to be verified, in other words we want to make sure that it behaves the way we expect it to.

I use the example of a 100kK CSPN with an apparent V magnitude of 15 observed at 1 kpc that I decline in seven cases. I assumed the precision on the photometric magnitudes to be 0.02 for B, V and I, yielding an error of 0.11 on the colour difference. The uncertainty on the temperature is 10kK. A summary of the information regarding

each synthetic star is provided in Table 1.2:

- CSPN A1 is single and the B and I magnitudes are adjusted to fit single CSPN intrinsic colours for $E(B-V)=0$
- CSPN A2 is similar to A1 but colours have been affected by a reddening corresponding to 0.05 magnitudes in B
- CSPN B1 is similar to A1 but has a cool companion. The system's I magnitude is brighter than A1 by 0.1 magnitudes
- CSPN B2 is similar to B1 but has a slightly brighter companion. The system's I magnitude is brighter than A1 by 0.2 magnitudes
- CSPN C1 is similar to B2. $E(B-V)$ for the system should be 0 but a simulated imprecision in the measurement of the B magnitude creates an artificial reddening of 0.05 magnitudes
- CSPN C2 is similar to B2. $E(B-V)$ for the system should be 0 but a simulated imprecision in the measurement of the B magnitude creates an artificial reddening of 0.1 magnitudes
- CSPN D1 is similar to A1. $E(B-V)$ for the system should be 0.2
- CSPN D2 is similar to D1 but colours have been affected by a reddening corresponding to 0.2 magnitudes in B
- CSPN D3 is similar to D2 but a simulated imprecision in the B magnitude creates artificial blue colours of 0.1 magnitudes

The results of the verification are presented in Table 1.3 and Figure 1.2. The cases of CSPN A1 and CSPN A2 confirm that the reddening is determined properly. CSPN B1 has a companion generating a colour difference of 0.10. It is lesser than the error of 0.11 therefore no companion is detected and an upper limit for the companion spectral type is given. CSPN B2 has a brighter companion than CSPN B1 and a NIR

Name	Expected reddening	Simulated error in the reddening	Companion	Note
CSPN A1	0	no	no	–
CSPN A2	0.05	no	no	–
CSPN B1	0	no	M2V	$I_C = I_A - 0.1$
CSPN B2	0	no	M0V	$I_D = I_A - 0.2$
CSPN C1	0	yes	M0V	B is 0.05 magnitudes too faint
CSPN C2	0	yes	M0V	B is 0.1 magnitudes too faint
CSPN D1	0.2	no	no	–
CSPN D2	0.2	yes	no	B is 0.1 magnitudes too bright
CSPN D3	0	yes	no	B is 0.2 magnitudes too bright

Table 1.2: Summary of the artificial CSPN properties for verifying our method and algorithm

Name	$E(B-V)$	$(V-I)_0$	$\Delta(V-I)$	M_{I2}	Comp. spec. type
CSPN A1	0.001 ± 0.03	−0.35± 0.11	0.00 ± 0.11	> 7.65	Later than M1
CSPN A2	0.051 ± 0.03	−0.35± 0.11	0.00 ± 0.11	> 7.49	Later than M1
CSPN B1	0.001 ± 0.03	−0.25± 0.11	0.10 ± 0.11	> 6.90	Later than K9
CSPN B2	0.001 ± 0.03	−0.15± 0.11	0.20 ± 0.11	7.08 [8.16 – 6.43]	M0 [M2 – K6]
CSPN C1	0.051 ± 0.03	−0.21± 0.11	0.14 ± 0.11	7.35 [9.35 – 6.54]	M1 [M4 – K7]
CSPN C2	0.101 ± 0.03	−0.27± 0.11	0.08 ± 0.11	> 6.71	Later than K8
CSPN D1	0.201 ± 0.03	−0.35± 0.11	0.00 ± 0.11	> 7.02	Later than M0
CSPN D2	0.101 ± 0.03	−0.23± 0.11	0.12 ± 0.11	7.37 [10.86 – 6.48]	M1 [M5 – K7]
CSPN D3	0.000 ± 0.10	−0.35± 0.36	0.00 ± 0.36	> 6.04	Later than K5

Table 1.3: I-band excesses ($\Delta(V-I)$), companion absolute I-band magnitudes (M_{I2}) and spectral types (or limits) of our synthetic targets.

excess equivalent to a spectral type M0V is detected. CSPN C1's B-band magnitude is too faint by 0.05 compared to what should have been measured. This discrepancy is interpreted as interstellar reddening. When the star is dereddened, it is dereddened too much because the reddening has been over-estimated. Therefore the red signal is diminished from 0.20 as for CSPN B2 to 0.14: an M1V companion is detected instead of an M0V. The same scenario applies for CSPN C2 but this time the red signal is altered so much that the colour difference drops under the value of the error and the companion, although present, is not detected. The cases of CSPN D2, and D3 are

the most critical for our statistics because they could lead to false detections: in these cases B is too faint compared to what it should be and the reddening is underestimated. The colours of CSPN D2 are not dereddened enough (compared to CSPN D1, the same star with appropriate dereddening) and create artificial red signal yielding to the false detection of a companion. In the case of CSPN D3, the error is such that it would lead to a negative reddening. We claim that a negative reddening is non-physical and reset the value to 0 whenever a negative value is obtained. This prevents false detections as no artificial red signal is added. We use the maximum between the actual error and the absolute value of the reddening as our error value. This is why the error bars on the colour difference of CSPN D3 are bigger: the actual error on the reddening is 0.03 but the value of the reddening without being reset would be -0.1, whose absolute value becomes the error.

All our synthetic stars behave the way we expect them to. All in all, the only case where false detections can happen is if one of the calibrated magnitudes has not been measured correctly and is affected by a shift:

- roughly as large as the error on the colour excess (which itself is typically a few times the error on a magnitude), so quite unlikely. In our example, our error of 0.11 arises from the optimistic choice of an error of 0.02 magnitudes in each band. In our analyses (Chapter 2 and Chapter 3), the errors will be larger for the majority of objects.

- and smaller than the reddening value, otherwise this will translate into a negative reddening that will be corrected in our procedure.

Fortunately, the circumstances for these conditions to occur are very limited as the objects that are the most likely to suffer from those kind of photometric glitches are the ones with high reddening. This shows using our algorithm, a false-detection is very improbable.

Summary

In this section I have reviewed the previous studies aiming at detecting cool companions around CSPN using the NIR excess technique and underlined the need for excellent photometry quality in B, V, I and J for our targets. The B and V-bands are used to determine the reddening and deredden our magnitudes, while the dereddened $V-I$ and $V-J$ colours, compared the those of a single CSPN at a given temperature, yield the colour difference. If this colour difference is superior to its associated error, then the companion spectral type consistent with this NIR excess is determined by converting the putative companion's I or J-band magnitudes to absolute values using the distance to the system. When no excess is detected an upper limit for the companion spectral type is given. The algorithm has been tested on nine synthetic CSPN with and without companions and with and without photometric inconsistencies. I showed that in all combinations our approach is conservative and that the chances of false detections are really slim and considered negliglible. Therefore, the worst-case scenario was the non-detection of an actual NIR excess. Now that a consistent method has been established, it is time to apply it on our observed targets.

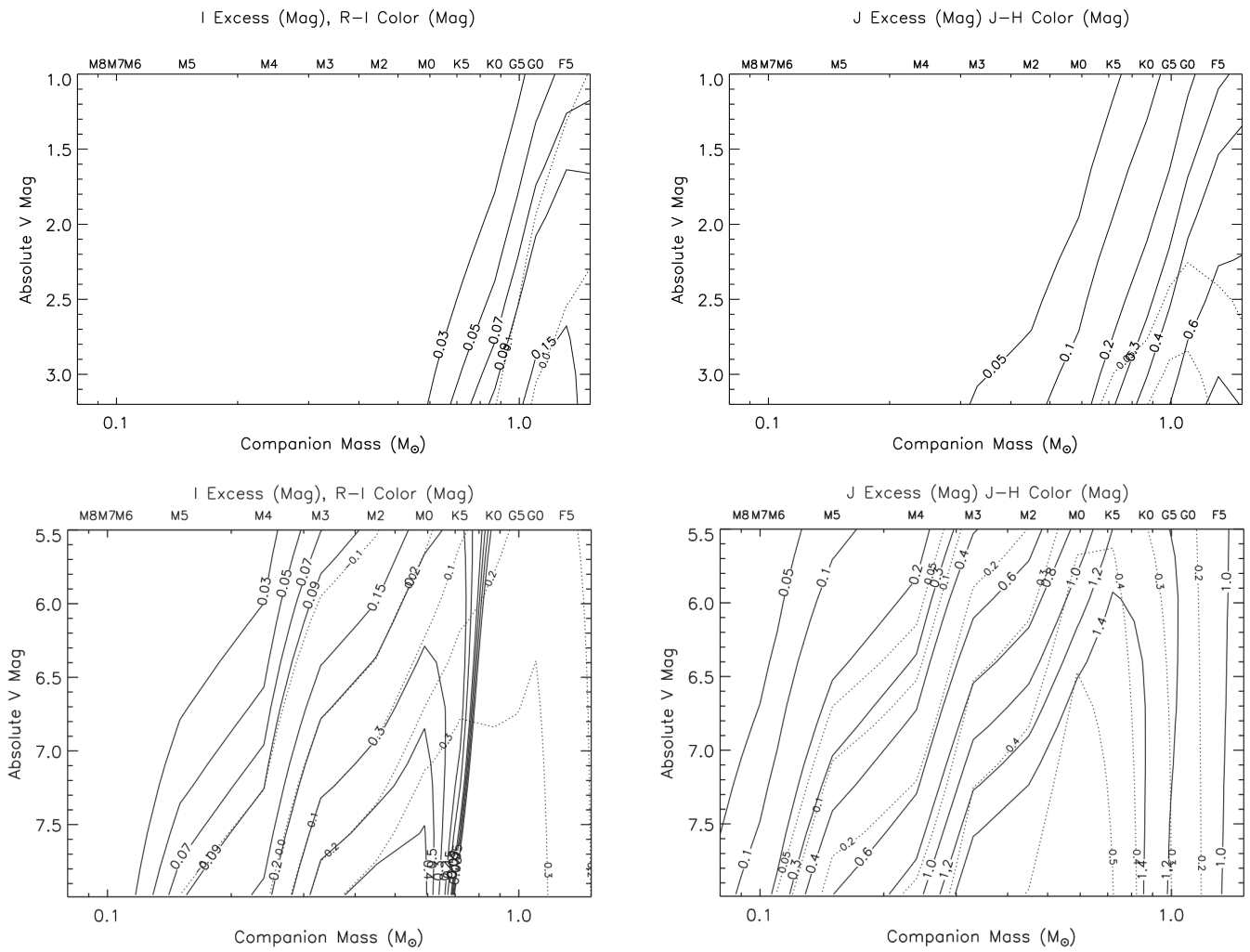

FIGURE 1.1: NIR excess predictions for CSPN on the AGB branch (top) and CSPN on the cooling track (bottom) in the I (left) and J (right) bands. The excesses (solid lines) are more or less detectable as a function of two competing parameters: the primary's brightness (absolute V magnitude) and the companion brightness (companion mass and spectral type). The I R and J H colours (dotted lines) can be used to discriminate the companion spectral type, although we adopted a different strategy where the star's distance is used to deduce the absolute I (or J) magnitude. The plots on the top are obtained by assuming that the central stars are on the horizontal AGB branch while the ones on the top are obtained assuming that the central stars are on the cooling track. Most of our PN are evolved objects, therefore the bottom plots are more suited to our sample. Meanwhile, it is visible that only brighter companions can be detected surrounding young PN. Adapted from De Marco et al. (2013).

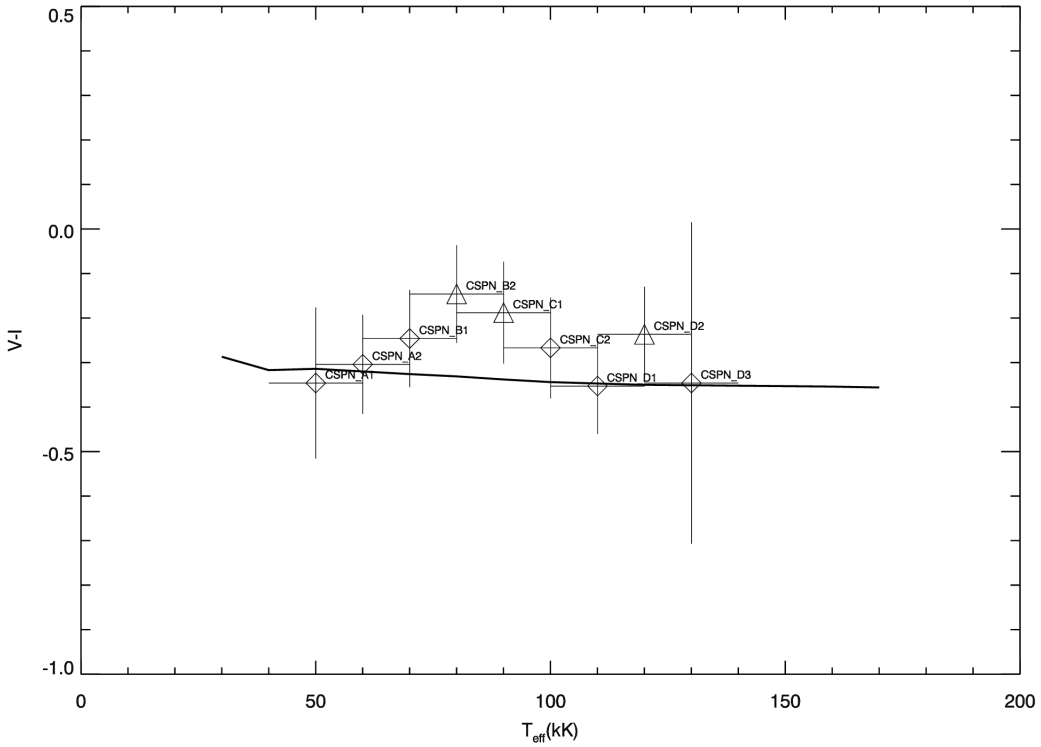

Figure 1.2: NIR excess colours for our synthetic CSPN. All stars have the same temperature, they have been staggered for visibility. The continuous line corresponds to the expected intrinsic colours for a single CSPN. The objects above the line error bar included are NIR excess detections, in this case CSPN B2, CSPN C1 and CSPN D2. Of this three simulated objects, only the two first ones are real detections, whereas the last one is an artifact.

Chapter 2

The NIR excess technique: observations and analysis

Since excellent photometric accuracy is required, the most natural approach to carry out this project is to observe the targets ourselves. 2m-class telescopes are suitable for our targets with V magnitudes between 15 and 20. In this chapter, I present the observations that have been made at the Kitt Peak National Observatory (KPNO) 2.1m telescope in 2011 and at the Siding Spring Observatory (SSO) 2.3m telescope in 2012 and their analysis.

2.1 The determination of the calibrated magnitudes

Before giving details of the observations, I show that our photometric data treatment provides a determination of the magnitudes that suits our requirements. This is crucial to detect companions to CSPN which tend to be faint compared to the star itself.

2.1.1 The determination of the instrumental magnitudes

Measuring accurate fluxes from our images is a critical step in our procedure. In the following paragraphs, I justify our choice of the software and more importantly of the input parameters. The influence of the main parameters on calibrated magnitudes have

been tested and a set of optimal parameter values has been determined. The photometric protocol described here was tested on targets from the KPNO 2.1m observing run.

Different tools for photometry

Several tools are available for performing photometry on optical images. Below we list (non-exhaustively) the most used ones and explain our choice of `DAOPHOT` for our analysis.

DAOPHOT

This software uses PSF fitting photometry. Made for the purpose of stellar photometry in crowded regions by Stetson (1987), it has been improved and re-arranged over the years. It is broadly used by the community and has been embedded into `IRAF`[1]. The procedure works in four steps: finding the sources, performing coarse aperture photometry, getting the average PSF for sources on the image and fitting the averaged PSF to each star in the image.

DOPHOT

`DOPHOT` is also built for PSF fitting photometry. Developed by Schechter et al. (1993), the program is based on different model PSF for different types of objects. The different steps are very similar to the ones described for `DAOPHOT`.

Sextractor

This software developed by Bertin & Arnouts (1996) and based on aperture photometry has been created for optimised source detection and non-stellar objects (typically galaxies). It is known to perform better than most routines for extended object photometry, but to have lower performances for faint stellar profiles (Becker et al. 2007, see below).

PSFextractor

`PSFextractor` is the PSF fitting package of `Sextractor`. Recently developed by Bertin (2011), it has been tested and has proven to provide consistent results (see below).

IRAF

[1]Image Reduction And Analysis Facility, `http://iraf.noao.edu//`

`IRAF` is an old, well-known platform for data reduction and analysis and contains a number of routines, including standard algorithms for aperture photometry (`APPHOT`) as well as an implementation of `DAOPHOT`. `IRAF` is a versatile platform with solid routines. It also has a well-founded reputation of being delicate to automatise because of its package system and unique syntax. De Marco et al. (2013) used `APPHOT` to obtain their instrumental magnitudes.

Each software has different capabilities in source detection, source classification (stellar or non-stellar), photometry and centroid determination. Our main concern is to obtain accurate magnitude measurements for our CSPN and for our standards. I wanted to select a routine with easy implementation and robust stellar photometry. To test how accurately a certain program measures the magnitudes of faint stars, they have to be compared with known input magnitudes. The literature provides us with some photometric tests of the different tools: Becker et al. (2007) used observed stars whose flux have already been measured whereas Annunziatella et al. (2013) used simulated observations of stars with known input distributions.

Becker et al. (2007) compared the photometry obtained using `Photo` (SDSS's[2] photometric pipeline), `DAOPHOT`, `DOPHOT` and `Sextractor` with the SDSS ones in the context of the science requirements for the future LSST[3]. They do not pick a best method, but rather list pros and cons of each software. They find the following characteristics (`Photo` is excluded):

- `DAOPHOT` gives the best PSF photometry, a robust star/galaxy separation and an efficient solution to deblending PSF in crowded fields. It suffers from being quite slow and not offering extended objects characterisation.

- `DOPHOT` has few input parameters and is easily pipelined. However its PSF model is not adjustable and it returns less accurate photometric and astrometric results with respect to the SDSS measurements.

[2]Sloan Digital Sky Survey: `http://www.sdss.org`
[3]Large Synoptic Survey Telescope: `http://www.lsst.org`

- `Sextractor` is fast and portable. It benefits from numerous modules and improvements that allows it to provide consistent measurements. However, its PSF modeling is not easily accessible and the program is likely to give biased centroid positions in the case of faint objects. The photometric error determined is 2-3 times smaller than ones from their reference algorithm.

Annunziatella et al. (2013) tested and compared the photometry obtained by `DAOPHOT` and `PSFextractor`. They tested the performance of the two pieces of software against virtual images created by `Stuff` for the galactic contributions and `SkyMaker` for the stellar contribution (both `SkyMaker` and `PSFextractor` have been developed by E. Bertin). They concluded that `DAOPHOT` and `PSFextractor` have very similar performance for stellar photometry, with the difference that `PSFextractor` performs fainter detections (by 2 magnitudes) than `DAOPHOT`. They point out that `DAOPHOT` tends to give magnitudes rather too low than too high, however since the SNR of their generated maps is not indicated it is hard to know if this will be true for our observations.

We first thought about averaging photometric measurements coming from different software but we realised that if two pieces of software were outputting different final numbers this was more due to a lack of fine tuning of the input parameters than an intrinsic difference in the procedures themselves. Therefore we decided to restrict ourselves to the usage of one software only with fine-tuned parameters tested on our sample. We selected `DAOPHOT` as it seemed to provide the most accurate measurements from stellar PSF. Furthermore `DAOPHOT` is easy to use as stand-alone package and has only $\sim$ 15 input parameters. It is also very well documented (Stetson, 1987, 2000). In our study we do not suffer too much from computation-time limitations as our reductions only include a few hundred images of mostly non-crowded fields, nor do we need extended source classification for which `DAOPHOT` lacks capabilities. Our targets (CSPN and standards) are mainly located in non-crowded regions, therefore there is no real need for PSF fitting photometry. However, using this technique decreases the chances of contamination by a field star blended with the CSPN and or contaminating the background sampling regions.

ID	Description (Note)	Routines Affected	Permitted values	Default value	Our adopted value
RE	Readout noise, 1 exposure (ADU)	FIND	positive	0	4.57
GA	Gain, 1 exposure (photons per ADU)	FIND	positive	0	1.04
LO	Low good datum (standard deviations)	FIND	non-negative	7	5
HI	High good datum (ADU)	FIND	non-negative	32766.5	50000
FW	FWHM of objects for which FIND is to be optimized (in pixels)	FIND	0.2 - 15.0	2.5	1 FWHM[1]
TH	Significance threshold for detection (standard deviations)	FIND	non-negative	4.0	5.0
LS	Low sharpness cutoff	FIND	0.0 - 1.0	0.2	0.2
HS	High sharpness cutoff	FIND	0.6 - 2.0	1.0	1.0
LR	Low roundness cutoff	FIND	-2.0 - 0.0	-1.0	-1.0
HR	High roundness cutoff for the profile fits	FIND	0.0 - 2.0	1.0	1.0
WA	Watch progress of reductions on terminal	FIND,PHOT,PICK,PSF NSTAR,SUBSTAR,SORT	-2 - 2	1	-1 (non-interactive mode)
FI	The fitting radius (in pixels)	PSF,PICK,GROUP,NSTAR	1.0 - 10.0	2.0	2×FWHM
PS	PSF radius: radius (in pixels) within which the PSF is to be defined.	PSF	1.0 - 35.0	11.0	4×FWHM
VA	Degree of variation in the PSF	PSF	-1 - 2	0	0
AN	Which analytic formula for PSF	PSF	1 - 6	1	1
EX	How many passes to clean discordant pixels from the PSF table(s)	PSF	0 - 9	0	5
PE	Percent error (e.g. flat-field)	NSTAR	0 - 100	0.75	0.75
PR	Profile error (inadequate PSF)	NSTAR	0 - 100	5.0	5.0
IS	Inner radius of annulus for background estimation	PHOT, PSF	0- OS	2.0	4 FWHM
OS	Outer radius of annulus for background estimation	PHOT, PSF	0- n/a	PS	5 FWHM

[1] The median full-width at half maximum of the PSF in the image, obtained independently. Typically for our runs, $FWHM \approx 5$pix (1.5")

Table 2.1: DAOPHOT input parameters. Adapted from the DAOPHOT manual, Stetson (2000).

Basic functioning of DAOPHOT

Below is a concise description of how DAOPHOT works and how we chose our input parameters to obtain our CSPN magnitudes. Default values along with our adopted values for the various parameters described in this section are listed in Table 2.1. DAOPHOT photometry is performed in four steps: FIND, PHOT, PICK and PSF.

The routine FIND detects the stars in the image by convolving the image with a Gaussian function with a width input by the user. This allows a clearer detection of peaks and a more accurate selection of the source type (stellar or extended, Stetson 1987). Positive features in the convolved image are detected if the height of their central pixel has a value greater than n times the average noise value on the image. They are then considered potential star centroids and the surrounding pixels intensity is integrated. In DAOPHOT, n is input by the user as the THRESHOLD (TH) parameter and the noise value is taken to be the mode of a distribution of 10,000 clipped random pixels

in the image. The input parameters required by FIND are RE, GA, LO, HI, FW, TH, LS, HS, LR, HR and WA. RE, GA and HI have been assigned as per the CCD characteristics, FW has been chosen to be the median PSF in the image determined independently (later FWHM), whereas all the other parameters have been setup with the default values given in Stetson (2000), allowing satisfactory source detection (see Table 2.1).

The routine PHOT performs aperture photometry in a traditional way on the stars detected by FIND. The user defines as input the aperture(s) (AP1(,AP2...)) in which the counts around the centroid are summed as well as between the inner and outer radii of the sky annulus determination, respectively IS and OS. The background counts are determined from the annulus and subtracted from the stellar counts integrated in the central aperture. The output of the aperture photometry step is used as initial conditions for the PICK and PSF routines used subsequently. We found the choice of the aperture to have no influence on the final magnitudes, consistent with the fact that this initial photometry is then adjusted by the PSF fitting process.

The routine PICK is used to determine which stars will contribute in estimating the model PSF for the image. For each picked star, an analytic model (parameter AN, by default AN=1 and corresponds to a bi-variate Gaussian) of the PSF is fitted and subtracted from the image; then the residuals are interpolated every half pixel and also subtracted from the sky level. The instrumental magnitude is the sum of these two contributions. This estimation is then scaled and applied to all the detected stars of the image using the routine PSF. The user needs to pick bright stars with well-defined profiles. The routine PICK allows the user to input an upper-limit magnitude for stars to be selected for building the model PSF. Alternatively, the user can define how many stars must be taken into account in this averaging process. This step is somewhat similar to the aperture correction step in aperture photometry where the sources with the best SNR are used to determine the PSF wing contribution. When possible, we used a minimum of 10 bright stars to contribute to the model PSF, where Stetson (1987) recommends a strict minimum of 3. Given the high SNR of our data ($\sim$ 100) 10 bright reference stars is sufficient.

The routine PSF is used to determine the actual instrumental magnitude of all stars

in the image. It uses the PSF modelled with PICK and scales it to each star detected with FIND. The two main parameters are the PSF radius (PS), which quantifies the spatial extension of the star on the image and the fitting radius (FI), which defines the region that will be used when scaling the model PSF to the field star. The PSF radius can be determined by the limit radius at which the PSF wings blend with the background. Experimentation with our data led us to use a PSF radius of 4 FWHM (see next paragraph). The fitting radius, that by definition is smaller than the PSF radius, is the radius up to which the observed PSF is considered good and defines the region where the model PSF is fitted to the star's profile. We have chosen FI = 2 FWHM which is the threshold at which the magnitudes do not change with increasing FI.

The magnitude determination works as follows: all the pixels in the PSF radius are fitted analytically as described above, while the deviation from the analytic model is interpolated only in the fitting radius region. At each iteration, all the measured PSF are subtracted from the image creating a residual image. The star-finding procedure is called again on this residual image to detect stars that would have originally been blended together. The stars are then added to the list of detected stellar-objects. Iteratively, source detection, aperture photometry, PSF-modeling, PSF fitting and subtraction are applied until all signal identified as stars has been detected. The sky background is determined every three iterations in the annulus given in input (parameters IS and OS), after the detected stars have been subtracted. Note that this allows one the best estimate of the background photons contributing to the star light. The inner radius of the background annulus can thus be inside the fitting radius and allows to sample a more meaningful region backgrounds counts than taking an annulus farther out around the object, as in standard aperture photometry. On the other hand, we observed this change to have no effect on the final instrumental magnitudes.

Fine-tuning of the DAOPHOT input parameters

In Figure 2.1, we show the influence of a selection of DAOPHOT parameters on the instrumental magnitudes for a range of representative CSPN in our sample (see Table 2.2), engineered to have a range of magnitudes and different levels of PN contamination.

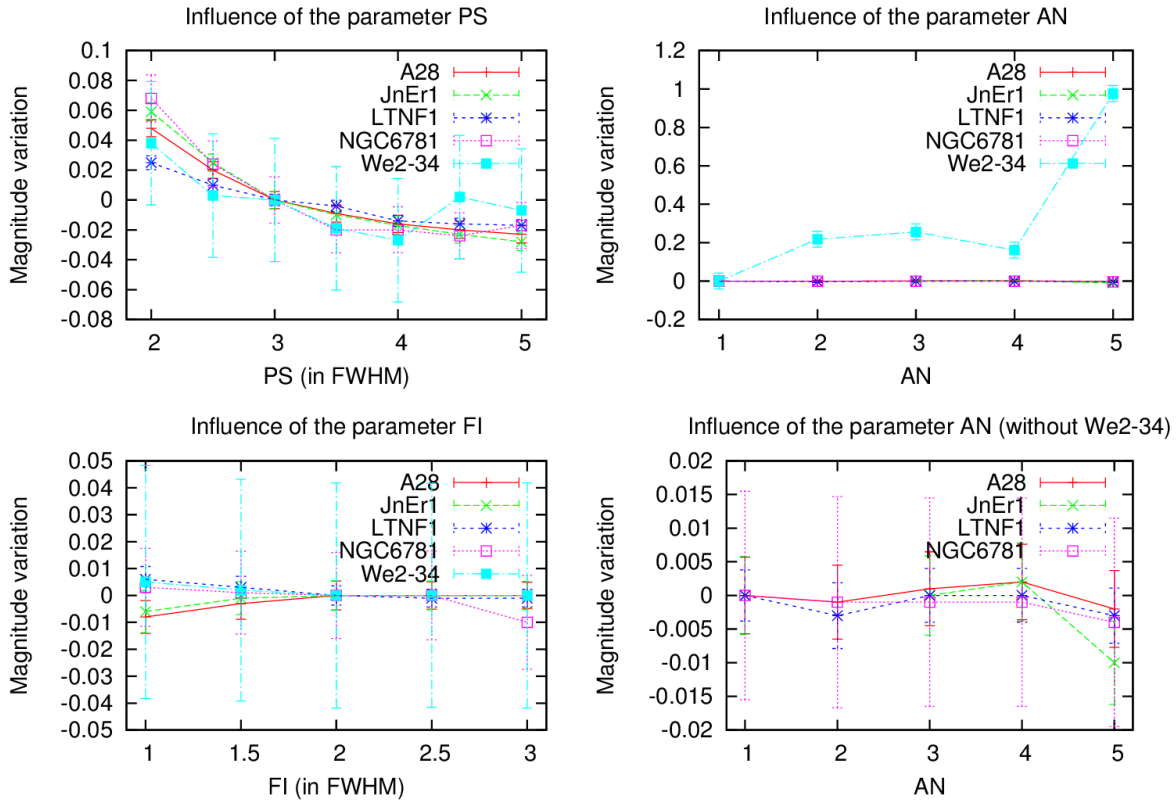

FIGURE 2.1: Change of the instrumental magnitudes using different DAOPHOT input parameters for a sample of CSPN. The CSPN are listed in Table 2.2

PN Name	V	Bright nebula
Abell 28	16.5	no
JnEr 1	17.1	no
LTNF 1	15.2	no
NGC 6781	16.8	yes
We 2-34	19.4	no

TABLE 2.2: PN used for the determination of optimal DAOPHOT parameters

The DAOPHOT parameters being compared are PS, AN, and FI (see Table 2.1) as they have the largest repercussion on the final magnitudes. The magnitude variation (y-axis of Figure 2.1) is the difference between the star magnitude for a range of parameter values and the magnitude for the reference value (all stars have a magnitude difference of 0 for the parameter reference value).

In the top-left panel of Figure 2.1, we present the influence of the parameter PS. Increasing this parameter is very similar to plotting growth curves in aperture photometry (Howell, 1989): the bigger the PSF radius (the aperture in the case of aperture photometry) the more flux from the wings of the PSF is harvested, but the more contamination from the sky is included. A flattening is observed in the curve for a value of 4 FWHM. For larger values of PS, no more light from the star is added but noise increases. A PS value of 4 FWHM offers a good compromise yielding the best SNR for our photometry. The curve for We 2-34 is noisy because this is the faintest object in this test-sample (V≈20).

On the top right-hand side of Figure 2.1 we show that the curve of We 2-34 is not in line with the behavior of the other objects and that faint object's instrumental photometry is sensitive to the value of AN. The same plot without We 2-34 on the bottom-right shows that brighter star photometry is not influenced by variations of the analytic fitting function. After inspections of the instrumental magnitudes of stars in the field of We 2-34, it was noticeable that the variations of instrumental magnitude with AN seemed to be constant for one given frame, i.e. all stars in the frame were affected by the same constant shift. This shift disappears while calibrating the instrumental magnitudes (see Figure 2.2), although the process through which the shift is taken into account is not clear.

In the bottom-left panel, we show a test of the influence of FI, the Fitting Radius. The scatter across our test-sample is negligible. It is bigger for the curve of NGC 6781 that has a bright nebula offering a more scattered background and adding noise to the CSPN flux measurement.

To insure that no systematic error was introduced during the photometry calibration step, the calibrated magnitudes of the targets observed during night 6 of the KPNO

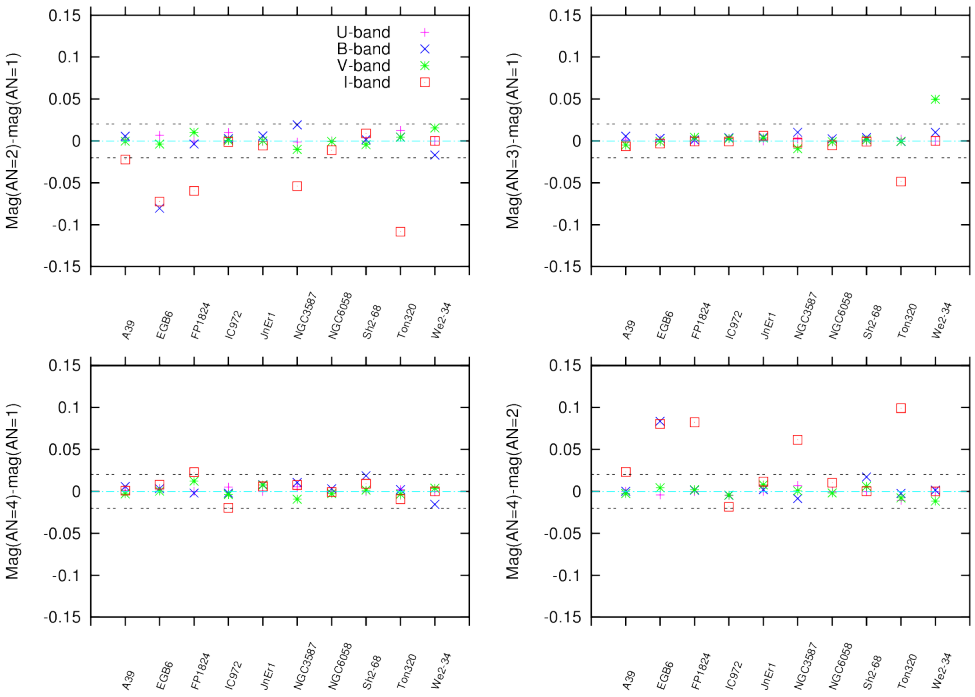

FIGURE 2.2: Difference in the calibrated magnitudes of the targets of night 6 using different value for the input parameters AN

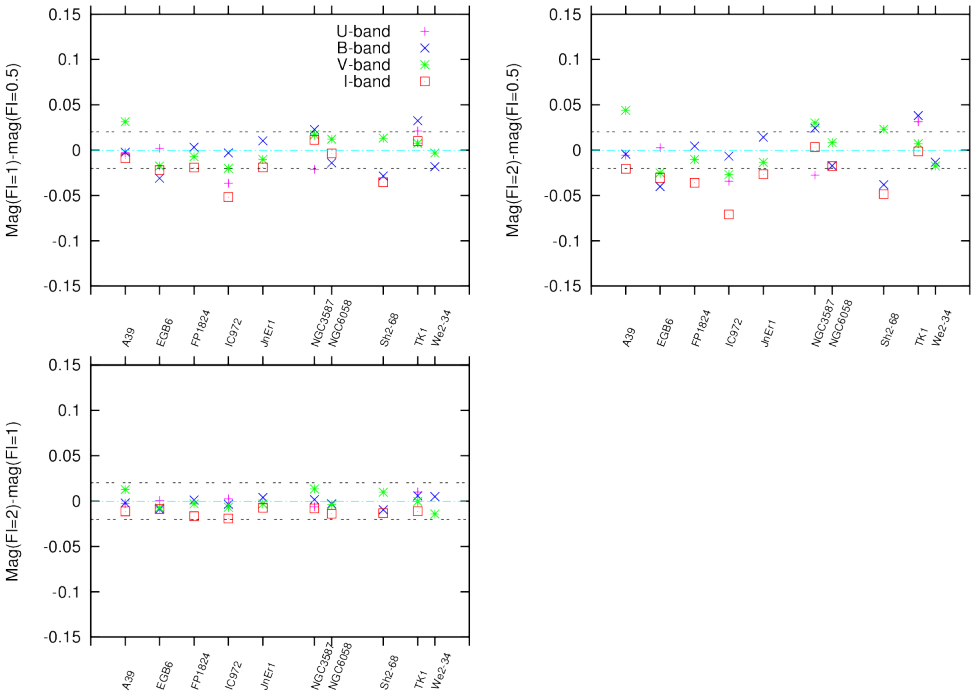

FIGURE 2.3: Difference in the calibrated magnitudes of the targets of night 6 using different value for the input parameters FI

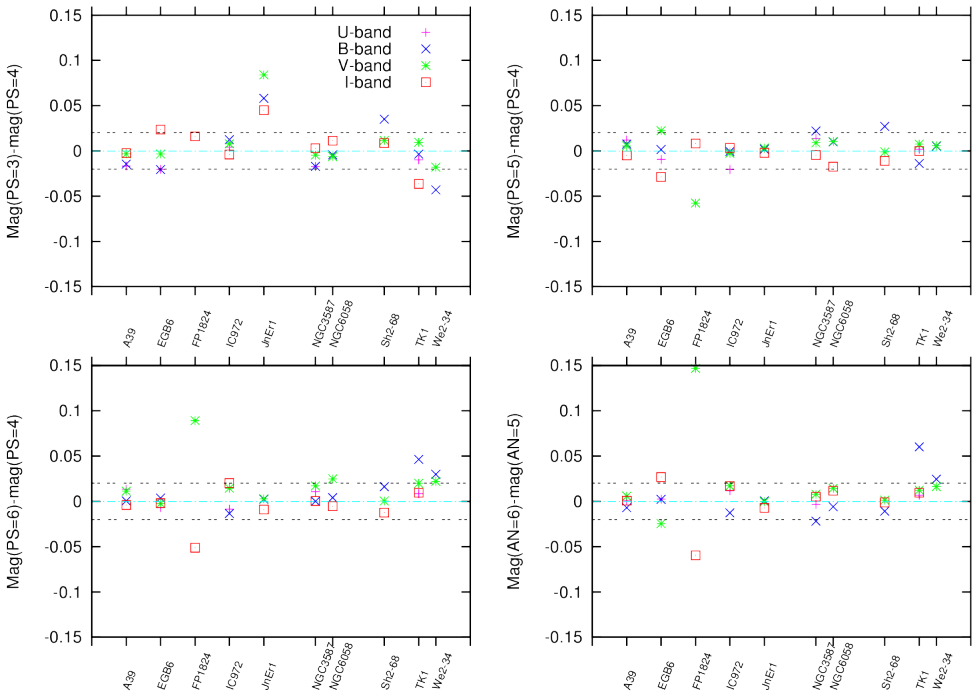

Figure 2.4: Difference in the calibrated magnitudes of the targets of night 6 using different value for the input parameters PS

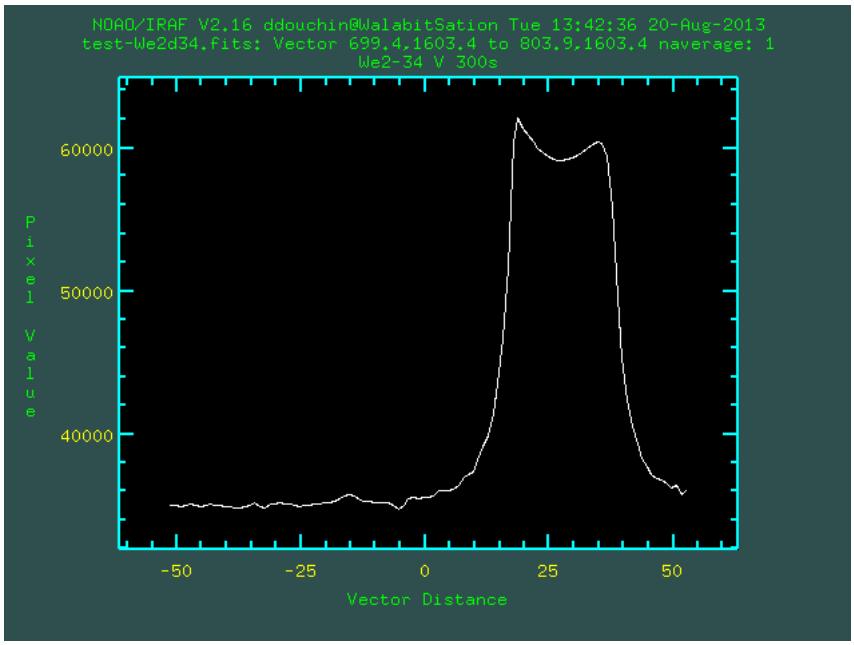

Figure 2.5: Erratic PSF behavior of a bright field star in a long exposure-time frame. Instead of a plateau, a trough can be observed, taking the star's model PSF into account whereas it would be excluded with a traditional saturated PSF profile.

2.1m run were plotted against different values of AN (Figure 2.2), PS (Figure 2.4) and FI (Figure 2.3). We adopted a least dispersion approach in order to select the most suitable values of these three parameters by excluding those values of the parameters that introduced the most scatter in the difference plots. On each figure we calculate the difference in magnitudes for our targets when one of the parameter's value is changed. We repeat this difference calculations to obtain cross-comparisons between parameter values (for example for AN 2 with 1, 3 with 1, 4 with 1 and 4 with 2). The correlations shown in the plots for (AN=2) vs. (AN=1) (Figure 2.2, top-left) and AN=4 vs. AN=2 (bottom-right) showing more scattering than the correlations AN=3 vs. AN=1 (top-right) and AN=4 vs. AN=1 (bottom-left). This shows that the magnitudes calculated with AN=2 are discrepant with magnitudes obtained with other AN values, therefore the choice of AN=2 (a Moffat function with an index of 1.5) has been excluded. The AN=3 vs. AN=1 and AN=4 vs. AN=1 correlations display that for all objects the dispersion stays within a 0.02 magnitude error indicating that AN=1, AN=3 and AN=4 are equally suitable choices. We used AN=1 in our photometric procedures.

The same reasoning has been applied for the choice of FI on Figure 2.3. While FI=0.5 induces dispersion in the magnitude differences because the fitting region is too small, FI values of 1 and 2 are in good agreement which is expected given the high SNR of our images. We adopted a value of 2 $FWHM$ to be consistent with our choice of the other parameters, notably FI $<$ PS.

The parameter PS is the most sensitive because it directly affects the surface of light that is integrated in a low SNR region at the star's edge. Figure 2.4 shows that magnitudes obtained with PS values of 4, 5 and 6 show low dispersion. We kept a value of PS=4 that agrees with the value determined from Figure 2.1.

Issues happened with saturation on long exposure images ($\geq$ 200s). The HI input parameter is used to indicate the maximum count value before which a star reaches saturation and is excluded. In our images, saturation happens near 60,000 counts but on bright stars, notably those field stars that are used for fitting the model PSF, the top of the observed PSF displays a peculiar feature: instead of a regular saturation plateau a trough appears (see Figure 2.5), the centre does not reach saturation value

and therefore the star is not considered saturated. To avert this problem, the `HI` threshold has been set to 50,000.

2.1.2 Standard calibration of the instrumental magnitudes

The calibration of the instrumental magnitudes is similar to the procedure described in De Marco et al. (2013) except that the filters used for our observations were U, B, V, I and not B, V, R, I. The resulting photometric system is therefore:

$$\begin{aligned} U &= O_U + u + C_U(U-B) - K_U \times Z_U \\ B &= O_B + b + C_B(B-V) - K_B \times Z_B \\ V &= O_V + v + C_V(B-V) - K_V \times Z_V \\ I &= O_I + i + C_I(V-I) - K_I \times Z_I \end{aligned} \tag{2.1}$$

where O, C and K are the calibration coefficients, O_U, O_B, O_V, O_I are the instrumental offsets, C_U, C_B, C_V, C_i are the colour terms, K_U, K_B, K_V, K_I are the extinction coefficients, and Z is the airmass of the observation. These coefficients were determined for each night of observation by using a standard least square procedure in order to solve numerically the system 2.1 for our selection of Landolt standards. To insure a photometric solution as accurate as possible, outliers have been visually removed through a series of sanity checks when estimating the standard solution.

For a given calibrated magnitude in a given bandpass b, the error is defined as

$$\begin{aligned} \sigma_U^2 &= \sigma_{O_U}^2 + \sigma_u^2 + \sigma_{C_U}^2(U-B)^2 + \sigma_{U-B}^2(C_U)^2 \\ &\quad + \sigma_{K_U}^2 Z_U^2 + \sigma_{Z_U}^2 K_U^2 \\ \sigma_B^2 &= \sigma_{O_B}^2 + \sigma_b^2 + \sigma_{C_B}^2(B-V)^2 + \sigma_{B-V}^2(C_B)^2 \\ &\quad + \sigma_{K_B}^2 Z_B^2 + \sigma_{Z_B}^2 K_B^2 \\ \sigma_V^2 &= \sigma_{O_V}^2 + \sigma_v^2 + \sigma_{C_V}^2(B-V)^2 + \sigma_{B-V}^2(C_V)^2 \\ &\quad + \sigma_{K_V}^2 Z_V^2 + \sigma_{Z_V}^2 K_V^2 \\ \sigma_I^2 &= \sigma_{O_I}^2 + \sigma_i^2 + \sigma_{C_I}^2(V-I)^2 + \sigma_{V-I}^2(C_I)^2 \\ &\quad + \sigma_{K_I}^2 Z_I^2 + \sigma_{Z_I}^2 K_I^2 \end{aligned} \tag{2.2}$$

De Marco et al. (2013) had a term for the error on aperture correction. This source of error is taken into account in our statistics during the calculation of the model PSF and is included in the photometric error. The averaged magnitudes and errors have followed the same statistical treatment as in De Marco et al. (2013): The calibrated magnitudes for one night were calculated as the weighted average of the different measurements. The weights for averaging magnitudes on different images within one night are defined as the inverse of the uncertainty σ_b for a given measurement normalised by the sum of these weights. The error on the averaged calibrated magnitudes from several nights is the weighted standard deviation of the averaged calibrated magnitudes on the different nights. This estimator, although statistically correct, is not well-suited for our low-number statistics (objects have been observed between 1 and 5 times in total) especially when the standard deviation comes from two measurements only, however all the flux excess we detected come from reasonable error values. The maximum between the error we used and the average photometric and calibration error for a given object might would constitute a safer alternative. When the target has been observed only one night, the error is the quadratic sum of the instrumental photometric error and the errors from the calibration.

Our targets showed a typical scatter of $\sim$ 0.02 calibrated magnitudes when varying `DAOPHOT` input parameters. These variations of the magnitudes with respect to input photometric parameters are partly accounted for in the errors because they would have affected the standards' calibration. We also guard against poorly quantified errors by relying on multiple observations and observations on multiple platforms (see Chapter 3).

Accurate flux measurements can now be retrieved to look for NIR excess flux. The next section deals with the analysis of our KPNO 2.1m run.

2.2 The KP 2.1m observing run and its analysis

2.2.1 Observations

Our U, B, V and I images were taken during a seven night observing run at the National Optical Astronomical Observatories 2.1-m telescope at Kitt Peak between the 11th and the 17th of March, 2011. Only nights 1, 4 and 6 were partially photometric and the results we present here derive from these photometric data only. During nights 2, 3, 5 and 7 and non-photometric parts of nights 1, 4 and 6 we carried out photometric monitoring of those targets that will be presented in Chapter 4. We used the optical camera STA2 binned in 2×2 with 2000×1300 pixels yielding a field of view of $10' \times 6.5'$on the sky. In this configuration the camera has an equivalent pixel size of 24 μm with a typical read-out noise of 4 electrons rms. We used a gain of 1.04 electron/ADU with a pixel saturation of 65,000 ADU.

2.2.2 Data reduction

The images have been reduced using the standard `ccdproc` procedure provided within `IRAF` allowing de-biasing, overscanning and flat-fielding. A total of 10 bias frames have been taken at the beginning of each night as well as 10 dome-flat images in each filter at the beginning and end of each night. The dark current noise of the STA2 CCD, $<$ 4 electrons/hour/pix, is negligible in comparison with the other sources of noise expected in our data, therefore no dark-frame subtraction has been used in the reduction process, although dark images have been acquired for precaution in the morning after each observation.

2.2.3 Target selection

The targets selected for the observation were the ones from the sample of Frew (2008) observable at this time of the year above 30° to the horizon and matching the selection

criteria detailed in Section 1.3.3. The best available literature data for our targets is presented in Table 2.3, as well as the new values determined here. Due to a scarcity of targets available in our observing window, we tentatively added targets with PN that were too compact or too bright to achieve good background subtraction. A handful of objects for which a distinct image of the PN was required were added for narrow-band imaging. For our faintest objects, no U-band images have been taken due to the longer exposure times required in this band. A compilation of the NIR magnitudes available from online surveys is also shown in Table 2.4.

Name	Sp. Type[1]	PN[2] morph.	D[3] (kpc)	M_V (mag)	$E(B-V)$ (mag)	$T_{\rm eff}$ (method) (kK)	log g (cm s^{-2})	Reference & Comment
Abell 39	hgO(H)	R	1.4	4.8	0.02	117 ± 11 (m)	6.28 ± 0.22	Napiwotzki (1999)
EGB 9†	–	I	0.34	4.6	$\leq$ 0.056[4]	–	–	Ali et al. (2012)
FP J1824-0319	DA	Ra	0.29	7.3	–	–	–	–
H 4-1⋆	–	E	–	–	–	82 ± 2 (tzHeII)	–	Phillips (2003)
HaWe 10	hgO(H)	R	3.01	5.5	0.02	80 ± 10 (s)	8.0:	Girven et al. (2011)
IC 972⋆	–	Rr	2.78	2.4	–	89 ± 11 (tzHeII)	–	Phillips (2004),Phillips (2003)
IC 3568⋆	O3(H)	Rs	2.71	–	0.17	50 ± 5 (m)	4 ± 0.2	Gabler et al. (1991)
IC 4593⋆	O7(H)	Ra	1.57	–	0.07	49 ± 2 (tzHeII)	–	Phillips (2003)
Jacoby 1	PG1159	Ra	0.57	6.8	0.02	150± 10	7.0 ± 0.4	Jacoby & van de Steene (1995)
LTNF 1	O(H) + K5: V	B	2.00	3.23	0.03	105 ± 11 (s)	6.5 ± 0.25	Liebert et al. (1995)
Na 1⋆	–	E	–	–	–	43 ± 10 (tzHeI)	–	Phillips (2003)
NGC 3587	DAO	R	0.78	6.3	0.01	95 ± 8 (m)	6.94 ± 0.31	Napiwotzki (1999)
NGC 6058	O9(H)	Ebp	2.73	1.6	0.03	77 (m)	4.8 ± 0.3	Herald & Bianchi (2011)
NGC 6781	hgO(H)	Eb	0.75	5.7	0.61	104[6] (tzHeI)/123 ± 9 (m)	–	Schwarz & Monteiro (2006)
Sa 4-1⋆	O(H)	R	–	–	–	75± 10 (s)	7.9[3]	Feibelman & Bruhweiler (1989)
Sh 2-68†	PG1159	I	0.7[9]	5.6	–	96 ± 9 (m)	6.78 ± 0.32	Napiwotzki (1999)
Sh 2-216	DAO	Ra	0.129[8]	6.83[8]	0.08[8]	95 ± 2 (m)	6.9 ± 0.2	Harris et al. (2007), mimic
SkAc 1	–	Rc	1[10]	8.5	–	–	–	–
We 2-34	–	Bap:	1.59	7.7	–	–	–	–

[1] The spectral types are from Weidmann & Gamen (2011)

[2] The morphological classes are mainly from Frew (2008), based on the scheme of Parker et al. (2006)

[3] Distances, M_V, $E(B-V)$ and temperatures are from Frew (2008) unless otherwise indicated

[4] Schlafly et al. (2010)

[5] Balick & Frank (2002)

[6] Phillips (2003)

[7] Agüeros et al. (2009)

[8] Rauch et al. (2007)

[9] Ali et al. (2012)

[10] Assumed value

†: mimic, ⋆: excluded from sample for statistics

TABLE 2.3: New and updated data for our targets. See Section 2.2.7 for details on individual objects. The same stellar parameters as in De Marco et al. (2013) have been used for the targets in common

We have used a selection of equatorial Landolt photometric standards (Landolt,

Object	J (mag)	H (mag)	K (mag)	Data source
A 39	16.296 ± 0.10	16.409 ± 0.025	16.550 ± 0.052	UKIDSS
IC 972	15.778 ± 0.07	15.412 ± 0.11	15.160 ± 0.14	2MASS
FP J1824-0319	15.505 ± 0.07	–	–	2MASS
Jacoby 1	16.381 ± 0.12	–	–	2MASS
LTNF 1	13.960 ± 0.03	13.712 ± 0.03	13.634 ± 0.03	2MASS
NGC 6058	14.457 ± 0.04	14.621 ± 0.06	14.576 ± 0.10	2MASS
NGC 6781	16.243 ± 0.11	< 14.614	< 14.96	2MASS
Sh 2-68	16.044 ± 0.10	16.008 ± 0.17	–	2MASS
SkAc 1	18.500 ± 0.05	18.156 ± 0.05	18.268 ± 0.13	UKIDSS
We 2-34	18.466 ± 0.05	17.577 ± 0.04	17.527 ± 0.10	UKIDSS

Table 2.4: Near IR magnitudes from the 2-micron All Sky Survey (2MASS) and the UKIRT Deep Sky Survey (UKIDSS)

1992) containing blue stars when possible and standards situated in non-crowded regions to allow the best possible photometry. The list of the standard we used is presented in Table 2.5. We have observed one standard before and after each target to insure a sufficient sampling of standards for the magnitude calibration. We observed only few standards at high airmass ($\sim$ 2) because we only observed targets at low airmass ($\sim$ 1) and this might have limited the fit accuracy.

Name	# Stars (incl. # blue stars)	Observed nights
100 280	2	6
107 601	3	1,6
G163	2	1,6
PG0918+029	5 (1)	1,4
PG1034+001	1 (1)	1,6
PG1323-085	4 (1)	1,4,6
PG1633+099	5 (1)	1,4,6

Table 2.5: Landolt standards used for our observing run

2.2.4 Determination of the calibrated magnitudes

The photometry was processed on our targets with `DAOPHOT` and calibrated as described in Section 2.1. The zeropoints, colour-index coefficients and atmospheric absorptions for each night and filter are indicated in Table 2.6. The values of the calibrated magnitudes and errors for each night are provided in Appendix B.1.

To check the consistency of our photometry, we report in Table 2.7 and Figure 2.6 the magnitudes of objects that have been observed both during this observing run and the one of De Marco et al. (2013): A 28, EGB 6, JnEr 1, NGC 3587, Ton 320 and WDHS 1. In the B and V bands the agreement is better than ~ 0.03 mag and is mostly justified by the error bars. In the I band the disagreement is as large as 0.06 mag, with half the objects within the 0.03-magnitude limit. The error bars cannot explain all of these discrepancies. The origin of these differences can be multiple, including intrinsic low level variability. We average all values and adjust the error accordingly (see 2.1.2).

Night	Filter	Zeropoint (O)	Colour-index (C)	Atmospheric absorption (K)	# Standards observed
1	U	24.212 ± 0.032	0.058 ± 0.004	0.711 ± 0.024	35
	B	25.305 ± 0.032	0.066 ± 0.007	0.270 ± 0.024	34
	V	25.401 ± 0.023	−0.015 ± 0.005	0.120 ± 0.017	46
	I	24.492 ± 0.028	−0.001 ± 0.005	0.015 ± 0.020	40
4	U	24.019 ± 0.031	0.033 ± 0.008	0.556 ± 0.023	26
	B	25.234 ± 0.027	0.056 ± 0.008	0.227 ± 0.019	37
	V	25.436 ± 0.020	−0.028 ± 0.006	0.148 ± 0.014	37
	I	24.532 ± 0.030	−0.008 ± 0.009	0.059 ± 0.022	43
6	U	24.000 ± 0.022	0.038 ± 0.006	0.497 ± 0.015	53
	B	25.331 ± 0.015	0.059 ± 0.005	0.242 ± 0.011	45
	V	25.468 ± 0.016	−0.023 ± 0.005	0.113 ± 0.011	46
	I	24.604 ± 0.021	0.006 ± 0.006	0.066 ± 0.015	40

TABLE 2.6: Calibration coefficients for the photometric nights of observations

In addition, we have U-band information for many of our targets. We have a way to check the $B-V$-derived reddening using the $U-B$ colours. This provides a consistency check and can be beneficial in those cases when a bright companion (brighter than K0-5V; see Section 1.2.3) is present and contaminates the V band. Figure 2.7 shows the

Name	B	V	I
		Paper I	
A 28	16.280 ± 0.008 (3)	16.557 ± 0.009 (3)	16.877 ± 0.014 (3)
EGB 6	15.692 ± 0.002 (2)	15.999 ± 0.002 (2)	16.300 ± 0.009 (2)
JnEr 1	16.775 ± 0.005 (2)	17.13 ± 0.013 (2)	17.501 ± 0.023 (2)
NGC 3587	15.414 ± 0.001 (3)	15.777 ± 0.009 (3)	16.194 ± 0.029 (3)
Ton 320	15.379 ± 0.007 (2)	15.725 ± 0.006 (2)	16.105 ± 0.018 (2)
WDHS 1	16.958 ± 0.007 (3)	17.226 ± 0.004 (3)	17.489 ± 0.016 (3)
		This Paper	
A 28	16.273 ± 0.009(1)	16.523 ± 0.007(1)	16.83 ± 0.010(1)
EGB 6	15.689 ± 0.001(2)	15.997 ± 0.006(2)	16.328 ± 0.003(2)
JnEr 1	16.750 ± 0.008(2)	17.107 ± 0.008(2)	17.487 ± 0.004(2)
NGC 3587	15.390 ± 0.002(2)	15.772 ± 0.007(2)	16.161 ± 0.002(2)
Ton 320	15.360 ± 0.007(2)	15.693 ± 0.004(2)	16.05 ± 0.018(2)
WDHS 1	–	–	17.43 ± 0.022(1)

Table 2.7: Comparison of the magnitudes of objects overlapping between the analysis of De Marco et al. (2013) and this analysis. For this thesis work, the magnitudes of De Marco et al. (2013) and this analysis have been combined

comparison between reddening values obtained with the two colours. Only in one case, LTNF 1 (BE UMa), is the V-derived reddening larger. This star is a known close-binary. Although its M4V companion is not likely to contaminate the V band, the companion shows a hot spot (Shimanskii et al., 2008) likely contaminating the V band. For the other three objects (A 28, IC 972 and EGB 9), the V-derived reddening is lower, contrary to the contamination hypothesis. In two cases, it is significantly lower (IC 972 and EGB 9). EGB 9 is a mimic. Interestingly the upper limit to its reddening of 0.056 mag imposed by Schlafly et al. (2010) is lower than both values obtained from the star, likely indicating internal reddening. We leave this reddening discrepancy unresolved and use the $B-V$-derived value as done by De Marco et al. (2013). We note that while for EGB 9 we detected a bright companion, for A 28 we did not. Using higher reddening values for these objects would have decreased the excess detected for EGB 9, but not eliminated it. The large flux excess for IC 972

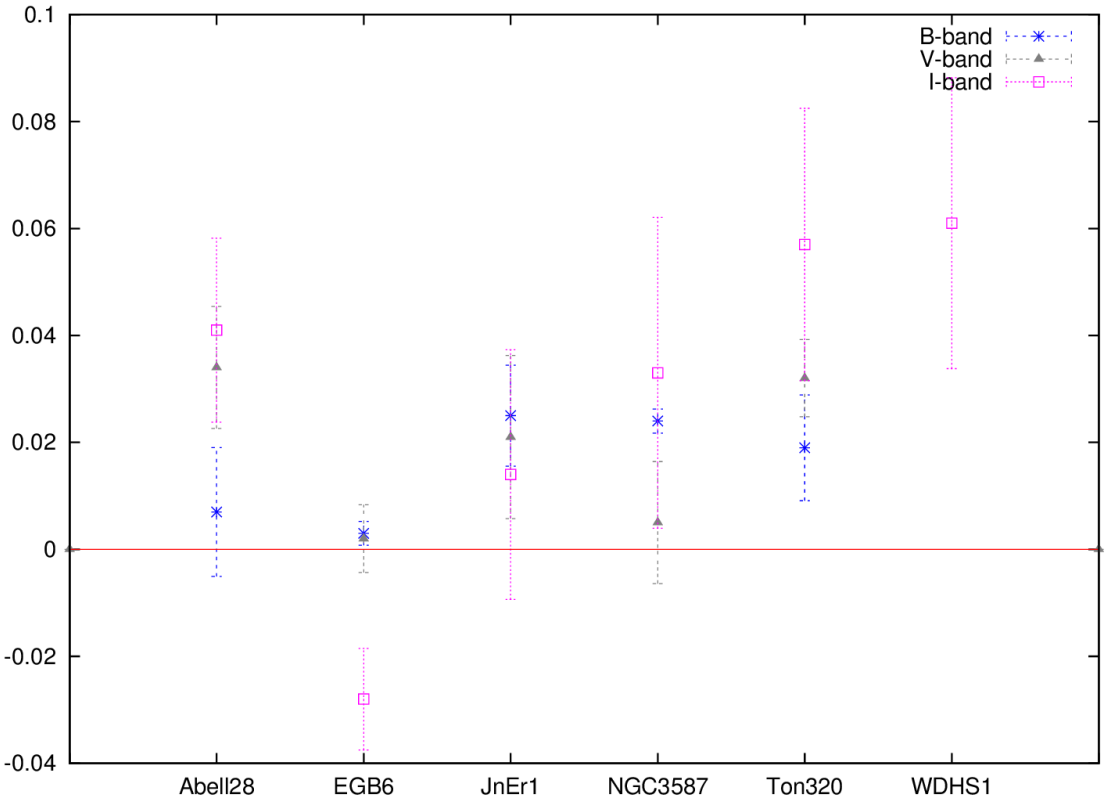

FIGURE 2.6: Magnitude difference for common targets to De Marco et al. (2013) and this work. The y-axis shows the magnitude difference "De Marco et al. (2013) − our magnitudes"

is not significantly decreased even using the larger reddening value, although nebular contamination is likely to affect the measured colours of this CSPN surrounded by a bright nebula.

2.2.5 Rejected targets

Our goal is to provide a more robust estimate of the CSPN binary fraction by extending the analysis of Paper I to a bigger sample. In an effort to add objects to our sample, we observed targets that were at the limit of our selection criteria. As a result, our sample included a few distant, compact PN (H 4-1, Na 1, Sa 4-1) and some CSPN surrounded by bright nebulae (IC 3568 and IC 4593). These features represent a challenge to our analysis primarily because of the difficulty of subtracting the nebula. We have analysed these objects to quantify the problem, but they are rejected from the final analysis.

Objects with a bright and compact PN suffer nebular contamination as the PN

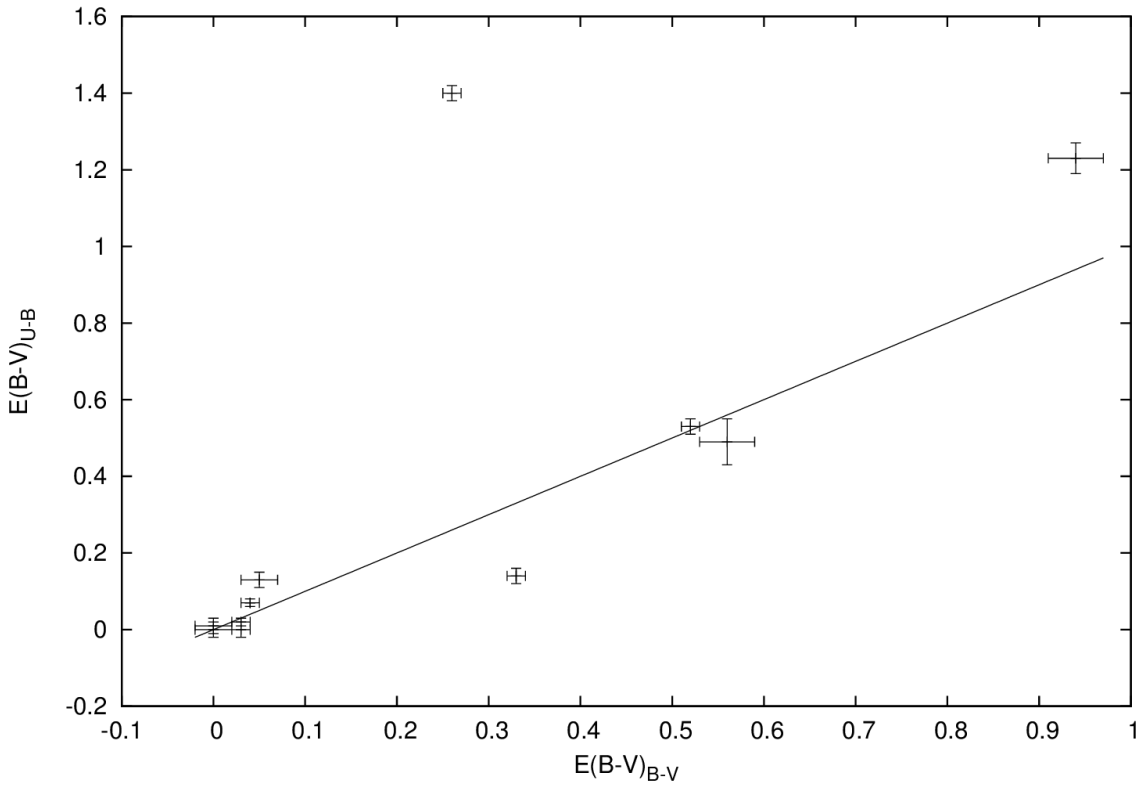

Figure 2.7: Comparison of the reddening obtained using the $U-B$ and $B-V$ colours.

cannot be adequately subtracted. Objects with a bright *extended* PN result in either too much nebular subtraction, when the nebular light overlapping the stellar PSF is less than the light sampled in the background region, or, more commonly, too little nebular subtraction if the opposite takes place. Nebular contamination affects the B-band (Hβ is included in the bandpass as well as the [O III] λ5007 at the red end of the bandpass) and its V-band (which includes the λ5007 [O III] line in the middle of the wavelength range). In most cases, the V-band will be more affected than the B band. The U and I bands are more immune to PN line contamination. However, for some of the objects the PN is still visible in images taken in these bands, possibly due to PN continuum emission. In the case of a very compact PN, nebular light remains in the photometry of the star and the CSPN appears too red in its $B-V$ colour. The derived reddening will hence be too large. De-reddened $V-I$ colours will then tend to be too blue for the stellar temperature and this will result in a "red deficit", i.e.,

Object	U	B	V	I
A 28	15.153 ± 0.009(1)	16.277 ± 0.007(4)	16.543 ± 0.017(4)	16.855 ± 0.022(4)
EGB 6	14.465 ± 0.010(2)	15.690 ± 0.001(4)	15.997 ± 0.005(4)	16.319 ± 0.014(4)
JnEr 1	15.519 ± 0.008(1)	16.759 ± 0.013(4)	17.116 ± 0.014(4)	17.491 ± 0.015(4)
NGC 3587	14.148 ± 0.008(2)	15.400 ± 0.011(5)	15.774 ± 0.008(5)	16.172 ± 0.022(5)
Ton320	14.156 ± 0.009(2)	15.366 ± 0.011(4)	15.704 ± 0.016(4)	16.063 ± 0.031(4)
WDSH1	–	16.961 ± 0.018(2)	17.225 ± 0.004(2)	17.463 ± 0.031(3)
Abell 39	14.129 ± 0.005(2)	15.314 ± 0.003(2)	15.616 ± 0.002(2)	15.929 ± 0.004(2)
(EGB 9)[1]	12.863 ± 0.009(1)	13.062 ± 0.008(1)	13.133 ± 0.009(1)	13.037 ± 0.010(1)
FP J1824-0319	–	14.601 ± 0.006(1)	14.841 ± 0.004(1)	15.159 ± 0.010(1)
(H 4-1)[3]	15.971 ± 0.019(1)	16.704 ± 0.183(2)	15.571 ± 0.155(2)	17.580 ± 0.117(2)
HaWe 10	–	17.549 ± 0.008(1)	17.888 ± 0.005(1)	18.259 ± 0.009(1)
(IC 3568)[2]	11.3 ± 0.1(1)	12.2 ± 0.1(1)	12.2 ± 0.1(1)	12.7 ± 0.1(1)
(IC 4593)[2]	9.7 ± 0.1(1)	–	–	11.1 ± 0.1(1)
(IC 972)[2]	17.761 ± 0.1(1)	18.049 ± 0.1(1)	17.446 ± 0.1(1)	16.530 ± 0.1(1)
Jacoby 1	13.963 ± 0.005(1)	15.216 ± 0.008(1)	15.610 ± 0.005(1)	16.020 ± 0.010(1)
LTNF 1	14.610 ± 0.011(1)	15.739 ± 0.007(1)	15.746 ± 0.006(1)	15.269 ± 0.008(1)
(Na 1)[3]	15.810 ± 0.036	16.310 ± 0.084	15.570 ± 0.102	15.879 ± 0.0.060(1)
NGC 6058	–	13.452 ± 0.004(1)	13.802 ± 0.004(1)	14.169 ± 0.007(1)
NGC 6781	16.243 ± 0.039(1)	17.111 ± 0.021(1)	16.880 ± 0.016(1)	16.439 ± 0.029(1)
(Sa 4-1)[3]	12.249 ± 0.004(1)	13.427 ± 0.004(1)	13.721 ± 0.005(1)	14.064 ± 0.006(1)
(Sh 2-216)	11.228 ± 0.007(1)	–	–	–
(Sh 2-68)[1]	15.809 ± 0.007(1)	16.647 ± 0.010(2)	16.453 ± 0.001(2)	16.173 ± 0.020(2)
SkAc 1	–	18.192 ± 0.006(3)	18.487 ± 0.010(3)	18.563 ± 0.027(2)
We 2-34	–	19.877 ± 0.002(2)	19.836 ± 0.004(2)	19.217 ± 0.015(1)

[1] These objects were discovered to be mimics, i.e. not *bona fide* PN.

[2] These objects have large bright PN which tend to be poorly subtracted.

[3] These objects have bright PN which are not subtracted: the B and V bands are the sum of the stellar and nebular fluxes.

TABLE 2.8: Calibrated magnitudes for our sample. The targets common to De Marco et al. (2013) are listed first. For these objects, the photometric measurements of De Marco et al. (2013) have been averaged with the new ones. The numbers in parenthesis indicate the number of observations. The magnitudes for each night separately are given in Appendix B.1. The PN names marked with a [1,2,3] have been observed but excluded from our sample, see Section 2.2.5 and Appendix B.2 for an explanation of individual objects

in a $V - I$ colour bluer than the single star prediction. For bright extended PN the opposite could also happen, if the nebula is over subtracted, but this is not as common.

For all our bright compact or extended PN (H 4-1, Na 1, Sa 4-1, IC 3568 and IC 4593) we obtained a "red deficit".

For objects with a bright extended PN (IC 3568, IC 4593), we artificially increased the error to 0.1 mag in Table 2.8 to reflect this difficulty. We did not increase the errors on photometry of central stars of bright compact PN (H 4-1, Na 1 and Sa 4-1), because the photometry is accurate although it includes star and nebula, something that increases the flux primarily the B and V bands. We have however marked them as unsuitable for the detection of companions as the colours are arbitrarily altered.

2.2.6 I and J-band detections

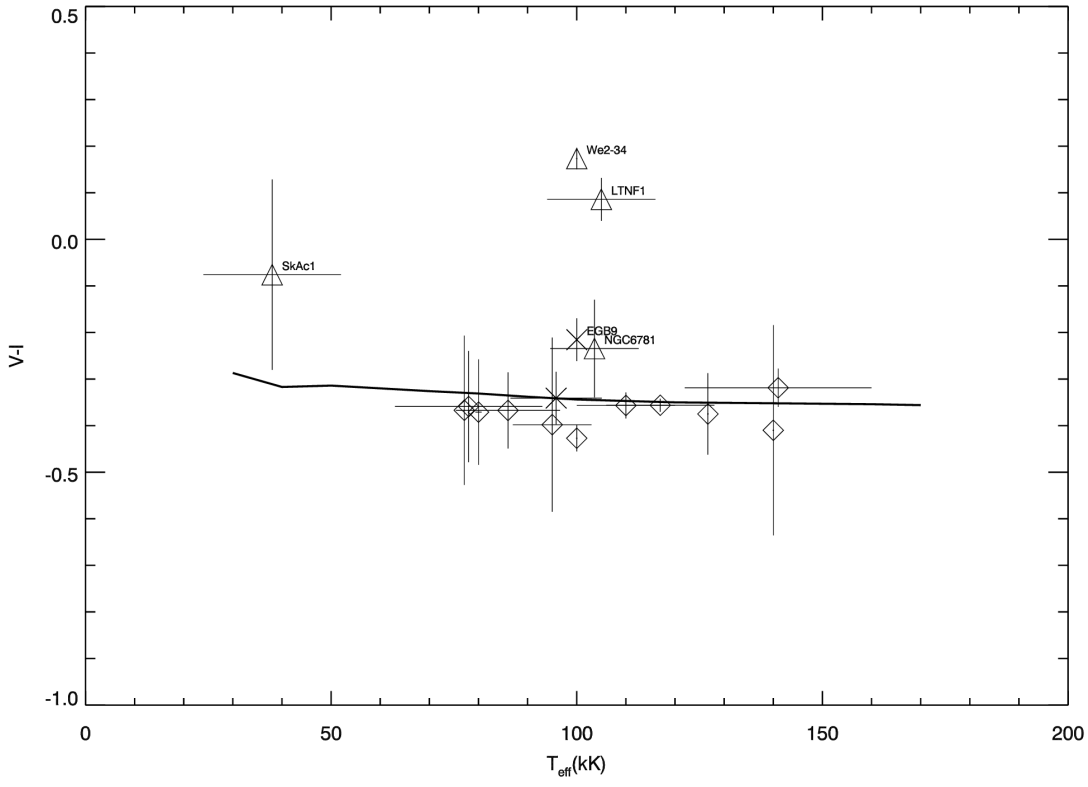

Figure 2.8: Predicted (solid line) vs. observed (symbols) $V-I$ colours as a function of stellar temperatures for our sample.

The target list for our observing run originally comprised 26 objects. However, due to the weather conditions, some overlap with the sample in De Marco et al. (2013), new

Name	$E(B-V)$	$(V-I)_0$	$\Delta(V-I)$	M_{I2}	Comp. spec. type
A 28	0.05 ± 0.02	−0.37± 0.08	−0.03± 0.08	> 9.62	Later than M4
A 39	0.04 ± 0.01	−0.36± 0.01	−0.01± 0.01	> 10.27	Later than M4
EGB 6	0.03 ± 0.01	−0.36± 0.03	−0.01± 0.03	> 11.69	Later than M5
EGB 9†	0.26 ± 0.01	−0.22± 0.05	0.13 ± 0.05	4.14 [4.67 – 3.75]	G4 [G8 – G0]
FP J1824-0319	0.09 ± 0.01	−0.43± 0.03	−0.08± 0.03	–	–
HaWe 10	0.00 ± 0.03	−0.37± 0.11	−0.04± 0.11	> 8.59	Later than M3
Jacoby 1	0.00 ± 0.06	−0.41± 0.23	−0.06± 0.23	> 8.92	Later than M3
JnEr 1	0.00 ± 0.02	−0.38± 0.09	−0.02± 0.09	> 10.11	Later than M4
LTNF 1	0.33 ± 0.01	0.09± 0.05	0.43± 0.05	4.35 [4.54 – 4.17]	G5 [G7 – G4]
NGC 3587	0.00 ± 0.05	−0.40± 0.19	−0.05± 0.19	> 8.71	Later than M3
NGC 6058	0.00 ± 0.04	−0.37± 0.16	−0.04± 0.16	> 4.10	Later than G4
NGC 6781	0.56 ± 0.03	−0.23± 0.10	0.11± 0.10	8.50 [11.57 – 7.64]	M3 [M5 – M1]
Sh 2-68†	0.52 ± 0.01	−0.34± 0.06	0.00 ± 0.06	> 9.04	Later than M3
SkAc 1	0.00 ± 0.06	−0.08± 0.20	0.24± 0.21	10.33 [12.92 – 9.32]	M4 [M6 – M4]
Ton 320	0.00 ± 0.03	−0.36± 0.12	−0.03± 0.12	> 9.85	Later than M4
WDHS 1	0.06 ± 0.01	−0.32± 0.04	0.04± 0.04	> 10.71	Later than M5
We 2-34	0.37 ± 0.01	0.17± 0.02	0.52± 0.02	8.55 [8.62 – 8.48]	M3 [M3 – M3]

†:mimic

TABLE 2.9: I-band excesses for our targets ($\Delta(V-I)$), companion absolute I-band magnitudes (M_{I2}) and spectral types (or limits) of our targets.

Name	$E(B-V)$	$(V-J)_0$	$\Delta(V-J)$	M_{J2}	Comp. spec. type
A 39	0.04 ± 0.00	−0.76± 0.10	0.06 ± 0.10	> 7.56	Later than M3
EGB6	0.03 ± 0.01	−0.50± 0.20	0.32 ± 0.20	9.03 [10.22 – 8.37]	M5 [M6 – M4]
FP J1824-0319	0.09 ± 0.01	−0.87± 0.07	−0.05± 0.07	> 12.26	Later than M4
Jacoby 1	0.00 ± 0.06	−0.77± 0.23	0.06 ± 0.23	> 8.74	Later than M5
NGC 6058	0.00 ± 0.04	−0.66± 0.15	0.13 ± 0.15	> 3.60	Later than G4
NGC 6781	0.56 ± 0.03	−0.61± 0.14	0.20 ± 0.14	8.29 [9.77 – 7.55]	M4 [M6 – M3]
Sh 2-68†	0.52 ± 0.01	−0.74± 0.11	0.07 ± 0.11	> 8.23	Later than M4
SkAc 1	0.00 ± 0.06	−0.01± 0.19	0.73 ± 0.22	9.28 [9.97 – 8.59]	M5 [M6 – M4]
We 2-34	0.37 ± 0.00	0.54± 0.51	1.36 ± 0.51	7.50 [8.32 – 6.82]	M3 [M4 – M2]

†:mimic

TABLE 2.10: J-band excess for our targets ($\Delta(V-J)$), companion absolute J-band magnitudes (M_{J2}) and companion spectral types (or limits) of our targets. All detections and limits are consistent with the results of the I-band excess (Table 10) and of De Marco et al. (2013).

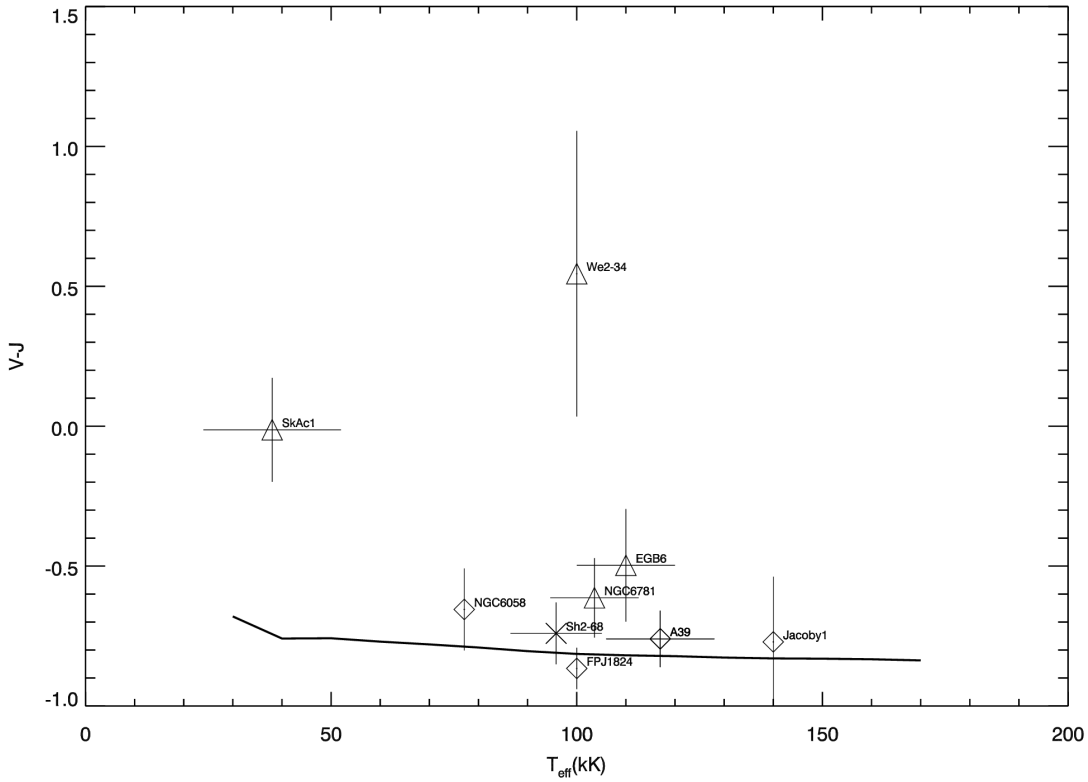

Figure 2.9: Predicted vs. observed $V - J$ colours as a function of stellar temperatures for our sample

discoveries of mimics in the observed sample (Frew & Parker, 2010), technical issues and the fact that some of our targets were at the detection limit, we only add 9 new CSPN to the De Marco et al. (2013) sample of 25 objects in the I-band and 7 to the sample of 9 from De Marco et al. (2013) in the J-band[4].

We carried out the look for detections according to the procedure described in Section 1.2. In the I-band, we report 4 detections of flux excess in our sample of CSPN (see Table 2.9, Figure 2.8): a 26-σ detection for We 2-34, an 8-σ detection for LTNF 1 (BE UMa, already known to be a close binary) and 1-σ detections for SkAc 1 and NGC 6781. We also report a 2-σ I-band excess for the mimic EGB 9. In the J-band, we confirm 3 of the detected I-band detections with a 3.5-σ detection for SkAc 1,

[4]Note that the number of bona fide PN listed in De Marco et al. (2013) (27 in the I band and 11 in the J band) has been revised here because of the discovery that 2 additional objects are mimics. These are EGB 1 and K 2-2.

a 2-σ detection for We 2-34 and a 1-σ detection for NGC 6781 (Table 2.10, Figure 2.9). Also, the J-band excess for EGB 6 - already detected in De Marco et al. (2013) - has been refined by including the newly measured magnitudes and is in agreement with the upper limit found from I-band excess. The spectral types of the companions for the detections in the I and J-band agree within one spectral subtype. This agreement adds confidence in our analysis.

2.2.7 Notes on individual objects

A 28

This dim round nebula has also been discussed in De Marco et al. (2013). Including the data from that paper, we find an upper limit for an M4V companion to the central star.

A 39

This canonical round nebula (Jacoby et al., 2001) is at a distance of 1.5 kpc (Danehkar et al., 2012). We find an upper limit of M4V for the companion spectral type in the I-band and an M3V limit in the J-band. We used the J-magnitude from DR8 of the UKIDDS survey instead of the less accurate 2MASS J-magnitude.

BD+33 2642

Recent radial velocity monitoring by Van Winckel et al. (2014) has established an orbital period of 1105 $\pm$ 24 days for this intermediate-period binary.

EGB 1

Multi-wavelength images from the Wide-field Infrared Survey Explorer (WISE; Wright et al. (2010)) show a bifurcated and irregular morphology which is unlike that expected for a PN. Combined with the arguments presented in De Marco et al. (2013), this indicates that EGB 1 is likely to be a mimic, therefore it has been removed from our sample.

EGB 6

This object has been discussed in De Marco et al. (2013). As discussed there, we kept the magnitudes from Fulbright & Liebert (1993) yielding a more consistent $H - K$ colour index. Since then, there has been the detailed study of Liebert et al. (2013) who provide fundamental data on the DAO primary star and its resolved companion. This is a dM star and lies at a separation of 0.166″from the primary, equivalent to ~ 96 AU at a distance of 580 pc. At this distance, the I-band absolute magnitude from Liebert et al. (2013) suggests a companion type of M3 V, earlier than our estimate of M5 V from De Marco et al. (2013) and this work.

EGB 9

Ellis et al. (1984) noted this faint object from the POSS, suggesting it may be a very low surface brightness dwarf galaxy. Hoessel et al. (1988) took CCD images, suggesting it was more likely to be a diffuse nebula. It is seen on SHASSA Hα images of Gaustad et al. (2001) as an irregular elongated patch, indicating an emission rather than a reflection nebula. Narrow-band CCD images (though not reproduced in their paper) have been obtained by Kerber et al. (2000). It appears on our 2.1-m Hα+[N II] image to be a wisp of ionized interstellar medium (ISM), probably similar to the nebula around PHL 932 (Frew et al., 2010). Frew (2008) noted the unusual colour of the putative ionising star, which matches a mid-B star. As this is too cool to ionise the surrounding material, there must be an additional source of ionisation present.

FP J1824-0319

This is the largest and closest PN discovered from the MASH[5] survey (Parker et al., 2006), with an angular diameter of nearly 30′, and a distance of about 380 pc (Frew et al., 2013). Preliminary photometry of the CSPN was presented by Frew (2008), refined here. We find no clear I-band or J-band excess; using the latter, we estimate an upper limit of M4V for the companion.

[5]Macquarie/AAO/Strasbourg/Hα Planetary Nebula Catalogue

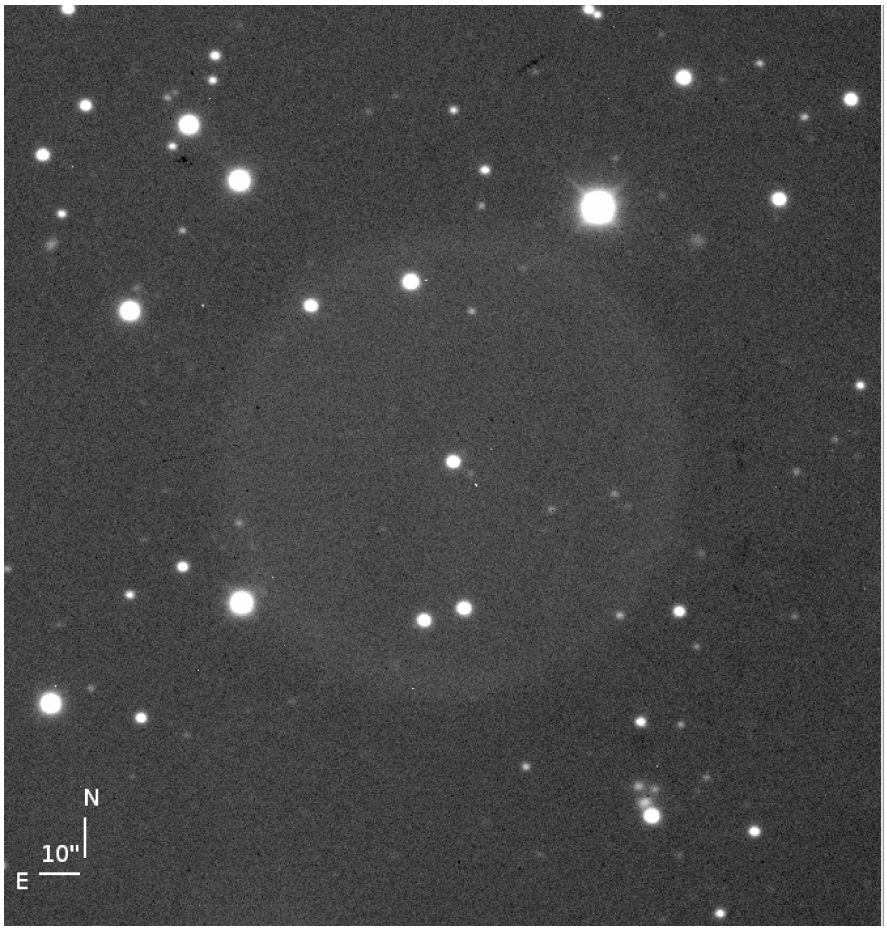

FIGURE 2.10: 300s exposure of the PN HaWe 10 in the V-band. The nebula has a radius of $\sim 110\ ''$.

HaWe 10

This is a beautiful round PN similar to A 39 (Section2.2.7) and Patchick 9 (Jacoby et al., 2010). We find no statistically significant IR excess for the CSPN.

Jacoby 1

This faint, round, high-excitation PN was discovered by Jacoby & van de Steene (1995). There have been several analyses of its hot hydrogen-deficient PG 1159 ionising star published in the literature. We find no IR excess.

K 2-2

We have also revisited the nature of this object here. Deep g' and r' images from DR 7 of the SDSS and r' and Hα images from the INT Photometric H-Alpha Survey (IPHAS; Drew et al. (2005)) show that the observed nebula is seemingly connected to widespread diffuse material, suggesting the ionised ISM interpretation (see De Marco et al. 2013) is the more likely. Therefore we have removed K 2-2 from our statistical analysis on central star binarity.

LTNF 1

We have confirmed this known close-binary CSPN (BE UMa; Ferguson et al. (1987, 1999); Ferguson & James (1994); Shimanskii et al. (2008) independently with our technique. The surrounding PN (Liebert et al., 1995) is extremely faint ($\log S_{\mathrm{H}\alpha} \simeq -6.3$) and our photometry is immune from any problems of nebular contamination. However our estimated spectral class of G5 disagrees with the temperature of the companion (4750 K) determined by Shimanskii et al. (2008) from detailed modelling of the system, which corresponds to a later spectral class of K3V. Shimanskii et al. (2008) also determined the companion mass to be only 0.25 $M_{\odot}$ which normally would indicate a M4 V companion. Thus, the companion is hotter and more luminous than its mass indicates, as is well-known for strongly irradiated companions in close binary systems. Although this system was known to be a close-binary, we have added it to our observation target list as we observe the biggest number of CSPN in our observability window, regardless if they are known binaries or not. This helps obtaining a sample unbiased with respect to binarity to represent the whole CSPN Galactic population.

Sh 2-68

The status of this nebula is uncertain, with two alternative hypotheses to explain its morphology and origin (Frew, 2008). Kerber et al. (2003) find that this PN moves the fastest in the ISM among all Galactic PN (53.2±5.5 mas yr^{-1}) and that the interaction with the ambient ISM shapes the nebula, progressively shifting it from the CSPN at its

centre. Kerber et al. (2004) also report the discovery of a "cometary tail" aligned with the central star Galactic proper motion and claim this comforts the hypothesis of the PN being shaped by its movement through the ISM magnetic field. The extraordinarily detailed image taken with the 4-m Mayall Telescope at Kitt Peak[6] lends weight to the conclusions of Frew (2008), namely that this is probably an irregular, stratified H II region in the ambient ISM, despite the commentary provided on the NOAO webpage. Owing to this ambiguity, we exclude Sh 2-68 from our statistical study.

SkAc 1

This little known nebula was discovered by Skiff and Acker (see Acker et al. 1996) and independently as a candidate low-surface brightness galaxy by Schombert et al. (1992) and Karachentseva et al. (1999), designated F 650-1 and KKR 4 respectively. It was reconfirmed as a PN by Makarov et al. (2003). As far as we know, no narrow-band image has been published in the literature, so we present our 2.1-m Hα image in Figure 2.11.

We 2-34

This is a new binary CSPN. It has a very strong I and J band excess. The morphology of this faint nebula is either cylindrical or bipolar, viewed at modest inclination, illustrated in Figure 2.12.

2.3 The SSO 2.3m observing run and its analysis

2.3.1 Observations

The images for this dataset have been obtained at the 2.3m RSAA telescope at the Siding Spring Observatory during the nights of the 15^{th}, 16^{th} and 17^{th} of May 2012. Orsola DE MARCO and David FREW were observing while I was working at Université de Montpellier 2. The default imager was used mounted at the Nasmyth focus of the

[6] See http://www.noao.edu/image_gallery/html/im1164.html

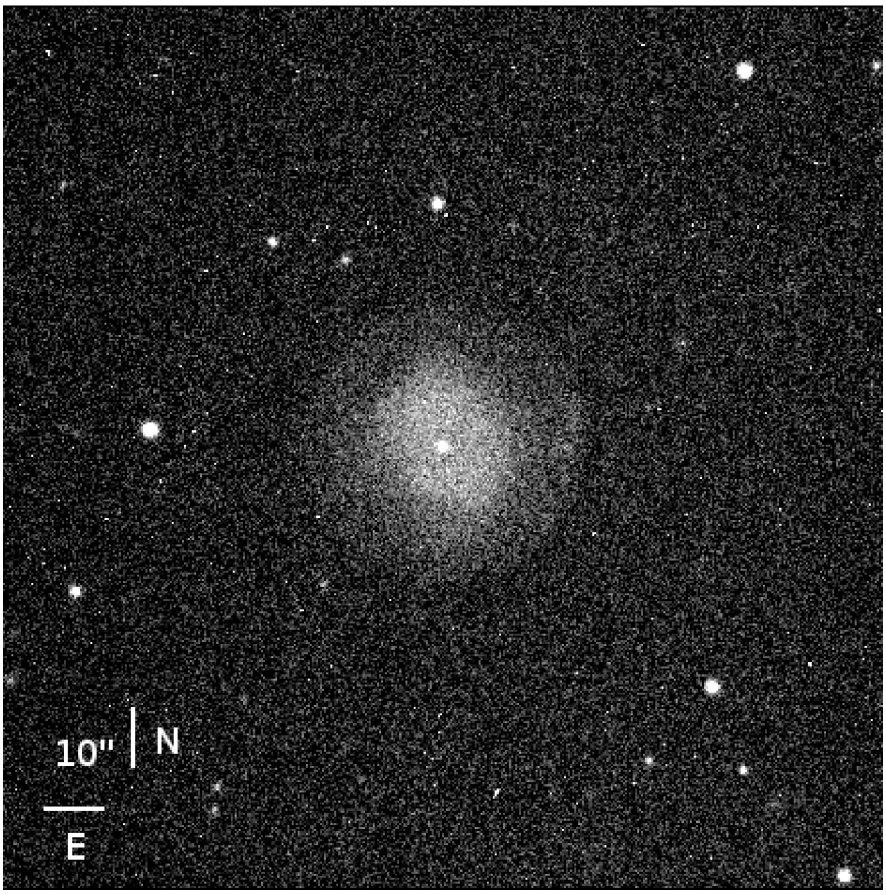

Figure 2.11: High contrast image of a 600s exposure of the PN SkAc 1 in the [O III] filter from our observations.

telescope. The CCD model was a 2048x2048 E2V with a pixel size of 13.5 μm. The field of view is circular with a diameter of 6.62′ , yielding a projected resolution of 0.338 arcsec/pixel.

The targets for this run were selected by following the same criteria as the ones described in Section 1.3.3: we selected central stars with V magnitudes between 13 and 20 surrounded by an evolved, faint, extended nebula if they were observable in our observation window 30° above the horizon. Some of the targets (e.g. the PHR[7] ones) were also chosen to overlap with the targets observed during a NIR observing run of ours at the SSO 4m, the data of which have not been analysed yet. We obtain the B and V-bands of the overlapping targets from this observing run while the infrared magnitudes will be obtained once the SSO 4m data are analysed. During night 1 it

[7]Parker, Hurtley, Russeil (Parker et al., 2006)

FIGURE 2.12: IPHAS three colour (red=Hα, green=R, blue=I) image of the nebula surrounding We 2-34. The image has been extracted from the Macquarie University GPN Database (Bojičić et al. 2014, in preparation)

was not realised that the filter names on computer console were mismatched to the filters physically in place. Only after a methodical mapping on the filter wheel and on the filters in the wheel were the V and I band images were obtained for the observed targets. However no B band images were obtained on the first night. For this reason, objects that were observed only during night 1 cannot be analysed as the B-band images are missing, therefore no reddening is available for these objects.

The reduction was made as with the KPNO 2.1m images (Section 2.2.2) using the *ccdproc* package in `IRAF`. The flat-field correction has been made using the sky-flats taken each night. Due to the confusion in filters during the first night, the master flat-fields have been made with $\sim$ 10 sky-flats which appeared to be sufficient to remove most of the image aberrations but a larger number number would have been more

Name	Sp. Type[1]	PN[2] morph.	D[3] (kpc)	M_V (mag)	$E(B-V)$ (mag)	$T_{\rm eff}$ (method) (kK)	log g (cm s^{-2})	Reference & Comment
Abell 48⋆	[WN4-5]	Emprs	1.53	1.3	1.9	70 ± 5	–	Frew et al. (2014b); Todt et al. (2013)
BMP J1808-1406	Blue	Eapr	1.40	7.0	0.44	–	–	–
FP J1912-0331	–	–	–	–	0.12	–	–	–
LoTr 8	–	Baps	–	–	1.2:/0.61	–	–	Tylenda et al. (1992)
NGC 2899⋆	–	Bamps	1.37	3.9	0.44	215 ± 16	–	Corradi & Schwarz (1995); Drew et al. (2014)
PHR J1408-6106	–	Ears	1.70	4.4	0.46	–	–	Cohen et al. (2011)
PHR J1418-5144	–	Ears	0.94	6.5	0.26	–	–	–
PHR J1432-6138	–	Bas	1.25	7.4	0.26	72.8	–	Cohen et al. (2011); Preite-Martinez et al. (1989)
PHR J1510-6754	–	Ear	1.10	4.9	0.19	–	–	–
HaTr 5	–	Rars	1.25	3.7	0.75	–	–	–
K 1-22	F V	Ears	1.33	5.3	0.076	141	6.73	Ciardullo et al. (1999) Bilíková et al. (2012)
K 1-23	–	Emr	2.89	6.0	0.1	72.8	–	Tylenda et al. (1992); Phillips (2003)
Lo 5	–	Eaprs	1.52	5.6	0.4/0.14	42.2	–	Preite-Martinez et al. (1989); Tylenda et al. (1992)
MeWe 2-4	–	–	1.13	7.0	0.2	–	–	–
YM 16	–	Eams	0.5[4]/1.29	5.7	1.29	–	–	–
RCW 69	–	Ems	1.00	6.3	0.52(s)	–	–	Frew et al. (2006)
Sh 2-68⋆	hybrid/DAO	As	0.7[4]/1.30	4.2	0.56	95.8 ± 9.3	6.78	–
Sh 2-71⋆	–	Bmps		–	–	129	–	Mikulášek et al. (2005)

[1] The spectral types are from Weidmann & Gamen (2011) unless otherwise indicated

[2] The morphological classes are mainly from the PN Macquarie University Database (Bojičić et al. 2014, in preparation)

[3] Distances, M_V, $E(B-V)$ and temperatures are from Frew (2008) unless otherwise indicated

[4] Ali et al. (2012)

⋆: excluded from sample for statistics

Table 2.11: New and updated data for the targets observed at the SSO 2.3m. See Section 2.3.4 for details on individual objects.

suitable.

2.3.2 Photometry and determination of the absolute magnitudes

The photometry on the images for this run have been performed in the same fashion as for the Kitt Peak 2.1m analysis. Indeed, the characteristics of the two CCD cameras are similar and there is no technical difference that would justify a different set of parameters. The only noticeable difference, the circular field of view, had an impact when adding the WCS to the images but has not caused any difficulties once this was taken into account. The only factors that would have implied a change of the photometry input parameters were related to the observing conditions. The weather

Name	J	H
Abell 48*	13.508 ± 0.027	12.834 ± 0.028
LoTr 8	16.193 ± 0.127	15.386 ± 0.110
PHR J1418-5144†	15.800 ± 0.072	15.281 ± 0.111
HaTr 5	13.563 ± 0.048	13.017 ± 0.072
K 1-22	15.033 ± 0.048	14.464 ± 0.057
K 1-23	16.701 ± 0.149	15.941 ± 0.158
Sh 2-68*	16.044 ± 0.101	16.008 ± 0.176

†: CSPN photometry contaminated by nearby companion

⋆: excluded from sample for statistics

TABLE 2.12: 2MASS J and H magnitudes for our targets.

for the whole run was photometric and the seeing similar to the Kitt Peak 2.1m run (1-2″), so we kept the same input parameter values as the ones described in Section 2.1.1.

The statistics used to estimate the average magnitudes and errors are the same as the ones described in Section 2.2. The calibration procedure is also similar.

The calibrated magnitudes of our 17 targets are presented in Table 2.13. The first thing that stands out from these results is that more magnitudes have been obtained from this three day observing run (effectively two days) compared to the seven days at the Kitt Peak observatory. The main reasons for this is excellent weather during the SSO 2.3m run. Also, no target at the edge of our observation criteria were observed during the SSO 2.3 run: none of the observed CSPN were surrounded by a bright or compact nebula, and all CSPN were within close distance (D $<$ 3 kpc) and in a reasonable range of magnitudes (13$<$ V $<$20), which was not the case for the KP 2.1m run. Sh 2-71 has been observed only during night 1, therefore as explained in Section 2.3.1 only the V and I magnitudes have been determined.

2.3.3 Infrared excess detections

Using the same procedure as described in Section 1.2 and using the magnitudes shown in Table 2.13, we obtain the colours of our 14 targets listed in Table 2.14. We find 8 infrared excesses in the I-band: a 1$-\sigma$ detection corresponding to a M4V companion for

Name	U	B	V	I
Abell 48⋆	20.584 ± 0.084(1)	19.627 ± 0.028(1)	18.079 ± 0.019(1)	15.654 ± 0.015(1)
BMP J1808-1406	–	19.117 ± 0.026(1)	19.072 ± 0.019(1)	18.804 ± 0.027(1)
FP 1912-0331	12.760 ± 0.009(1)	13.860 ± 0.025(1)	13.997 ± 0.016(1)	14.259 ± 0.016(1)
LoTr 8	19.019 ± 0.031(1)	18.918 ± 0.001(2)	18.074 ± 0.035(2)	16.995 ± 0.030(2)
PHR J1408-6106	–	17.953 ± 0.026(1)	16.982 ± 0.017(1)	15.948 ± 0.011(1)
PHR J1418-5144	15.962 ± 0.021(1)	17.120 ± 0.004(2)	17.204 ± 0.028(3)	17.320 ± 0.022(2)
PHR J1432-6138	–	19.067 ± 0.027(1)	18.711 ± 0.019(1)	17.704 ± 0.020(1)
PHR J1510-6754	15.283 ± 0.012(1)	15.876 ± 0.028(1)	15.662 ± 0.018(1)	15.146 ± 0.015(1)
HaTr 5	18.667 ± 0.026(1)	17.746 ± 0.021(1)	16.557 ± 0.011(2)	14.920 ± 0.009(2)
K 1-22	14.877 ± 0.023(1)	15.868 ± 0.022(1)	16.062 ± 0.096(2)	15.571 ± 0.013(2)
K 1-23	17.138 ± 0.024(1)	18.286 ± 0.116(2)	18.648 ± 0.084(3)	18.832 ± 0.114(3)
Lo 5	15.388 ± 0.009(1)	16.600 ± 0.023(1)	16.972 ± 0.026(2)	17.297 ± 0.053(2)
MeWe 2-4	–	17.682 ± 0.025(1)	17.890 ± 0.017(1)	17.944 ± 0.013(1)
YM 16	–	20.715 ± 0.053(1)	20.252 ± 0.023(1)	19.043 ± 0.041(1)
RCW 69	18.602 ± 0.022(1)	19.403 ± 0.028(1)	19.409 ± 0.020(1)	18.945 ± 0.038(1)
Sh2-68⋆	15.809 ± 0.007(1)	16.625 ± 0.049(3)	16.465 ± 0.027(3)	16.171 ± 0.019(3)
Sh 2-71⋆	–	–	13.507 ± 0.009(1)	12.874 ± 0.007(1)

⋆: excluded from sample for statistics

Table 2.13: Calibrated magnitudes obtained for the targets observed during the SSO 2.3m run. The magnitudes obtained from each night independently are given in Appendix B.3.

BMP 1808-6106, a $4-\sigma$ detection corresponding to a K9V companion for PHR J1432-6138, a $1-\sigma$ detection corresponding to a K4V companion for PHR J1510-6754, a $1-\sigma$ detection corresponding to a G0V companion for HaTr 5, a $1-\sigma$ detection corresponding to a K3V companion for K 1-22, a $1-\sigma$ detection corresponding to an M4V companion for MeWe 2-4, a $2-\sigma$ detection corresponding to an M2V companion for YM 16 and a $3-\sigma$ detection corresponding to an M4V companion for RCW 69. Sh 2-68 is the only target to overlap with the Kitt Peak sample of the Kitt Peak 2.1m and the upper limit of K5V determined here is consistent with the detection of a M3V companion determined in the KPNO 2.1m analysis. The excess detected for the [WN] CSPN of Abell 48 is not necessarily ascribable to a companion (see Section 2.3.4) and is flagged for further observations. For this reason, we remove it from the sample used for statistics. Two objects show blue excesses that are not consistent within the error bar:

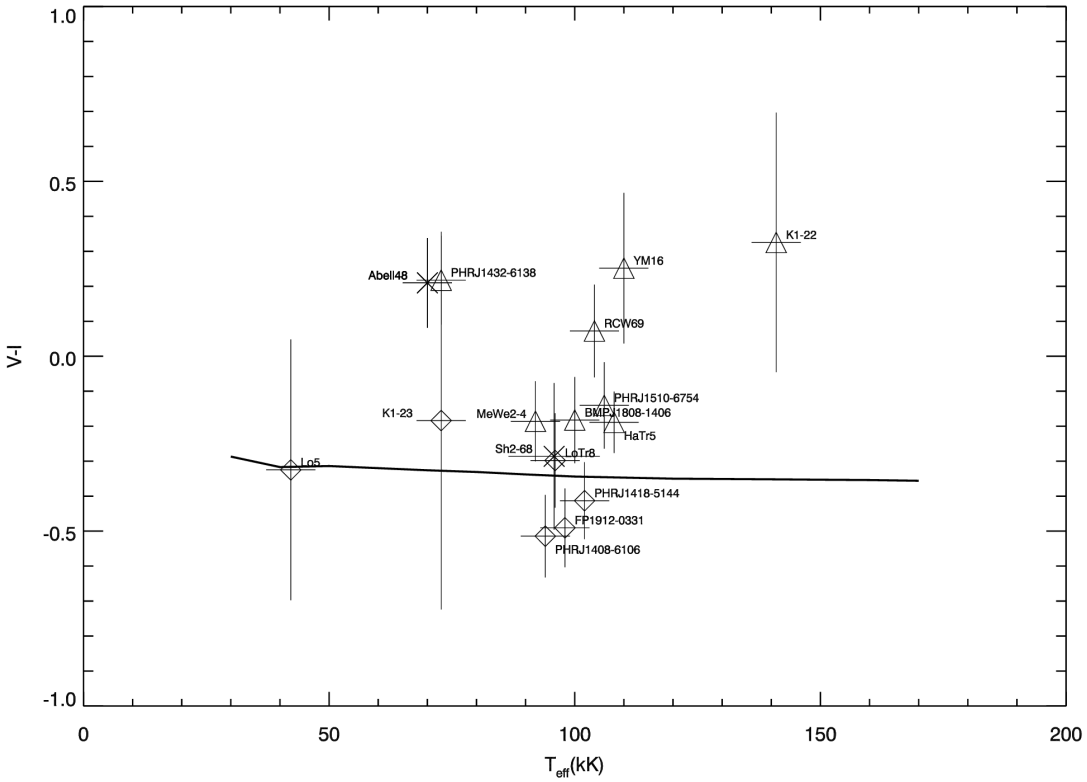

FIGURE 2.13: $V - I$ colours for the targets of the 2.3m run.

FP 1912-0331, first referenced by Frew et al. (2013) is not referenced in Simbad and has the status of "possible PN" in the Macquarie PN Database. The other one, PHR 1408-6106, has a high E($B - V$) of 1.30. At such high reddenings, it is possible that the determined value is slightly too high introducing a blue excess while dereddening the magnitudes too much.

Little vetted data is available from near-infrared surveys (2MASS and UKIDSS). The retrieved magnitudes for our objects are shown in Table 2.12, all from 2MASS. A $4 - \sigma$ flux excesses is detected for HaTr 5 corresponding to an F8V companion and a $4 - \sigma$ excess as well for K 1-22 corresponding to a K1V companion. A common caveat when retrieving 2MASS data from the CDS is that the wrong central star is referenced, as in the case for NGC 2899 and MeWe 2-4. Also, there is a faint red star near the CSPN of PHR J1418-5144 that is resolved in our images but that is unresolved in the 2MASS images. It is likely that the photometry of the central star includes both

Name	$E(B-V)$	$(V-I)_0$	$\Delta(V-I)$	M_{I2}	Comp. spec. type
Abell 48⋆	1.85 ± 0.03	0.21 ± 0.13	0.54 ± 0.13	1.76 [2.23 – 1.35]	A5 [F0 – A2]
BMP J1808-	0.38 ± 0.03	−0.18± 0.12	0.16 ± 0.12	9.49 [11.18 – 8.71]	M4 [M5 – M3]
FP 1912-03	0.19 ± 0.03	−0.49± 0.11	−0.15± 0.11	–	–
LoTr 8	1.17 ± 0.04	−0.31± 0.13	0.04 ± 0.13	> 6.56	Later than K7
PHR J1408-	1.30 ± 0.03	−0.53± 0.12	−0.18± 0.12	–	–
PHR J1418-	0.25 ± 0.03	−0.41± 0.11	−0.07± 0.11	> 10.26	Later than M4
PHR J1432-	0.66 ± 0.03	0.22 ± 0.13	0.55 ± 0.13	6.97 [7.43 – 6.56]	K9 [M1 – K7]
PHR J1510-	0.54 ± 0.03	−0.14± 0.12	0.21 ± 0.12	5.79 [6.95 – 5.11]	K4 [K9 – K0]
HaTr 5	1.52 ± 0.02	−0.18± 0.09	0.16 ± 0.09	3.68 [4.68 – 3.08]	G0 [G8 – F6]
K 1-22	0.14 ± 0.10	0.33± 0.37	0.68 ± 0.37	5.52 [6.89 – 4.51]	K3 [K9 – G6]
K 1-23	0.00 ± 0.14	−0.18± 0.54	0.15 ± 0.54	> 6.36	Later than K6
Lo 5	0.00 ± 0.10	−0.32± 0.37	−0.01± 0.37	> 7.05	Later than M0
MeWe 2-4	0.12 ± 0.03	−0.20± 0.11	0.14 ± 0.11	9.70 [11.53 – 8.91]	M4 [M5 – M3]
YM 16	0.79 ± 0.06	0.26 ± 0.22	0.60 ± 0.22	7.90 [8.68 – 7.26]	M2 [M3 – M0]
RCW 69	0.33 ± 0.03	0.07 ± 0.13	0.42 ± 0.13	9.56 [10.15 – 9.07]	M4 [M4 – M3]
Sh 2-68⋆	0.48 ± 0.06	−0.29± 0.21	0.06 ± 0.21	> 5.94	Later than K5

⋆: excluded from sample for statistics

Table 2.14: I-band excesses for our targets ($\Delta(V-I)$), companion absolute I-band magnitudes (M_{I2}) and spectral types (or limits) of our targets.

stars, which would justify a brighter companion limit (M0V) when using the J-band photometry as opposed to our I-band images (M4V).

For this observing run sample, the biased binary fractions are higher than for any other sample: 57 percent (8/14) in the I-band and 67 percent (2/3) in the J-band. These numbers will be taken into account to build the final sample in Chapter 6.

2.3.4 Notes on individual objects

The available information about the objects that have been observed during the SSO 2.3m run is given below. Most of our targets have little if any published information.

A 48

Full spectroscopic (Todt et al., 2013) and multi-wavelength (Frew et al., 2014b) studies are available for this object, one of the few [WN] CSPN known to date. Frew et al. (2014b) note that a binary post-AGB evolutionary channel with mass exchange

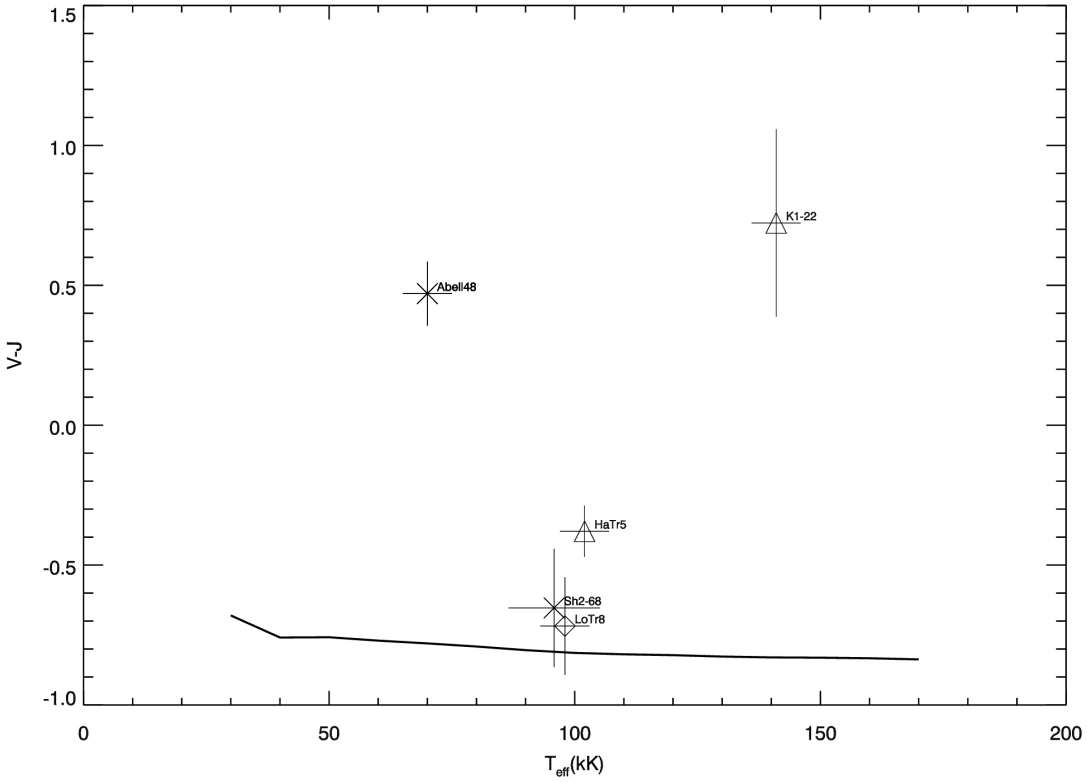

FIGURE 2.14: $V - J$ colours for the targets of the SSO 2.3m run.

Name	$E(B-V)$	$(V-J)_0$	$\Delta(V-J)$	M_{J2}	Comp. spec. type
Abell 48⋆	1.85 ± 0.03	0.47 ± 0.11	1.25 ± 0.11	0.89 [1.18 – 0.62]	A1 [A2 – A0]
HaTr 5	1.52 ± 0.02	−0.38± 0.09	0.44 ± 0.09	2.93 [3.32 – 2.60]	F8 [G0 – F5]
K 1-22	0.14 ± 0.10	0.72 ± 0.34	1.55 ± 0.34	4.59 [5.38 – 3.84]	K1 [K6 – G5]
LoTr 8	1.17 ± 0.04	−0.72± 0.17	0.09 ± 0.17	> 6.51	Later than M1
Sh2-68⋆	0.48 ± 0.06	-0.65 ± 0.21	0.16 ± 0.21	> 6.00	Later than M0

⋆: excluded from sample for statistics

TABLE 2.15: J-band excesses for our targets ($\Delta(V-J)$), companion absolute J-band magnitudes (M_{J2}) and spectral types (or limits) of our targets.

may be required to produce the [WN] central stars. However they do not find any evidence for the presence of a companion and estimate that if the system is a binary, the companion must have a spectral type later than $\sim$ F0V. Our technique reveals an A5V companion to the CSPN in the I band and A1V in the J band. However, the dense, extended wind surrounding the [WR] central stars affect their colours making the SED naturally redder. Even using single star colours appropriate for a [WR] star, it is doubtful whether a companion could be detected around such a naturally red star. Additionally, as pointed out by Frew et al. (2014b) using the available NIR flux measurements it can already be seen that the star is not strongly variable, like the vast majority of [WR] CSPN (Hajduk et al., 2010). The nebula is visible but faint on the V images so that photometric nebular contamination should be negligible.

NGC 2899

Although this type-I PN has been known for a long time, there has been a lot of confusion regarding the position of its CS. Many of the available data refer to the association of two stars in the centre of the nebula. Instead, Drew et al. (2014) used u and g-band images from their VPHAS+ survey to show that the central star is located a few arcsec from this pair. At the time of observation, we thought that the CSPN was one of the two stars in the centre of the nebula (with a V magnitude $\sim$ 16), therefore we used low exposure time for these bright objects. However the real central star is more than 3 magnitudes fainter (g=19.32, Drew et al. 2014). The combination of too short an exposure time and poor seeing make the CSPN invisible or blended with the two neighboring bright stars. As a results, we could not measure the brightness of this object.

PHR J1418-5144

For this object, a faint star is located very near the CSPN in the I-band image while it is not resolved in the 2MASS images with lower spatial resolution. For this object, the 2MASS magnitudes have been disregarded.

K 1-22

As stated by Chu et al. (2011), K 1-22 is a known binary resolved by the HST (Ciardullo et al., 1999). Hubble images show two sources 0.35 ″apart in the centre

of the nebula, the northeast one is the CSPN while the southwest one is the cool companion. The two stars are completely blended in our I-band images. Ciardullo et al. (1999) determined a K2V spectral type for the companion. Its near and mid-infrared SEDs have been plotted from Spitzer's IRAC and MIPS images (Chu et al., 2011) and modelled using 4 blackbodies: one for the CS, one for the companion, and two for emitters at 700 and 150K likely associated with dusty structures. Some spectral features in Spitzer's IRS are described by Chu et al. (2011). The 24μ MIPS image shows the nebula. The IRS spectrum shows that the diffuse emission comes from the [O IV] 25.89 μm line. It is not known if the dust is associated with the CSPN or its companion.

We find a K3V companion in the I-band and a K1V companion in the J-band. The nebula is visible on the image but is rather smooth and non-clumpy so it is likely that background subtraction was carried out accurately. This object is a great confirmation of companion detection consistent with other methods of detection and shows that if the nebula is visible but reasonably faint and homogeneous, the IR excess can be recovered safely.

K 1-23

This object shows a constant shift of 0.2 magnitudes in all filters between night 2 and night 3 of our observing run (see Table B.2). No such shift is obvious when comparing the magnitudes from nights 1 and 2, but we flag this object as being a potential photometric variable requiring follow-up observations. The variability between nights 2 and 3 explains the large errors on the photometry because they may have been taken at different phases of the variability cycle. We find a lower limit for the companion spectral type of K6V, whereas in the J-band we detect a 5-σ K1V companion. We justify this discrepancy by the assumption that the star is variable and therefore our magnitudes and the 2MASS ones are incompatible. We exclude this object from the statistical sample in the J-band but keep it for the I-band sample.

MeWe 2-4

The 2MASS photometry available for this object used the wrong star, therefore no NIR photometry is available.

RCW 69

This type-I PN shows a bipolar morphology and is nitrogen-enhanced as typical of its class. Frew et al. (2006) used narrow-band photometry and low-resolution spectroscopy to deduce a variety of parameters from this nebula and its CSPN. We find a 3-σ flux excess detection indicative of an M4V companion.

Sh 2-68

Sh 2-68 is the only object in common with the southern and northern hemisphere samples. Notes on this object are available in Section 2.2.7.

Summary

In this section, we have determined a photometric method suited for our targets. We have fine-tuned the input parameters of our photometric routine, `DAOPHOT`, to obtain the best possible photometric consistency. The reduction and analysis of data acquired at the KPNO 2.1m in the U, B, V and I bands were presented, including the determination of the instrumental magnitudes, calibrated magnitudes and the associated statistics. The reddening was estimated using a CCM law (with R_V=3.1) in both the $B-V$ and $U-B$ colours. The obtained reddenings from each colour are in good agreement. We carried out a search for NIR excess on this first sample of 9 *bona fide* PN observed in the I-band and found 4 detections. Upper limits for the companion spectral type were determined when no excess was detected. Additional J-band data were obtained from online surveys (DENIS, 2MASS and UKIDSS) for 9 CSPN of the same sample, confirming 3 of the 4 NIR excess flux detected in the I-band with an excellent agreement of 1-2 spectral subtypes, while adding one excess that had not been revealed in the I-band analysis.

We carried out a similar study on B, V and I-band data collected at the SSO 2.3m for 14 CSPN (2 newly discovered mimics are excluded from the sample) and found a high rate of 8 detections. J-band photometry of 3 objects – excluding the mimics – have been analysed in addition and yields 2 NIR excess consistent with our I-band findings within 2 spectral subtypes.

These samples are combined with the 25 CSPN previously analysed by De Marco et al. (2013). The comparison of the photometry on overlapping targets is very satisfactory. The technique demonstrated in this chapter is a robust tool for building an unbiased sample to determine the binary fraction of CSPN. The main drawback of this strategy is that it is demanding in observing time. In the next chapter, we attempt to combine the rigour of our method with the potential of large samples from available online optical and NIR surveys.

Chapter 3

NIR excess search from available surveys

Dedicated observations to obtain optical data for $\sim$ 20 targets at a time has proven to be possible and quite fruitful. This strategy suffers from being quite time and effort-consuming if the goal to attain is $\sim$ 150 objects. In a totally opposite approach, we tried to use online available NIR surveys to look for NIR excess in catalogued objects and draw statistics out of these analyses. Ideally we would use archival survey data often including reasonable PN sample sizes to determine the CSPN binary fraction. Unfortunately, either the precision of the survey is not sufficient (e.g., the 2MASS survey has a limiting J-band magnitude of 16.5 and the error bars for magnitudes approaching this limit are large), or the difficulties present because of PN subtraction render the final magnitudes unreliable. Finally, the need for blue and red photometry means that many surveys can contribute to our search but are not sufficient. For example 2MASS can provide some near-IR measurements, but these are not useful unless high quality B and V observations are also available.

We looked for red/NIR excesses using the data from the SDSS DR7 survey that offers the spectral range we need and a promising photometric precision, while using the stellar parameters available from the extended catalogue of Frew (2008). This study is presented in Section 3.1. We also sought NIR excesses using the data from the extended catalogue of Frew (2008), a compilation of the best photometry available

from online surveys. How this analysis was led as well as the results we obtained are presented in Section 3.2.

3.1 The analysis of the overlap between the sample of Frew (2008) and the SDSS DR7 survey

We carried out our analysis using Sloan Digital Sky Survey (SDSS) data to determine the ability of this survey to detect companions. This survey is in principle ideal because it covers all the optical spectrum (u, g, r and i) and a NIR band (z). We first analyse objects in common between the objects we observed ourselves and the SDSS to test the feasibility of the study, and then extend the analysis to any SDSS-observed PN.

3.1.1 Estimating the SDSS ability to detect faint companions

The sample of this analysis has been created by cross-matching the catalogue of Frew (2008) with the SDSS data release 7 (Abazajian et al., 2009). The magnitudes were downloaded using the VIZIER[1] query form. We used the photometric measurements from the SDSS DR7, after applying the calibration corrections described by Covey et al. (2007). These corrections are specific to the SDSS DR7 "model" magnitudes, rather than to the PSF or Petrosian magnitudes of our objects, hence our choice of using the model magnitudes for our targets. The corrected SDSS magnitudes are presented in Table 3.1.

The coefficients for the reddening (Table 3.2) have been obtained after convolving the SDSS filter passbands with a 100,000 K, $log\ g = 7$ star, using the CCM reddening law with $R_V = 3.1$. We used the $g - r$ colour to determine $E(B - V)$ for our targets. Although the r band is more prone to contamination by a companion, the $u - g$ colour resulted in a reddening that was systematically slightly high, producing de-reddened colours that were systematically bluer than the model colours. The SDSS u filter is known to have a red leak, however this would have had the opposite effect. The

[1] the CDS catalogue service, http://vizier.u-strasbg.fr/

Name	u	g	r	i	z
A 28	15.871 ± 0.004	16.291 ± 0.004	16.739 ± 0.005	17.115 ± 0.006	17.438 ± 0.017
A 31	14.674 ± 0.004	15.203 ± 0.005	15.757 ± 0.004	16.116 ± 0.005	16.396 ± 0.008
A 39	14.845 ± 0.007	15.317 ± 0.007	15.824 ± 0.007	16.201 ± 0.009	16.532 ± 0.013
EGB 6	15.199 ± 0.004	15.660 ± 0.005	16.216 ± 0.004	16.563 ± 0.004	16.906 ± 0.010
HaWe 4	16.770 ± 0.004	17.019 ± 0.005	17.263 ± 0.007	17.572 ± 0.007	17.767 ± 0.017
HaWe 10	17.035 ± 0.005	17.554 ± 0.007	18.123 ± 0.009	18.532 ± 0.010	18.944 ± 0.042
IC 4593	11.804 ± 0.008	11.535 ± 0.003	11.446 ± 0.009	11.425 ± 0.004	11.969 ± 0.004
IsWe 1	16.027 ± 0.003	16.313 ± 0.004	16.640 ± 0.005	16.922 ± 0.005	17.198 ± 0.014
Jacoby 1	14.692 ± 0.003	15.237 ± 0.003	15.850 ± 0.004	16.283 ± 0.004	16.685 ± 0.009
JnEr 1	16.263 ± 0.004	16.781 ± 0.005	17.357 ± 0.006	17.756 ± 0.007	18.144 ± 0.026
K 2-2	13.524 ± 0.004	14.395 ± 0.004	14.462 ± 0.003	14.811 ± 0.005	15.153 ± 0.005
NGC 3587	14.934 ± 0.004	15.480 ± 0.004	16.046 ± 0.004	16.456 ± 0.005	16.831 ± 0.010
NGC 6058	14.029 ± 0.004	13.359 ± 0.011	14.302 ± 0.012	14.627 ± 0.005	14.771 ± 0.008
SkAc 1	17.665 ± 0.006	18.180 ± 0.009	18.651 ± 0.010	18.882 ± 0.013	19.022 ± 0.042
Ton 320	14.869 ± 0.004	15.361 ± 0.004	15.946 ± 0.004	16.328 ± 0.005	16.723 ± 0.009

Table 3.1: Corrected SDSS magnitudes for targets in common with our sample (De Marco et al. (2013) and Section 2.2). We used the "model" DR7 magnitudes and applied the calibration corrections detailed in Covey et al. (2007)

model colours have been obtained using the `SYNPHOT` package in `IRAF` by convolving the CSPN model spectra from TheoSSA and TMAP with temperatures between 40 and 170kK used previously (see Section 1.2) with the SDSS filters. The SDSS colours of main-sequence stars for our cool-companion grid were adopted from the synthetic photometry of Covey et al. (2007). However on their recommendation, we did not use their approximate values for M_J but those determined in De Marco et al. (2013).

We apply the method used in Chapter 2 on the corrected SDSS magnitudes for the 15 objects in common between our sample studied so far (De Marco et al. (2013) and Section 2.2) and the SDSS sample and present the results in Figure 3.2 and Table 3.3. We recover our detections with great consistency (A 31, EGB 6, SkAc 1). The CSPN of SkAc 1 shows a 4-σ z-band excess consistent with an M5V companion, in good agreement with the M4V companion detected at the 1-σ level in the I-band and the M5V companion detected at the 3-σ level in the J-band. EGB 6 shows a 2-σ detection

Band	λ_0	$A_\lambda/E(B-V)$	Band	λ_0	$A_\lambda/E(B-V)$
U	3597 Å	4.86	u	3586 Å	4.86
B	4386 Å	4.12	g	4716 Å	3.62
V	5491 Å	3.10	r	6165 Å	2.66
R	6500 Å	2.10	i	7475 Å	2.01
I	7884 Å	1.90	z	8922 Å	1.40
J	1.237 μm	0.889	$J_{\rm 2MASS}$	1.241 μm	0.885
H	1.645 μm	0.562	$H_{\rm 2MASS}$	1.651 μm	0.349
K	2.212 μm	0.349	$K_{\rm 2MASS}$	2.165 μm	0.361

TABLE 3.2: Bandpass central wavelengths after convolution with a 100 kK, log g=7, solar abundance synthetic stellar atmosphere and resulting extinctions according to CCM with R_V=3.1

in the z-band of an M5V companion, comparable to the 2-σ M5V companion detected in the J-band. A 31 shows a 4-σ detection of an M4V companion in the z band, comparable to the 5-σ M4V companion detection in the J-band.

It is possible that the reddening obtained from the $g-r$ colour is slightly too high, implying too high a dereddening and yielding to too blue a $g-z$ colour (i.e. the star is bluer than the single star limit, even accounting for the uncertainty) on stars with no infrared excess or diminishing the excess if there is one. This may be shown by the existence of small blue excesses for A 28, HaWe 10 and IsWe 1 (see Figure 3.2). HaWe 4 shows a puzzling red deficit that cannot be accounted for by this effect nor by nebular contamination. It is unclear why the SDSS photometry is inconsistent for this object.

The differences in spectral types between those derived in this analysis and the ones from Section 2.2.6 lies in the difficulty of calibrating the SDSS colours. This caveat eventually hampers detection of faint companions but guards us from false detections. The SDSS g and r images of IC 4593 and K 2-2 show strong nebular emission explaining strong phony red deficits for these objects. The reddening obtained for NGC 6058 is strongly negative and the object has been excluded from the study. We conclude that *provided that no nebular contamination affects the central star photometry*, the SDSS

photometry can be used safely to detect infrared excesses with the precision of one companion spectral type, although some of the fainter companions may elude detection.

Name	$E(B-V)$	$(g-z)_0$	$\Delta(g-z)$	M_{z2}	Comp. spec. type
A 28	0.12 ± 0.01	−1.41± 0.03	−0.08± 0.04	–	–
A 31	0.01 ± 0.01	−1.22± 0.03	0.12 ± 0.03	9.88 [10.23 – 9.58]	M4 [M4 – M4]
A 39	0.07 ± 0.01	−1.38± 0.04	−0.02± 0.04	> 10.13	Later than M4
EGB 6	0.02 ± 0.01	−1.29± 0.03	0.06 ± 0.03	11.13 [11.76 – 10.70]	M5 [M5 – M5]
HaWe 4	0.33 ± 0.01	−1.47± 0.03	−0.17± 0.03	–	–
HaWe 10	0.00 ± 0.01	−1.39± 0.06	−0.09± 0.06	–	–
IsWe 1	0.25 ± 0.01	−1.45± 0.04	−0.10± 0.06	–	–
Jacoby 1	0.00 ± 0.04	−1.45± 0.14	−0.09± 0.14	> 10.90	Later than M5
JnEr 1	0.00 ± 0.01	−1.37± 0.04	−0.01± 0.04	> 11.72	Later than M5
NGC 3587	0.00 ± 0.01	−1.36± 0.03	−0.01± 0.03	> 11.82	Later than M5
SkAc 1	0.07 ± 0.01	−0.99± 0.06	0.25 ± 0.06	10.64 [11.06 – 10.31]	M5 [M5 – M4]
Ton 320	0.00 ± 0.03	−1.36± 0.11	−0.06± 0.11	> 11.05	Later than M5

Table 3.3: $g-z$ excess for objects in our sample

3.1.2 New infrared excess detections using the SDSS

With knowledge of the limitations likely to affect the SDSS we have established in Section 3.1.1, we attempt to use the SDSS survey to detect new CSPN with red excess likely to host a companion. We cross-matched the vetted sample of Frew (2008) with the SDSS DR7 photometric catalogue. We used distances from Frew (2008) or assumed a distance of 1 kpc where a value was not available. We adopted temperatures from Frew (2008) or Phillips (2003) or assumed a temperature of 100,000 K and log g = 7 for all other stars of this sample. The magnitudes are presented in Table 3.4 and the results in Table 3.5 and Figure 3.2.

A majority of the objects display a red deficit, due to too high a reddening. Small red deficits can be due to the SDSS-calibration errors discussed above. This is the case

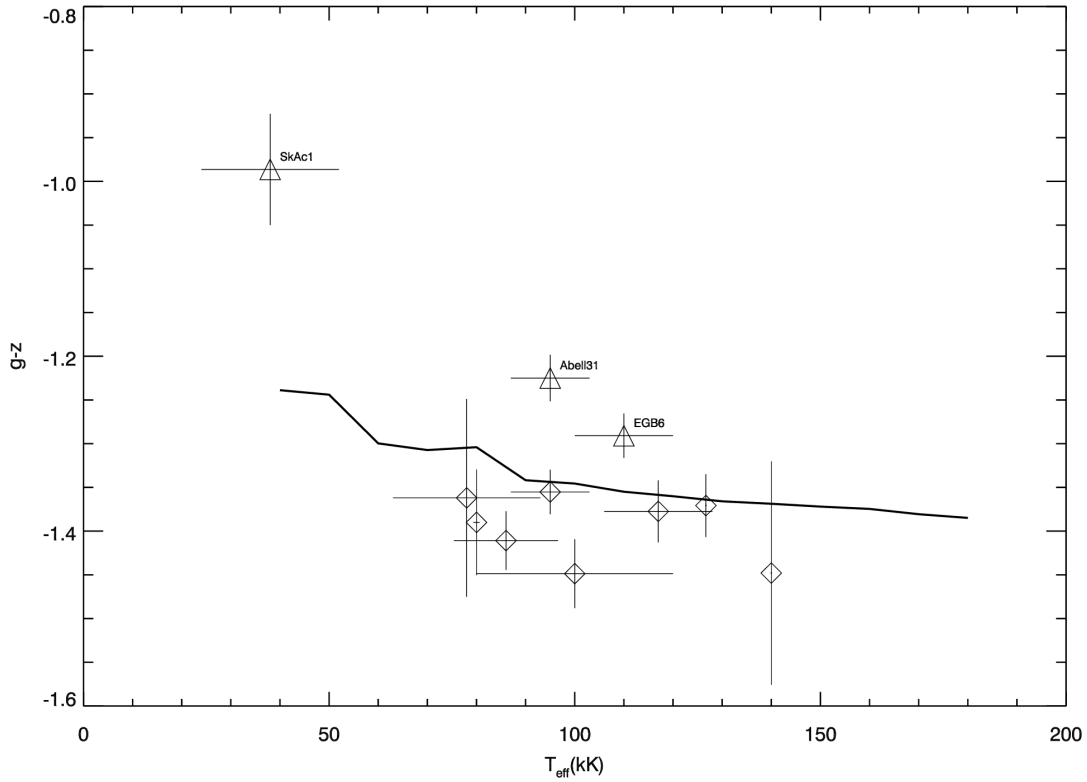

FIGURE 3.1: $g - z$ excess for our observed targets observed with SDSS

for the central stars of A 13, A 33, K 1-16, KLW 10, Kronberger 61, KUV 03459+0037, NGC 6894 and WPS 54. For several objects, the photometry of the central star is likely contaminated by the surrounding nebula. Nebular contribution in the g-band is expected due to the presence of the [O III] λ5007 line in the middle of the filter bandpass. Nebular contamination in the r-band also happens due the presence of the Hα line in the filter bandpass. However, the Hα line tends to be weaker than the [O III] line especially in mature PN. There is no way to correct simply for nebular contamination as it changes according to filters, nebular excitation class and nebular morphology. Therefore we exclude here objects with a strong nebular contamination, either because the nebula is bright, because it is compact, or both. This is the case for M 1-1, M 1-75, Sn 1 and TS 1. For some objects the magnitudes display strong, unexpected excursions, indicating some flaw in the photometry that could be due to nebular contamination (IC 1747) or also possible to an erratic value from the SDSS

Name	D(kpc)	Teff(kK)	u	g	r	i	z	nebular contamination
Abell 30	2.0	115 ± 5	14.051 ± 0.004	14.191 ± 0.010	15.221 ± 0.003	14.888 ± 0.004	15.042 ± 0.005	faint
Abell 33	1.16	100 ± 5	15.213 ± 0.004	15.620 ± 0.003	16.116 ± 0.003	16.411 ± 0.004	16.857 ± 0.012	faint
Abell 52	2.0	150 ± 20	17.514 ± 0.005	17.599 ± 0.006	17.722 ± 0.011	17.821 ± 0.008	17.936 ± 0.031	very faint nebula in g
Abell 73	2.7	66 ± 10	22.151 ± 1.082	21.385 ± 0.042	20.906 ± 0.048	20.453 ± 0.045	20.196 ± 0.113	faint nebula in all bands
BD+33 2642	3.1	20.2 ± 0.5	10.824 ± 0.001	10.635 ± 0.001	11.023 ± 0.001	11.360 ± 0.001	12.040 ± 0.003	neb. unresolved
HaWe 4	1.2	125 ± 5	16.770 ± 0.004	17.019 ± 0.005	17.263 ± 0.007	17.572 ± 0.007	17.767 ± 0.017	v. faint
IC 1747	2.6	74 ± 3	19.436 ± 0.064	16.851 ± 0.009	17.579 ± 0.006	19.052 ± 0.025	18.432 ± 0.045	bright compact nebula in g and r
IRAS 21282+5050	2.4	20 ± 5	16.654 ± 0.003	15.161 ± 0.007	13.655 ± 0.008	13.408 ± 0.003	12.911 ± 0.004	compact nebula with [WCL] CSPN
K 1-16	1.9	140 ± 5	14.183 ± 0.003	14.731 ± 0.004	15.282 ± 0.003	15.705 ± 0.004	16.101 ± 0.008	nebula present in g
K 3-82	2.8	80 ± 10	21.734 ± 6.384	16.543 ± 0.006	16.196 ± 0.006	16.208 ± 0.009	15.278 ± 0.013	nebula present in g
KLW 10	3.1	100 ± 10	19.717 ± 0.014	19.798 ± 0.020	19.821 ± 0.043	19.987 ± 0.035	20.144 ± 0.177	v. faint
Kn 31	3.1	100 ± 10	21.080 ± 0.115	20.552 ± 0.025	20.097 ± 0.027	19.874 ± 0.028	19.746 ± 0.090	v. faint
Kn 34	2.8	100 ± 10	21.629 ± 0.046	21.089 ± 0.056	20.867 ± 0.204	20.847 ± 0.087	21.851 ± 0.633	v. faint
Kn 61	2.6	140 ± 20	17.621 ± 0.006	18.047 ± 0.008	18.485 ± 0.011	18.811 ± 0.014	19.052 ± 0.046	faint
LDu 1	2.6	100 ± 10	23.307 ± 0.052	21.388 ± 0.055	21.231 ± 1.951	21.284 ± 0.104	22.091 ± 1.318	v. faint
LoTr 5	0.50	100 ± 5	11.080 ± 0.001	13.279 ± 0.007	12.143 ± 0.009	12.817 ± 0.009	9.275 ± 0.001	v. faint
M 1-1	4.0:	38 ± 10	14.893 ± 0.003	14.159 ± 0.002	14.173 ± 0.002	15.297 ± 0.003	15.220 ± 0.016	bright compact nebula in g and r
NGC 650-1	1.2	140 ± 5	16.823 ± 0.008	16.892 ± 0.005	17.220 ± 0.004	17.511 ± 0.007	17.697 ± 0.021	bright nebula in all bands
NGC 6210	2.1	61 ± 3	10.786 ± 0.007	11.459 ± 0.001	10.250 ± 0.011	11.382 ± 0.008	11.185 ± 0.002	very bright, compact nebula
NGC 6309	2.1	97 ± 6	13.943 ± 0.003	12.504 ± 0.002	12.833 ± 0.002	13.547 ± 0.002	13.129 ± 0.003	bright nebula in g and r
NGC 6894	1.2	100 ± 10	18.232 ± 0.011	18.786 ± 0.012	18.649 ± 0.018	18.361 ± 0.011	18.601 ± 0.036	bright rim in g and r
NGC 7008	1.0	96 ± 4	13.792 ± 0.003	13.694 ± 0.010	13.948 ± 0.003	14.738 ± 0.011	13.074 ± 0.004	faint nebula in g
Sn 1	6.5	80 ± 5	13.856 ± 0.004	14.150 ± 0.002	13.551 ± 0.003	14.598 ± 0.003	14.628 ± 0.004	bright compact nebula in g
Te 2	2.0	100 ± 10	21.442 ± 0.033	21.046 ± 0.041	20.924 ± 0.141	20.811 ± 0.058	21.594 ± 1.096	v. faint
TS 1	1.0	90 ± 5	17.178 ± 0.005	17.479 ± 0.006	17.652 ± 0.009	18.208 ± 0.010	18.429 ± 0.038	bright compact nebula in g and r
We 2-5	2.3	100 ± 10	20.121 ± 0.021	20.286 ± 0.030	20.409 ± 0.051	20.504 ± 0.055	21.729 ± 1.221	v. faint
WPS 46	0.7:	100 ± 10	16.094 ± 0.003	16.440 ± 0.004	16.942 ± 0.006	17.314 ± 0.006	17.687 ± 0.016	no neb.
WPS 54	0.45	125 ± 10	14.342 ± 0.003	14.850 ± 0.003	15.467 ± 0.003	15.873 ± 0.004	16.232 ± 0.007	no neb.

Table 3.4: Corrected SDSS magnitudes for targets cross-matching with the sample of Frew (2008). Here again we applied the calibration corrections detailed in Covey et al. (2007)

photometry (for Abell 30, the r-band is not in line with other values). Some objects are either too bright or too faint to consider using their SDSS photometric measurements: the central stars of BD+332642 and NGC 6210 are saturated, while the ones of A 73, Kronberger 34, LDu 1, Teutsch 2, and We 2-5 are too faint to provide adequate precision on the flux measurements. IRAS 21282+5050 is a cool hydrogen-deficient object in transition between the AGB and the PN phase and no information can be extracted from its colours due to nebular contamination and the dust surrounding this new PN.

This quick analysis reveals that the use of the SDSS survey to infer a statistical binary fraction is not straight-forward. The photometric precision of SDSS observations is intrinsically sufficient for the data quality we are looking for. The calibration of the SDSS photometry is also very good, with only a slight systematic effect when compared

Name	$E(B-V)$	$(g-z)_0$	$\Delta(g-z)$	M_{z2}	Comp. spec. type
Abell 13	0.45 ± 0.02	−1.50± 0.14	−0.15± 0.14	–	–
Abell 33	0.08 ± 0.00	−1.41± 0.02	−0.06± 0.02	–	–
Abell 52	0.45 ± 0.01	−1.34± 0.05	−0.04± 0.05	> 12.10	Later than M6V
Abell 73	1.07 ± 0.05	−1.19± 0.23	0.12± 0.23	> 9.63	Later than M4V
K 1-16	0.03 ± 0.00	−1.44± 0.02	−0.07± 0.02	–	–
K 3-82	0.95 ± 0.01	−0.83± 0.03	0.48± 0.03	2.87 [3.00 – 2.75]	F2V [F3V – F1V]
KLW 10	0.43 ± 0.04	−1.58± 0.23	−0.28± 0.23	–	–
Kn 31	0.13 ± 0.01	−1.28± 0.06	0.02± 0.06	> 11.58	Later than M5V
Kn 61	0.15 ± 0.03	−1.54± 0.15	−0.23± 0.15	–	–
NGC 650-1	0.26 ± 0.01	−1.39± 0.03	−0.02± 0.03	> 12.33	Later than M6V
NGC 6309	0.25 ± 0.00	−1.18± 0.01	0.16± 0.01	2.96 [3.08 – 2.85]	F3V [F4V – F2V]
NGC 6894	0.73 ± 0.02	−1.42± 0.08	−0.12± 0.08	–	–
NGC 7008	0.33 ± 0.01	−0.11± 0.04	1.24± 0.04	5.02 [5.11 – 4.94]	G8V [G9V – G8V]
WPS 46	0.06 ± 0.01	−1.38± 0.03	−0.07± 0.03	–	–
WPS 54	0.00 ± 0.06	−1.38± 0.24	−0.08± 0.24	> 7.93	Later than M2V

TABLE 3.5: $g-z$ excess for the CSPN cross-matching with sample of Frew (2008).

to our I-band work. However, if an unvetted sample is considered, in which bright nebulae are common then, as expected, the survey becomes non-viable for our analysis. This reduces considerably the number of PN that can be used for our statistical purpose. Time allowing, one could remeasure the photometry from the SDSS raw images, but the effort is probably excessive for the meagre harvest it would offer.

Although we cannot use the entire sample to infer the binary fraction, we find 4 objects with colours consistent with single star colours, therefore showing no infrared excess: A 52, Kn 31, M 76 (the CSPN is surrounded by a bright nebula) and PG0948+534 (the SuperCosmos images[2] reveal an asymmetric diffuse feature in blue and red bands, so contamination from the nebula cannot be excluded). The only objects compatible with our selection criteria (Section 1.3.3) would be A 52 and Kn 31.

[2] Hambly et al. (2001), images available at `http://www-wfau.roe.ac.uk/sss/`

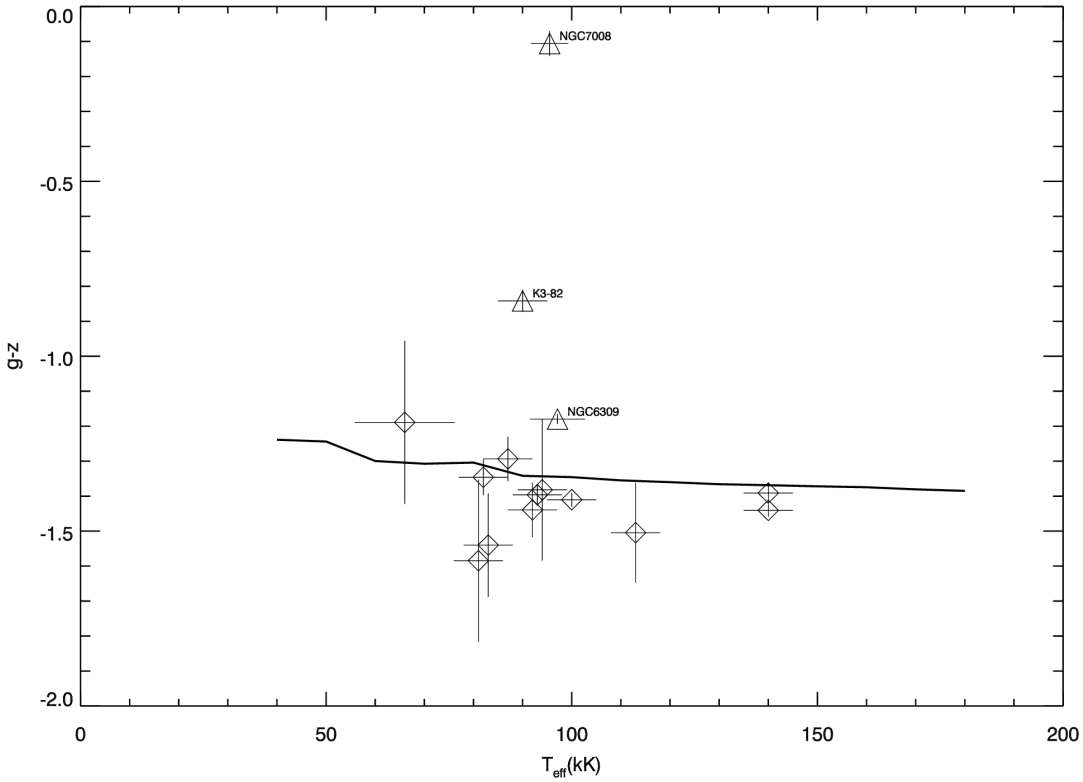

Figure 3.2: Predicted (solid line) vs. observed (symbols) $g - z$ colours as a function of stellar temperatures for the DR7 SDSS objects. The objects with an assumed temperature of 100kK have been spread between 80kK and 100kK for clarity. All symbols below the line are erroneous "red deficits" (see text). Such a high number of red deficit objects highlights the importance of target selection and therefore the difficulty of using archival data for estimating the binary fraction of CSPN

However including these two objects in the sample would introduce a source of heterogeneity for a meagre contribution. We do not take them into account in our sample for statistics but flag them for future observations. More importantly, we also find 4 objects that show large red flux excess that we flag for further study.

NGC 6309

The central star of this quadrupolar, high excitation PN (Vázquez et al., 2008) shows an excess corresponding to an F3V companion. Bilíková et al. (2012) could not discern the CSPN from the nebula in the IRAC bands. The SDSS images for this PN show that the nebula is as bright as the central star, implying serious nebular contamination

in the photometry of the central star. Although this is a strong 16-σ detection, it is possible that the PN alone could create such a photometric artifact.

LoTr 5

This system is composed of an O-type subdwarf (150,000 K; Feibelman & Kaler 1983) and a chromospherically active, fast rotating (v sin i=60 km.s^{-1}) G5III companion (5,230K; Jasniewicz et al. 1996). Van Winckel et al. (2014) have recently monitored the radial velocity of the barium-enhanced G5 giant, finding slow variations consistent with a binary orbital period of a few years. Thus, LoTr 5 represents another newly-discovered system of intermediate period. This agrees with Jasniewicz et al. (1996) who first suggested that LoTr 5 is a wide binary in which accretion from the ABG wind induces the fast rotation of the giant (Montez et al., 2010). Montez et al. (2010) indicate that there is evidence that the X-ray emission observed at the system's position is due to coronal activity associated to the rapidly rotating companion.

Our grid of cool star colours has been designed for main sequence companion and is not suitable for giants. Furthermore, the CSPN is very bright and is saturated for this object. A quick look at the object's magnitudes shows that it gets brighter in the redder bands (especially in z), although no spectral type can be determined in this study.

NGC 7008

The central star of this PN has been resolved by the HST into a detached binary. Ciardullo et al. (1999) find a K3 companion if the object is placed at 0.4 kpc, implying a separation of 160 AU. Using their distance and a temperature of 95.5k $\pm$ 3.8K (Phillips, 2003), we find a 31-σ detection consistent with a G8V companion. The difference in spectral type can be explained by the calibration shift of the SDSS photometry and slight nebular contamination, given the nebula is visible - but not very bright - on the SDSS plates. However, Frew et al. (2014, in preparation) find that the CSPN is likely to be a G8 subgiant rather than a main-sequence star. There is also an X-ray point source detected by the Chandra X-ray Observatory (Kastner & Montez, 2012), which

is coincident with the CSPN, possibly suggesting the presence of an active companion.

K 3-82

Little information is available about this object in the literature. As described above, we assumed a temperature of 100 kK and log g = 7. Placed at 2.76 kpc (Frew, 2008), it displays a 16-σ z-excess consistent with an F3V companion. Its round/elliptical PN shows mostly in the g band, but contamination is expected to be minimal, as the PN is faint on the SDSS images.

3.2 An I and J-band analysis of the volume-limited sample of Frew (2008)

In the following study, we have used the magnitudes listed by Frew (2008) (including updates) for his volume-limited PN sample to look for IR excess associated with an unresolved companion.

This analysis is a redux of the analysis carried out by Frew & Parker (2007), but using our own method and procedure described in Section 1.2. Here we attempt for the second time (see Section 3.1) to use a large sample strategy instead of a one by one approach where we carry out the observations ourselves. The analysis of the SDSS data has revealed the ability to detect flux excess for objects with little or no nebular contamination. In this study, we target a sample that was already used to detect companions and which resulted in a similar detection rate to that of Douchin et al. (2014, submitted). The main caveat in using the Frew (2008) sample is the fact that all magnitudes come from literature compilations. This implies a great heterogeneity of data from different types of observations and data quality. However, the data put together in the catalogue has been systematically vetted homogeneously (for details on the vetting see Frew (2008) and Frew 2014, in prep.) and for each object the most consistent measurements have been retained in view of the available data for this

object, flux and measurement magnitudes, spectra or stellar parameters previously determined. We have therefore performed this study by trusting that this vetting technique would compensate for the inherent heterogeneity of the data gathered in the catalogue.

3.2.1 Target selection

At the moment, the ever-growing - yet still unpublished - catalogue of Frew (2008) contains nearly 1000 objects with data gathered consistently from all available literature. We had to select targets within this catalogue for which our IR excess detection procedure could be attempted. To do so, we applied the same selection process as for establishing the target list in preparation for an observing run. We selected targets with available B, V and I or J magnitudes, a selection that decreased the sample size from 1000 to just over 100 objects. A handful of candidates that were surrounded by a PN smaller than 25″ were excluded. PN contamination was also avoided by checking the available optical images in the Macquarie PN Database. This is once again to prevent bright, compact nebulae to affect the central star photometry. Objects from the IC and NGC catalogues[3] (Corwin, 2004) were excluded also to avoid bright nebulae contaminating the CSPN background. Objects analysed in any of the previous chapters have been removed as they have benefited from a dedicated observing run with photometric weather. The updated Frew (2008) database always lists our magnitudes (Sections 2.2 and 2.3) therefore using his numbers does not add to our knowledge. Nonetheless, we added objects for which new NIR magnitudes had become available since the analysis of Frew & Parker (2007). Objects known to be PN mimics (Frew & Parker, 2010) have been excluded. Objects flagged as *likely mimics* in the catalogue have been excluded whereas those flagged as *possible mimics* have been retained. Finally objects with an error more than a few tenths of a magnitude have not been retained as little knowledge can come from them.

The magnitudes in the updated catalogue of Frew (2008) have been systematically

[3]See also http://www.ngcicproject.org/

collected either from a variety of surveys (APASS[4], UCAC4 (Zacharias et al., 2012), DENIS, 2MASS and UKIDSS) or from published articles on the objects themselves. For some CSPN, the magnitude is an average of independent measurements. Notwithstanding the fact that the magnitudes and most stellar parameters were all available in the catalogue of Frew (2008), none of the errors - so critical in our detection scheme - had been catalogued. We therefore retrieved the errors in B, V, I and J for about a hundred objects to assess the feasibility of their analysis. The error on magnitudes for objects observed within surveys is the error provided by the surveys themselves (they are all available via VIZIER[5] except for the APASS[6] measurements). Frew (2008) did not make a selection when several J-band magnitudes were available. In the case when they came from surveys (the great majority of cases) we used preferentially the J-band magnitudes from UKIDSS (the most recent), if no UKIDSS measurements were available we used the ones from 2MASS, and when 2MASS magnitudes were not available the ones from DENIS. Errors on magnitudes from specific analyses in a given literature article have been assigned the error listed in the article. Most of the times, either a quality flag or an approximate error is given, in which case we adopted that error. When the magnitude was an average of different measurements we used the standard deviation of those measurements as the error estimator. For the J-band magnitude errors, we used the error on the most up-to-date measurement even when several measurements were available, as in many cases the agreement between surveys was really good and the standard deviation on these measurements would have been very small or null.

No cut-off on PN distance has been included. The original analysis of Frew & Parker (2007) included all PN within 1 kpc, the limit for completeness at the time (i.e. it is estimated that all PN within this radius have been discovered). Although the advantage of completeness offers the possibility of a study with the best possible representation of the Galactic population, some objects within the completion limit

[4]AAVSO Photometric All-Sky Survey: a description of the survey is available at http://www.aavso.org/aavso-photometric-all-sky-survey-data-release-1

[5]VIZER archives available at http://vizier.u-strasbg.fr/

[6]Query form available at http://www.aavso.org/download-apass-data

are surrounded by a bright nebula and cannot be analysed within the frame of our method. Moreover for some objects within the completeness limit (currently at 2 kpc, Frew, private communication) the catalogue is lacking one or more of the magnitudes to carry out our calculations. Therefore we abandon the goal of having a complete statistical sample for this study and use PN in the catalogue of Frew (2008) at any distance.

Name	Sp. Type	PN[1] morph.	D[2] (kpc)	M_V (mag)	$E(B-V)$[3] (mag)	$T_{\rm eff}$ (kK)
Alves 2	–	–	(1)	(5.7)	0.06	101 ± 10
AMU 1	sdO	–	(1)	(3.3)	0.10	–
DeHt 2	–	Rars	2.63	2.9	0.21	–
Fr 2-22	–	–	(1)	(4.4)	0.04	–
Fr 2-23	–	–	(1)	(4.1)	0.12	–
Fr 2-8	–	Ea	1.49	5.2	0.34	–
Fr 2-9	sdOB+MS	–	0.40	4.0	0.05:	–
HaWe 4	DAO	Ear	0.80	7.6	0.25	125 ± 28
HaWe 7	hgO(H)	Am	(1)	(4.4)	0.60	–
Hen 2-36	A2III	Bs	(1)	(0.3)	0.36	47 ± 2
IPHAS XJ184800+025420	–	Ears	(1)	(-4.2)	2.15	–
Jn 1	PG1159	Eams	(1)	(5.9)	0.06	–
KUV 03459+0037	DAO	–	(1)	(5.3)	0.16	–
Lo 1	–	Bars	(1)	(5.2)	0.01	–
M 1-46	Of(H)	Rmprs	2.98	0.45	0.3	120 ± 10
MWP 1	PG1159	Baps	(1)	(3.0)	0.02	–
PHR 0905-4753	F5III[e]	Baps	(1)	(0.2)	0.8	–

[1] The morphological classes are from the PN Macquarie University Database (Bojičić et al. 2014, in preparation)

[2] We assumed a distance of 1 kpc when no distance was found in Frew (2008)

[3] These reddenings have been compiled by Frew (2008) from nebular or interstellar methods

TABLE 3.6: Stellar parameters for the selected objects from the catalogue of Frew (2008). All data come from the catalogue and are a synthesis of available literature except the PN morphologies.

3.2.2 Reddening comparison to assess the photometry consistency

Among the 27 objects that fit our selection criteria we compare the reddening obtained using the magnitudes of the catalogue of Frew and the extinction extracted from the

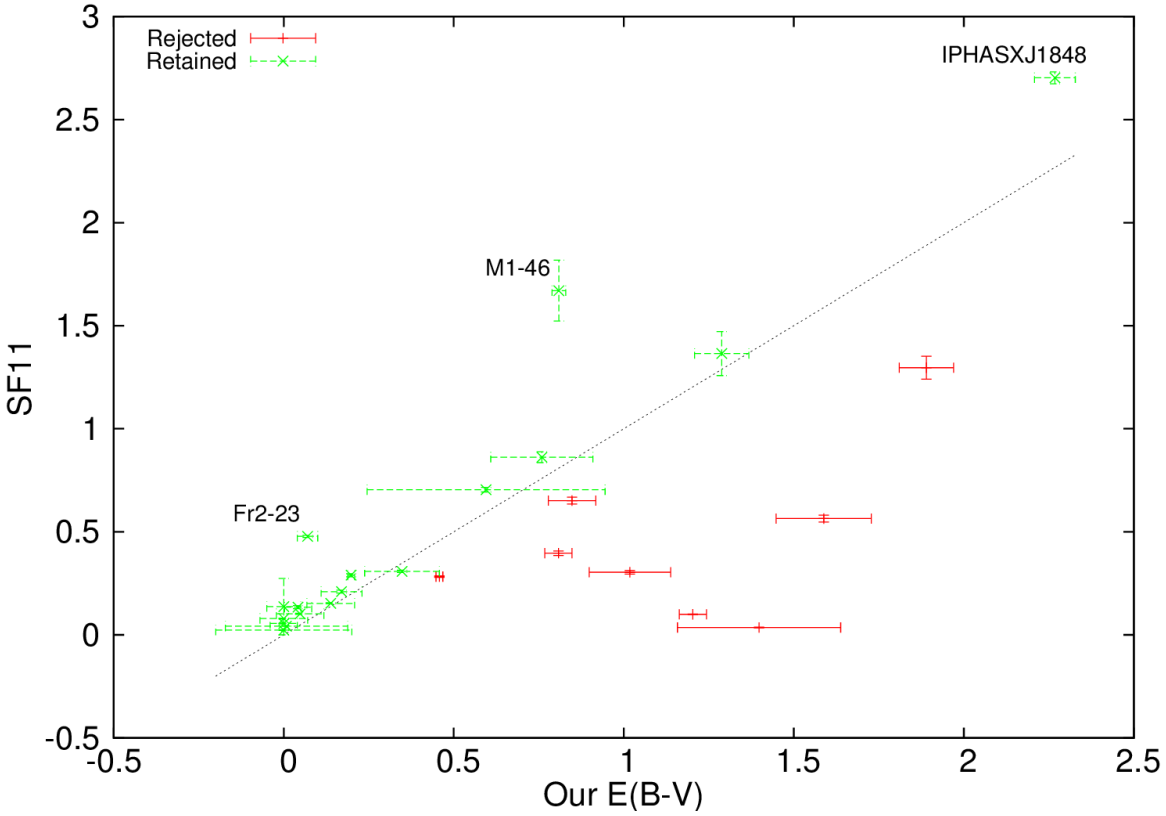

Figure 3.3: Comparison of the values of E$(B-V)$ obtained using the $B-V$ colours from the catalogue of Frew (2008) and from the interstellar dust maps of Schlafly & Finkbeiner (2011). Green symbols represent objects we retain in our analysis while red symbols are rejected objects.

galactic dust maps of Schlafly & Finkbeiner (2011) using the online NED[7] form. The interstellar dust maps are a good way to obtain an upper value of the interstellar extinction along the line of sight to a given coordinate on the sky. The value of the reddening might be overestimated as the dust content is integrated along the line of sight and could include interstellar dust that is behind the object, especially along the Galactic plane. This check allows us to estimate the quality of our photometric data and guards us against any strongly erratic value for $B-V$. This is a necessary condition to insure that the detected flux excesses are worthy of trust.

We show this comparison in Figure 3.3. As expected the higher the reddening the more scatter is observed. We exclude from this analysis all the eight objects that do not fit a 1-to-1 relationship for the $E(B-V)$ value within the error bars and for which

[7]NASA Extragalactic Database form: http://irsa.ipac.caltech.edu/applications/DUST

our reddening is larger than the one of Schlafly & Finkbeiner (2011). Three objects (IPHAS XJ184800+025420, M 46 and Fr 2-23) have higher values for their reddening estimated from dust extinction than our own estimates. To confirm that the reddening values deduced from dust maps is over-estimated, we compare these values with the ones independently gathered by Frew (2008) using methods other than stellar colours (see Table 3.6). This is fundamental because under-estimating the reddening would lead to the object having too red a colour, potentially creating a false NIR excess detection (see Section 1.4). Our own values for extinction for IPHAS XJ184800+025420, M 1-46 and Fr 2-23 are closer to the ones of Frew (2008) than those of Schlafly & Finkbeiner (2011). This is consistent with the fact that all three objects are within 10° of the Galactic plane and therefore more dust has been integrated along the line of sight than is in front of these three objects. We therefore consider our calculated extinctions to be acceptable.

The targets that have passed this selection process and their stellar parameters are presented in Table 3.6. All the data come from the Frew (2008) catalogue. When any of the distances, temperatures and log g were unknown we assumed a distance of 1 kpc, a temperature of 80,000kK and log g=7.

3.2.3 IR excess detections

As has been done with all the other datasets, we look for NIR excess in the colours of the 17 objects that have passed all the selection criteria. The magnitudes for these objects are shown in Table 3.7.

In the I-band sample we find no detections (see Table 3.8 and Figure 3.4). The upper-limit for the luminosity of the companion consistent with the IR excess of IPHASX J184800+025420 is highly improbable, it is that of an O-type star not included in our cool companion grid. This is improbable as it would correspond to a very young binary with a primary mass greater than ~ 8 $M_{\odot}$. The inferred limit could also imply that the companion is a giant and not a main-sequence star.

The findings in the J-band are shown in Table 3.9 and Figure 3.5. We find a $1-\sigma$ NIR excess detection consistent with an M7V companion for HaWe 4 for which

Name	B	V	I	J
Alves2	15.64 ± 0.03	15.93 ± 0.06	16.17 ± 0.04	–
AMU1	13.39 ± 0.07	13.65 ± 0.02	13.92 ± 0.02	–
DeHt2	14.90 ± 0.04	15.04 ± 0.04	–	15.32 ± 0.09
Fr2-22	14.15 ± 0.04	14.45 ± 0.17	14.34 ± 0.11	14.83 ± 0.04
Fr2-23	14.21 ± 0.01	14.45 ± 0.02	–	14.84 ± 0.01
Fr2-8	16.15 ± 0.08	16.11 ± 0.06	16.08 ± 0.06	16.17 ± 0.11
Fr2-9	11.79 ± 0.03	12.10 ± 0.02	12.39 ± 0.03	12.69 ± 0.02
HaWe4	17.08 ± 0.01	17.19 ± 0.01	–	17.48 ± 0.03
HaWe7	16.55 ± 0.25	16.29 ± 0.25	15.85 ± 0.05	15.80 ± 0.06
Hen2-36	11.87 ± 0.08	11.39 ± 0.13	10.60 ± 0.06	9.87 ± 0.03
IPHASXJ184800+025420	14.43 ± 0.04	12.47 ± 0.04	9.97 ± 0.01	8.38 ± 0.02
Jn1	15.74 ± 0.02	16.09 ± 0.07	16.46 ± 0.05	16.70 ± 0.14
KUV03459+0037	15.63 ± 0.03	15.80 ± 0.06	15.96 ± 0.05	16.25 ± 0.01
Lo1	14.85 ± 0.1	15.21 ± 0.17	15.59 ± 0.06	15.90 ± 0.08
M1-46	13.29 ± 0.01	12.82 ± 0.02	12.21 ± 0.02	11.66 ± 0.03
MWP1	12.73 ± 0.01	13.09 ± 0.01	13.50 ± 0.05	13.82 ± 0.02
PHR0905-4753	13.63 ± 0.03	12.65 ± 0.08	11.19 ± 0.02	9.97 ± 0.02

Table 3.7: Magnitudes for the targets selected from the catalogue of Frew (2008). All numbers have been rounded to two decimal places.

we had UKIDSS J-band photometry not included in the analysis of De Marco et al. (2013). The excess is consistent with the M4V upper-limit determined by De Marco et al. (2013) from $I-$band photometry. This is the faintest companion implied by the analysis we have detected to date, thanks to a combination of small errors in the selected magnitudes in all bands. We also find a $2-\sigma$ detection consistent with an M1V companion in Fr 2-23, a $1-\sigma$ detection consistent with an M2V companion in Fr 2-9 in agreement with the K5V upper limit determined in the I-band. Additionally, three IR excess detections associated to hotter companions are detected: a $1-\sigma$ excess corresponding to a B9V companion for the CSPN of Hen -2-36, in agreement with the B3V upper-limit from the I-band, a $2-\sigma$ detection consistent with an A0V companion

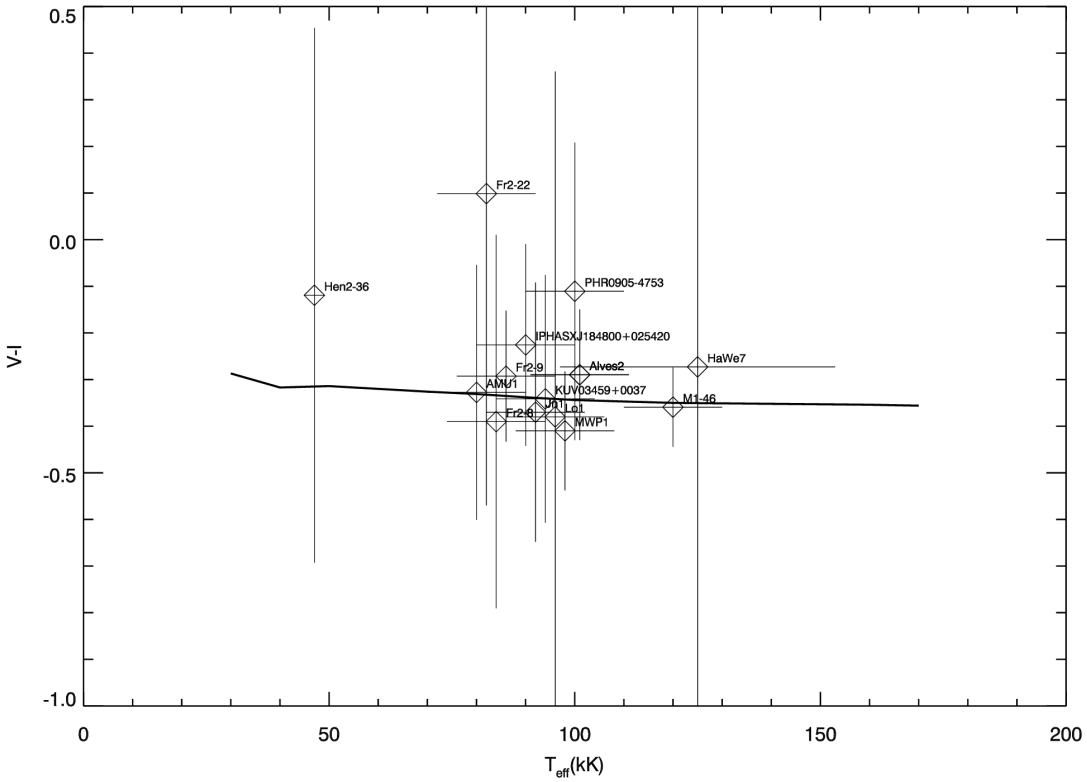

FIGURE 3.4: $V-I$ colours for the sample selected from the catalogue of Frew (2008).

around the CSPN of M 1-46 in reasonable disagreement with the A1V limit from the I-band and a $2-\sigma$ detection consistent with a B7V companion, in good agreement with the B5V upper-limit determined in the I-band, for the CSPN of PHR 0905-4753. It is noticeable that these three objects have pretty high values of interstellar reddenings compared to our typical targets (> 0.7, Hen 2-36 is in the Galactic plane). M 1-46 has a multiple shell PN, surrounded by a bright halo that could explain the high reddening. Hen 2-36 and PHR 0905-4753 also have a high error value for the colour excess (> 0.2) since the V magnitude has been obtained for both objects by combining measurements from different sources in acceptable, but not very good, agreement. It also noticeable that nebular contamination is non-negligible for all these objects except maybe for PHR 0905-4753 whose nebula is fainter and more extended. The CSPN of M 1-46 is a weak emission-line star (Marcolino & de Araújo, 2003) and it is likely that the detected NIR excess is affected by stellar emission lines as well as nebular contamination. We

Name	$E(B-V)$	$(V-I)_0$	$\Delta(V-I)$	M_{I2}	Comp. spec. type
Alves2	0.04 ± 0.07	−0.29± 0.26	0.06 ± 0.26	> 7.10	Later than M0
AMU1	0.05 ± 0.07	−0.33± 0.27	0.01 ± 0.27	> 4.93	Later than G9
Fr2-22	0.01 ± 0.18	0.10± 0.67	0.43 ± 0.67	> 3.57	Later than F9
Fr2-8	0.35 ± 0.11	−0.39± 0.40	−0.05± 0.40	> 5.22	Later than K1
Fr2-9	0.00 ± 0.04	−0.29± 0.14	0.04 ± 0.14	> 6.15	Later than K5
HaWe7	0.60 ± 0.35	−0.27± 1.31	0.08 ± 1.31	> 2.63	Later than F2
Hen2-36	0.76 ± 0.15	−0.12± 0.57	0.20 ± 0.57	> −1.18	Later than B3
IPHASXJ18	2.27 ± 0.06	−0.22± 0.21	0.12 ± 0.21	> −3.30	–
Jn1	0.00 ± 0.07	−0.37± 0.28	−0.04± 0.28	> 7.70	Later than M1
KUV03459+	0.14 ± 0.07	−0.33± 0.26	0.01 ± 0.26	> 6.84	Later than K8
Lo1	0.00 ± 0.20	−0.38± 0.74	−0.05± 0.74	> 5.02	Later than K0
M1-46	0.81 ± 0.02	−0.36± 0.09	−0.01± 0.09	> 1.04	Later than A1
MWP1	0.00 ± 0.05	−0.41± 0.20	−0.08± 0.20	> 5.60	Later than K3
PHR0905-4	1.29 ± 0.08	−0.08± 0.32	0.25 ± 0.32	> −0.89	Later than B5

Table 3.8: I-band excesses for the selected objects from the catalogue of Frew (2008) ($\Delta(V-I)$), companion absolute I-band magnitudes (M_{I2}) and spectral types (or limits) of our targets.

present it to flag the high NIR excess for future studies.

The companions of Hen 2-36 and PHR 0905-4753 are known to have giant companions (see Section 3.2.4), consistent with the early spectral type we find. Additionally, our method is designed to translate the colour excess into a main-sequence companion spectral type and a bright giant star will be interpreted as an *earlier* main sequence star spectral type. A bias for bright companions is likely in a brightness limited sample such as this. The high number of giant companions from this study is therefore not representative of the Galactic population Contamination by the giant companion in the bluer part of the spectrum could be the cause of the discrepancy between our determined spectral type and the one from Frew (2008) (see 3.2.4).

The lack of detections in the I band is fully consistent with the bright upper limits and easily explained by the relatively much larger errors. In the J band both limits and detections are also comparatively brighter than in our other studies, due to, in this case, large errors primarily on the B and V bands. Interestingly, the detection rate in the J band alone is not particularly low (31%).

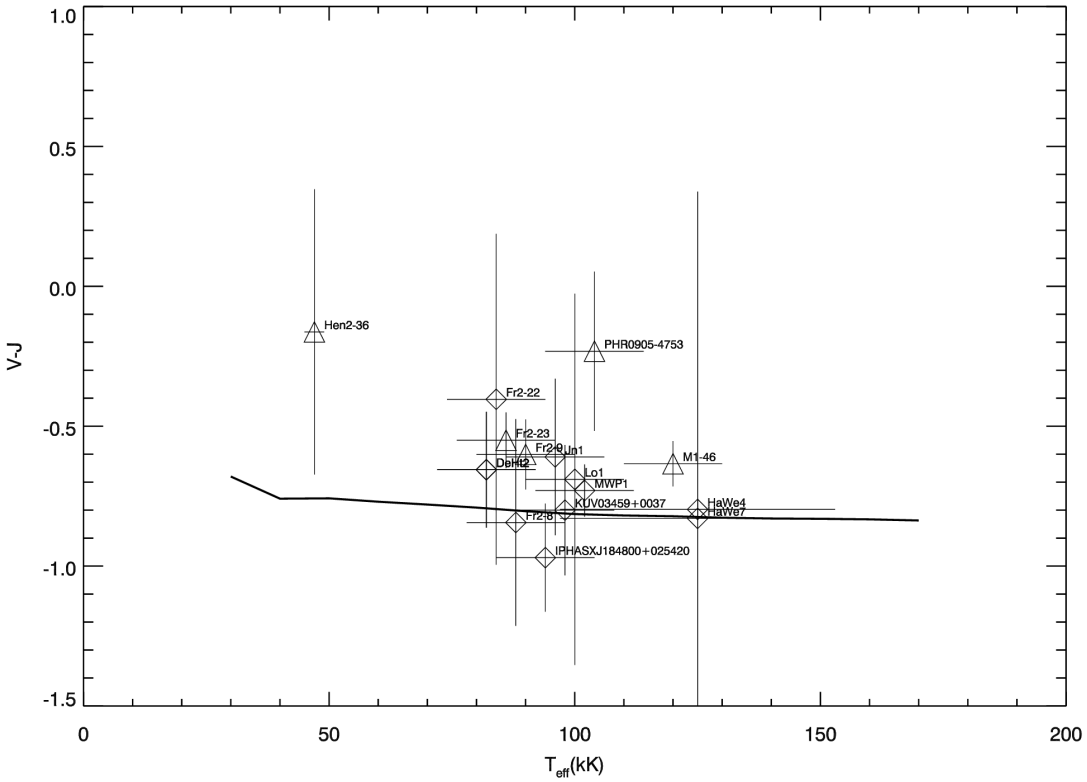

FIGURE 3.5: $V - J$ colours for the sample selected from the catalogue of Frew (2008).

This second large scale study suffers from the same limitations as the SDSS study carried out in Section 3.1. Large samples may seem suitable for a systematic, large scale analysis but they lose a lot of their strength after the target selection. In the case of this study, the Frew (2008) database built on a patchwork of available data offered photometry with a quality allowing to detect IR excesses associated to two already known CSPN-giant pairs (Hen 2-36 and PHR 0905-4753), a $1 - \sigma$ detection corresponding to a very cool companion for HaWe 4 using recent UKIDSS data, NIR excesses associated to cool companions for two CSPN that could not be ruled out as mimics (Fr 2-9 and Fr 2-23) and an IR excess associated to a hot companion for M 1-46, although in this case both emission lines and contamination from the bright multiple-shell nebula could affect the photometry. Our initial desire to use the sample for statistics has been adjusted to simple IR excess detections in view of the limited size of the sample after careful selection of our targets. Although we found some new

Name	$E(B-V)$	$(V-J)_0$	$\Delta(V-J)$	M_{J2}	Comp. spec. type
DeHt2	0.17 ± 0.06	−0.65± 0.21	0.14 ± 0.21	> 4.08	Later than G8
Fr2-22	0.01 ± 0.18	−0.40± 0.59	0.39 ± 0.59	> 4.21	Later than G9
Fr2-23	0.07 ± 0.03	−0.54± 0.10	0.25 ± 0.10	6.50 [7.19 – 5.98]	M1 [M3 – M0]
Fr2-8	0.35 ± 0.11	−0.83± 0.37	−0.04± 0.37	> 5.74	Later than K8
Fr2-9	0.00 ± 0.04	−0.59± 0.12	0.20 ± 0.12	6.61 [7.82 – 5.90]	M2 [M4 – K9]
HaWe4	0.23 ± 0.01	−0.79± 0.04	0.04 ± 0.04	> 10.63	Later than M7
HaWe7	0.60 ± 0.35	−0.83± 1.17	−0.01± 1.17	> 3.42	Later than G1
Hen2-161	0.82 ± 0.50	0.70± 1.61	1.44 ± 1.61	> −1.13	Later than B3
Hen2-36	0.76 ± 0.15	−0.16± 0.51	0.60 ± 0.51	0.14 [3.00 – -1.31]	B9 [F9 – B3]
IPHASXJ18	2.27 ± 0.06	−0.94± 0.19	−0.15± 0.19	> −0.47	Later than B6
Jn1	0.00 ± 0.07	−0.61± 0.28	0.18 ± 0.28	> 7.33	Later than M3
KUV03459+	0.14 ± 0.07	−0.76± 0.23	0.03 ± 0.23	> 7.32	Later than M3
Lo1	0.00 ± 0.20	−0.69± 0.66	0.10 ± 0.66	> 5.33	Later than K6
M1-46	0.81 ± 0.02	−0.63± 0.08	0.19 ± 0.08	0.57 [1.30 – 0.07]	A0 [A3 – B8]
MWP1	0.00 ± 0.05	−0.73± 0.17	0.06 ± 0.17	> 5.27	Later than K6
PHR0905-4	1.29 ± 0.08	−0.18± 0.28	0.61 ± 0.28	−0.26 [0.86 – -1.12]	B7 [A1 – B3]

Table 3.9: J-band excesses for the selected objects from the catalogue of Frew (2008) ($\Delta(V-J)$), companion absolute J-band magnitudes (M_{J2}) and spectral types (or limits) of our targets.

IR excesses, we do not want to include this study on the sample used to estimate the binary fraction. Only HaWe 4 could be added as its study strictly updates the work of De Marco et al. (2013) with a most recent J-band measurement.

3.2.4 Notes on Individual objects

Fr 2-9

This object is likely a hot B subdwarf. In Frew's (2008) catalogue the object is classified as possible mimic, meaning that more data are required to firmly exclude the chance for the object to be a mimic. Edelmann et al. (2006) led an RV variability survey and found that the system was a 0.42 day WD-MS pair with a 0.34-0.49 $M_\odot$ companion (depending on the orientation of the system), assuming a primary mass of 0.5 $M_\odot$. This mass range translates into an M2-M3V companion spectral type as detailed in the colour table provided in De Marco et al. (2013). We find an M2 companion in very

good agreement with their measurement.

HaWe 4

This DAO WD is surrounded by a low-brightness PN (Chu et al., 2009). Gianninas et al. (2010) found a mass of 0.57 $M_{\odot}$ from their spectroscopic survey of hot, hydrogen-rich WD. This CSPN is also part of our analysis that used the SDSS photometry (see Section 3.1), in which it showed a puzzling blue colour hampering the detection of any flux excess. It is also part of the sample analysed by De Marco et al. (2013), where using their own magnitudes they found a companion upper-limit of M4V. We used the newly obtained UKIDSS J magnitude that had not been exploited in their study and found an M7V companion, in good agreement with their previously determined I-band upper-limit.

Hen 2-36

Hen 2-36 is a known "cool" CSPN (too cool to ionise the nebula) with an A2III spectral type surrounded by an "S"-shape nebula classified as bipolar/elliptical (De Marco, 2009; Feibelman & Kondo, 2001). The cool spectral type corresponds in fact to the giant companion outshining the primary that is invisible. The giant is not detected in our I-band study due to a high error on the colour but is revealed in the J-band indicating a B9V companion. As explained in Section 3.2.3, for companions brighter than luminosity class V, we deduce brighter spectral types . Thus our estimation of the companion spectral type is not discrepant with the A2III one originally determined by Sanduleak (1975); Mendez et al. (1978) and Lutz et al. (1989). This nebula is at the edge of our detection criteria because the nebula is quite compact (19″) and bright, therefore it is also possible that nebular contamination affect the colour excess.

M 1-46

Hubble images are available showing this multiple-shell PN surrounded by a 28″bright asymmetric halo (Corradi et al., 2003; Sahai et al., 2011). The object is a known weak emission-line CSPN (Guerrero & Manchado, 1999).

PHR 0905-4753

Little literature is available for this MASH object (Parker et al., 2006). Frew (in prep.) claim a spectral type F5III[e] for the CSPN. We find an IR excess equivalent to

a B7V companion in the J-band, and once again we obtain no detection in the I-band due to the combination of high uncertainties and a lower colour excess in this band. In this case again, the two spectral types are in agreement with one another since our method yields an early spectral type for bright stars. No nebular contamination affect the CSPN here.

3.3 Summary

In this chapter, we have attempted to use large scale samples of already acquired photometry to detect NIR excess in CSPN. Our first attempt – using the SDSS DR7 survey – has revealed the possibility of using the SDSS to recover with a very good precision the NIR excess for targets already analysed and coming from our own target selection and dedicated observations. Extending the search to any SDSS-observed CSPN, we found that nebular contamination was an issue as no target selection had been included for this sample and that a careful analysis of each object independently was necessary. Out of the small number of objects yielding exploitable results, we find 4 good candidates for NIR excess. Given the small usable sample and its heterogeneity, we abandon the idea of using the sample for statistical purposes. Our second attempt at using large samples was to use the vetted photometry from the extended sample of Frew (2008). Here, the main hurdle was the different origin of each magnitude and their consistency with one another. In addition, the error bars of optical bands often resulted in large values, much larger than typical error of our own studies (Chapter 2). Yet we found 2 objects with NIR flux excess consistent with cool companions. We also found 3 objects with NIR flux excess consistent with giant companions, including one in very good agreement with the previously determined companion spectral type. The detection of giant companions is expected in a magnitude-limited sample like the one resulting from our target selection. Given the small size of the sample and the lack of homogeneity and completeness, we do not include these new findings in our sample for statistics.

Although appealing, the analysis of large samples is hampered by the need for a

strict target selection never applied to those samples themselves. The resulting findings are worthy of further consideration whereas the samples have no statistical value. We therefore conclude that using surveys is less fruitful at detecting NIR excess in CSPN than our tailored approach and cannot yield a conclusive binary fraction, contrary to the strategy described in Chapter 2 that we prefer. Methods other than NIR excess are available to detect CSPN binaries. They are illustrated in the two next chapters.

Chapter 4

The photometric variability technique

The photometric variability technique is based on the observation of flux variations due to the presence of a close, unresolved companions. Three mechanisms can produce light variation from the observed system: illumination from the bright hot primary onto the cool companion (De Marco et al., 2008), ellipsoidal distortion due to tides on the companion or both the primary and the companion according to the orbital parameters of the system and, lastly, eclipses (Bond, 2000), when the system is viewed approximately edge-on. This technique is very successful at detecting binaries as it only requires the monitoring of the targets in reasonable weather conditions with an adequate sampling followed by standard differential photometry to obtain the object's lightcurve (e.g. Figure 4.1). Difficulties arise when modelling the obtained lightcurves to determine the system's orbital parameters, as the models available (e.g. calculated with the Wilson-Devinney type code) suffer from degeneracy, unless additional data – such as RV curves – are procured. This technique is biased towards finding short-period binaries, which makes it inadequate to test the Binary Hypothesis. Indeed, irradiation effect and ellipsoidal deformation intensities increase with decreasing separation, and eclipses become less likely. Although this method is not well suited to our goal, we monitor our targets for a periodic signal during non-photometric weather.

In this chapter, I review the previous efforts to use this technique to find new binary

CSPN. I show in Section 4.2 that although we tried to use the photometric variability technique during the non-photometric parts of our observing nights, the sampling was suboptimal and resulted in the detection of only a few objects. Finally I discuss results from the analysis of a sample of 6 CSPN observed with the satellite Kepler, in light of previous findings from ground-based observations.

4.1 Previous efforts

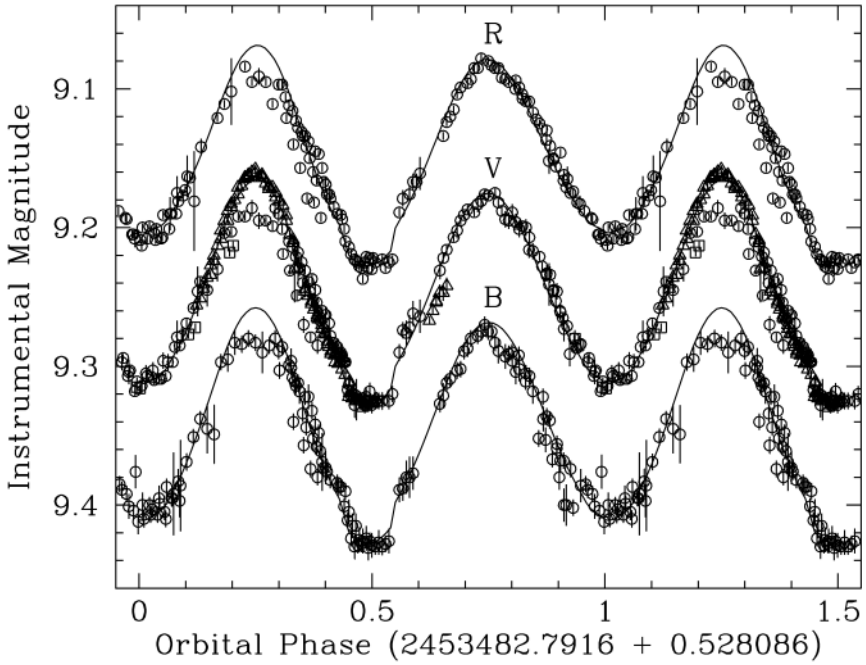

FIGURE 4.1: Phase-folded lightcurve of NGC 6026, a binary CSPN, in the three optical bands B, V and R. The lightcurve has been adequately sampled observations over a time span of three years, allowing to fit (continuous line) the lightcurve and determine the system's orbital parameters using the Wilson-Devinney code. From Hillwig et al. (2010).

As detailed in Section 0.6.2, two main surveys have been carried out using this technique: Bond (1990, 2000) has determined a close binary fraction of 10-15% by discovering 13 binary CSPN out of a sample of $\sim$ 100 CSPN. Miszalski et al. (2009) have determined a fraction of close binary CSPN of 12-21%, discovering 21 new binary CSPN by using the Galactic bulge data of the OGLE-III survey, therefore benefiting from a more homogeneous technique than their predecessors. The fact that almost

no binaries with periods longer than 3 days have been detected in both studies is at odds with the predictions of De Marco et al. (2008) who expect periods between a few hours and $\sim$ 15 days to be detectable by this technique. The fact that both surveys lack detections of binaries with periods longer than 3 days seems to suggest that the apparent scarcity of binaries with periods between 3 days and 2 weeks is a feature of the observed population, more so than a bias intrinsic to the method. Additionally, as a by-product of their survey, Lutz et al. (1989) found 1 close binary CSPN out of their 22 randomly selected CSPN yielding a fraction of $4.5\% \pm 4.5$ in acceptable agreement with the previous determination.

Several efforts to model the binaries detected in these studies have been carried out (Hillwig 2004, Hillwig 2011 and Hillwig 2014, non-exhaustive), especially those targets in the local sample of Frew (2008) due to the same advantages as the ones mentioned in Section 1.3. Out of the 45 detected binaries, half of them have been spectroscopically confirmed, 16 show a strong signature for a companion while 12 have been fully modelled (Hillwig, 2014). A fraction of 20-25% of the objects with well-sampled lightcurves show ellipsoidal variability and double eclipses, making them likely double degenerates (DD), since in CSPN+MS binaries the brightness and temperature ratios are such that the illumination effect dominates. This estimation is a lower limit since ellipsoidal variability disappears as the CSPN contracts to become a white dwarf, and the fraction of DD could be as high as in the WD population, i.e. 15%. Of the 16 modelled systems, 10 have main-sequence companions including 7 M, 1 K and 2 G-type companions. The modelled CSPN have masses between 0.51 $M_\odot$ and 1 $M_\odot$ and temperatures between 38 and 200kK and are all in agreement with evolutionary tracks for these primaries. The sample contains no low-mass He WD.

4.2 Tentative monitoring during non-photometric weather

As mentioned in Section 2.2, only 3 of the 7 nights of the KPNO 2.1m observing run were photometric. During the non-photometric nights, we imaged 20 objects in V and I to look for significant variability and, ideally, obtain lightcurves. The lightcurves we obtained are presented in Figure 4.2 and Figure 4.3. Our opportunist observing strategy – observing a maximum of objects whenever they were visible – does not provide an adequate sampling to obtain lightcurves that can be modelled. However, we obtained enough data to potentially detect new variables, or at least flag those objects with a significant photometric scatter for future observations.

Our lightcurves have been built from relative photometry. Our CSPN magnitudes, as well as the ones for the 1-6 brightest stars in the field, have been obtained using `IRAF`'s aperture photometry package `PHOT`. Each measurement on the lightcurve is the average difference between the CSPN after aperture correction and the field stars weighted the photometric error: the quadratic sum of the CSPN and the field star photometric errors. It is noticeable that our V-band lightcurves show less scatter due to a better photometric precision.

Out of our twenty tentative lightcurves, we point out the potential variability of 12 objects (see Table 4.1). Whether a star is variable or not has been assessed using two different tests: a visual one and a statistical one. The visual method consists in estimating visually if the lightcurve is scattered or not, and more importantly if any pattern ascribable to periodic variation is noticeable. We sort our 20 curves into three categories: no sign of variability (flag 0), significant, non-periodic scatter (flag 1) and visible periodic variability patterns (flag 2), but we point out that flags 1 and 2 indicate the need for more observations. The V-band lightcurves are used to determine the flag, whereas the I-band, intrinsically more scattered, is used to confirm the presence of periodic trends. The statistical method consists in estimating for each V-band lightcurve three quantities: μ the weighted average of all the measurements at different epochs (this value will depend only on the choice of the bright reference stars),

σ the average error from the different epochs and χ the dispersion obtained from the sum of the residuals, more precisely:

$$\mu = \sum_{i=1}^{N_{ep}} q_i \tilde{\mu}_i \tag{4.1}$$

$$q_i = \frac{1}{\tilde{\sigma}_i} / \sum_{j=1}^{N_{ep}} \frac{1}{\tilde{\sigma}_j} \tag{4.2}$$

$$\sigma = \sqrt{\frac{1}{N_{ep}} \sum_{i=1}^{N_{ep}} \tilde{\sigma}_i^2} \tag{4.3}$$

$$\chi = \sqrt{\frac{1}{N_{ep}} \sum_{i=1}^{N_{ep}} (\tilde{\mu}_i - \mu)^2} \tag{4.4}$$

where the $\tilde{\mu}_i$ are the photometric differences between the CSPN and the reference star for the N_{ep} epochs and the $\tilde{\sigma}_i$ their associated errors.

A star is estimated variable if $\chi > \sigma$ and is then flagged "A". Otherwise it is flagged B. The I-band lightcurves are not used here because almost all return an A flag due to their photometric scatter. The correlation between the tests is excellent with only two stars (KnPa 1 and Te 5) being labelled 0A due to the fact that the patterns in the V and I-band do not match visually. All other stars are flagged 0B, 1A or 2A.

This sample is obviously not to be used to derive statistics. Nonetheless, it is noticeable that the obtained "detection rate" of 60% is much higher than the 10-20% of close-binary CSPN. This indicates either that our method is over-sensitive, that the observed variations are not due to the presence of a companion but to pulsations or rotation, or that our target selection has been biased towards the detection of close-binaries. We remark the sinusoidal trend on the lightcurve of EGB 6 (mostly the V band), a known resolved binary, as well as the compelling apparent periodicity of the lightcurve of Na 1 (in both the V and I bands). The nature of these objects are discussed in Section 2.2.7 and Appendix B.2.2 respectively.

From these lightcurves, we conclude that monitoring during non-photometric weather is effective for finding new potential binaries. Yet, further observations of the most prominent targets are needed to allow improved sampling so as to detect periods.

Name	Flag		Name	Flag
A 13	0B		HoCr 1	0B
A 19	1A		KK 26	0B
A 25	0B		KnPa 1	0A[1]
A 29	1A		Kn 39[2]	2A
A 31	2A		Na 1	2A
A 34	0B		NGC 6058	1A
EGB 5[†]	2A		SkAc 1	0B
EGB 6	2A		Te 3	0B
EGB 9[†]	1A		Te 5	0A[1]
H 3-29	0B		We 3-1	1A

[1] The V and I-band lightcurves are not in visual agreement for this object.

[2] A similar pattern as the one seen on the V and I-band lightcurve is also observed in the B-band.

[†] Mimic

TABLE 4.1: Classification of our tentative lightcurves. Numbers are the result flag of a visual analysis: (0) no sign of variability, (1) significant, non-periodic scatter and (2) visible periodic variability patterns. Letters flag the result of the statistical analysis: (1) $\chi > \sigma$, (0) otherwise.

4.3 CSPN monitoring by the satellite Kepler

The Kepler satellite[1] was launched on the seventh of March 2007. Aiming at discovering Earth-size exoplanets using the transit method, the satellite is made of a Schmidt telescope with a 0.95-meter aperture equipped with 42 2200x1024 pixel CCDs. It has been observing a single field of 105 square degrees in the constellation of Cygnus, monitoring all the stars in that field with exquisite precision. During the time-frame of the mission, two of the four reaction wheels used for pointing the telescope stopped functioning. In August 2013, NASA announced they had given up trying to fix the

[1] http://kepler.nasa.gov/

reaction wheels. A backup plan dubbed "K2" or "Second light" consisting of the satellite keeping the Sun in the X-Y frame to allow satisfactory pointing, has been funded by NASA and is currently ongoing, limiting the loss of science due to the technical issues. Even after these incidents, Howell et al. (2014) report a photometric precision of 80 ppm at V=12 for an integration of 6 hours.

Out of the 150,000 stars monitored by Kepler in its field of view in the Cygnus constellation, 6 are CSPN and they can be investigated for binarity. Douchin et al. (2012) and Long et al. (2013) present the most up-to-date data and models for these CSPN:

- PN J19411+4324 shows strong periodic variability with an amplitude of $\sim 0.03\%$ and a period of 2.928 days, supported by a radial velocity variability of 92 km s^{-1} with a period of 2.926 days. It is an excellent binary candidate.

- Kronberger 61 shows a 4-6 day quasi-periodic variability of 10%. The variability is suspected to arise from winds or disks outbursts and make the star a good cataclysmic variable (CV) candidate although no CV has ever been observed with such short outburst periodicity. This PN has first been detected by the Deep Sky Hunters[2] team while searching new PN in the Kepler field by looking at coloured objects on the DSS[3] plates. We were asked to image such one PN candidate while observing at the Kitt Peak 2.1m in March 2010. The image we obtained confirmed morphologically that the object was a strong PN candidate, and it was therefore re-imaged (Figure 4.4) using the Gemini telescope. This discovery has been the object of a press-release (http://www.gemini.edu/node/11656).

- NGC 6742 shows no sign of variability. Its photometry may be affected by the bright, circular nebula.

- Abell 61 shows no sign of variability. The nebula is circular.

- NGC 6826 is a strong semi-periodic variable with an amplitude of $\sim 0.02\%$. It has a dominant periodicity of 0.619 days and an occasional periodicity of 1.238 days.

[2]https://groups.yahoo.com/neo/groups/deepskyhunters/info
[3]Digitized Sky Survey, http://archive.eso.org/dss/dss

Both periodicities appear only in half of the observed time. The star displays a weak radial velocity variability and is rotating rapidly (50 kms^{-1}), a suggested cause for the observed variability. Handler et al. (2013) suggest that the radial velocity and flux variabilities are due to rotationally-modulated winds similar to those in massive stars and not the signature of a binary.

- Pa 5 shows a variability of 0.05% with a period of 1.121 and a radial velocity variation <5 km s^{-1}, ascribable to a binary if the system is seen approximately face-on.

Ongoing efforts are being made to model these lightcurves although due to the extreme precision and complexity of the photometry, the task is difficult (Hillwig, 2014). None of these 6 PN were known binaries from the ground. Observing them with a more sensitive telescope and technique has helped determining that PN do display variability amplitudes that are not readily accessible from the ground. Despite the low number statistics the numbers obtained are very encouraging results. As it stands, 2 PN are almost certain binaries (Pa 5 and PN J19411+4324). Two are likely binaries or ex-binaries: NGC 6826, if indeed the variability can be interpreted as fast rotation, must have been a merger (this amount of angular momentum can only be brought in by a companion, as also demonstrated by the very low number of fast rotating white dwarfs Nordhaus 2014), while Kn 61 is almost certainly related to cataclysmic variables. The last two PN, which both have round morphologies, seem to have no variability at all at the Kepler sensitivity. More is to be discovered at this level of variability and K2 "time" has already obtained for this purpose.

Summary

We have seen that the photometric variability technique was an efficient technique to detect binaries. So far the binary fraction detected thanks to this technique is $\sim$ 10-15%. As already pointed out by De Marco (2009) the close CSPN binary fraction is

substantially higher than what can be predicted by the main-sequence period distribution, a discrepancy which calls for an explanation. Before a solution can be found, however, it is required to determined whether there are binaries with periods longer than $\sim$ 3 days but shorter than a few years.

We searched for photometric variability during non-photometric weather. A high 60% of our observed targets show evidence of photometric variability but no periods have been detected. Results are also obtained from the Kepler satellite where 2 CSPN are likely binaries. Modelling of the ground-obtained lightcurves – and even more so for the complex, high-precision lightcurves obtained from space – is delicate due to the degeneracy of solutions, and reserved for future work.

In the next chapter, we investigate the potential of spectroscopy thanks to radial velocity measurements to find binaries.

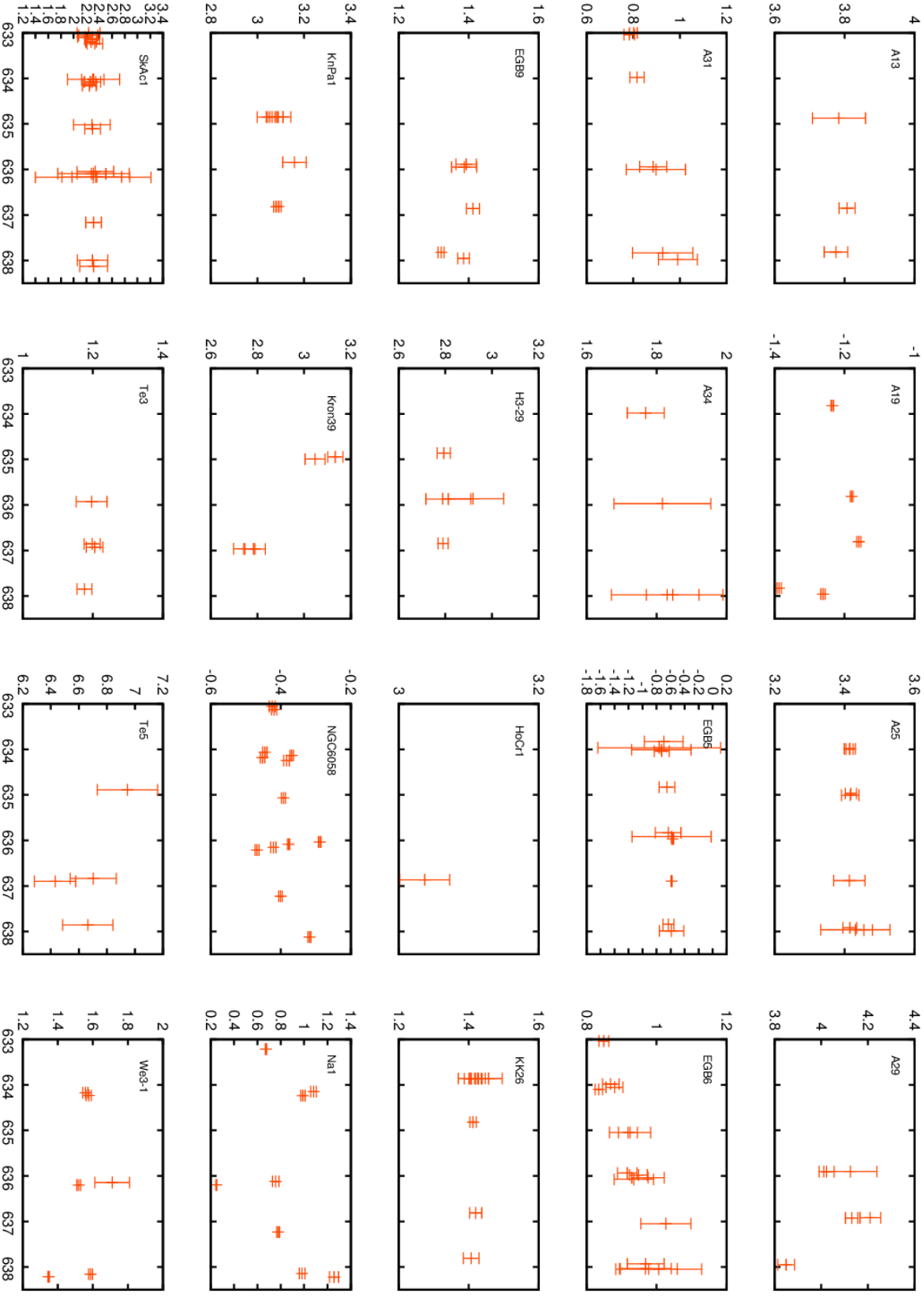

FIGURE 4.2: V-band lightcurves for our targets observed in non-photometric conditions

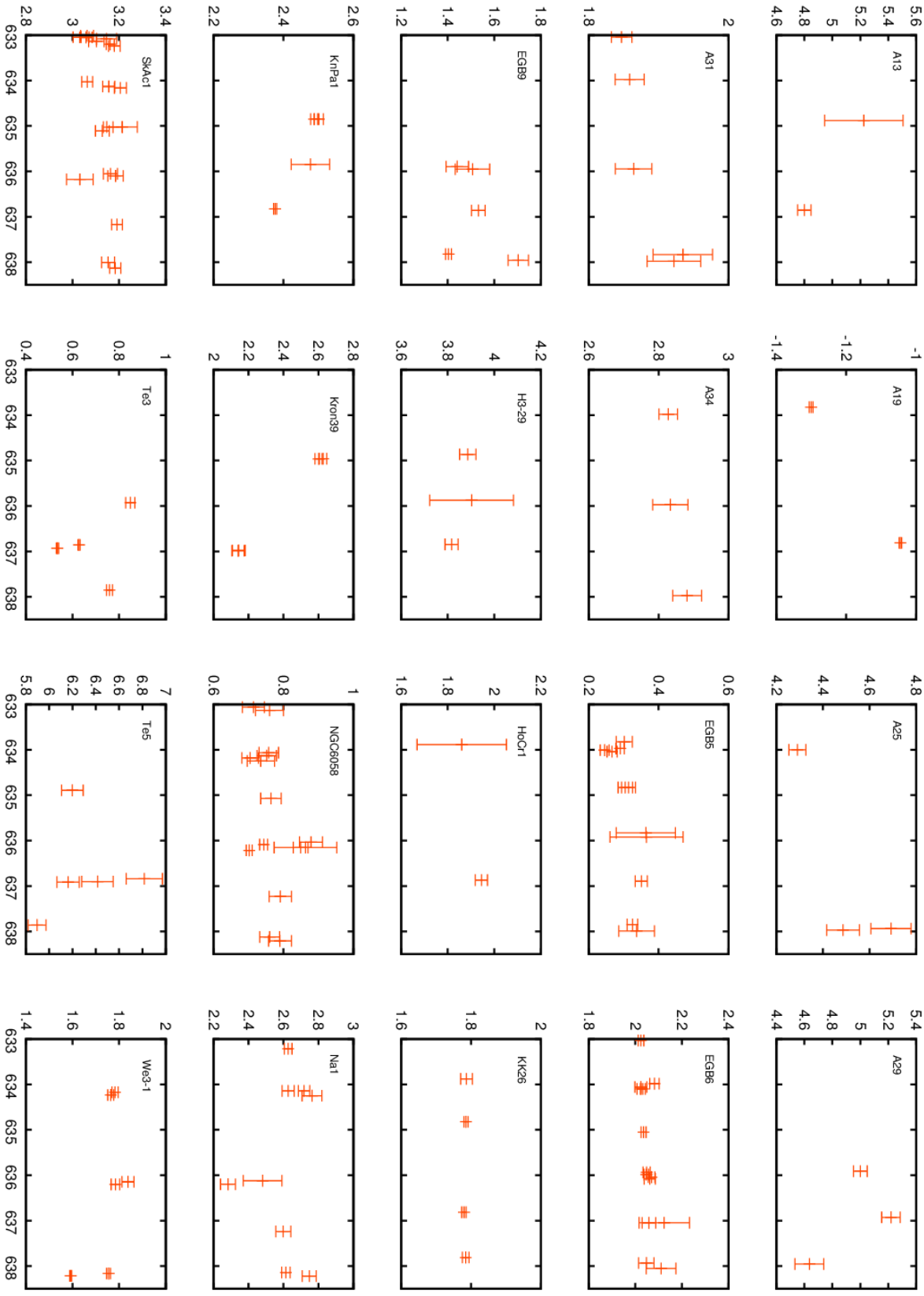

Figure 4.3: I-band lightcurves for our targets observed in non-photometric conditions

FIGURE 4.4: RGB image of PN Kronberger 61. Credit: Travis Rector, Gemini Observatory/AURA.

Chapter 5

The radial velocity variability technique

The radial velocity (RV) variability technique consists in looking for the Doppler shifts in the spectra of CSPN, a shift due to the wobble of the primary around the centre of mass of the system due to the presence of a companion. This technique requires a high SNR and resolution, which makes it quite demanding for faint targets. In this chapter, I review previous work that looked for binary CSPN using this method and present the analysis of a set of VLT/UVES spectra for 14 CSPN.

5.1 Previous work using the RV method

Several surveys have used this technique. Méndez (1989) point out the necessity of using this method to access medium to long-period binaries. They observed 28 CSPN with magnitudes 10-14 with a high resolution of 0.3 Å. They found 5 spectroscopic variables by comparing the Galactic systemic velocities derived from the nebula to that of the CSPN. They also acquired multiple epoch observations. They underline the necessity of a longer time-sampling to confirm that the variability is indeed due to orbital motion and not to the presence of winds. Later, De Marco et al. (2004) used the Hydra spectrograph on the WYIN 3.5m telescope and looked for radial velocity variability. They found a variability fraction of 91% as 10 out of 11 objects were

identified as RV variables, although again, the lack of detected periods prevented the confirmation that these variables are indeed binaries. Sorensen & Pollacco (2003) present a 4 year-long RV survey of 45 CSPN with a resolution of $\sim$ 10 km s^{-1}. They find 13 variable out of 33 objects for which they could measure the RV. Again a sub-optimal time-sampling prevented them to confirm that the detections were binaries, as wind variability could not been excluded as a cause of variability. They also point out that that the binary fraction should be estimated carefully from this detection rate, because biases in a magnitude sample such as theirs can favour the detection of bright companions. Afšar & Bond (2005) have undertaken the southern counterpart of the work of De Marco et al. (2004) with a resolution of 2.2 Å. They used multi-epoch cross-correlation to look for variability in their spectra, after what they shifted all spectra to a zero-shift to build a master template for each object. They deduced a fraction of 37% out of 33 CSPN, a fraction similar to the one of Sorensen & Pollacco (2003). Yet again, no periods were found. Afšar & Bond (2005) assume that this is due to periods being of the order of days, instead of years, hence their cadence was not optimal.

Another method consists in looking for CSPN with cool spectral types, i.e. too cool to ionise the nebula. Depending on the flux ratio between the primary and the companion, the spectrum can either be composite or dominated by the cool star. In both cases, there is an ambiguity that the cool star in the system could be a chance of alignment of a field star, Composite spectra allow to rule out any ambiguity that the observed system contains both the actual central star and binary, whereas cool spectra can be the result of the observation of a field star, but proper motion and distance measurements can help discriminating against these associations. About 20 CSPN have been discovered in this manner (see the review of De Marco 2009).

5.2 Analysis of a three-epoch mini-survey

A dataset of spectra for 14 CSPN have been acquired in August 2008 at the Very Large Telescope (VLT), Paranal using the Ultraviolet and Visual Echelle Spectrograph (UVES). The three image slicer of the instrument has been used to insure a maximum

spectral coverage (320 Å to 1050 Å) combined with a high resolution power (R=40,000, Dekker et al. 2000). The observations were carried out in service mode and as a "poor" weather programme which effectively meant that the seeing was poor and the SNR of most images is unfortunately lower than optimal ($\lesssim$ 10). Spectra at three different epochs have been obtained for each target. The images have been reduced and calibrated by the UVES pipeline insuring that no sky subtraction was included. This is because in a good fraction of the objects the PN lines contaminate the stellar spectrum. Sky sampling regions almost always sample the PN. However, it is impossible to cleanly subtract the PN. As a result a lot of noise affects regions where PN lines have been poorly subtracted. Since PN lines often contaminate stellar lines, it is better to leave them which lets us assess their contribution. In most cases the stellar absorption line wings can be used and can also indicate when there is a shift between the PN and the stellar lines.

We present here an analysis aiming at finding the spectral signature of a companion: out of the 14 objects, 10 show hot star spectra and 4 show spectra of cool stars. For each star set, we cross-correlate the spectra obtained at different epochs to find significant spectral shift consistent with reflex motion caused by an orbiting companion. The cool stars are analysed individually, a spectral type is determined as well the likelihood of association with the CSPN. The spectra of hot objects are presented in Figure 5.1 while the spectra of cool stars are shown in Figure 5.5.

5.2.1 Multi-epoch spectra cross-correlation

In this section, we attempt to cross-correlate the spectra taken at three different epochs with one another for each hot object to find a significant spectral shift due to the presence of a companion. The cross-correlation has been made using the `FXCOR` task from the `rv` package in `IRAF`. The heliocentric correction has been applied to our measurements using the task `rvcorrect`. To determine the sampling regions in each spectrum, we note the presence or absence and position of the most common H and He II lines in the optical spectrum of each object (see Table 5.1), as well as the positive and negative

features of the different spectra. We classify our spectra into 3 categories: stellar absorption features, emission features or both. Three objects belong to the first category for which the position of each line at each epoch has been measured (Table 5.1). Even in the case where absorption features are visible, the SNR is low (Figure 5.2) and the Hα and Hβ lines are dominated by the nebular emission lines, so the position of these absorption lines cannot be determined accurately. Our spectra present a non-identified "bump" from the start of the second spectral slice to $\sim$ 4710 Å that seems to be the result of an instrumental artifact and prevents the measurement of the He II 4686 Å line. NGC 7293 has been observed twice only to be used as a reference spectrum. Those spectra that present absorption features have been cross-correlated using the features present in the 3800-4500 Å interval as sampling region while excluding the Ca II λ3933 H and λ3968 K line (which is blended with H6 λ3970). When the He II λ5412 line was present, it was added to the sampling region.

Line	A 51	Lo 17	NGC 7293
H9 λ3835	n	y	n
H8 λ3889	n	n	n
Hϵ λ3970	n	n	n
Hδ λ4102	y	y	y
Hγ λ4340	y	y	y
Hβ λ4861	PN contamination	PN contamination	PN contamination
He II λ5412	y	y	n
Hα λ6563	PN contamination	PN contamination	PN contamination

TABLE 5.1: Presence and absence of common absorption features in the three CSPN that show absorption lines.

We call X1 the correlation of epoch 1 with epoch 2, X2 the correlation of epoch 1 with epoch 3 and X3 the correlation of epoch 3 with epoch 2 – where epoch 1 is the most recent. This means that, for example, in X1 epoch 1 is the object spectrum and epoch 2 is the reference spectrum. Both the object and the reference spectra are filtered in Fourier space before the cross-correlation is carried out using a boolean low-pass filter

with a cutoff at a wavenumber of 5000 to filter part of the noise affecting from the cross-correlations. A parabola function has been used to fit the correlation peak, with the fitting region being approximately the upper half of the curve. The results of the cross-correlations are shown in Table 5.2. The correlations are all weak, except X2 for A 51 that reveals a shift of -21.2±0.2 km s^{-1} with a 62% intensity (Figure 5.3. This result is obtained even by choosing a smaller sampling region as long as it lies in the blue or green part of the spectrum. The fact that only the correlation X2 reveals a detection is not due to one epoch having a significantly larger SNR in which case two cross-correlations would show such detection. The detected shift for X2 could indicate RV variability as the signal is strong, although using a correlation between two epochs only it is hard to build any hypothesis without additional data.

The spectra of the remaining hot stars cannot be analysed: the SNR of the spectra of IC 1295, NGC 6720, NGC 6842 and NGC 6853 is too low and no lines appear in absorption. Absorption lines are visible on the spectra of IC 5148 and NGC 6804 but the signal is weak and contamination from the nebular lines is significant.

On all these spectra, the absorption line positions cannot be determined with a precision better than 1 Å or 60 km s^{-1} at 5000 Å . This is insufficient to detect likely Doppler shifts. The possibility of the cross-correlation allows to add signal that would not be visible – for example in narrow lines – however our low SNR on the hot star spectra is not sufficient for this technique to provide any substantial advantage. On the other hand, the cool star spectra are rich in features and in spite of the low SNR of the spectra, some information can be extracted.

Xcor	A 51	Lo 17	NGC 7293
	(shift [km s^{-1}]; peak [%])	(shift [km s^{-1}]; peak [%])	(shift [km s^{-1}]; peak [%])
X1	-16.5 ± 31.3; 0.13	12.7 ± 12.3; 0.25	-3.6 ± 29.0; 0.33
X2	-21.2 ± 0.2; 0.62	-9.7 ± 10.0; 0.31	–
X3	1.6 ± 4.30; 0.18	4.4 ± 9.7; 0.27	–

Table 5.2: Results of the multi-epoch correlations. The shift is expressed in km s^{-1} while the peak intensity is in percentage.

5.2.2 Spectra of exotic and cool stars

Abell 72: a new PG1159 central star

PG 1159 stars are likely the progenitors of the hydrogen-deficient white dwarf population and the progeny of the [WR] CSPN population. With high temperatures (between 75,000K and 200,000K) and log g values between 5.5 and 8, their composition is poor in hydrogen and enriched in He, C and O (Werner et al. 1996; Dreizler et al. 1994 and Werner & Herwig 2006). The most up-to-date scenario to explain how these stars are depleted of their hydrogen is a late thermal pulse. Similar to the massive Wolf-Rayet stars, they have spectroscopic lines of elements produced by helium burning and dredged up after the mixing processes in the AGB star interior. Phillips et al. (2005) obtained long-slit spectra for six evolved Abell PN including Abell 72. They derived the PN line intensities and underline the complex architecture of the shell surrounding the CSPN. It has also been observed by De Marco et al. (2013) who determined an upper limit of M0V from J-band photometry for a possible companion spectral type. From our spectra of the CSPN, several features typical of PG1159 stars are observable, notably C IV and O VI lines, and the absence of hydrogen lines. The features can be seen in emission and absorption, as the star is affected by winds. We detect the following features in our spectra (see Figure 5.4): the He II λ3968, C IV λ4441 lines in absorption and the O VI λ3811 and λ3833, N V λ4944, O VI λ5920, C IV λ5800 and λ5811 lines in emission. The Ne VIII λ4340 is present and suggests a temperature greater than $\sim$ 150,000K (Werner et al., 2007). Unfortunately as described above, an instrumental artifact prevents the detection of the C III, IV lines at λ4650 Å and the trough expected at λ4670. Nonetheless, the wealth of spectroscopic signatures described above allows us to classify Abell 72 as member of the PG1159 class. The spectra at different epochs were showing different lines in absorption with only one line in common between two epochs. We did not cross-correlate the spectra with one another for this object as there would be little clue regarding the nature of the signal we are correlating.

Spectral variability of the CSPN of Abell 14

Surrounded by its bipolar PN, the CSPN of Abell 14 is a known "cool" CSPN (T< 30,000K, Frankowski 2003). The bright companion is outshining the CSPN, which is itself invisible in the spectra. Lutz & Kaler (1987) used the KPNO 2.1m telescope to obtain spectra for this object. They found a spectral type of B5III-V for the V=15.24 central star, harbouring a complicated, symmetric morphology. It is surprising that no dedicated study has been carried out on this unusual object.

From our spectra, the presence of the Balmer jump and the deep H lines indicate a main-sequence B star, the presence of the He I λ4026 line indicates that the star as a subtype earlier than B9. The intensity ratio of $\sim$ 1.3 between the He Iλ4471 and the Mg II λ4481 lines is a good diagnostic to indicate that the star's spectral type is B7 (Vogt et al., 1990).

Xcor	Shift	Peak
X1	16.5 $\pm$ 14.9	0.59
X2	-36.1 $\pm$ 14.9	0.59
X3	52.6 $\pm$ 1.9	0.86

Table 5.3: Results of the multi-epoch cross-correlations for the CSPN of Abell 14. A significant shift is obtained for each correlation, notably X3 that has a high shift value, small error and a high correlation peak.

As in Section 5.2.1, the spectra at different epochs are cross-correlated to look for a Doppler shift. The sampling was made between the Balmer jump to the end of the blue section at $\sim$ 4500 Å, excluding the Ca II H and K lines. The results of the analysis – shown in Table 5.3 – are conclusive: 1-σ, 2-σ and 26-σ shifts are detected, all with sufficient to high peak intensities. X1 and X2 have in common the first epoch spectrum (HJD 2454724.87563644) that has a lower SNR than the two other epochs (HJD 2454710.3890989 and 2454706.3835265), hence the much better correlation when epochs 2 and 3 are correlated. This allows us to classify Abell 14 as a new spectroscopic variable and strongly supports that the targeted star is the actual CSPN. The determination of the companion spectral type allows us to constrain the

primary's progenitor mass: the CSPN originated from a star with a mass greater than 4 $M_\odot$ (De Marco et al., 2013), indicating that the system is about 2×10^8 years old (Schaller et al., 1992).

The cool CSPN of HaTr 5

HaTr 5 is one of the objects that has been observed during the SSO 2.3m run (Section 2.3). We found an IR excess equivalent to a G0V companion in the I band (Table 2.14) and to an F8V companion in the J-band (Table 2.15) with an uncertainty equivalent to a range G8 to F5 and the implicit assumption that the companion is a main-sequence star. The position of the central star has not been confirmed yet for this PN. The field of HaTr 5 is quite dense in stars and it is not obvious visually which one is the CSPN. Our star is the closest to the geometric centre of the PN. For both runs, the coordinates referenced in SIMBAD were used, corresponding to the centroid of the PN (see Figure 5.6). Comparing our spectra with a compilation of reference spectra[1], we observe features ascribable to a spectral type between G5 and K0 as shown on Figure 5.5, namely the shapes of the Ca II H and K lines, the shape of the G-band peaking at 4308 Å , the ration of Fe I λ4046 to Hδ indicates that the spectral type is later than or equal to G5, the ratio of Mn I λ4032 to Hδ indicates that the companion is earlier than K0, the Sr II λ4077, Cr I λ4290, Sr II λ4216 and Fe I λ4326 to Hδ ratios are that of a G5 star, the ratio of the Fe I λ4271 line to Hδ is between that of a G5 star and K0 spectral types and the Fe I λ4326 to Hγ ratio is that of a K0 star. The luminosity class is IV-V: the trough of the CN complex ending at 4215 Å – characteristic of giants – is visible. The Y II λ4376 to Fe I λ4383 ratio is that of luminosity classes $\sim$ III-V. The CN complex trough at λ3883 is present but not as strong as for giants. We conclude that the star's spectral is a G8IV. This is fully consistent with our identification of a G0-F8 spectral type if we recall that our photometric method assumes a luminosity class V and a more luminous companion would be interpreted by our method as an earlier spectral type. On the other hand, since the hot star is not visible in the blue part of the spectrum, our reddening method cannot have worked. This is consistent

[1] http://www.phys.appstate.edu/spectrum/GM/GM.html

with a high reddening derived by us (Table 2.14), higher than the reddening obtained using other methods (Table 2.11). Even with too high a reddening the colours of the cool star were only partly masked.

Emission lines from the nebula provide no information that can show that star and the nebula have significantly different proper motions. Further observations need to be carried out on this object to insure it is the actual central star of HaTr 5, as there are several other candidates inside the nebula and with similar colours.

A field star near Lo 17

Spectra have been obtained for this star that was believed to be the CSPN at the moment of the observation. It is 13.1″ W of the CSPN (see Figure 5.6). The same features as in the spectrum of HaTr 5 that allowed us to classify it as G8 are observable in this star's spectrum, making it also a G8 type. The CSPN complex shape at 3883 Å is characteristic of main-sequence stars. It is conspicuous that stellar absorption lines in the spectra are shifted to a radial velocity of $\sim$ 320 km s^{-1}. The star is probably a halo object, and is not related to the PN that has a proper motion of -65.3 km s^{-1} (Durand et al. (1998) confirmed by this work).

A field star near K 1-14

This star is also a field star, one of the two very close neighbours to the actual CPSN (see Figure 5.6). Using the same features as for the two previous objects, we find that the star is on the main-sequence and has the spectral type of a G5V.

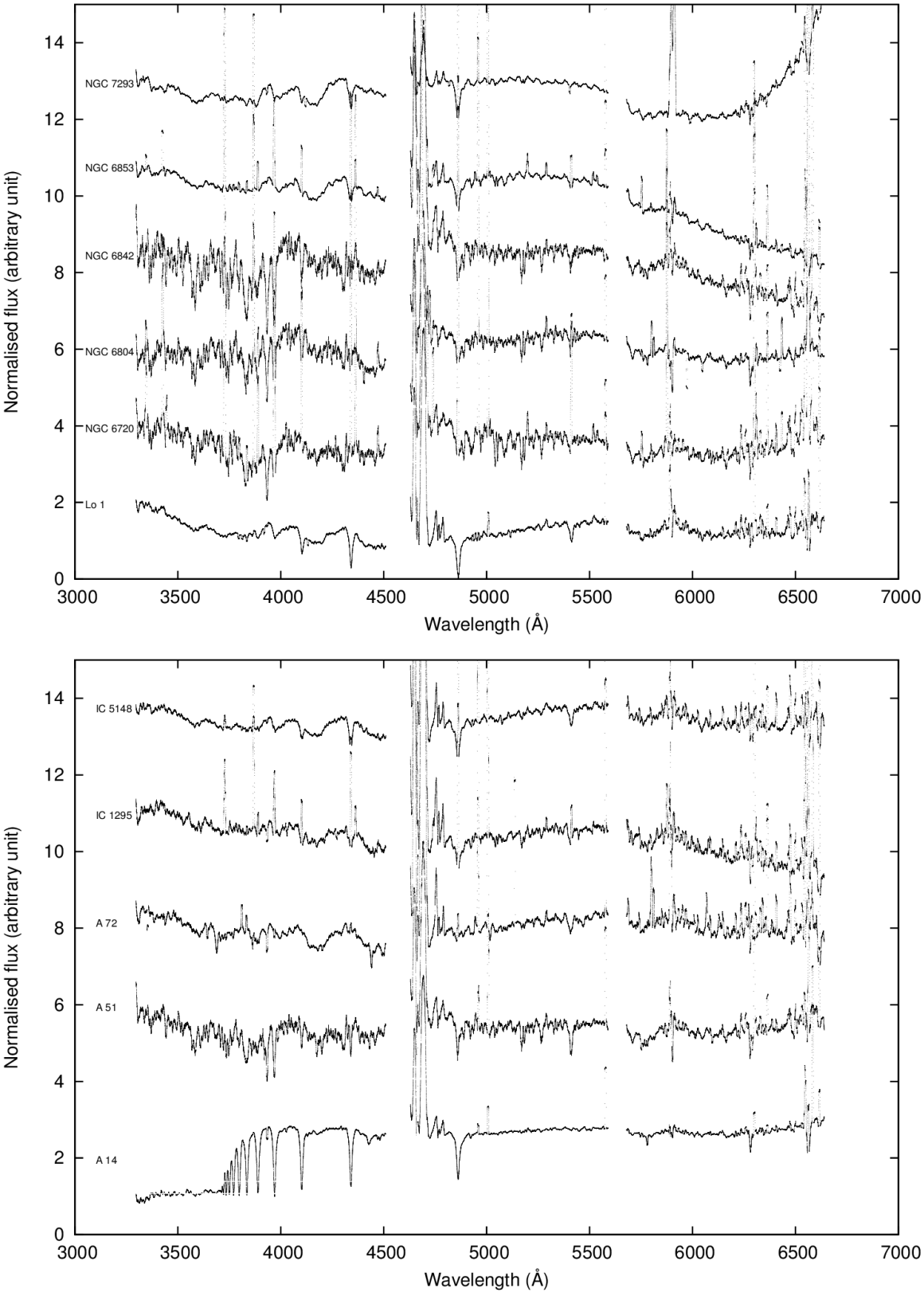

FIGURE 5.1: Approximately normalised VLT/UVES spectra for the hot sample and Abell 14. The spectra have been shifted for clarity.

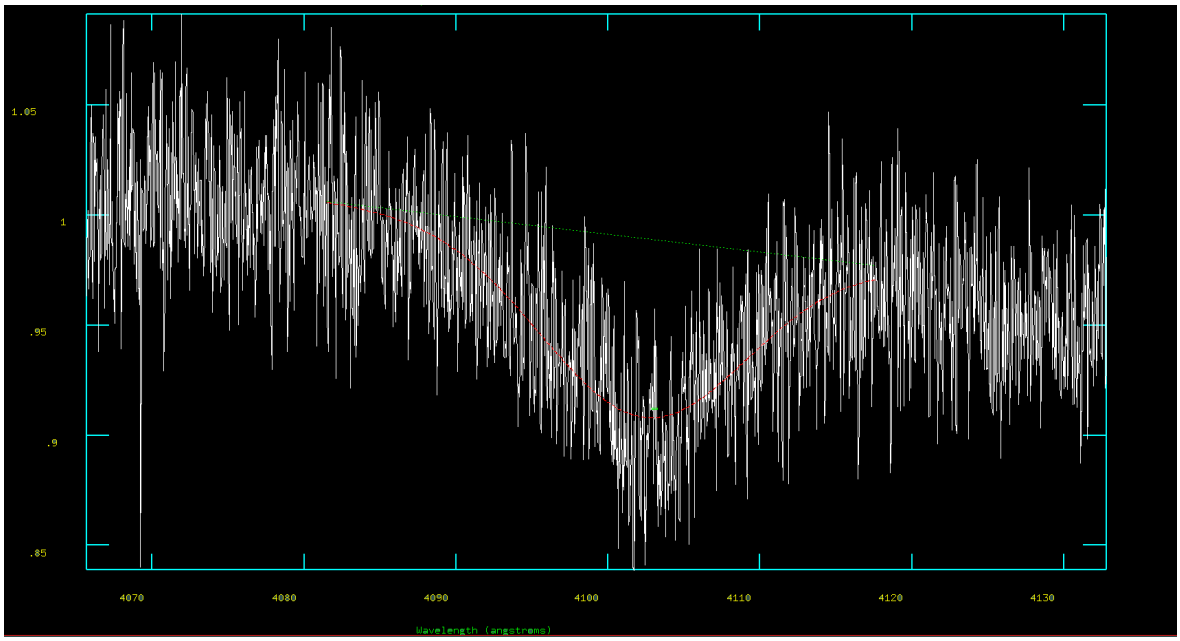

Figure 5.2: Absorption feature on the spectrum of A 51. The SNR is low.

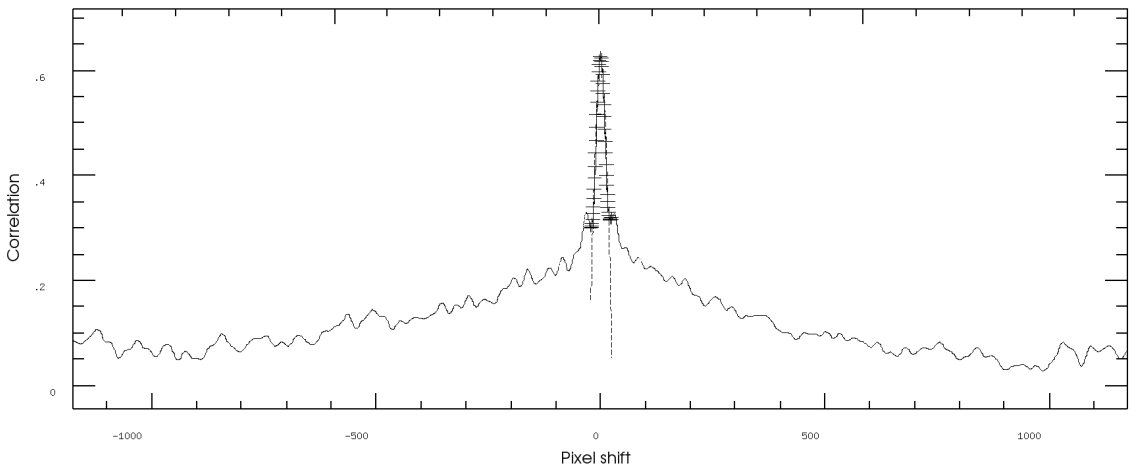

Figure 5.3: Cross-correlation X2 for the CSPN of Abell 51. The pixel shift on the plot does not take into account the heliocentric correction between the two epochs.

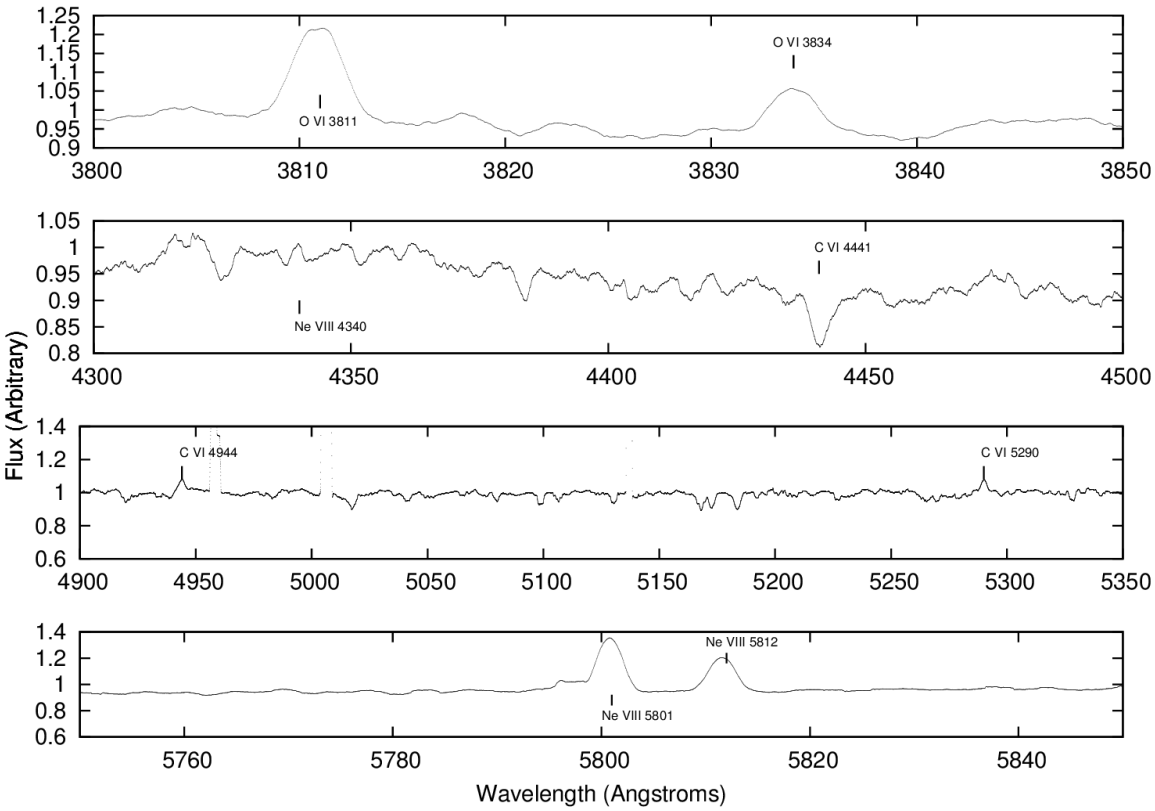

FIGURE 5.4: Main spectroscopic features indicating the PG 1159 nature of Abell 72.

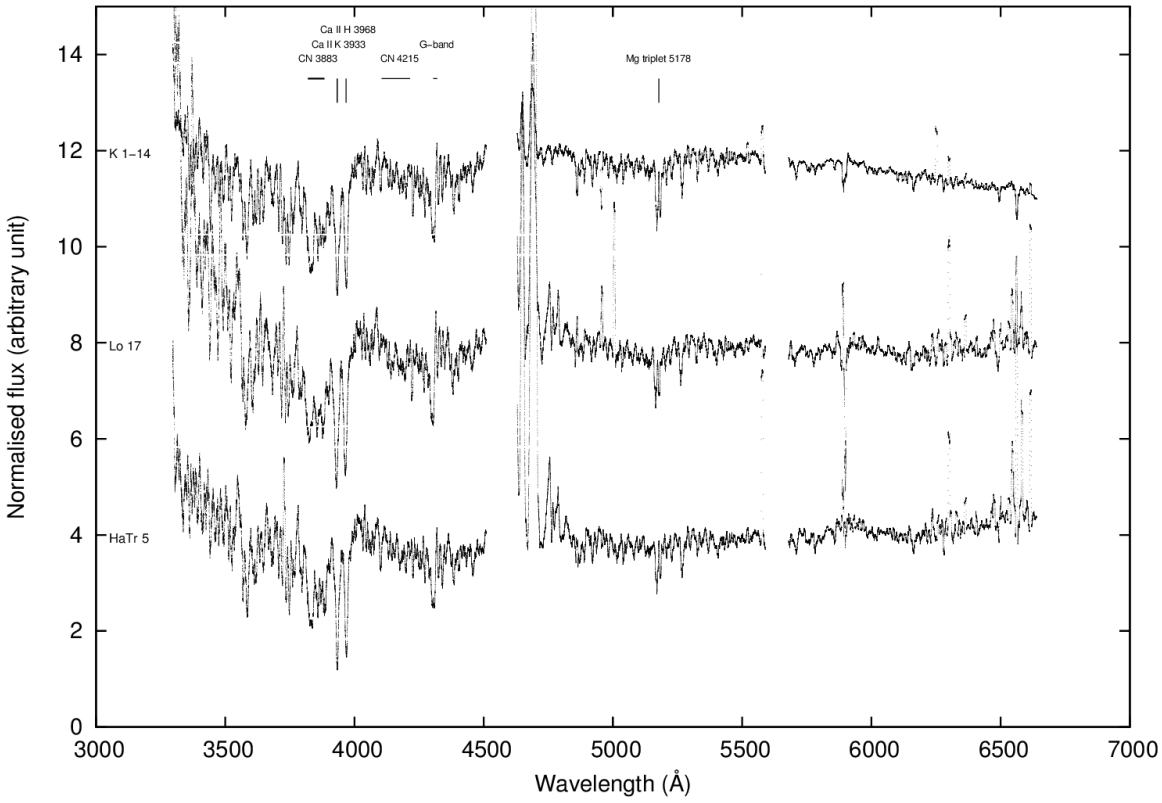

Figure 5.5: Approximately normalised VLT/UVES spectra for the HST 5, Lo 17 and K 1-14. All three are G8 stars. The main bands to identify the spectral type and luminosity classes are indicated at the top. Of these, only HaTr 5 may be a cool companion to an invisible hot CSPN. The other two stars are not related to the nebula. The spectra have been shifted for clarity.

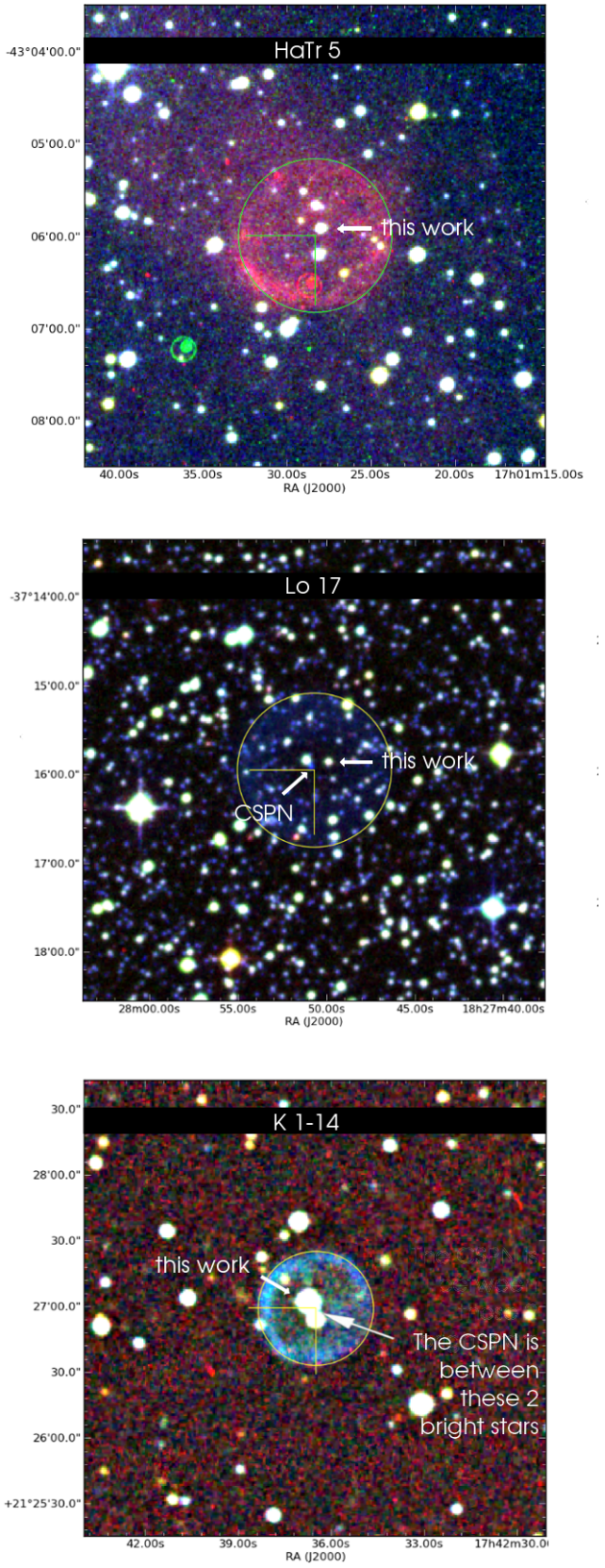

FIGURE 5.6: The field and neighbouring stars of 3 of our targets: HaTr 5, Lo 17 and K 1-14. The montages of SuperCosmos[3] images are from the Macquarie PN Database. HaTr 5: blue: B, green: short-red, red: Hα | Lo 17: B, R, I | K 1-14: B, R, I.

Chapter 6

The binary fraction of CSPN

Different methods have been used to find binary CSPN in the previous chapters, both to create an unbiased sample and simply to find more binaries. It is now time to determine the main result of this work: the binary fraction of CPSN. Under the assumption that the NIR excesses we have correspond to actual companions, the binary detection fraction is estimated in Section 6.1 from the objects analysed by De Marco et al. (2013) and in Chapter 2 for both the I and J-bands. These fractions are then debiased in Section 6.2 to add all the binary systems that we could not detect using our technique. Finally the estimated binary fraction is compared to that predicted using the main-sequence binary population in Section 6.3.

6.1 The fraction of PN central stars with a detected I and/or J-band excess

The goal of our study is to estimate the binary fraction of central stars of PN using a statistically reasonable sample size. In the I-band, combining the results from De Marco et al. (2013) and our two observing runs (Chapter 2) and excluding mimics and objects that were specified in Chapter 2, our sample counts 48 *bona fide* CSPN. We detected 19 objects with NIR excess flux yielding a non-debiased binary fraction of 40 per cent. This number is higher that the fraction of 28 per cent (7/25) from De

Marco et al. (2013) (revised from 32 per cent or 8 objects out of 27 because of the late identification of two mimics in that sample) and the fraction 27 per cent from Section 2.2.6. This is due to the high detection rate within the SSO 2.3m sample that has been added in our statistics (54 per cent, 8 out of 14, Section 2.3.3). Nonetheless, it is noticeable that two out of three independent observing runs yield comparable fractions, considering that the telescopes were different and that the analysis technique has been completely revised.

In the J-band, we find a fraction of 53 per cent: 10 detections out of a subsample of 19 CSPN, to be compared with the detected fraction of 56 per cent (5/9) from De Marco et al. (2013) and 50 per cent (4/8) from Section 2.2.6. As mentioned in Chapter 1, a higher detection rate in the J-band is expected with respect to the I-band because of the higher sensitivity of the J-band to fainter companions. There may also be a small bias towards finding more binaries because a companion adds J band flux and may push the object over the detectability limit - this however is not expected to be a large effect.

We estimate the error on our fractions by determining their statistical significance in the normal approximation. If we consider the Bernoulli experiment of picking a random CSPN of our sample and testing if it is a binary, the probability of success is p (the detected fraction) for the n objects in our sample. The normal approximation can be used to extrapolate the Galactic PN binary fraction from our sample as $np > 5$ and $n(1-p) > 5$ for both the I and J bands (Brown et al., 2001). The Wald interval was used to calculate the confidence interval, yielding an error of 14 per cent in the I-band and 22 per cent in the J-band with a 95 per cent confidence level. The detected fraction of I-band excess is therefore 40 ± 14 per cent and of the J-band 53 ± 22 excess per cent.

6.2 Accounting for completion effects

Faint companions outshone by the CSPN cannot be observed with our technique. To correct for completeness with respect to faint companions we determine the companion spectral type detection limit of our entire survey by estimating the median of the upper limits for non detections for the entire sample. In the I-band, we find a median M3V spectral type limit, fainter than which companions cannot, on average, be detected. In the J-band, we find a median spectral type limit of M4V.

Several companion spectral distributions can be used to debias for companion faintness. The spectral type of the companions of 174 main-sequence binary systems from Raghavan et al. (2010) are plotted in Figure 6.1 (top panel), excluding the four systems with degenerate companions. Companions hotter than M0 have not been plotted but have been taken into account in the normalisation. The mode of the distribution is M2V. Farihi et al. (2005) have carried out a study to detect companions to white dwarf stars using the proper motion technique, and a NIR excess search for 371 Galactic white dwarfs. Their non-corrected companion spectral-type distribution (Figure 6.1, middle panel) peaks at M3V. Their work has been updated Rebassa-Mansergas et al. (2012), shifting their distribution mode slightly towards M2V (Farihi, private communication). Lastly Debes et al. (2011) used a cross-correlation of the preliminary SDSS DR7 WD catalogs with the 2MASS, UKIRT, SDSS and WISE (Wright et al., 2010) catalogs to look for NIR and IR excesses in 1020 WD+M dwarf systems. Their companion spectral type distribution's mode is M5V (Figure 6.1, lower panel). The difference between the companion distribution of Debes et al. (2011) compared to the ones of Raghavan et al. (2010) and Farihi et al. (2005) is puzzling, and we decided to exclude it from any further calculation.

We see that with our detection limit of M3V/M4V, about half of the companions are left undetected both using the distributions of Raghavan et al. (2010) and Farihi et al. (2005). Using the normalised companion spectral type distribution of Raghavan et al. (2010) we find a binary fraction debiased for companion faintness of 56 per cent in the I band and 65 per cent in the J band. The distribution of Farihi et al. (2005)

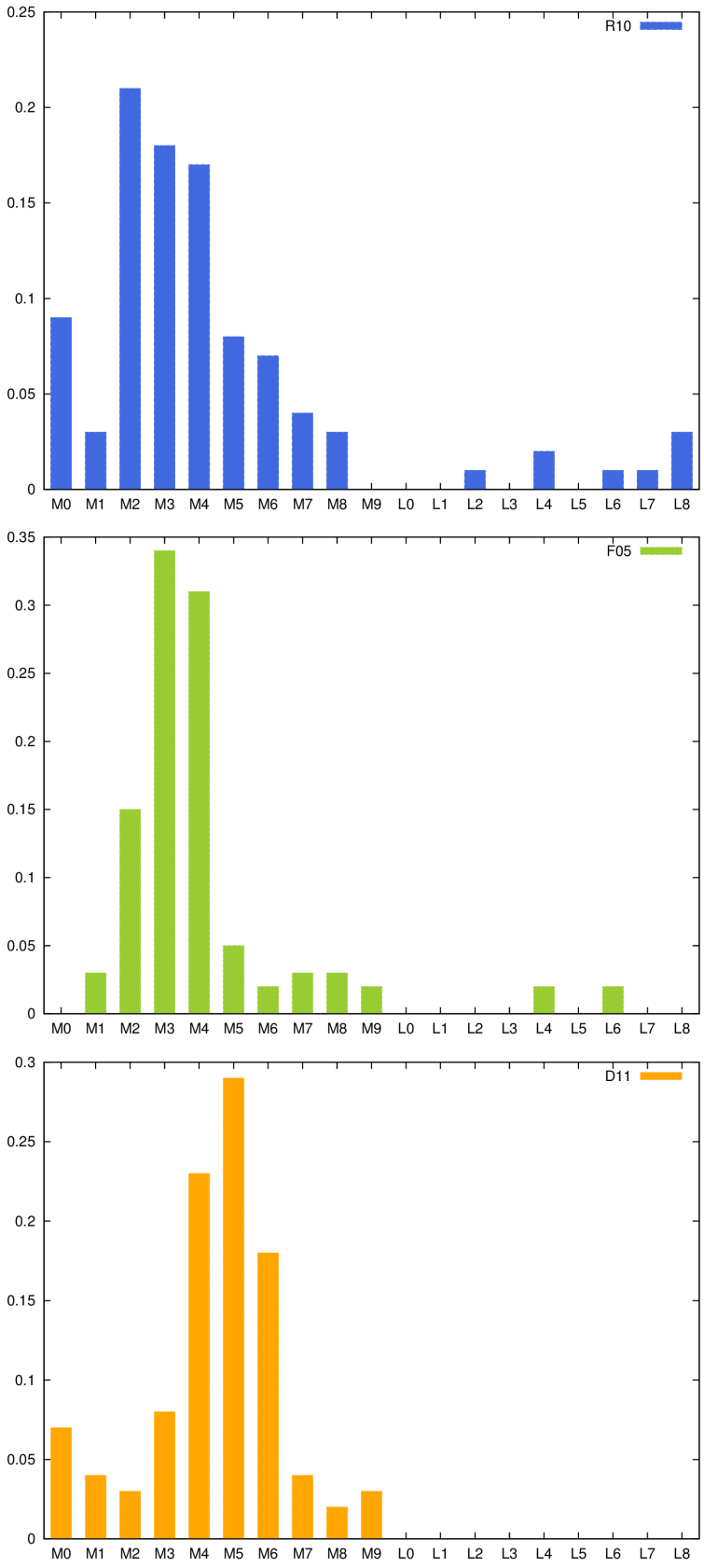

FIGURE 6.1: Spectral type distributions for the companions of main sequence stars (Raghavan et al. (2010), upper panel) and white dwarfs (Farihi et al. (2005)), middle panel; Debes et al. (2011), lower panel

yields a fraction of 148 per cent in the I band and 88 per cent in the J band. The discrepancy between these two numbers is puzzling and could be due to the fact that the distribution of Farihi et al. (2005) is not corrected for volume and sky coverage. Unfortunately, our detection limit is located near these distribution peaks and the choice of the distribution influences considerably the value for the binary fraction.

The WD+MS distributions lead to unseemingly high debiased fractions, even considering the large errors. This could be due to the companion spectral types being restricted to the M and L types only, whereas the main-sequence distribution of Raghavan et al. (2010) also includes hot companions. This is understandable since dim white dwarfs can be outshone by brighter companions. Farihi et al. (2005) show that the median companion spectral type for close (likely to interact) binaries is cooler by one spectral type than that of the resolved, longer period binaries. However close binaries represent an insufficient fraction of the whole binary population to affect the whole companion spectral type distribution and explain the shift of the peak to cooler spectral types for WD primaries. It is also possible that some of the fainter companions in Raghavan et al. (2010) have remained undetected despite their claim to completeness.

Because main-sequence stars are the progenitor population and have undergone less interactions that their WD counterpart, we rely on the companion spectral type distribution by Raghavan et al. (2010). We will account for companion-destroying interactions in our arguments below. Companions cooler than our detection limits contribute to 29 per cent in the I band and 20 per cent in the J band according to the distribution of Raghavan et al. (2010). The error has been determined by taking the median absolute deviation of our sample of non-detections, yielding an uncertainty of one companion subtype in both the I- and J-band. We correct the binary fraction for undetected companions and add this error to the one determined in § 6.1, we find a binary fraction of 56 ± 17 per cent in the I-band and 65 ± 23 per cent by averaging the upper and lower errors in the J-band. This is the PN binary fraction for separations smaller than the spatial resolution of the observations, a number we estimate next.

6.3 Comparison with the main-sequence binary fraction

Our targets are selected from the non-resolved binary pool. Once images are obtained with a particular setup, we double-check that none of the targets can be resolved into multiple sources by our detection algorithm. The algorithm will detect a pair of sources if they are farther apart than $\sim 0.5''$, or approximately one third of our median seeing in photometric conditions. However this number is determined for when both stars have the same luminosity, but will change as a function of the flux ratio of the observed couple of stars. We use a magnitude difference of 2 between the primary and its companion and look for the smallest separation between two resolved stars with such a flux ratio in our images, yielding a $\sim$ $2''$ separation. We therefore use this number equivalent to 1.4 times the median seeing of our observations as the separation limit outside which binaries are excluded from our sample by design in the I band. Similarly for the J-band limit, we use $2.8''$ corresponding to 1.4 times the 2MASS resolution of $2''$ (Skrutskie et al., 2006). The values we used here are slightly higher than those used by De Marco et al. (2013) because it was realised that a binary with such a flux ratio would be harder to resolve.

The median distance of our 46 targets (two targets from the SSO 2.3m sample have unknown distances) is 1.14 kpc while for the 17 J-band sub-sample it is 0.75 kpc. As discussed in De Marco et al. (2013), using a de-projection factor of 0.9 to account for random phase, random orientation and the fact that eccentric systems spend more time at apastron, we obtain a corresponding median orbital separation of 2530 AU in the I-band and 2330 AU in the J band. In other words, our I-band sample contains, on average, only binaries with a projected separation smaller than 2530 AU (2330 AU for the J-band sample) or else the binary would have been detected as resolved. Hence, to obtain the binary fraction at all separations one needs to add the binaries with separations larger than these limits.

Ultimately we want to compare the PN binary fraction with that of the main sequence progenitor population. Since the main sequence binary fraction is for binaries

at all separations we need to exclude those main sequence wide binaries that evolve into central star binaries with separations larger than 2560 (or 2360) AU. Orbital separation increases after the primary's main-sequence lifetime because of mass-loss during the giant phases, therefore the main sequence binary separation will be smaller. De Marco et al. (2013) had estimated that binary separations will increase by a factor of ~ 2.5. In other words a central star binary with a separation of 2530 AU (2330 AU) had a separation of 1010 AU (930 AU) while on the main sequence. We therefore scale the main sequence binary fraction down by taking out all those binaries with separations larger than 1010 AU (930 AU). Only then can we compare the main-sequence binary fraction to the central star binary fraction of 56 ± 17 per cent from the I-band analysis or 65 ± 23 per cent from the J band analysis. These numbers should be the same. At the moment they are within the still large error bars.

To take out the wide main-sequence binaries we convert the 1010 AU (930 AU) limits into periods by using Kepler's third law and a system's mass of 1.5 $M_{\odot}$: log P=7.1 (7.0). We also need to be aware that main sequence binaries with periods smaller than log P<2.43 (De Marco et al., 2013) will go through a common envelope on the RGB, and never ascend the AGB, thereby eliminating themselves from the pool of binaries that become binary CSPN. Using a Gaussian fit of the main sequence binary period distribution of Raghavan et al. (2010) and integrating under the curve between log P=2.43 and 7.1 (or 7.0) we discover that 79 per cent (78 per cent) of all main-sequence binaries reside within those limits. The errors on these estimate are very small because of the logarithmic nature of the period limits.

The blue subsample (F6V-G2V) of the analysis of Raghavan et al. (2010) is consistent with a 1.2 $M_{\odot}$ median mass progenitor of PN (Moe & De Marco 2006, see Chapter 1). The binary fraction of this subsample is 50 ± 4 per cent. Eliminating the binaries with periods smaller than log P=2.43 and larger than 7.1 (7.0) one obtains a main sequence binary fraction of 35 per cent (33 per cent), which will presumably become the CSPN binary fraction for system closer than 2530 AU (2330 AU). The different CSPN binary fractions for the I and J-band analyses as well as the prediction from the main sequence binary fraction are listed in Table 6.1. We note that when we

	Fraction (a <2530 [I] or 2330 AU [J])	Fraction all a
I band analysis	0.56 ± 0.17	0.71 ± 0.22
J band analysis	0.65 ± 0.23	0.84 ± 0.30
Prediction from main-sequence binaries	0.34 ± 0.02	0.45 ± 0.04

TABLE 6.1: The binary fraction of CSPN. The I and J band estimates should agree, and do within the error limits. The prediction from the main sequence binary fraction should only agree with the observations if the entire main sequence population (singles and binaries) minus those close binaries that go through a CE on the RGB, make a PN

compare the binary fraction determined for CSPN binaries with maximum separations of 2530 AU (2330 AU), we should not use the entire main-sequence binary fraction. Those main sequence binaries with log P<2.43 go through a CE on the RGB and never ascend the AGB. This is equivalent to 5% of all main sequence stars. In Table 6.1 we thus compare our CSPN binary fraction within our separation limits to a main sequence binary fraction of 45±4 per cent, where we acknowledge that the error bar of this fraction does not account for the error on the period limit adopted (log P<2.45), although due to the logarithmic limit, the additional error should not be large.

Thus, the main result of this thesis are the following numbers: a CSPN binary fraction of $56 \pm 17\%$ for systems with separations lesser than 2530AU from I-band analysis and a binary fraction of CSPN from J-band analysis of $65 \pm 23\%$, to be compared with a MS binary fraction of $34 \pm 2\%$ for the corresponding population. Taking into account the same biases to extrapolate these fractions to binaries at all separations, we find binary fractions of $71 \pm 22\%$ from I-band analysis and $84 \pm 30\%$ from J-band analysis, to be compared with $45 \pm 4\%$ for the main-sequence binary fraction. A brief return on the study using morphologies is offered in Section 6.4 while the consistency and implications of the above numbers are discussed in Section 6.5.

6.4 Binary fraction and PN morphologies

As mentioned in Section 0.4, our approach to the link between binary CSPN and PN shapes is not based on the shapes themselves. Yet, now that our fractions are obtained, it is possible to try and link PN shapes with our binary fraction. We used the morphologies of our own Tables 2.3 and 2.11 and the Table 1 of De Marco et al. (2013) (objects with morphologies marked with a "?" were updated using the Macquarie University PN database). When a PN had two morphological types we took both into account, so that the 46 objects that are analysed are normalised over 55 in total. The morphological repartition of our sample is shown in Figure 6.2.

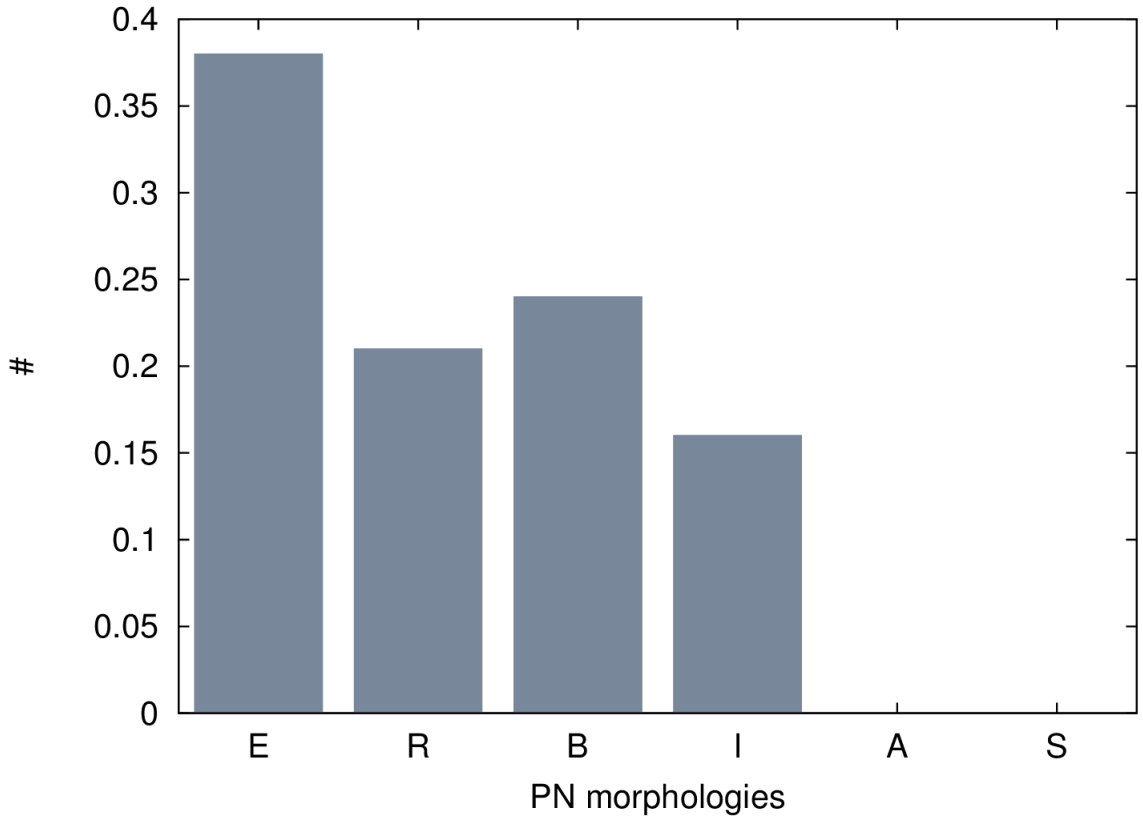

Figure 6.2: PN morphology distribution of our sample. The distribution is normalised to 57. When a PN had two indicated morphologies we took both into account. The ERBIAS classification was used: elliptical (E), round (R), bipolar (B), asymmetric (A) and quasi-stellar, i.e. point source (S)

The sample seems to form a satisfactory representation of the Galactic population with 21% round PN similar to the $\sim$ 20% of spherical Galactic PN (see Section 0.2).

The absence of quasi-stellar (S) PN is a bias from our method as we purposefully avoided observing compact PN in our selection criteria (see Section 1.3.3). The absence of asymmetric (A) PN is not accountable by any effect to our knowledge, except for the fact that some irregular (I) PN may also be asymmetric and not classified as such. This is acceptable as it does not affect the count of round PN.

We assume the null hypothesis that both the detected binary CSPN population and non-detected binary CSPN population have the same fraction of round PN and want to test the alternative hypothesis that there are more round PN in the non-detected binary pool. Using a Z-test to compare these two populations, we find that there is a 95% chance that the proportion difference between these two populations for a random sample is within 0.25 of the value for this sample, 0.08. In order to reject the null hypothesis, we would need a Z-score of 0.90 corresponding in our situation to a confidence level of 36%. We conclude that there is no statistical evidence that binarity is less associated with spherical shapes. Although this test is unsuccessful, it should be noted that – strictly speaking – the only PN that undergo shaping by the companion are the ones where the companion has a period $\lesssim$10,000 days ($a \lesssim$10AU), which accounts for only the half of all PN. This orbital separation is slightly smaller than our resolution limit, meaning that some of our binaries may be too wide for binary shaping to have taken place. However, assuming that the only PN that undergo shaping by the companion are the ones we resolve, we find – by averaging the I and J-band results – a fraction of $\sim$ 55% of binary CSPN and $\sim$ 45% of single stars, mergers or stars with planets (see Table 6.1). Using the morphology distribution we find in our sample (see Figure 6.2), it is possible to envisage a scheme where the $\sim$ 20% of round PN and some of the mildly elliptical PN ($\sim$ 25%) correspond to the 45 percent of the population of non-binary CSPN, while the rest of the ellipticals ($\sim$ 10%), the bipolars ($\sim$ 25%) and the irregular PN (15%) correspond to 55% of binary CSPN. Extending the sample size and carrying out a more accurate determination of the morphological types thanks to deeper, better resolved observations in a broader coverage in wavelengths (e.g. thanks to more survey observations) will help relating binarity to morphology more meaningfully.

6.5 Discussion

Taken at face value, these numbers indicate a rather larger CSPN binary fraction, superior to the that of the main sequence. However, the error bars are still significantly large due to the size of our sample. Taking into account the error bars on our numbers, both the I and J band binary fractions are only marginally superior to those of the main-sequence. These errors have been determined as accurately as possible while a special care has been applied to remain extremely conservative. Therefore, and owing to the fact that these fractions are only lower limits, our results seem to indicate a trend in favor of a binary fraction being larger than that of the main-sequence. As illustrated in Section 0.4, this seems to indicate, if extrapolated, that binaries are indeed a preferred channel for PN formation. This amazing conclusion challenges the current model for stellar evolution. Before asserting that the current model needs changes, cautions have to be taken to ascertain that this study suffers no obvious caveat.

It has been seen in Section 1.4 that the chances of false detections are very small and that such an artifact cannot plague our study and results in a substantial manner. Although we set our detection threshold at the lowest level (namely $1-\sigma$ detections), we have found that many of the NIR excesses we found are very consistent and supported by a variety of independant cross-checks. These meaningful detections are summaried in the conclusion. Also, a large number of our detections are first detections and consequently there exists no material to support these discoveries yet. We rely on the successful cross-checks carried out for excesses detected using at least two different techniques and on the numerous checks we carried out all along the different steps of our procedure to trust these new excesses.

The distributions we use have also been chosen carefully. It is not clearly understood why the companion white-dwarf populations are different by one or two sub-spectral type to the companion main-sequence distribution. Unfortunately our detection limit is located precisely near the mode of these distributions, nonetheless we believe that using the companion main-sequence distribution by Raghavan et al. (2010) in union with their period distribution minimises the sources of heterogeneoty and is a safe approach.

The last parameter that could skew these distributions is the median mass for PN progenitor, for which we chose $1.2M_{\odot}$. As a more massive star implies an increased multiplicity, an increase in this parameter's value could raise the main-sequence binary fraction and bring to better agreement with our high CSPN binary fractions. However, substantial proofs would be needed to increase the median mass progenitor to such a value, and such change might imply a re-arrangement in the statisitcs of the de-biasing.

In our findings, we expected that the detection rates of the I and J-band flux excess are different, as the J band is more sensitive to detect fainter companions. However the debiased binary fractions should be equal in both bands as this effect should be accounted for. The I and J-band fractions are reasonably close and indistinguishable within the error bars. As the sample size is increased, the discrepancy between the I and J-band results should be eliminated and in so doing provide support to the debiasing process.

This work suggests than PN are the product of binary systems, however firm conclusions are hard to draw yet. In spite of the efforts shown in this work, the error bars are still large due to a small sample size. We estimate that for a sample size of $\sim$ 150 objects in the I band and of $\sim$ 100 objects in the J band with the same detection rate and debiasing properties, the total error (on the binary fraction at all separations) should be 16 per cent in both bands. Any effort beyond this sample size is likely not worth it as the observation of an additional $\sim$50 objects in each band would only decrease the error to a value of 15 per cent in both bands due to the error being proportional to $\frac{1}{\sqrt{N}}$ (where N is the sample size). Since our ideal sample size is $\sim$ 150 objects, one cannot exclude the case where the main-sequence binary fraction and the CSPN binary fraction are different, but only within the error bars in which case the study will be non-conclusive. However given the numbers obtained here (Table 6.1), this seems to be an unlikely outcome.

The technique and limitations have been clearly defined and tested. With an average of $\sim$ 20 CSPN observed per observing run and each observing run counting $\sim$ 4 photometric nights, we foresee that 3-4 additional runs in good conditions should be

sufficient to allow us to complete the sample and conclude on the viability of the Binary Hypothesis. This translates into ∼120-160 hours of photometric weather in grey time. This high number of hours can be shortened if service-mode is used while special care must be addressed regarding the observation of standards bracketting the science targets.

The use of telescopes bigger than the 4m class to shorten the exposure times and tackle the faint end of the population seems unlikely, unless the observation of faint targets serves a specific purpose additional to the increase of the sample size only. No proposal for big telescopes have been written in the frame of this project (apart from the VLT data dealt with in Chapter 5) and although this initiative could be very fruitful if granted, the chances are very narrow for the time to be granted and I would not advise to do so. Planning a small telescope survey, however, would be a very profitable endeavour. Such an attempt has been proposed and denied (see Appendix D.2) due to a bad estimation of the exposure times, however this could guarantee the observations of enough targets in one year (see the strategy presented in the proposal). 65% of the stars from the sample of Frew (2008) are located in the Southern hemisphere, therefore more observations should be sought in the South. The SSO 2.3m is very suited to our needs and has a reputation for being underused, therefore I strongly recommend to propose there as much as possible, especially given the geographic proximity and involvment of Macquarie University. In the North, the KPNO 2.1m telescope has been decomissioned. Observing time can be sought at the KPNO WIYN telescope, otherwise it might be needed to create new connections with some of the sub-4m-class Northern telescopes.

Some data have been acquired in the J-band that have not been analysed. Although it is possible to acquire new data in this spectral range in addition, for example at the SSO 4m using IRIS2, it is unlikely that this will allow to collate the sample faster than using optical data only. Confirmation of already obtained optical excesses from IR data would be, however, a very comforting addition.

Little help is to be expected from the technologies and telescopes to come. In our case, a long time coverge is necessary more than any technological advancement. Yet in

terms of photometric variability, the incredible sky coverage, cadence and depth of the LSST will certainly allow a huge number of discoveries of faint, variable CSPN provided the data are easily reduced and at hand. Nonetheless, satisfying orbital parameters have been estimated from modelling for only about a half of the known photometric variables known to date. Although many new lightcurves will be obtained, it is not obvious that their modelling will occur smoothly, even less so when witnessing the difficulties to model lightcurves of greater precision, like those obtained recently with Kepler. Finally, one cannot ignore –without a certain irony– the future power of the JWST[1] in the NIR with its photometer NIRCAM, that will be able to observe targets with J-band magnitudes down to $\sim$28 in the interval of a 10,000-second exposure.

[1]James Webb Space Telescope: http://www.jwst.nasa.gov/

Conclusion

In this work, we have explored the different methods to find unresolved binary CSPN: NIR excess detection, photometric variability and spectroscopy. The final aim of our search has been to determine the binary fraction of CSPN. Our primary detection tool has been the NIR excess detection method, applied to this problem by De Marco et al. (2013) and refined and extended here.

Including the 25 objects analysed by De Marco et al. (2013), we have searched for companions in 48 CSPN using the the I-band photometry, 19 having additional J band data. The I band offers a higher efficiency as all necessary data for a given target can be obtained in one observing run. However, its detection power is lower. The J band is the ideal spectral range with a strong potential for finding cool, faint companions, but the drawbacks are the necessity of two observing runs, one in the optical to determine the target's reddening and one in the NIR bands to find the colour excess.

This constraint can be overcome by retrieving NIR data from available online surveys. The quality of data of DENIS, 2MASS and UKIDSS is sufficient for our purpose. However, the number of observed CSPN is, at the moment, limited. The analysis of large samples from online surveys would appear efficient to carry out this project. Nevertheless, a drastic target list reduction is observed once target selection criteria are applied. As a result, the sample size is reduced dramatically Using online surveys is useful extract information on the targets for future observing, but cannot provide us the information to carry out this project. The ideal strategy is to observe the maximum of targets during an observing run in B, V and I while making sure that the weather is photometric and the SNR large enough ($\gtrsim 100$). This way, carefully selected objects can benefit from high-precision photometry and be added to the sample dedicated to

statistics. The main drawback of this method is that it is time consuming (16 objects per observing run on average so far). Still, it is the only way to derive the CSPN binary fraction. The acquisition of $\sim$ 100 targets from the southern hemisphere sample is not an unachievable goal.

Photometric monitoring has been carried out during non-photometric weather. This method allows one to detect close binaries (P $\lesssim$ few days). While the binary fraction of close binaries has already been determined ($\sim$ 15%, Miszalski et al. (2009)), only $\sim$ 40 such binaries are known, and a large sample is necessary if we are to relate PN characteristics to those of the binary system. We have therefore searched for additional variables. The main issue we have had lies in the inadequate sampling of this opportunist strategy. This approach allows to infer variability only in the most dramatic cases or in the rare cases where the sampling is fortuitously adequate. The possibilities of analyses of such data are limited since the lightcurves are too under-sampled to allow any kind of modelling, therefore no physical parameters can be deduced from the observed systems, only the potential variability.

On the other hand, extremely precise and well-sampled data have been obtained thanks to the observation of the six PN in the field of the Kepler satellite. The analysis of the data reveals that two CSPN of the sample are likely short-period binaries. The modeling of the complex lightcurves obtained with this ground-breaking precision is difficult, but ongoing efforts are made decipher the nature of the variability observed in all CSPN in the field. Future plans include the analysis of K2 lightcurves, a larger sample of CSPN with a decreased photometric precision compared to that of the K1 plan. More observing time has been granted for the acquisition of photometric and spectroscopic data of detected or suspected short-period binaries. These objects will be modelled to obtain stellar and systems' parameters. observation of the faint end of the local sample of PN the modeling of which is less a novelty but still delicate.

Spectroscopy is the third pillar of the search for binary CSPN. The data we used came from a VLT poor weather programme and the SNR was unfortunately critically low. A mini-survey of 10 hot stars observed at three different epochs has been carried out, aiming to find RV variability from the Doppler shift of the CSPN lines

due to the presence of a companion. Only three hot stars had sufficient signal to attempt multi-epoch cross-correlation. One objects showed a remarkable strong signal for the cross-correlation between two epochs and warrants more observations. Four stars have the spectrum of objects too cool to ionise the PN, making them potential bright companions to faint, hot CSPN. One of them, also revealed thanks to the multi-epoch cross-correlations method, was indeed a B7III-V star outshining its primary. The other three stars' spectral types and luminosity class have been determined and are G8V, G5V and G8IV. Two of them appeared to be field stars. No CSPN was detected in the spectrum of the subgiant, leaving open the question of its authenticity as the CSPN. One of our hot stars is a member of the PG1159 CSPN class.

The combination of techniques presented allows to check the consistency of our binary detections when objects have been analysed using at least two different methods, or when combining our work from analyses available from the literature. For example:

- We detected red or NIR flux excess in more than one band. All the objects for which a NIR excess was detected in the J band but not in the I band, have I band limits consistent with the J band detections, while the spectral types obtained in case of detection in both the I and J bands agree within one-two sub-types at most.

- We observed the same objects across different observing runs and online surveys. For example, the NIR excess detected for the CSPN of SkAc 1 corresponds to an M4-5V companion from our I and J bands photometry and to an M5V companion from the SDSS photometry,

- We checked for consistency with literature values when possible. For instance, we found a NIR excess consistent with an M2-3V companion for Fr 2-9. The RV study of Edelmann et al. (2006) has revealed an M2V companion. Another example: our NIR excess for EGB 6 consistent with an M4-5V companion in agreement with the spectral type determined from the analysis of HST images by Liebert et al. (2013). Our detection of a NIR excess consistent with a K1-3V companion is in agreement with the K2V companion also imaged by the HST

(Ciardullo et al., 1999). The NIR excess consistent with a G8V companion from our SDSS analysis in agreement with the K3V companion observed by Ciardullo et al. (1999).

- We also check for consistency between spectral type and luminosity class. Our NIR excess method determines companion spectral types by assuming that the companion is a main-sequence star. When companions have luminosity classes IV-V, hotter spectral types are found by our method. This was the case for the giant companion of the CSPN of PHR 0905-4753 (Frew et al., in preparation), for which we found a NIR excess detection consistent with the presence of a B7V companion. Another example: our spectroscopic analysis reveals the spectrum of a G8IV for HaTr 5, while we found a NIR excess consistent with a F8-G0V companion from our SSO 2.3m observing run.

Subject to these consistency checks, only the NIR excess detected from our own dedicated observations allow the sample selection and detection confidence necessary to estimate the binary fraction. From our total sample, we found a detection rate of 40% in the I band and 53% in the J band, where as explained, the J-band detection rate is higher due in part to its expected fainter detection threshold. The debiased binary fraction for CSPN is obtained by adding systems with companions we could not detect because they were either too faint, too far from their primary and resolved from the ground or because they went through a strong interaction with the primary during the RGB phase. We obtain a total binary fraction of 0.71 $\pm$ 0.22 from the I-band sample and 0.84 $\pm$ 30 from the J-band sample. These two fractions have been corrected for biases and agree, although the error bars are still large. These numbers are to be compared with the main-sequence binary fraction estimated at 0.45 $\pm$ 0.04. Although there is a tendency towards a high fraction of binary CSPN, implying that PN derived preferentially from binaries, the error bars need to be both better quantified and reduced. The reduction of the error bars by increasing the sample size to a number of $\sim$ 150 CSPN should bring these two fractions in agreement and allow a more statistically robust conclusion on whether the Binary Hypothesis can

describe tomorrow's paradigm of stellar evolution.

Appendix A

A.1 Sample used for statistics

We present the complete sample that is used to draw the statistics of Chapter 6 in Table A.1.

Object	Observing run	Companion sp. type	Companion sp. type	Exclusion from sample
		I band	J band	
A 7	DM13+	Later than M4V	M5V	–
A 16	DM13+	M3V	–	–
A 20	DM13+	Later than M0V	–	–
A 28	DM13+, KPNO2.1	Later than M4V	–	–
A 31	DM13+	Later than M3V	M4V	–
A 57	DM13+	K3V	–	–
A 71	DM13+	Later than M5V	–	–
A 72	DM13+	Later than K8V	Later than M1V	–
A 79	DM13+	F6V	G7V	–
A 84	DM13+	M4V	–	–
DeHt 5	DM13+	Later than M3V	M5V	mimic
EGB 1	DM13+	M4V	M5V	mimic
EGB 6	DM13+, KPNO2.1	Later than M5V	M5V	–
HaWe 5	DM13+	Later than M5V	–	mimic
HDW 3	DM13+	Later than M4V	–	–
HDW 4	DM13+	M7V	–	mimic
IsWe 1	DM13+	Later than M4V	–	–
IsWe 2	DM13+	Later than M4V	–	–
JnEr 1	DM13+, KPNO2.1	Later than M4V	–	–
K 1-13	DM13+	Later than M3V	–	–
K 2-2	DM13+	Later than M1V	Later than M4V	mimic
NGC 3587	DM13+, KPNO2.1	Later than M3V	Later than M6V	–
NGC 6720	DM13+	Later than M2V	Later than M4V	–
NGC 6853	DM13+	Later than M3V	M5V	–
PuWe 1	DM13+	Later than M4V	–	–
Sh 2-78	DM13+	M4V	–	–
Sh 2-176	DM13+	M5V	–	–
Sh 2-188	DM13+	M4V	–	–
Ton 320	DM13+, KPNO2.1	Later than M4V	Later than M6V	–
WDHS 1	DM13+, KPNO2.1	Later than M5V	–	–
A 39	KPNO2.1	Later than M4V	Later than M3V	–
EGB 9	KPNO2.1	G4V	–	mimic
FP J1824-0319	KPNO2.1	Red deficit	Later than M4V	–
HaWe 10	KPNO2.1	Later than M3V	–	–
Jacoby 1	KPNO2.1	Later than M3V	Later than M5V	–
LTNF 1	KPNO2.1	G5V	not applicable (photometric variable)	–
NGC 6058	KPNO2.1	Later than G4V	Later than G4V	–
NGC 6781	KPNO2.1	M3V	M4V	–
SkAc 1	KPNO2.1	M4V	M5V	–
We 2-34	KPNO2.1	M3V	M3V	–
A 48	SSO2.3	A5V	A1V	[WN]
BMP J1808-1406	SSO2.3	M4V	–	–
FP J1912-0331	SSO2.3	Red deficit	–	–
HaTr 5	SSO2.3	G0V	F8V	–
K 1-22	SSO2.3	K3V	G5V	–
K 1-23	SSO2.3	Later than K6V	–	–
Lo 5	SSO2.3	Later than M0V	–	–
LoTr 8	SSO2.3	Later than K7V	Later than M1V	–
MeWe 2-4	SSO2.3	M4V	–	–
PHR J1408-6106	SSO2.3	Red deficit	–	–
PHR J1418-5144	SSO2.3	Later than M4V	–	–
PHR J1432-6138	SSO2.3	K9V	–	–
PHR J1510-6754	SSO2.3	K4V	–	–
Sh 2-68	SSO2.3	Later than K5V	Later than M0V	mimic
	KPNO2.1	Later than M3V	Later than M4V	
RCW 69	SSO2.3	M4V	–	–
YM 16	SSO2.3	M2V	–	–

TABLE A.1: Sample used for statistical purposes in Chapter 6.

Appendix B

B.1 Photometric results for each night (KPNO 2.1m)

In this Appendix, we present the individual photometric measurements for each object and each night in Table B.1.

B.2 Objects excluded from the KPNO 2.1m run analysis

We have observed CSPN according to the selection criteria described in the introduction. Some objects, however were at the limits of our criteria and were observed anyway due to target availability constraints but their analysis revealed to be unsuccessful. Three PN (H 4-1, Na 1 and Sa 4-1) out of these five are distant and not part of the volume-limited sample of Frew (2008). They are surrounded by bright PN, thus the PN and the central star essentially form a point source than is then taken into account when integrating the flux within the PSF profile. The two other objects (IC 3568 and IC 4593) are both bright compact PN affecting the photometry of the central star. All these objects showed a great sensitivity to photometric input-parameter values, artificially high $E(B-V)$ values, and systematically displayed a blue-excess in our $V-I$-temperature diagram, typical of objects displaying contamination at least in the Johnson $V-$band by various nebular lines (notably the strong [O III] line) and inducing an erroneously high reddening. Their I-band magnitudes are given here as

Object	Night	U	B	V	I
A 28	1	15.153 ± 0.009	16.273 ± 0.009	16.523 ± 0.007	16.836 ± 0.010
A 39	4	14.137 ± 0.007	15.310 ± 0.007	15.613 ± 0.006	15.935 ± 0.009
A 39	6	14.125 ± 0.004	15.317 ± 0.004	15.619 ± 0.004	15.925 ± 0.008
EGB 6	1	14.479 ± 0.008	15.688 ± 0.008	15.991 ± 0.007	16.331 ± 0.007
EGB 6	6	14.457 ± 0.005	15.691 ± 0.006	16.004 ± 0.008	16.323 ± 0.014
EGB 9	1	12.863 ± 0.009	13.062 ± 0.008	13.133 ± 0.009	13.037 ± 0.010
FP J1824-0319	4	–	14.601 ± 0.006	14.841 ± 0.004	15.159 ± 0.010
FP J1824-0319	6	–	14.755 ± 0.003	14.596 ± 0.006	15.120 ± 0.012
H 4-1	4	–	16.465 ± 0.068	15.384 ± 0.081	17.491 ± 0.046
H 4-1	6	15.971 ± 0.019	16.846 ± 0.040	15.701 ± 0.056	17.736 ± 0.080
HaWe 10	1	–	17.549 ± 0.008	17.888 ± 0.005	18.259 ± 0.009
IC 3568	6	11.336 ± 0.015	12.204 ± 0.055	12.249 ± 0.072	12.752 ± 0.028
IC 4593	4	–	–	–	11.119 ± 0.006
IC 4593	6	9.719 ± 0.004	–	–	–
IC 972	4	17.774 ± 0.012	18.110 ± 0.008	17.471 ± 0.007	17.359 ± 0.011
IC 972	6	17.761 ± 0.022	18.049 ± 0.013	17.446 ± 0.007	16.530 ± 0.008
Jacoby 1	4	13.963 ± 0.005	15.217 ± 0.008	15.610 ± 0.005	16.020 ± 0.010
JnEr 1	1	15.519 ± 0.008	16.759 ± 0.008	17.101 ± 0.007	17.484 ± 0.009
JnEr 1	6	–	16.742 ± 0.009	17.118 ± 0.010	17.494 ± 0.016
LTNF 1	1	14.610 ± 0.011	15.739 ± 0.007	15.746 ± 0.006	15.269 ± 0.008
Na 1	6	15.810 ± 0.036	16.310 ± 0.084	15.570 ± 0.102	15.879 ± 0.060
NGC 3587	1	14.137 ± 0.008	15.394 ± 0.009	15.764 ± 0.007	16.165 ± 0.010
NGC 3587	6	14.155 ± 0.005	15.388 ± 0.006	15.779 ± 0.006	16.159 ± 0.009
NGC 6058	6	–	13.452 ± 0.004	13.802 ± 0.004	14.169 ± 0.007
NGC 6781	4	16.243 ± 0.039	17.111 ± 0.021	16.880 ± 0.016	16.439 ± 0.029
Sa 4-1	6	12.249 ± 0.004	13.427 ± 0.004	13.721 ± 0.005	14.064 ± 0.006
Sh 2-216	1	11.228 ± 0.007	–	–	–
Sh 2-68	4	15.809 ± 0.007	16.639 ± 0.009	16.455 ± 0.008	16.159 ± 0.008
Sh 2-68	6	–	16.661 ± 0.014	16.451 ± 0.009	16.203 ± 0.016
SkAc 1	1	–	18.198 ± 0.008	18.480 ± 0.007	18.535 ± 0.014
SkAc 1	4	–	18.182 ± 0.008	18.504 ± 0.008	–
SkAc 1	6	–	18.196 ± 0.005	18.482 ± 0.006	18.590 ± 0.013
Ton 320	1	14.171 ± 0.010	15.371 ± 0.009	15.687 ± 0.008	16.073 ± 0.012
Ton 320	6	14.150 ± 0.005	15.355 ± 0.005	15.697 ± 0.005	16.035 ± 0.007
WDSH 1	1	–	–	–	17.428 ± 0.022
We 2-34	1	–	19.876 ± 0.023	19.833 ± 0.017	19.217 ± 0.015
We 2-34	6	–	19.881 ± 0.040	19.844 ± 0.042	–

TABLE B.1: Measured magnitudes of each object per night

for completeness, as this band is relatively immune to nebular contamination.

B.2.1 H 4-1

This is a low-metallicity PN belonging to the Galactic halo (Otsuka et al., 2003).

B.2.2 Na 1

Allen (1973) estimated a visual diameter of 10″. Kaler (1983) measured the integrated Hβ flux. The spectrum from Jones et al. (2009) indicates an optically-thin PN of

moderately-high excitation.

B.2.3 Sa 4-1

Discovered by Sanduleak (1983), this is an optically-thin PN of moderate excitation. The hydrogen-rich CSPN has been analysed by Feibelman (1987) and Feibelman & Bruhweiler (1989). The object was first picked up in the Palomar-Green Survey of hot blue stars, designated PG 1712+493. Zwitter & Munari (1994) confirmed its PN nature spectroscopically, and found a diameter of 10″. For the CSPN, they inferred $V - I = -0.17$ from the slope of the stellar continuum.

B.2.4 IC 3568

IC 3568 is the archetypal round, double-shelled PN (Harrington & Feibelman, 1983). The parameters of the CSPN were determined by Mendez et al. (1992). Owing to contamination from this bright nebula ($\log S_{\mathrm{H}\alpha} = -2.0$ erg cms^{-2} s^{-1}), photometry of the central star is difficult.

B.2.5 IC 4593

This is another high surface brightness PN ($\log S_{\mathrm{H}\alpha} = -1.7$), leading to nebular contamination of the stellar photometry. The central star has been extensively studied (see De Marco et al. (2007); Herald & Bianchi (2011); Bilíková et al. (2012)), and shows radial velocity variations now attributed to wind variability (Mendez et al., 1990; De Marco et al., 2003, 2007).

B.3 Photometric results for each night (SSO 2.3m)

In this Appendix, we present the individual photometric measurements for each object and each night in Table B.2.

Name	Night	U	B	V	I
Abell 48	n1	–	–	–	–
Abell 48	n2	–	–	–	–
Abell 48	n3	20.584 ± 0.084	19.627 ± 0.028	18.079 ± 0.019	15.654 ± 0.015
BMP J1808-1406	n1	–	–	–	–
BMP J1808-1406	n2	–	–	–	–
BMP J1808-1406	n3	–	19.117 ± 0.026	19.072 ± 0.019	18.804 ± 0.027
FP 1912-0331	n1	–	–	–	–
FP 1912-0331	n2	–	–	–	–
FP 1912-0331	n3	12.760 ± 0.009	13.860 ± 0.025	13.997 ± 0.016	14.259 ± 0.016
LoTr 8	n1	–	–	–	–
LoTr 8	n2	19.019 ± 0.031	18.920 ± 0.022	18.035 ± 0.021	–
LoTr 8	n3	–	18.916 ± 0.025	18.107 ± 0.017	–
PHR J1408-6106	n1	–	–	–	–
PHR J1408-6106	n2	–	–	–	–
PHR J1408-6106	n3	–	17.953 ± 0.026	16.982 ± 0.017	15.948 ± 0.011
PHR J1418-5144	n1	–	–	17.228 ± 0.007	–
PHR J1418-5144	n2	15.962 ± 0.021	17.125 ± 0.019	17.196 ± 0.015	17.350 ± 0.021
PHR J1418-5144	n3	–	17.115 ± 0.025	17.156 ± 0.017	17.303 ± 0.013
PHR J1432-6138	n1	–	–	–	–
PHR J1432-6138	n2	–	–	–	–
PHR J1432-6138	n3	–	19.067 ± 0.027	18.711 ± 0.019	17.704 ± 0.020
PHR J1510-6754	n1	–	–	–	–
PHR J1510-6754	n2	–	–	–	–
PHR J1510-6754	n3	15.283 ± 0.012	15.876 ± 0.028	15.662 ± 0.018	15.146 ± 0.015
HaTr 5	n1	–	–	16.566 ± 0.008	14.925 ± 0.005
HaTr 5	n2	18.667 ± 0.026	17.746 ± 0.021	16.541 ± 0.017	14.900 ± 0.021
HaTr 5	n3	–	–	–	–
K 1-22	n1	–	–	16.122 ± 0.007	15.578 ± 0.005
K 1-22	n2	14.877 ± 0.023	15.868 ± 0.022	15.908 ± 0.018	15.543 ± 0.024
K 1-22	n3	–	–	–	–
K 1-23	n1	–	–	18.706 ± 0.015	18.769 ± 0.013
K 1-23	n2	17.138 ± 0.024	18.175 ± 0.022	18.520 ± 0.019	18.718 ± 0.026
K 1-23	n3	–	18.408 ± 0.024	18.702 ± 0.018	18.990 ± 0.017
Lo 5	n1	–	–	16.993 ± 0.009	17.343 ± 0.008
Lo 5	n2	–	–	–	–
Lo 5	n3	15.388 ± 0.009	16.600 ± 0.023	16.939 ± 0.015	17.234 ± 0.011
MeWe 2-4	n1	–	–	–	–
MeWe 2-4	n2	–	–	–	–
MeWe 2-4	n3	–	17.682 ± 0.025	17.890 ± 0.017	17.944 ± 0.013
YM 16	n1	–	–	–	–
YM 16	n2	–	–	–	–
YM 16	n3	–	20.715 ± 0.053	20.252 ± 0.023	19.043 ± 0.041
RCW 69	n1	–	–	–	–
RCW 69	n2	–	–	–	–
RCW 69	n3	18.602 ± 0.022	19.403 ± 0.028	19.409 ± 0.020	18.945 ± 0.038
Sh 2-68	n1	–	–	–	–
Sh 2-68	n2	–	–	–	–
Sh 2-68	n3	–	16.522 ± 0.025	16.525 ± 0.020	16.163 ± 0.021
Sh 2-71	n1	–	–	20.455 ± 0.035	18.969 ± 0.037
Sh 2-71	n2	–	–	–	–
Sh 2-71	n3	–	–	–	–

TABLE B.2: Calibrated magnitudes obtained for each night for the targets observed during the SSO 2.3m run

Appendix C

C.1 Résumé de thèse en Français

Dans cet appendice, je présente un résumé de thèse en Français, en vertu des consignes pour la soumission de thèses en Cotutelle à l'Université de Montpellier 2.

C.1.1 Contexte

Scénario actuel de formation des nébuleuses planétaires

Les nébuleuses planétaires sont le résidu de l'évolution d'étoiles de masses 1-8 $M_{\odot}$. A la fin de leur vie sur la séquence principale, les étoiles de 1-8 $M_{\odot}$commencent l'ascencion de la branche des géantes rouges, au cours de laquelle leur enveloppe s'étend et leur temperature efficace diminue. La convection devient le mecanisme de transport d'énergie dominant au sein de l'étoile et les produits issus de la fusion de l'hydrogène sont transportés à la surface : c'est le premier dredge-up. Quand la température dans le noyau atteint 10^8 K, la fusion de l'hélium commence grace à la réaction triple α, par un flash en milieu dégénéré pour les étoiles de masse > 1.8 $M_{\odot}$, ou de manière plus progressive pour les étoiles plus massives. La phase de fusion de l'hélium dure environ 10% de la phase de fusion de l'hydrogène, après quoi la majorité de l'hélium est consumé. Le noyau s'effondre de nouveau sur lui-même et l'atmosphère de l'étoile refroidit et s'étend une fois de plus pour atteindre un rayon d'environ 300 $R_{\odot}$. L'étoile entame sa phase de géante rouge asymptotique (AGB). Une fois de plus, les boucles convectives transportent à la surface les produits des réactions de fusion nucléaire à la surface, carbone et

azote. C'est le second dredge-up qui se produit à la base de la phase AGB. L'apparition de pulses thermiques, une succession d'épisodes de fusion de l'hélium résiduel dans le noyau et de fusion de l'hydrogène dans une couche entourant le noyau, marque la fin de la phase AGB de l'étoile. Après ∼10-20 pulses, la métallicité de l'étoile est à nouveau altérée : c'est le troisième dredge-up. À la fin de la phase AGB, l'enveloppe est moins gravitationnellement liée au noyau et une phase de perte de masse débute. La phase de vents stellaires se divise en deux régimes : une phase où les pulsations dominent puis une phase où la pression de radiation exercée sur les grains nouvellement formés intensifie la perte de masse. Tandis que l'enveloppe continue de perdre de la masse, la photospère est de plus en plus profonde et l'étoile paraît de plus en plus chaude. Dans la phase finale de perte de masse, les vents atteignent des vitesses 10 fois plus élevées que précédemment. A ce stade l'étoile est désormais ce qui fut le noyau de son progéniteur et est appelée étoile post-AGB. Quand la photosphère atteint une température de 30,000K, le rayonnement thermique émis est assez dur pour ioniser la nébuleuse entourant le noyau, qui n'est autre que l'enveloppe stellaire une fois éjectée. Dès lors, la nébuleuse rayonne, majoritairement par émission dans les raies interdites. Elle porte le nom de nébuleuse planétaire.

Le problème des morphologies

Environ 80% des NP sont non-shériques. Une fraction aussi importante est inattendue, si l'on considère que les NP proviennent d'étoiles post-AGB qui sont quasi-sphériques. Les formes obtenues sont elliptiques, bipolaires ou irrégulières, et présentent des traits particuliers tels que jets, ondes de chocs et noyaux excentrés. Il n'existe pas, à l'heure actuelle, de scénario permettant d'expliquer ces morphologies. La première hypothèse émise fut celle de la présence de champs magnétiques mettant en forme la nébuleuse au moment de la phase de perte de masse à la fin de la phase AGB. En utilisant ce scénario, de nombreuses simulations parvinrent à recréer les morphologies observées. En parallèle, des observations venaient annoncer l'existence de champs magnétiques dans les NNP.

Cependant, dans tous les modèles décrits précédemment, la perturbation à l'origine

de la perte de masse asymmétrique – la surdensité équatoriale ou le champs magnétique lui-même, était contrainte par le modèle, et non un résultat de ce dernier. Deux études se reposant sur des considérations énergétiques et de moment cinétique annoncèrent que le couplage entre rotation et champs magnétiques conduisait le champ magnétique à disparaître en un temps bien inférieur à celui nécessaire pour permettre la mise en forme de la nébuleuse. Sans un mécanisme particulier pour ré-alimenter la rotation différentielle dans les couches intérieures de l'étoile et ainsi maintenir la dynamo stellaire, ce mécanisme de formation n'était pas viable. Observationnellement, d'autres observations furent conduites dans le but mesurer le champ magnétique des NNP mais sans succès, tandis que pendant ce temps, la première équipe à avoir détecté ces champs annonça que leurs détections étaient une fausse alerte.

L'Hypothèse Binaire

Si l'on met à l'écart un instant l'hypothèse des champs magnétiques, l'explication la plus simple pour justifer des ruptures de symétries dans les formes des NP est la présence d'un compagnon orbitant le noyau. Cette fois-ci, c'est le companion qui fournit l'énergie et le moment cinétique nécéssaires à la mise en forme de la NP au moment de la perte de masse à la fin de la phase AGB. Plus le compagnon est proche du noyau, plus il va affecter le mécanisme de mise en forme de la nébuleuse. Le continuum de séparations disponibles permet d'exliquer la grande variété de formes observées. A partir d'une séparation de 100 AU, il est attendu que la présence du compagnon l'agent principal de la mise en forme de la nébuleuse. Le champ magnétique ne joue plus de rôle, ou seulement un rôle mineur : il est qualifié d'agent secondaire si l'échange de moment cinétique entre le compagnon et le NNP permet de ré-alimenter la dynamo stellaire et permet l'action du champ magnétique.

L'Hypothèse Binaire consiste à postuler que les 80% de NP non-sphériques sont issues de noyaux binaires en interaction. Cela équivaut à postuler que la majorité des NP observées sont formées par seulement 10-15% des progéniteurs considérés comme viable dans la paradigme de formation actuel. Le reste des étoiles de 1-8 $M_{\odot}$forment des NP sous-lumineuses ou pas de NP du tout. Pour tester cette hypothèse, un diagnostic

s'impose de lui-même : mesurer la fraction binaire de nébuleuses planétaires. Après estimation de ce nombre et comparaison avec la fraction de binaire pour la population progénitrice dans la séquence principale : soit les deux nombres sont égaux, auquel cas le paradigme actuel de formation est cohérent; soit la fraction binaire de NP est plus élevée que celle de la population mère, auquel cas la présence d'un compagnon autour du noyau favorise la formation des NP et, ainsi, l'Hypothèse Binaire est un scénario envisageable.

Dans les pages qui suivent, trois methodes vont être présentées permettant de détecter des NNP binaires, ainsi que leur potentiel pour estimer la fraction binaire de NNP.

C.2 La technique d'excès infrarouge

La technique d'excès infrarouge consiste à comparer les couleurs intrinsèques d'un NNP avec celles observées. Si le noyau est plus rouge que les couleurs attendues pour une étoile simple, cela indique la possibilité que l'éxcès infrarouge vienne de l'émission thermique d'un compagnon. La difficulté de cette technique est bien évidemment que les noyaux sont brillants ce qui rend la détection de compagnons sur la séquence principale difficile. Cette technique n'est pas nouvelle. Elle a été utilisée dans plusieurs études pour détecter de nouveaux noyaux binaires et même estimer la fraction binaire de NNP. Des excès infrarouges ont été détectés pour 9 NNP dont l'origine stellaire est presque certaine, cependant comparé au nombre d'objets sondés, ce taux de détection est faible. Comme indiqué dans ces études, la difficulté de cette technique réside dans un certain nombre de particularités qui, combinées, rendent les détections difficiles, notamment la nécessité d'un excès important ou d'une précision photométrique excellente pour être détecté, la nécessité de savoir connaissances précédant l'observation des sources concernées, la nécéssité de la connaissance du rougissement interstellaire ou de photométrie optique pour déterminer le rougissement, la faible luminosité des compagnons à observer qui, outre la complexité de détection, ajoute un biais à notre population de compagnons détectés.

C.2.1 La méthode de détection d'excès infrarouge

La détermination d'une méthode implique trois choix pour répondre aux difficultés soulevées par les études précédentes, et pour établir la stratégie la plus adéquate pour déterminer la fraction de NP binaires : une méthode pour déterminer le rougissement interstellaire, le choix d'un intervalle spectral approprié et le calcul de l'excès et l'erreur sur l'excès. Pour le rougissment interstellaire, plusieurs techniques sont disponibles : la mesure du décrément de Balmer dans la nébuleuse, l'utilisation de cartes de poussières interstellaires ou le choix d'une courbe d'extinction paramétrée. Nous avons adopté cette dernière option en utilisant une loi de Cardelli et al. (1989) avec R_V=3.1. L'extinction est déterminée par la couleur $B-V$ car ces deux bandes sont les plus immunes à la contamination par un compagnon froid.

L'intervalle spectral idéal est déterminé par la bande dans laquelle les chances de détection d'un compagnon froid sont maximales, tandis que les chances de contamination par de la poussière chaude sont minimales. Les bandes H et K son sensibles à la fois à l'émission thermique d'un compagnon et à l'émission thermique de poussière chaude. La bande J offre un bon compromis entre ces deux signaux. La bande I est moins sensible que J, et elle est immune à la contamination par la poussière. La bande J est spectralement idéale pour notre étude, cependant cela implique la nécéssité d'observations dans l'infrarouge. Cette difficulté peut-être contournée par l'utilisation de données archivées de sondages en ligne, notamment DENIS, 2MASS et UKIDSS. La bande I, elle dans le domaine optique, peut-être acquise en même temps que les bandes B et V nécéssaires pour la mesure du rougissement interstellaire, permettant l'extraction de résultats grace à l'analyse d'une seule série d'observations. Nous retenons donc, pour leurs avantages respectifs, les bandes I et J pour déterminer l'excès infrarouge.

L'excès infrarouge lui-même n'est autre que la différence de couleur $V-I$ ($V-J$) entre les couleurs théoriques de l'étoile observée et les couleurs dérougies observées. Les couleurs théoriques sont obtenues par la connaissance a priori de la température de l'étoile observée, à partir de laquelle est lue une grille de couleur construite pour les NNP sur la branches des naines blanches. L'erreur sur cette couleur est la suivante :

si l'étoile a été observée une fois, l'erreur dans chaque bande est la somme de l'erreur photométrique et de calibration, et l'erreur sur la différence est la somme quadratique des erreurs dans chaque couleur. Si l'objet a été observé plusieurs fois, l'erreur est estimée par l'écart type sur les magnitudes pondéré par l'erreur sur chaque époque. Si la différence de couleur $V - I$ ($V - J$) est plus grande (strictement) que l'erreur sur la couleur, alors nous retenons une détection et un type spectral est déterminé pour le compagnon. Sinon un limite supérieure pour le type spectral d'un éventuel compagnon est estimée.

C.2.2 L'échantillon de Frew (2008)

Pour pouvoir estimer la fraction binaire de NNP, il convient de contrôler au maximum les biais intrinsèques non-seulement à la méthode mais aussi à l'échantillon de population étudiée. Pour ce faire, une bonne connaissance de l'échantillon est nécéssaire. Frew (2008) a construit un échantillon limité en volume jusqu'à approximativement 3 kpc. Pour la majorité des NNP inclus dans cet échantillon (∼400), la distance a été déterminée grace à une nouvelle relation distance-luminosité Hα. De plus, les classifications morphologiques, rougissements, masses ionisées, diamètres, ges cinématiques et vitesse d'expansion ont répertoriées en utilisant la litérature disponible sur ces objets.

Outre le nombre de connaissances rassemblées pour chaque NP dans le catalogue de Frew (2008), l'avantage majeur de cet echantillon est la complétion en volume, c'est-à-dire la forte probabilité pour que le catalogue contienne presque tous les objets existants dans un rayon de 2kpc. Cela permet d'utiliser une liste de cibles à observer représentative de la population du voisinage solaire, i.e. une population la moins biaisée possible.

Notre stratégie de précision a été établie et testée sur des étoiles synthétiques. En utilisant l'échantillon de Frew (2008), nous pouvons constituer un échantillon de cibles à observer pour determiner la fraction de NNP binaires.

C.2.3 Critères de sélection

En dépit de la nécessité d'un échantillon complet et représentatif de la Galaxie, tous les NNP ne sont pas observables. Nous avons exclu l'observation de NNP entourés d'une nébuleuse brillante, notamment la majorité des catalogues IC et NGC, et selectionné les nébuleuses âgées, peu lumineuses et étendues, qui ne sont pas problématiques lors de la soustraction de l'arrière-plan lors de l'étape de photométrie sur les noyaux. Nous avons aussi sélectionné les noyaux avec une magnitude $M_V > 5$ pour éviter les étoiles intrinsèquement trop brillantes ainsi que sujettes à des variations photométriques dues à la présence de vents stellaires.

C.3 Excès infrarouge : analyse des observations

C.3.1 Les observations du 2.1m de l'observatoire de Kitt Peak

Des observations ont été menées dans le but d'enrichir l'échantillon de 25 objets obtenus par De Marco et al. (2013) avec la procédure décrite dans les paragraphes précédents. Une vingtaine d'objets ont été observés en Mars 2011 à l'Observatoire de Kitt Peak sur le télescope de 2.1m. Seules les données obtenues en temps photométrique ont été retenues. Les images prises dans les bandes B, V et I ont été corrigées pour l'illumination à l'aide de *flats* de dômes. La calibration a été effectuée grace à l'observation de standards photometriques équatoriaux observés en alternance avec les NP ciblées, en résolvant le système photométrique suivant un algorithme des moindres cqrrés.

Les magnitudes calibrées ont été obtenues dans les bandes B, V, I et pour quelques objets dans la bande U à l'aide du package de photométrie de `DAOPHOT`. Un certain nombre de vérifications ont été réalisés pour s'assurer de la cohérence des résultats obtenus : les magnitudes calibrées ont été obtenues et comparées en faisant varier les paramètres d'entrée de `DAOPHOT`, notamment la fonction d'ajustement de la PSF et les régions d'ajustement et d'intégration du flux pour chaque étoile. Une vérification du rougissement a été faite en comparant les valeurs obtenues avec les couleurs $B - V$

et $U - B$ quand cette dernière était disponible. Enfin les magnitudes des objects en commun entre ces observations et celles obtenues par De Marco et al. (2013) ont été comparées. Tous ces tests se sont avérés concluants et ont prouvé la solidité de notre routine de photométrie et de notre approche statistique. Une série d'objets à la limite de nos critères de sélection a été observée et, lorsque leur étude s'est avérée non-conclusive, ont été rejetés.

Une fois les magnitudes obtenues, les différences de couleur en $V-I$ ont été obtenues pour un total de 16 objets. Nous reportons la détection de 5 excès infrarouge de NNP et une détection pour une mimique de NP. Les magnitudes dans la bande J disponibles dans la literature ont aussi été utilisées. Nous détectons 4 excès infrarouge dans notre échantillon de 9 objets. Les types spectraux et limites de type spectraux trouvés sont tous en accord : la bande J vient confirmer ou contraindre d'avantage les limites déterminées dans la bande I. Les types spectraux des détections sont similaires dans les bandes I et J, et avec les excès infrarouges détectés auparavant, dans une marge de 1-2 sous type spectraux.

C.3.2 Les observations du 2.3m de l'observatoire de Siding Spring

Les observations pour cette étude ont été menées sur le télescope de 2.3m à l'observatoire de Siding Spring en May 2012. Le dispositif instrumental était similaire à celui utilisé pour les observations à l'observatoire de Kitt Peak. Des images ont été obtenues pour $\sim$20 objets dans les bandes B, V et I. Les réduction et calibration des ces données ont été similaires à celles des observations de Kitt Peak si ce n'est que des *flats* de ciels ont été utilisés, plutôt que des *flats* de dôme.

La determination des couleurs des objets observés a révélé 8 détections dans notre échantillon de 16 objets observés dans la bande I. Des données pour 3 objets ont été récupérées d'archives de sondages en ligne et ont permis la détection de 2 excès infrarouges. La comparaison du type spectral pour un des objets obtenus dans les bandes I et J est en accord avec le types spectral du compagnon résolu par Hubble et

détecté par un étude indépendante dans une marge de 1 sous type spectral.

C.4 Excès infrarouge : exploitation des archives de sondages

Dans la section précédente nous avons vu que des observations dédiées à l'analyse d'une quinzaine d'objets à la fois était une méthode fiable. Cependant, pour atteindre une taille d'échantillon statistiquement significative de 100-150 objets, cette approche est relativement lente et requiert une quantité importante d'observations et d'analyse. La qualité des sondages optiques et infrarouge proche les plus récents semblent avoir une précision photométrique et une couverture spatiale suffisante pour offrir la possibilité d'analyses d' échantillons de grandes tailles et éventuellement offrir l'opportunité statistique de déterminer la fraction binaire de NNP. C'est ce que nous avons tenté de réaliser grace à l'analyse de données SDSS DR7 adjointes à l'échantillon de Frew (2008). Une deuxième tentative d'analyse d'échantillons de grande taille, l'analyse du catalogue étendu de Frew (2008), a fourni quelques résultats additionnels.

C.4.1 Détections d'excès infrarouge à l'aide de donnéees SDSS DR7

Estimation des capacités des données SDSS DR7 pour la détection d'excès infrarouge

Afin d'estimer si cette stratégie était viable, nous avons utilisé les données SDSS pour les objets issus de nos propres observations. Les magnitudes ont été récupérées grace au gestionnaire d'archive `VIZIER`. Le rougissement a été déterminé à partir de la couleur $g-r$. Les magnitudes ont été affectées de corrections photométriques pour compenser des valeurs estimées a posteriori légèrement érronées lors de la calibration des données SDSS DR7. Les couleurs théoriques pour les NP ont été obtenues en utilisant des spectres synthétiques pour ces étoiles convolués avec les bandes passantes des spectres u, g, r, i and z.

Nous avons ensuite appliqué la méthode pour calculer la différence de couleur $g - z$ pour les 15 objets étudiés dans nos précédents échantillons et aussi présents dans les archives SDSS DR7. Les 3 excès infrarouges détectés précédemment dans cet échantillon ont été retrouvés avec une très bonne cohérence de 2 sous types spectraux. Certains objets ont présenté un léger "déficit de rouge" correspondant à une estimation imprécise du rougissement due à des imprécisions sur les corrections de calibration mentionnées précédemment, propagées lors de la détermination de la différence de couleur. Néanmoins, nous avons conclu que les données SDSS DR7 étaient utilisables pour détecter des excès infrarouges dans les NNP et avons étendu notre analyse à tous les objets présents dans le catalogue de Frew (2008) et SDSS DR7.

Utilisation des données SDSS DR7 pour la détection de nouveaux excès infrarouges

La stratégie décrite ci-dessus a été appliquée à tous les objets en commun entre le catalogue de Frew (2008) et les données SDSS DR7, soit 27 objets. Une dizaine d'objets ont présenté des couleurs trop bleues pour pouvoir être interprétées comme erreur due à des imprécisions photométriques, la cause de ces erreurs étant majoritairement la contamination par une nébuleuse brillante, des images saturées ou au contraire sous-lumineuses, ou des incohérences de magnitudes d'un filtre à l'autre. En effet, contrairement à l'analyse de nos observations, l'échantillon analysé ici n'a bénéficié d'aucune sélection et tous les NNP ont été retenus. La qualité des résultats s'en voit affecté immédiatement. D'autres objets ont présenté des couleurs trop bleues interprétables comme conséquence de l'incertitude sur la calibration des magnitudes. Enfin pour quelques objets, des limites de type spectraux de compagnons ont été déterminés, et 4 nouveaux excès infrarouges ont été détectés et nécessitent confirmation.

C.4.2 Détections d'excès infrarouge à l'aide du catalogue étendu de Frew (2008)

Avec cette même intention d'exploiter des échantillons de grande taille, nous avons cherché des excès infrarouge dans le catalogue étendu de Frew (2008). Le catalogue est constitué des magnitudes disponibles dans la littérature pour les objets du calalogue de Frew (2008). Les magnitudes proviennent des archives de surveys disponibles en ligne (APASS, UCAC4, DENIS, 2MASS, UKIDSS) ou d'études spécifiques des objets en question. Pour tous ces objets, une sélection et vérification minitieuse des magnitudes a été appliquée. Cette étude a été pensée en pariant sur le fait que la vérification systématique des magnitudes pouvait compenser l'hétérogénéité des données rassemblées. Comme pour préparer une série d'observations, les critères de sélection décrits précédemment ont été appliqués pour exclure les objets non-analysable avec notre technique. De plus, seulement les objets pour lesquels les magnitudes dans les bandes B, V et I ou J ont été analysés, par design de notre technique. Aucune sélection n'a été faite sur la distance des objets car, dû aux critères de sélection appliqués, l'échantillon ne pouvait plus être complet en volume ; nous avons donc préféré maximiser les chances de détection avec un échantillon le plus large possible plutôt que d'approcher la complétion de l'échantillon.

Les rougissements obtenus grace à la couleur $B - V$ ont été comparés aux limites supérieures obtenues grace aux cartes de poussière Galactique. Comme décrit précédemment, les différences de couleur ont été calculées pour les 16 objets qui ont passé les critères de sélection, tandis que l'échantillon original comportait près de 1000 objets. Aucune détection n'est obtenue dans la bande I. Nous détectons 2 excès infrarouge correspondant à des compagnons froids et 3 excès infrarouge correspondant à des compagnons géants. Un tel biais est attendu dans un échantillon limité en luminosité comme celui-ci, où les compagnons les plus brillants sont détectés favorablement.

Contrairement à nos attentes, l'analyse d'échantillon de grande taille ne permet pas de pouvoir estimer la fraction binaire de NNP. Le pouvoir statistique des échantillons de grande taille est amenuisé par la sélection des objets analysables selon les critères

nécessaires au bon fonctionnement de notre méthode. Plusieurs excès infrarouges ont été détectés, mais nous ne les ajoutons pas à notre échantillon stastistique pour déterminer la fraction binaire. Nous les notons pour de futures obervations.

C.5 La technique de variabilité photométrique

La technique de variabilité photométrique consiste à observer une cible au cours du temps dans une bande donnée et à chercher des variations périodiques de flux. Trois processus peuvent être à l'origine de variabilité photométrique pour une NNP possédant un compagnon : l'effet d'illumination du primaire chaud et brillant sur le compagnon froid, les déformations ellipsodales dues aux forces de marées et les éclipses. Cette technique est simple à mettre en œuvre. Cependant, l'analyse des données et l'adjustement des courbes de lumière pour déterminer les paramètres orbitaux du système sont délicates, dû à la dégénérescence des solutions possibles. Cette méthode est biaisée vers les systèmes de petites séparations puisque l'intensité des trois processus augmente à mesure que la période décroît. Cette méthode n'est donc pas adaptée à la détermination de la fraction binaire, mais elle permet la détection potentielle de nouveaux NNP binaires.

Deux études mettant en jeu l'analyse d'une quarantaine d'objets permettent de déterminer une fraction de binaire post enveloppe commune de 10-20%, systèmes de périodes entre un jour et deux semaines. Des efforts sont mis en œuvre pour observer et modéliser le plus d'objets possibles de l'échantillon de Frew (2008) pour caractériser la population post enveloppe commune du voisinage solaire.

Nous avons tenté de construire les courbes de lumière de certaines de nos cibles lorsque le temps n'était pas photométrique lors de nos observations. Les courbes de lumières pour 20 objets ont été obtenus dans les bandes V et I lors de nos observations à l'observatoire de Kitt Peak. En dépit d'un échantillonnage faible, nous utilisons une technique visuelle et une technique statistique pour détecter des dispersions remarquables dans nos courbes de lumière. Les deux techniques sont en bon accord avec seulement deux objets en désaccord. Nous détectons 60% d'étoiles variables dans notre

échantillon, un nombre élevé comparé aux 10-20% attendus. Quatre courbes de lumière semblent présenter des variations périodiques.

Six NNP ont été obervées par le satellite Kepler. La modélisation des courbes de lumière obtenues avec une précision jamais atteinte auparavant est d'autant plus délicate. Cependant, il a été estimé que deux d'entre elles présentent des variabilités périodiques associables à la présence de compagnons. Un autre noyau est en rotation rapide, probablement consequence d'une coalescence de binaire passée. Un noyau semble présenter des variations caractéristiques des variables cataclysmiques. Les deux derniers noyaux ne présentent pas de variations de flux et sont entourés de NP sphériques.

C.6 La technique de variabilité de la vitesse radiale

La technique de variabilité de la vitesse radiale consiste à détecter l'effet Doppler dû aux oscillations du primaire autour du centre de masse du système créées par la présence du compagnon. Une série d'études consacrées à la détection de NNP grace à cette technique révèle que la méthode est difficile à mettre en œuvre pour détecter des compagnons. Le taux de détection des différentes études diffère en fonction du dispositif d'observation. Toutes les études ont en commun l'absence de confirmation de périodicité lorsqu'une variabilité de vitesse radiale a été détectée.

Nous avons tenté de détecter la signature Doppler de la présence d'un compagnon à travers l'analyse d'un mini-sondage de 14 objets observés avec le spectrographe UVES au VLT en Août 2008. Chaque objet a été observé à trois époques différentes. Nous avons cross-correllé les trois époques entre elles pour chercher un décalage Doppler remarquable. Le rapport signal à bruit de nos spectres était faible dû aux mauvaises conditions d' observations. Aucune corrélation ne révèle l'existence d'un décalage remarquable sauf pour un de nos objets, cependant le décalage Doppler n'est détecté que pour une cross-corrélation entre deux époques et n'est pas visible dans les autres corrélations pour cet objet.

Cinq spectres comportaient des éléments particuliers : un objet a été classifié comme

nouvelle étoile PG1159, quatre autres objets présentaient des spectres d'étoiles trop froide pour pouvoir ioniser la nébuleuse. L'un d'eux a été classifié binaire spectroscopique après résultat des cross-corrélations entre les différentes époques, le spectre est en fait celui du compagnon, le spectre du noyau est invisible mais sa signature Doppler a été détectée. Un autre a vu son type spectral être estimé G8IV sans trace de la présence du noyau, cependant il reste à confirmer que cette étoile est bien celle qui, dans le champ, correspond au noyau de la NP. Les deux autres étoiles froides sont des étoiles de champ, et non les noyaux contrairement à ce qu'indiquait l'état des connaissances au moment des observations.

C.7 La fraction binaire de NNP

Nous avons estimé le pouvoir de détection et l'importance statistique de trois différentes méthodes pour estimer la fraction binaire de NNP : la détection d'excès infrarouge, grace à l'utilisation de données obtenues lors d'observations dédiées, et grace aux données des archives de sondage disponible en ligne, la détection de variabilité photométrique et la détection de variabilité de vitesse radiale. De ces trois méthodes, seulement la détection d'excès infrarouge à partir d'observations dédiées peut permettre un traitement statistique adapté à la détermination de la fraction binaire de NNP.

Nous avons construit notre échantillon en rassemblant ceux analysés à partir des données du 2.1m de l'observatoire de Kitt Peak et des données du 2.3m de l'observatoire de Siding Spring. L'échantillon analysé par De Marco et al. (2013) a aussi été ajouté. Nous obtenons les taux de détections suivants : dans la bande I, 20 excès infrarouge ont été détectés sur un échantillon de 49 NNP, soit un taux de détection de 41%. Dans la bande J ce taux est de 55%, 11 détections sur un échantillon de 20 NNP. Le fait que le taux de détection soit plus haut dans la bande J est attendu, cela est dû à ses meilleures capacités de détection de compagnons froids. L'erreur sur ces taux est estimée en utilisant l'intervalle de Wald avec un degré de confidence de 95%. Les taux de détection sont donc 41 ± 14 pourcents dans la bande I et 55 ± 22 pourcents dans la bande J.

Pour obtenir la fraction binaire de NNP et la comparer à celle de la population progénitrice, ces taux doivent être débiaisés : les compagnons non détectables avec notre méthode doivent être ajoutés, soit parce qu'ils ne sont pas assez brillants, soit parce qu'ils sont résolus à partir du sol et que, par conception, notre méthode exclut les systèmes résolus. Doivent aussi être exclus les systèmes qui forment une enveloppe commune lors de la phase géante rouge du primaire. Nous estimons notre limite de détection en type spectral être M3V dans la bande I et M4V dans la bande J. Nous utilisons ensuite la distribution des types spectraux des binaires de la séquence principale pour corriger notre population des compagnons moins lumineux que M3V/M4V. En incluant des compagnons de tout types spectraux, nous trouvons une fraction binaire de 58 ± 17 pourcents dans la bande I et 68 ± 23 pourcents dans la bande J. Pour corriger des compagnons résolus, nous estimons la distance médiane de notre échantillon et considérons la séparation sur nos images à partir de laquelle deux étoiles avec une différence de magnitude de 2 sont résolues. Nous trouvons 2 arcsec, le tiers de notre seeing moyen. En appliquant ce même rapport aux données de 2MASS pour les images dans la bande J, nous trouvons une séparation de 2.8 arcsec. Cela nous permet d'obtenir la distance à partir de laquelle un primaire et son secondaire seraient résolus. En utilisant cette information et la distribution des périodes pour la séquence principale, nous pouvons ajouter la fraction de système résolus qui n'a pas pu être détectée avec notre méthode. Nous trouvons une fraction binaire totale de 73 ± 22 pourcents dans la bande I et 91 ± 31 pourcents dans la bande J.

Plusieurs observations peuvent être faites à propos de ces résultats. La première est qu'une fois débiaisée, la fraction binaire de NNP ne devrait pas dépendre des bandes dans laquelle les données ont été obtenues, et donc ces deux nombres devraient être égaux. Il est à parier qu'un plus grand échantillon permettra d'amener ces deux nombres en accord. La deuxième obervation est que ces nombres peuvent être comparés à la fraction équivalente pour la population progénitrice, i.e. la séquence principale. En excluant les systèmes qui forment une enveloppe commune sur la branche géante rouge, la fraction binaire est de 45 pourcents plus ou moins quatre pour cents. Bien que les barres d'erreurs soient encore larges, cela semble indiquée significativement que

la fraction de binaires dans la population de NNP est plus élevée. Pour que cette conclusion prometteuse soit avérée, nous estimons qu'une taille d'échantillon d'environ 100-150 objets est nécessaire. Enfin, nous testons si, dans notre échantillon, la nature du noyau implique une rupture de la sphéricité ou non, mais ne trouvons aucune preuve statistiquement significative d'un tel lien causal.

Appendix D

D.1 SSO 2.3m observing run proposal

Here we present the proposal that has been written to access the SSO 2.3m to obtain B, V and I data for our sample. The observing time has been granted, and the analysis of the data is presented in Section

2.3.

RSAA Time Assignment Committee

Research School of Astronomy & Astrophysics
Cotter Rd, Weston Creek 2611 **Email: tacinfo@mso.anu.edu.au**

1. **Names and Institutions of Applicants**

	Observer	Student
Douchin D Mr (Macquarie University)	no	yes
Parker Q Prof (AAO / Macquarie University)	yes	no
De Marco O Ass. Prof (Macquarie University)	yes	no
Frew DJ Dr (Macquarie University)	no	no

Principal Contact: Dimitri Douchin
Telephone: +33 4 67 14 34 15
Fax:
Email: dimitri.douchin@mq.edu.au

Postal Address:
Laboratoire Univers et Particules de Montpellier (LUPM) UMR 5299 - CC72 Universit Montpellier 2 Place Eugne Bataillon 34 095 Montpellier Cedex 5 FRANCE

Name of Student Supervisor(s): Orsola De Marco

3. **Title of Project**

2. **Quarter** May-Jul

Estimating the fraction of binary planetary nebula central stars using infrared excess

Summary of Scientific Objectives

80% of planetary nebulae (PNe) show asymmetric shapes. The most plausible explanation of these shapes is the presence of a companion around the central star of the PN (CSPN). This paradigm can be tested by estimating the binary fraction of CSPNe: if the observed binary fraction was much bigger that the expected one (40%) this would support that most PNe come from binary stars. To estimate this fraction, we look for binaries among the closest PNe from us. We aim to detect the infrared excess on the CSPN SED due to the companion, hence the need for absolute photometry in the BVI(JH) bands. So far, a binary fraction of $19-42\%$ has been determined. In June 2011, J and H band images of 15 CSPNe were taken to enlarge our sample's size. We need the BVI counterpart of the J, H set already in hand.

4. **Telescope, Instrument and Detector**

Telescope:	Instrument(s):	Gratings/Filters:
2.3m	Imager	BVI

5. **Scheduling Information**

Number of nights requested *this quarter*	Dark:		Grey:		Bright:	3	If grey, is 1st or 3rd qrt preferred
Minimum useful allocation	Dark:		Grey:		Bright:	1	
Additional nights required to to complete project in future	Dark:		Grey:		Bright:		

Preferred dates:	May, 1-15 June
Impossible dates: *(Give reasons)*	15 June-July No observers are available
Special scheduling constraints *(eg lunar position)*	
Remote Observing from MSO: **(WiFeS Only)**	Yes [ ] No [X]

6. **Observing Requirements**

Average signal-to-noise ratio required:	100
Any seeing limitations:	Photometric conditions are required.
Required spectra resolution (if applicable):	
Range in Brightness/ Surface Brightness:	15-20

7. **Assistance Required (only available during day-time)**

8. **A short description of your project for the public.**

When they die, stars like the Sun explode and create objects that are called planetary nebulae. These nebulae are not spherical, contrary to what can be expected from the explosion of a star that is spherical. One hypothesis that could explain these shapes is that there would be not one but two stars in the center. The goal of our observation tonight is to determine how frequent these binary stars are.

9. **List of Principal Targets** (a representative list)

Name	α	δ	mag	Comment
PHR1553-5738	15 53 10.00	-57 38 06.8	15.84	
PHR1602-4127	16 02 18.13	-41 26 49.5	15.8	
IC 5148/50	21 59 35.13	-39 23 08.1	16.16	
Abell 65	19 46 34.20	-23 08 12.9	15.60	
FP1824-0319	18 24 40.88	-03 19 59.6	14.92	
HaWe 13	19 31 07.20	-03 42 31.5	16.90	

10. **Other applications for observing time for this project in this quarter**

Telescope/satellite:	Title of programme: *(include applications from all telescopes)*
AAT 4m Service Time	Estimating the binary fraction of planetary nebula central stars

11. **Report on previous applications for time for this and related projects**.

Show all allocations for RSAA time in past 3 years

RSAA Reference (give # if known)	Allocation	% useful	Publications (or Comments)

12. **Scientific Justification:** Attach a case of no more than 2 pages, in a font no smaller than 11pt.

Scientific and Technical Justification

The PN binary hypothesis. We currently understand planetary nebulae (PNe) as gas ejected by intermediate mass stars (1-8 $M_{\odot}$) just before they become white dwarfs (WD). A high 80% of all PNe have elliptical and bipolar shapes, often containing complex substructures such as bubbles and jets. These shapes are traditionally explained by the action of rotation and magnetic fields during the mass-losing asymptotic giant branch (AGB) progenitor phase (e.g., Garcia-Segura et al. 1999) and in a *f*ew cases, binary interactions. However, Soker (2006) and Nordhaus et al. (2006) showed that rotation and global magnetic fields are unlikely to be sustained in single AGB stars for long enough to impart the observed shapes. These theoretical considerations, together with a host of observational conundrums, such as outflow momenta 1000 times larger than can be explained by radiation pressure on dust (Bujarrabal et al. 2001), have left binary interactions as the most plausible mechanism for the explanation of a large majority of all PNe (for a review see De Marco 2009).

The prediction. The best way to test the extent to which binarity is responsible for the PN phenomenon is to determine the central star of PN (CSPN) binary fraction and period distribution. The prediction of the current scenario for the formation of PNe is that 40% of all CSPNe should be in binaries with cool companions hotter than M9V, and with separation smaller than ∼500 AU (i.e, unresolved from the ground; Duquennoy & Mayor 1991, Han et al. 1995). If PNe are preferentially a binary phenomenon, then we expect the fraction to be substantially larger and as large as the fraction of PN with a non-spherical morphology ($\lesssim 80\%$) and their orbital separations to be smaller than ∼10-15AU.

In the binary scenario, single stars and very wide binaries make spherical PN, or make no PN at all. Such *n*aked central stars are would transit between the AGB and the WD domain with no PN or a very under-luminous PN (Subag & Soker 2005, Moe and De Marco 2006).

The known binary CSPN. The most successful survey technique to date to find binary CSPNe has been photometric variability able to detect close binaries due to irradiation of the cool companion by the hot CSPN, ellipsoidal variability or eclipses. These surveys have revealed that 15-20% of all CSPNe have companions with P $\lesssim$ few days (Miszalski et al. 2009), but they are biassed to periods smaller than about 2 weeks (De Marco et al. 2008). Radial velocity surveys are not a good way to search for binaries because of the pervasive wind variability found in all but the very faintest CSPNe that causes spectral variability scrambling even strong binary signal (De Marco et al. 2004, 2007). We have no knowledge of intermediate period binaries.

Preliminary results. The period distribution of CSPN binaries may for now be out of reach since intermediate mass-binaries, close enough to have shaped their PN but with periods longer than 2 weeks will not be apparent in current binary surveys. However, we can determine the actual overall binary fractions and test whether it is larger than predicted by current PN making scenarios. We have therefore used the NOAO 2.1 m telescope to look for I-band excess that would reveal the presence of a cool companion to the CSPN down to spectral type ∼M5V. The results have been extremely promising: we found that 19-42% of the CSPNe observed (5-11 out of 26) have an I-band excess at the 3-2σ level indicating the presence of cool companions. This number is a strict lower limit. The J band is far more sensitive to detect fainter companions and obtain a more complete fraction. Frew (2008) used the 2MASS and DENIS databases to carry out a similar investigation using the more sensitive J band; his results were in line with our I-band excess findings, showing that 53% of the only 34 objects that have a J-band excess down to ∼M6-7V (at the 2σ level). Combining these results and de-biasing them to include companions down to the M9V limit using the companion mass distribution for the WD population (Farihi et al. 2005), we conclude that 45-65% of all central stars have a stellar companion closer than ∼500 AU. This may be higher than predicted by the current PN formation scenario (40%). However, with a small sample size and a shallow companion detection limit, we cannot call this a solid result.

This proposal. We have already observed 14 targets in the J and H band at the AAT 4m in June 2011 (see proposal attached and target list). We now need to observe them in the B, V and I band. The optical bands are necessary to determine the reddening, while the V-J colour can be used to determine a possible excess. We have demonstrated the ability of this technique to detect

faint excess, provided at least 3 independent SNR=100 observations are taken. We ask for 3 nights of 2.3 m ANU telescope (bright) time to observe these 14 targets as well as an additional 15 targets for which BVI will be obtained (which can already reveal an I-band excess), with an aim to target them in the J band in a future AAT proposal.

The target list is drawn from our new, volume-limited sample (Frew 2008), a tremendous new asset in PN research, which allows us to reduce biases. Together with data already in hand, we will have a first solid result on the PN binary fraction and we will be able to seek additional observing time to complete the entire local ($\lesssim$ 2.5 kpc) PN population. With this proposal we plan to observe $\sim$30 objects in BVI, 14 of which also have J observations. Together with the northern sample (40 targets already observed in 2007 and 2011 in BVI with a third of them having also J observations) we will have observed $\sim$70 of the $\sim$200 suitable objects <2.5 kpc. These data, will be sufficient to make a dent in the binary fraction problem and to create a strong precedent to finalise the result by observing the rest of the sample.

The PNe of these objects have low surface brightness, fundamental for precision photometry of the central stars and have old, hot and faint CSPNe that will allow us to detect fainter companions. This sample also has well determined distances (with an error of $\sim$20%) obtained via the newly-developed radius-surface brightness relation (Frew 2008). This powerful relation has been carefully calibrated with parallax distances and other primary indicators and that has been checked against all available other methods to attain the best consistence ever achieved in a sizeable sample of PNe. About one third of the original 2.5-kpc sample are eliminated because of CSPN extreme faintness (V > 19 mag), too high in intrinsic brightness or with a bright contaminating nebula.

Exposure times and calibration overheads. A SNR of $\sim$100 is required for the needed photometric precision. Our exposure times have been scaled from indications from the responsible staff (Gary Da Costa). We will observe all of our targets in the B, V and I-bands with E2V. Firstly we calculated an approximate B and I-band mags for each CSPN based on the approximate V-band magnitudes and reddening tabulated by Frew (2008), assuming an intrinsic, single star, B-V and V-I of -0.34 and -0.35, respectively (calculated using the Tubingen stellar atmosphere models, assuming a 100kK stellar atmosphere of solar abundance; Rauch & Deetjen 2003). We will take 3 integrations for each CSPN in the B,V and I band to increase the precision (and to check for variability known to affect 15-20% of all CSPN). The photometric calibration will be performed by observing standard stars at similar airmass before and after each target. Allowing for overheads (slew, readout and flat-fields) of $\sim$20% of the exposure times, plus a 33% bad weather fraction gives a total of $\sim$27 hours of time required, including 3 hours to image the targets already observed in the J band at the AAT. We have therefore asked for three nights of bright time. This is appropriate, provided we avoid targets within 20 degrees from the Moon.

Poor weather programme. Lacking photometric conditions, we will revert to photometric monitoring that relies on relative photometry. As explained, 10-15% of all CSPNe are in *v*ery close binaries which exhibit periodic photometric variability. We currently know of only $\sim$35 such CSPNe (De Marco 2009) located in disparate positions and with a variety of parameters. Determining the *c*lose binary fraction of the *l*ocal, volume limited, sample is another key goal in the overall aim of understanding the binary properties of the PN population. In poor weather, we will be able to take 8-10, V-band observations of $\sim$30 targets (a lesser SNR is required), sufficient to discover binaries and determine preliminary periods for, predictably, $\sim$ 5 PNe.

Bond, H.E. 2000, ASPC 199, 115
Bujarrabal, V., et. al., A&A, 377, 868
De Marco, O., et al., 2005, ApJ, 632, 894
De Marco, O., et al., 2004, ApJ Letters, 602, L93
De Marco, O., et al., 2008, AJ 126, 323
De Marco, O., 2009, PASP Reviews, 121, 316
Duquennoy & Mayor, 1991.A&A 248, 485
Farihi, J. et al. 2005, ApJS, 161, 394
Frew, D., 2008, PhD Thesis, Macquarie University
Garcia-Segura et al., 1999, ApJ 517, 767
Han, Z., et al., 1995, MNRAS, 272, 800
Moe, M., & De Marco, O., 2006, ApJ, 650, 916
Moe, M., & De Marco, O., 2010, APN V, in press
Miszalski B., et al., 2009, A&A, 496, 813
Nordhaus, J., et al., 2007, MNRAS 376, 599
Preite-Martinez, A., et al., 1989, A&AS, 81, 309
Rauch, T. & Deetjen, J.L. 2003, ASP, 288, 103
Soker, N., 2006, PASP 118, 260
Vassiliadis, E., & Wood, P.R., 1994, ApJS, 92, 125

D.2 Proposal for an NOAO observing campaign

In this section, I present a proposal that I wrote aimed at obtaining telescope time so as to gather NIR data similar to those obtained in Chapter 2, for the whole local sample of PN. The project involved four observing runs of 10 nights each, one in each hemisphere per semester. The proposal has been rejected on the ground that the exposure times for the CTIO 1.3m/ANDI were wrong by an order of magnitudes. This is the unfortunate result of the absence of an exposure time calculator and conflicting indications between previous users and the local technical support.

NOAO Observing Proposal *Survey proposal* **Panel:** *For office use.*
Date: March 29, 2012 **Category:** Stellar Remnants

Estimating the binary fraction of planetary nebulae

PI: Dimitri Douchin **Status:** T **Affil.:** Macquarie University
Physics and astronomy department, Room 322, building E7A, Marsfield, NSW 2122 Australia
Email: dimitri.douchin@mq.edu.au Phone: +33 4 67143415 +61 2 98506288 FAX: _

CoI: Orsola De Marco **Status:** P **Affil.:** Macquarie University
CoI: George Jacoby **Status:** P **Affil.:** Giant Magellan Telescope, USA
CoI: David Frew **Status:** P **Affil.:** Macquarie University
CoI: Ivan Bojicic **Status:** P **Affil.:** Macquarie University
CoI: Gerard Jasniewicz **Status:** P **Affil.:** LUPM, France
CoI: Quentin Parker **Status:** P **Affil.:** Australian Astronomical Observatory

Abstract of Scientific Justification *(will be made publicly available for accepted proposals)***:**
Eighty percent of all planetary nebulae (PNe) are non-spherical.

Currently, the most plausible hypothesis to explain these shapes is the presence of a close stellar companion to the giant progenitor star. If binarity is necessary to form non-spherical PN, the binary fraction of central stars of PN (CSPNe) should be larger than predicted for the current scenario. We propose to search for the red excess of CSPNe deriving from a cold companion as a new, unbiased method for discovering binary CSPNe. B, V and I band images of CSPNe allow us to determine their colors and compare them with those expected from single stars. If the difference is bigger than expected, it indicates the presence of a companion. This technique has already given promising results from small observing runs. We want to survey ∼210 close CSPNe and estimate a global, unbiased binary fraction of CSPNe. We will carry out this survey in 1 year by observing 10 nights per hemisphere per semester using the SMARTS 1.3m in the South and the NOAO 2.1m in the North.

Summary of observing runs requested for this project

Run	Telescope	Instrument	No. Nights	Moon	Optimal months	Accept. months
1	KP-2.1m	CFIM + STA2	10	bright	Aug - Jan	Aug - Jan
2	CT-1.3m	ANDI + CCDIR	10	bright	Aug - Jul	Aug - Jul
3	KP-2.1m	CFIM + STA2	10	bright	Jan - Jul	Jan - Jul
4	CT-1.3m	ANDI + CCDIR	10	bright	Jan - Jul	Jan - Jul
5						
6						

Scheduling constraints and non-usable dates *(up to four lines).*

Scientific Justification *Be sure to include overall significance to astronomy. For standard proposals limit text to one page with figures, captions and references on no more than two additional pages.*

drivers, including the overall significance to astronomy compared with extant databases survey database science and (b) preparing observing programs for large ground-based and/or space-based facilities ongoing or planned Educational benefits (student roles; other education value-added) Transfer of survey experience to the community: algorithms; software packages; collaboration with/information transfer to the NOAO staff

Scientific goals

We currently understand planetary nebulae (PNe) as the the gas ejected by intermediate mass stars (1-8 $M_{\odot}$) just before they become white dwarfs (WD). A high 80% of all PNe have elliptical and bipolar shapes, often containing complex substructures such as bubbles and jets (Parker et al. 2006). These shapes are traditionally explained by the action of rotation and magnetic fields during the mass-losing asymptotic giant branch (AGB) progenitor phase (e.g., Garcia-Segura et al. 1999) and in a few cases, binary interactions . However, Soker (2006) and Nordhaus et al. (2007) showed that rotation and global magnetic fields are unlikely to be sustained in single AGB stars for long enough to impart the observed shapes. These theoretical considerations and other conundrums such as outflow momenta 1 000 times larger than can be explained by radiation pressure on dust (e.g., Bujarrabal et al. 2001) have left binary interactions as the most plausible mechanism for the explanation of a large majority of all PNe (for a review, see De Marco 2009). The best way to test the extent to which binarity is responsible for the PN phenomenon is to determine the central star of PN (CSPN) binary fraction and period distribution. The prediction of the current scenario for the formation of PNe is that ∼40% of all CSPNe should be in binaries with cool companions with separation smaller than ∼500 AU (i.e, unresolved from the ground; Duquennoy & Mayor 1991, Han et al. 1995). If PNe are preferentially a binary phenomenon, then we expect the fraction to be substantially larger: (70±15)%. This estimate derives from the prediction of Moe & De Marco (2011) that 51% of all PN have a companion that suffered a strong interaction (original separation <10-15 AU). To these we add 10% that suffered a lesser interaction with a wider companion out to ∼100 AU (Soker 1997). Since we will detect as unresolved also binaries with a separation up to ∼500 AU, we account for an additional fraction of 10%, using the binary period distribution of Duquennoy an Mayor (1991), scaled to include projection effects.

In the binary scenario, single stars and very wide binaries make spherical PN, or make no PN at all. Such "naked" central stars are would transit between the AGB and the WD domain with no PN or a very under-luminous PN (Soker & Subag 2005, Moe & De Marco 2006). Note that several stars in the correct gravity-temperature locus to be CSPN do not exhibit a PN at all (Napiwotzki 1999, Hirsch et al. 2008).

Advances compared with existing surveys

The most successful survey technique to date to find binary CSPNe has been photometric variability able to detect close binaries due to irradiation of the cool companion by the hot CSPN, ellipsoidal variability or eclipses. These surveys have revealed that 15-20% of all CSPNe have companions with P < few days, but they are biassed to periods smaller than about 2 weeks (De Marco et al. 2008, Miszalski et al. 2009). Radial velocity surveys are not a good way to search for binaries because of the pervasive wind variability found in all but the very faintest CSPNe that causes spectral variability scrambling even strong binary signal (De Marco et al. 2004, 2007).

The period distribution of CSPN binaries may be out of reach for now because intermediate mass-binaries (close enough to have shaped their PN but with periods longer than ∼2 weeks) will not be apparent in current binary surveys capable of detecting periods. However, we can determine the

actual overall binary fraction and test whether it is larger than predicted by current PN-making scenarios using a new, less biassed technique: the red/infrared excess technique. In a pilot project (De Marco et al., submitted) we have used the NOAO 2.1 m telescope to look for I band excess that would reveal the presence of a cool companion to the CSPN. Despite the small sample (27 objects) we detected several companions and the distribution of I band excesses indicates an over-abundance of binaries compared to the prediction from the current PN-evolution scenarios. Frew (2008) used the 2MASS and DENIS databases to carry out a similar investigation using the more sensitive J band; his results were in line with our I band excess findings, showing that 53% of the only 34 CSPN with adequate photometric precision, have a J band excess consistent with companions brighter than ∼M6V (at the 2σ level). This fraction should increase once it is de-biased to include fainter companions and is higher than predicted by the current PN formation scenario (40%). However, obtaining a suitably-sized sample of near-IR photometry is prohibitive, while it is simpler to obtain a larger sample of I band observations to treat the sample statistically and even compensate for the lesser sensitivity of the I band method.

The advances of our survey compared with existing survey are the selection of targets among the sample of Frew, 2008 that is not biassed with respect to binary separation, a new technique to investigate binarity among the CSPNe of our sample that is unbiassed with respect to binary separation and a sample size of ∼130 objects that will allow the determination of accurate statistics and determination of the global binary fraction of CSPNe never achieved so far on an unbiassed sample.

Additional uses of our survey

Our database will consist of a collection of high signal-to-noise ratio (SNR) B, V and I band images of ∼210 PNe. It will provide flux information for over a half of the 2 kpc volume-limited sample. The absolute magnitudes of many of objects will be acquired for the first time, completing current PN databases. The detection of a companion orbiting a CSPN will lead to photometric and spectroscopic follow-up of the target as well as infrared observations to constrain more the orbital and binary characteristics of the system (e.g. period, mass ratio, spectral types, etc). With sufficient follow-up observations, a determination of the binary CSPN period distribution will be possible. This survey will also constitute the main body of the PI's PhD thesis work providing enough data to yield satisfactory conclusions.

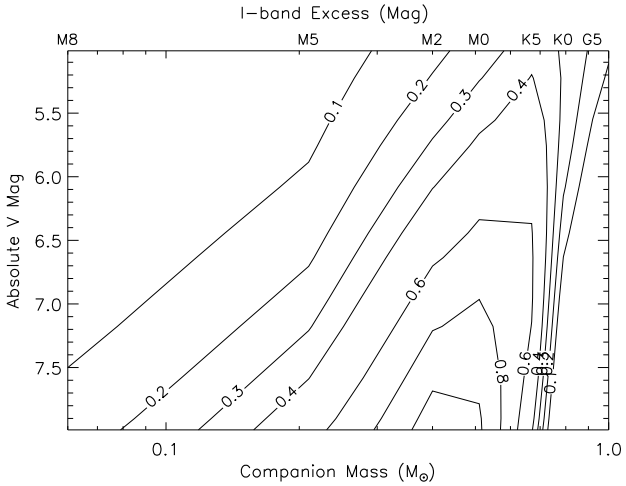

Figure 1: Red excess as a function of absolute V mag of the primary and the companion spectral type. With a limit magnitude of 5 and a precision of 0.03 mag, we can detect red excesses down to the M4V type.

Experimental Design *Describe the survey experimental design and the observations planned in detail. Justify choice of telescope, instrument, and sensitivity goals in terms of the survey science goals. A key part of the survey proposal process is to justify the total duration of the program both in terms of the number of nights and the number and distribution of observing runs required. Please show explicitly how on-target exposure time, setup, and calibration requirements determine these parameters. Please do not include any allowance for bad weather. Based on a clear understanding of your observational strategy as outlined in this section, we will evaluate the need for augmenting the allocation to allow for bad weather.*

Sample characteristics

The ∼210 targets we aim to observe come from the 2 kpc volume-limited sample of Frew (2008, thesis, Macquarie University). This new asset in PN research is a catalogue of the ∼400 PNe closest to the Sun within a radius of ∼3 kpc for which distances have been determined thanks to the newly calibrated PN radius-brightness relation. This offers an unbiassed source of targets for our study. We have extracted a sub-sample from Frew 2008 for our survey: we have excluded CSPNe with an absolute V magnitude (MV) < 5 to avoid stellar-wind induced flux variability and outshining of the companion by the primary. We have also excluded bright nebulae with a dimension <25 arcsec to limit nebular contamination on the CSPN photometry and facilitate background substraction. The final sample contains 100 northern and 110 southern targets with apparent V magnitudes mostly between 15 and 19.5.

Observing runs requested

Observing Runs Requested for this Project

Semester	Telescope	Instrument	# of Nights	Moon	Acceptable Months
2011B	KPNO-2.1m	STA2	10	bright	Aug-Dec
2011B	CTIO-1.3m	ANDICAM	10	bright	Aug-Dec
2012A	KPNO-2.1m	STA2	10	bright	Jan-Jul
2012A	CTIO-1.3m	ANDICAM	10	bright	Jan-Jul

We have separated our targets into northern and southern targets, and then each of these sets into semesters according to their RA. Hence, we propose 4 observing runs: 1 per hemisphere per semester, starting in semester 2011B. The runs at the KPNO 2.1m will be in regular observing mode, the runs at the SMARTS 1.3m will be in queue mode.

Experimental design

We intend to obtain B, V and I images of our targets. The apparent V magnitude for all the objects are approximately known. We have dereddened these values using the data of Frew 2008. To obtain the exposure time of each target, we have then used the single star predicted color, a B - V = -0.34 and a V - I = -0.4 appropriate for the hot temperature of our targets. The northern target exposure times have been calculated using the online KPNO 2.1m exposure time calculator. There is no SMARTS 1.3m exposure time calculator, therefore we have scaled the exposure times given by the KPNO 2.1m exposure time calculator to get approximate exposure times. The number of nights has been estimated by assuming nights of 10 hours by including overheads but not bad weather as requested. Our targets are relatively bright: they have apparent V mags between 15 and 19.5. We have made this selection to obtain fluxes of a statistically significant number of objects

with small-size telescopes. We have proposed the KPNO 2.1m because of its adapted size and our previous experience in imaging with the STA2 CCD, whereas we have proposed for the SMARTS 1.3m for its complementary location and available queue-mode that guarantees us more chances of photometric weather. Objects with magnitudes above 19.5 will be done later (therefore, although our sample is more unbiassed than in previous studies, there is a selection effect on brightness not to be forgotten).

We need 4 images in B, 4 images in V and 4 images in I all with a SNR of 100 (see below) for each target to insure consistency and detect variability expected in ∼20% of all targets. The optimal time separation between 2 images in a given filter for a given target is a few hours. We would not like images separated by less than 3 hours for a given object. We would like an H_α image in cases where the contamination by the bright nebula is important to perform proper background substraction. The exposure time for this image should be similar to one of the V band image. B, V, and I filter sequences should be obtained as closely as exposure times allow. Between each *long* sequence of B, V and I images of a target (e.g. if the sequence takes more than a few minutes), we need to image a close (i.e. at the same RA in a range of 1 hour) standard star in B, V and I as well. The standard stars we use have magnitudes of ∼13 - 15. To calculate the overheads, we have considered a slewing time of 3 minutes, a read-out time of 1 minute and an average exposure of 5 seconds per standard star with 1 standard star sequence taken for each CSPN. We would like dome-flats to be taken at the beginning and end of each night during daytime. As much as possible, we would like dark exposures of the longest science exposure time per night taken during the following day in each filter. The dome-flats and dark exposures have not been taken into account in the overheads as produced during daytime.

Sensitivity required for red excess detection

The intrinsic hot CSPN B - V colour is a very slow function of stellar temperature and varies only between 0.32 and 0.36 mag for T_{eff}=60 000 - 170 000 K (these are the stellar temperature limits for the selected CSPNe). From the predicted (0.34±0.02 mag) and observed B - V colours, the reddening can be obtained and applied to all photometry. Tlusty (Hubeny & Lanz 1995; De Marco et al. 2005, De Marco et al., submitted) stellar atmospheres to fit the intrinsic B - V colours, the (single star) I magnitudes can be predicted and a comparison with the observations will reveal the I band excess. Approximately half of the nearest CSPNe have been modelled and have excellent temperature determinations. For several others, Zanstra temperatures are available, usually correct within 20 000 K (e.g., Preite-Martinez et al. 1989). The total error we expect on B, V and I band is $\sigma_{noise} + \sigma_{T,E(B-V))} =$ ∼ 0.01 - 0.04 mag if 4 independent I band observations each with SNR ∼100 are obtained (multiple observations are also needed to assess variability affecting 20% of all CSPN and usually denoting binarity - variable targets will be followed up as needed). Finally, we do not expect near-infrared emission from dust. PNe dust temperature is < 800 - 1000 K (Phillips & Ramos-Larios 2006); it does not affect the I band ; therefore additional error from background subtraction of these low surface brightness PNe will be negligible. In Fig. 1 we present the predicted I band excess as a function of primary star absolute V magnitude and companion spectral type: in the worse case scenario, we can detect M6V companions at the ∼3σ level, if the primary has MV > 5.0 mag. By selecting intrinsically faint central stars, we can solidly detect companions down to the M4V spectral type in most cases. It would be advantageous to use J and H band images in which the infrared excess is more prominent. However, the need for optical and infrared observations requiring different telescopes per target made us chose the I band solution.

Management Plan *Describe the overall organizational plan for conducting the proposed survey, including data reduction and analysis, preparation of survey deliverables, and staffing requirements. List the roles and responsibilities of the Co-Is with their anticipated time commitments directed to achieving the goals of the survey. You may also wish to detail external sources of support that will be used in the program. Please detail any use of non-NOAO observational facilities that are required to achieve the overall goals of the survey program.*

General organisation

Given the two different observing modes, there will be a different policy for each observatory. The runs at the KPNO 2.1m will happen during the allocated dates. The reduction and analysis of the data will be performed before the beginning of the following semester in order to:

- insure that the data acquired during the first run are adequate
- insure that the second run will be reduced and analysed in time for the release and the PI's PhD completion.

The SMARTS 1.3m data will be acquired in queue mode. We suggest that all the data of a given observing run are stored by NOAO until the last image of the run is taken, after which the data will be sent physically or virtually according to NOAO preferences to Macquarie University. After the data have been received they will be reduced and analysed before the end of the current semester for the reasons mentioned above.

Reduction and analysis pipeline

The storage, reduction, analysis and distribution of the data will be done on one single server (currently referred as kosmos.science.mq.edu.au) located at Macquarie University and dedicated to astronomy related calculations and storage. It has enough disk capacity to store the full survey (estimated from previous observations to be <500 GB).
The reduction will be performed within IRAF (Image and Reduction Analysis Facility). It will include steps of flat-fielding and de-biasing hence we ask to take dome flats at the beginning and the end of each observing night. Dark removal should not be necessary, however dark exposures will be taken as checks. Fringe removal will be performed if necessary on the I band images.
Aperture photometry will be performed to determine the targets instrumental magnitudes. Observed magnitudes will then be calculated by inverting the color-coefficients and extinction matrix using a least square method algorithm (e.g. LAPACK). Finally these magnitudes will be rescaled thanks to the comparison between the standard stars observed magnitudes and their catalogued magnitudes.
The reduced data will be distributed from kosmos.science.mq.edu.au via FTP and a HTML-interfaced catalogue.

Role distribution

Dimitri Douchin will be in charge of the observations, reduction, analysis and distribution of the data.
Orsola De Marco, PI's PhD supervisor, will make sure that the data are processed in time and will help in the four steps described above, especially in the analysis thanks to her expertise on the topic.
George Jacoby will contribute with his knowledge of the KNPO installations and its expertise in CCD photometry.
David Frew will contribute with his specific knowledge of the sample.
Ivan Bojicic will contribute wih his knowledge in local servers, data distribution and PN surveys.

Gerard Jasniewicz, PI's PhD co-supervisor, will contribute with his expertise in CCD photometry. Quentin Parker, PI's PhD secondary supervisor, will contribute with his expertise in Galactic PN surveys.

Additional support

Macquarie University is willing to fund the KPNO 2.1m 2012A observing run and will cover the travel, accomodation and meals for one observer. The survey is also supported by the Australian Astronomical Observatory (Australia) and the Macquarie Research Center for Astronomy, Astrophysics and Astrophotonics (Australia) via Quentin Parker and the Université de Montpellier 2 (France) via Gérard Jasniewicz.

Use of Other Facilities or Resources *(1) Describe how the proposed observations complement data from non-NOAO facilities. For each of these other facilities, indicate the nature of the observations (yours or those of others), and describe the importance of the observations proposed here in the context of the entire program. (2) Do you currently have a grant that would provide resources to support the data processing, analysis, and publication of the observations proposed here?"*

Release of data

The data will be released 1 year after the last image has been taken. We will make individual calibrated images available. A catalogue of the derived magnitude sorted chronologically and by objects will be made available with links to the images.

Release of Data *Describe the data products (reduced observations, single or stacked images, spectra, object catalogues, and so on) to be releases, as well as the timeline and mechanism of their release to the community. Please differentiate between intermediate products developed during the execution of the survey versus the final products likely to be produced after the full observations have been obtained.*

Link with previous observations

The quest for data so as to estimate the binary fraction of CSPNe thanks to red and infrared excess has started 5 years ago (for a broader review, see De Marco, 2009). Since then, 3 observing runs have been carried out. In 2007, reliable absolute photometry of 27 CSPNe in B, V, and I has been acquired. The statistical analysis of this sample has led to a fraction of 19-42% with the method described in this proposal. The only hurdle here is the size of the sample. Another observing run has been dedicated to this method where absolute photometry data have been taken for an additional ~ 20 objects. The data are currently being analysed, although this run is less promising as bad weather has hampered the data harvesting (as a backup solution, differential photometry has been performed for flux monitoring). Finally, J band data have been obtained in 2011 at the 4m AAT. J and H images of 13 targets included in this proposal have been obtained that will complementate the B, V, I images obtained thanks to this survey.

Previous Use of NOAO Facilities *List allocations of telescope time on facilities available through NOAO to the PI during the last 2 years for regular proposals, and at any time in the past for survey proposals (including participation of the PI as a Co-I on previous NOAO surveys), together with the current status of the data (cite publications where appropriate). Mark with an asterisk those allocations of time related to the current proposal. Please include original proposal semesters and ID numbers when available.*

In the past 2 years, an observing run of 7 days (P.I.: Orsola De Marco, ⋆ 2011A-0430) has been carried out at the KPNO 2.1m with STA2. Its analysis is currently being finalised. Unrelatedly, this observing run has led to the discovery of Kronberger 61, a new PN in the field of view of the Kepler observatory. This discovery has been followed by a press review. Given the 2007 run at the KPNO 2.1m with TK2B in 2007 and the previous occupation of George Jacoby at the NOAO, the team is fairly familiar with KPNO installations.

Acknowledgements

We would like to thank Michelle Buxton, Nicole Van Der Bliek, Tod Lauer, Charles Bailyn, Dave Bell and Howard Bond for the information they have provided to put up this proposal.

O. De Marco, Astronomical Society of the Pacific Conference Series, 260 (2002) 517
O. De Marco, PASP 121 (2009), 316-342
O. De Marco et al., American Astronomical Society Meeting Abstracts, Bulletin of the American Astronomical Society, vol. 35, December 2003, p. 127.03
O. De Marco, 602 (2004), L93-L96
O. De Marco, T. C. Hillwig, and A. J. Smith, AJ 136 (2008), 323-336
A. Duquennoy and M. Mayor, 248 (1991), 485-524
G. García-Segura et al., ApJ 517 (1999), 767-781
Z. Han, P. Podsiadlowski, and P. P. Eggleton, MNRAS 272 (1995), 800-820
B. Miszalski et al., AA, 496 (2009), 813-825
M. Moe and O. De Marco, ApJ 650 (2006), 916-932
J. Nordhaus, E. G. Blackman, and A. Frank, MNRAS 376 (2007), 599-608
Q. A. Parker et al., MNRAS 373 (2006), 79-94
N. Soker, VizieR Online Data Catalog 211 (1997), 20487
N. Soker, PASP 118 (2006), 260-269

Observing Run Details for Run 1: KP-2.1m/CFIM + STA2

Technical Description *Describe the observations to be made during this observing run. Justify the specific telescope, the number of nights, the instrument, and the lunar phase. List objects, coordinates, and magnitudes (or surface brightness, if appropriate) in the Target Tables section below (required for queue and Gemini runs).*

This run will be performed in regular observing mode between August and December 2012 at the KPNO 2.1m. The protocol is as described in the experimental design. We aim to observe 40 CSPNe with magnitudes between 12 and 22. The total integration time for this run is 117 000 seconds. The overhead time is 223 000 seconds (including the short integration for standards). This represents a total of 94.5 hours hence we ask for 10 nights.

Instrument Configuration

Filters: B,V,I, Ha	Slit:	Fiber cable:
Grating/grism:	Multislit:	Corrector:
Order:	λ_{start}:	Collimator:
Cross disperser:	λ_{end}:	Atmos. disp. corr.:

R.A. range of principal targets (hours): 22 to 10

Dec. range of principal targets (degrees): 02 to 75

Special Instrument Requirements *Describe briefly any special or non-standard usage of instrumentation.*

Observing Run Details for Run 2: CT-1.3m/ANDI + CCDIR

Technical Description *Describe the observations to be made during this observing run. Justify the specific telescope, the number of nights, the instrument, and the lunar phase. List objects, coordinates, and magnitudes (or surface brightness, if appropriate) in the Target Tables section below (required for queue and Gemini runs).*

This run will be performed in queue mode between August and December 2012 at the SMARTS 1.3m. The protocol is as described in the experimental design. We aim to observe 56 CSPNe with magnitudes between 10 and 19.5. A detailed target list has been provided for this run. The total integration time for this run is 18 000 seconds. The overhead time is 312 000 seconds (including the short integration for standards). This represents a total of 92 hours hence we ask for 10 nights.

Instrument Configuration

Filters: B,V,I,Ha	Slit:	Fiber cable:
Grating/grism:	Multislit:	Corrector:
Order:	λ_{start}:	Collimator:
Cross disperser:	λ_{end}:	Atmos. disp. corr.:

R.A. range of principal targets (hours): 22 to 10

Dec. range of principal targets (degrees): -3 to -75

Special Instrument Requirements *Describe briefly any special or non-standard usage of instrumentation.*

Photometric conditions are required

Target Table for Run 2: CT-1.3m/ANDI + CCDIR

Obj ID	Object	α	δ	Epoch	Mag.	Filter	Exp. time	# of exp.	Lunar days	Sky	Seeing	Comment
001	NGC 246	00 47 03.35	-11 52 19.0	J2000	11.84	V	0	4	14	phot	1.1	
002	Lo 1	02 56 58.40	-44 10 17.9	J2000	15.16	V	3	4	14	phot	1.1	
003	NGC 1360	03 33 14.65	-25 52 17.9	J2000	11.34	V	0	4	14	phot	1.1	
004	NGC 1535	04 14 15.76	-12 44 22.0	J2000	12.11	V	0	4	14	phot	1.1	
005	Abell 7	05 03 07.52	-15 36 22.8	J2000	15.49	V	5	4	14	phot	1.1	
006	IC 418	05 27 28.20	-12 41 50.3	J2000	10.23	V	0	4	14	phot	1.1	
007	DeHt 1	05 55 06.70	-22 54 02.2	J2000	12.7	V	0	4	14	phot	1.1	
008	K 1-27	05 57 02.14	-75 40 22.5	J2000	16.13	V	9	4	14	phot	1.1	
009	PHR0615-0025	06 15 20.45	-00 25 49	J2000	19.5	V	273	4	14	phot	1.1	
010	TaWe 1	06 16 15.3	-00 00 23	J2000	18.7	V	121	4	14	phot	1.1	
011	BMP0642-0417	06 42 18.41	-04 17 48.9	J2000	18.5	V	99	4	14	phot	1.1	
012	HaWe 9	06 54 20.79	-25 24 33.5	J2000	19.2	V	202	4	14	phot	1.1	
013	MPA0655-2356	06 55 59.95	-23 56 49.5	J2000	19	V	165	4	14	phot	1.1	
014	BMP0700-2607	07 00 51.81	-26 07 18.5	J2000	18.6	V	110	4	14	phot	1.1	
015	PHR0701-0749	07 01 09.41	-07 49 23.9	J2000	13.6	V	1	4	14	phot	1.1	
016	NGC 2346	07 09 22.55	-00 48 23.6	J2000	11.27	V	0	4	14	phot	1.1	
017	BMP0713-0432	07 13 50.99	-04 32 52.0	J2000	19	V	165	4	14	phot	1.1	
018	Wra 17-1	07 14 49.36	-46 57 39.7	J2000	16.6	V	14	4	14	phot	1.1	
019	We 1-6	07 17 26.02	-10 10 37.7	J2000	15.76	V	6	4	14	phot	1.1	
020	PHR0719-1222	07 19 46.32	-12 22 34.9	J2000	15.4	V	4	4	14	phot	1.1	
021	PFP 1	07 22 17.75	-06 21 46.4	J2000	15.78	V	6	4	14	phot	1.1	
022	BMP0733-3108	07 33 24.12	-31 08 05.1	J2000	18.5	V	99	4	14	phot	1.1	
023	FP0739-2709	07 39 38.12	-27 09 30.3	J2000	19	V	165	4	14	phot	1.1	
024	BMP0739-1418	07 39 50.6	-14 18 26	J2000	16	V	8	4	14	phot	1.1	
025	NGC 2438	07 41 51.43	-14 43 54.9	J2000	17.6	V	40	4	14	phot	1.1	
026	NGC 2440	07 41 54.91	-18 12 29.7	J2000	17.63	V	41	4	14	phot	1.1	
027	HFG 2	07 42 23.81	-32 47 50.4	J2000	16.8	V	18	4	14	phot	1.1	
028	Abell 23	07 43 17.98	-34 45 15.6	J2000	18.5	V	99	4	14	phot	1.1	
029	PHR0743-1951	07 43 51.13	-19 51 16.7	J2000	15.8	V	6	4	14	phot	1.1	
030	Abell 25	08 06 46.49	-02 52 35.2	J2000	18.94	V	155	4	14	phot	1.1	
031	PHR0808-3745	08 08 23.24	-37 45 51.4	J2000	18.2	V	73	4	14	phot	1.1	
032	RCW 24	08 25 47.58	-40 13 10.0	J2000	18.21	V	74	4	14	phot	1.1	
033	VBRC 1	08 30 53.78	-38 18 04.1	J2000	18	V	60	4	14	phot	1.1	
034	NGC 2610	08 33 23.32	-16 08 57.7	J2000	15.97	V	8	4	14	phot	1.1	
035	PHR0834-2819	08 34 18.1	-28 19 03	J2000	19.2	V	202	4	14	phot	1.1	
036	He 2-11	08 37 08.34	-39 25 08.3	J2000	17.7	V	46	4	14	phot	1.1	
037	Abell 29	08 40 18.92	-20 54 36.3	J2000	18.33	V	83	4	14	phot	1.1	
038	BMP0844-2737	08 44 37.9	-27 37 15	J2000	19.2	V	202	4	14	phot	1.1	
039	MeWe 1-1	08 53 36.86	-54 05 09.8	J2000	17.7	V	44	4	14	phot	1.1	
040	K 1-2	08 57 45.95	-28 57 35.9	J2000	16.83	V	18	4	14	phot	1.1	
041	FP0905-3033	09 05 05.34	-30 33 12.0	J2000	16.49	V	13	4	14	phot	1.1	
042	PHR0905-4753	09 05 41.04	-47 54 05.2	J2000	12.66	V	0	4	14	phot	1.1	
043	IC 2448	09 07 06.26	-69 56 30.7	J2000	14.26	V	1	4	14	phot	1.1	
044	BMP0907-4146	09 07 24.33	-41 46 14.1	J2000	18.6	V	110	4	14	phot	1.1	
045	PHR0907-5722	09 07 51.0	-57 22 53	J2000	17.3	V	29	4	14	phot	1.1	
046	NGC 2792	09 12 26.60	-42 25 39.9	J2000	16.89	V	19	4	14	phot	1.1	
047	NGC 2867	09 21 25.34	-58 18 40.7	J2000	16.03	V	8	4	14	phot	1.1	
048	NGC 2899	09 27 03.12	-56 06 21.2	J2000	16.5	V	13	4	14	phot	1.1	
049	PHR0928-4936	09 28 40.99	-49 36 46.9	J2000	18	V	60	4	14	phot	1.1	

Target Table for Run 2: CT-1.3m/ANDI + CCDIR

Obj ID	Object	α	δ	Epoch	Mag.	Filter	Exp. time	# of exp.	Lunar days	Sky	Seeing	Comment
050	Wra 17-31	09 31 20.49	-56 17 39.4	J2000	17.94	V	56	4	14	phot	1.1	
051	IC 2501	09 38 47.5	-60 05 28	J2000	14.48	V	2	4	14	phot	1.1	
052	Abell 33	09 39 09.12	-02 48 31.5	J2000	16.03	V	8	4	14	phot	1.1	
053	He 2-36	09 43 25.62	-57 16 55.6	J2000	11.48	V	0	4	14	phot	1.1	
054	Abell 34	09 45 35.32	-13 10 15.6	J2000	16.4	V	12	4	14	phot	1.1	
055	HbDs 1	09 52 44.53	-46 16 47.4	J2000	12.53	V	0	4	14	phot	1.1	
056	IC 5148/50	21 59 35.13	-39 23 08.1	J2000	16.16	V	9	4	14	phot	1.1	
057	NGC 7293	22 29 38.51	-20 50 13.7	J2000	13.53	V	1	4	14	phot	1.1	

Observing Run Details for Run 3: KP-2.1m/CFIM + STA2

Technical Description *Describe the observations to be made during this observing run. Justify the specific telescope, the number of nights, the instrument, and the lunar phase. List objects, coordinates, and magnitudes (or surface brightness, if appropriate) in the Target Tables section below (required for queue and Gemini runs).*

This run will be performed in regular observing mode between January and July 2013 at the KPNO 2.1m. The protocol is as described in the experimental design. We aim to observe 62 CSPNe with magnitudes between 14 and 19. The total integration time for this run is 14 000 seconds. The overhead time is 346 000 seconds (including the short integration for standards). This represents a total of 100 hours hence we ask for 10 nights.

Instrument Configuration

Filters: B,V,I,Ha	Slit:	Fiber cable:
Grating/grism:	Multislit:	Corrector:
Order:	λ_{start}:	Collimator:
Cross disperser:	λ_{end}:	Atmos. disp. corr.:

R.A. range of principal targets (hours): 10 to 22

Dec. range of principal targets (degrees): 02 to 75

Special Instrument Requirements *Describe briefly any special or non-standard usage of instrumentation.*

Observing Run Details for Run 4: CT-1.3m/ANDI + CCDIR

Technical Description *Describe the observations to be made during this observing run. Justify the specific telescope, the number of nights, the instrument, and the lunar phase. List objects, coordinates, and magnitudes (or surface brightness, if appropriate) in the Target Tables section below (required for queue and Gemini runs).*

This run will be performed in queue mode between January and July 2013 at the SMARTS 1.3m. The protocol is as described in the experimental design. We aim to observe at least 50 CSPNe (out of 138 matching our criterea for this semester) a with magnitudes between 15 and 18. A detailed target list has been provided for this run. The total integration time for this run is 54 000 seconds. The overhead time is 279 000 seconds (including the short integration for standards). This represents a total of 92 hours hence we ask for 10 nights.

Instrument Configuration

Filters: B,V,I,Ha	Slit:	Fiber cable:
Grating/grism:	Multislit:	Corrector:
Order:	λ_{start}:	Collimator:
Cross disperser:	λ_{end}:	Atmos. disp. corr.:

R.A. range of principal targets (hours): 10 to 22

Dec. range of principal targets (degrees): -8 to -75

Special Instrument Requirements *Describe briefly any special or non-standard usage of instrumentation.*

Photometric conditions are required

Target Table for Run 4: CT-1.3m/ANDI + CCDIR

Obj ID	Object	α	δ	Epoch	Mag.	Filter	Exp. time	# of exp.	Lunar days	Sky	Seeing	Comment
058	NGC 6369	17 29 20.44	-23 45 34.2	J2000	15.13	V	3	4	14	phot	1.1	
059	IC 4663	17 45 28.37	-44 54 25.9	J2000	15.2	V	3	4	14	phot	1.1	
060	ESO 40-11	13 34 14.13	-75 46 31.3	J2000	15.23	V	4	4	14	phot	1.1	
061	PHR1757-1649	17 57 39.62	-16 49 19.7	J2000	15.38	V	4	4	14	phot	1.1	
062	Lo 16	17 35 41.80	-40 11 26.2	J2000	15.42	V	4	4	14	phot	1.1	
063	Abell 51	19 01 01.39	-18 12 15.3	J2000	15.42	V	4	4	14	phot	1.1	
064	NGC 3918	11 50 17.73	-57 10 56.9	J2000	15.49	V	5	4	14	phot	1.1	
065	NGC 6153	16 31 30.83	-40 15 14.2	J2000	15.55	V	5	4	14	phot	1.1	
066	Abell 65	19 46 34.20	-23 08 12.9	J2000	15.60	V	5	4	14	phot	1.1	
067	IC 4642	17 11 45.02	-55 24 01.5	J2000	15.66	V	6	4	14	phot	1.1	
068	NGC 6337	17 22 15.66	-38 29 03.5	J2000	15.67	V	6	4	14	phot	1.1	
069	NGC 6578	18 16 16.52	-20 27 02.7	J2000	15.68	V	6	4	14	phot	1.1	
070	NGC 3132	10 07 01.76	-40 26 11.1	J2000	15.76	V	6	4	14	phot	1.1	
071	PHR1602-4127	16 02 18.13	-41 26 49.5	J2000	15.8	V	6	4	14	phot	1.1	
072	MPA1858-1430	18 58 19.3	-14 30 26	J2000	15.8	V	6	4	14	phot	1.1	
073	Fr 2-8	14 00 41.75	-51 02 27.6	J2000	15.83	V	7	4	14	phot	1.1	
074	PHR1553-5738	15 53 10.00	-57 38 06.8	J2000	15.83	V	7	4	14	phot	1.1	
075	He 2-111	14 33 18.47	-60 49 36.3	J2000	16.1	V	9	4	14	phot	1.1	
076	Lo 17	18 27 49.93	-37 15 51.8	J2000	16.15	V	9.4	4	14	phot	1.1	
077	HaTr 5	17 01 27.98	-43 05 55.1	J2000	16.2	V	10	4	14	phot	1.1	
078	Hf 38	10 54 35.44	-59 09 47.3	J2000	16.2	V	10	4	14	phot	1.1	
079	He 2-115	15 05 16.69	-55 11 12.3	J2000	16.24	V	10	4	14	phot	1.1	
080	Wra 17-40	10 06 59.57	-64 21 50.0	J2000	16.3	V	11	4	14	phot	1.1	
081	M 1-41	18 09 29.90	-24 12 23.5	J2000	16.3	V	11	4	14	phot	1.1	
082	NGC 6309	17 14 04.32	-12 54 37.7	J2000	16.31	V	11	4	14	phot	1.1	
083	NGC 5979	15 47 41.55	-61 13 06.3	J2000	16.37	V	11	4	14	phot	1.1	
084	NGC 6326	17 20 46.30	-51 45 15.3	J2000	16.5	V	13	4	14	phot	1.1	
085	PHR1001-6152	10 01 18.75	-61 52 03.6	J2000	16.75	V	17	4	14	phot	1.1	
086	K 1-22	11 26 43.79	-34 22 11.0	J2000	16.83	V	18	4	14	phot	1.1	
087	PHR1040-5417	10 40 48.21	-54 17 57.6	J2000	16.85	V	19	4	14	phot	1.1	
088	My 60	10 31 33.39	-55 20 50.9	J2000	16.87	V	19	4	14	phot	1.1	
089	PHR1032-6310	10 32 14.4	-63 10 22	J2000	16.9	V	20	4	14	phot	1.1	
090	IC 1295	18 54 37.21	-08 49 39.1	J2000	16.9	V	20	4	14	phot	1.1	
091	HaWe 13	19 31 07.20	-03 42 31.5	J2000	16.9	V	20	4	14	phot	1.1	
092	Lo 5	11 13 54.15	-47 57 00.6	J2000	17	V	22	4	14	phot	1.1	
093	MeWe 2-4	14 01 15.42	-50 40 09.5	J2000	17	V	22	4	14	phot	1.1	
094	Hb 4	17 41 52.76	-24 42 08.1	J2000	17	V	22	4	14	phot	1.1	
095	M 1-51	18 33 28.94	-11 07 26.4	J2000	17	V	22	4	14	phot	1.1	
096	NGC 6818	19 43 57.84	-14 09 11.9	J2000	17.06	V	23	4	14	phot	1.1	
097	PHR1418-5144	14 18 25.83	-51 44 39.0	J2000	17.07	V	23	4	14	phot	1.1	
098	He 2-84	12 28 46.82	-63 44 38.7	J2000	17.1	V	24	4	14	phot	1.1	
099	PHR1335-6349	13 35 09.1	-63 48 57	J2000	17.1	V	24	4	14	phot	1.1	
100	He 2-133	15 41 57.5	-56 36 46	J2000	17.2	V	26	4	14	phot	1.1	
101	PHR1408-6106	14 08 48.07	-61 06 33.8	J2000	17.2	V	26	4	14	phot	1.1	
102	PHR1136-5235	11 36 00.0	-52 35 33	J2000	17.3	V	29	4	14	phot	1.1	
103	MeWe 1-11	17 52 47.06	-46 42 01.6	J2000	17.3	V	29	4	14	phot	1.1	
104	IC 4406	14 22 26.28	-44 09 04.4	J2000	17.38	V	32	4	14	phot	1.1	
105	HaTr 9	18 08 58.86	-41 48 37.6	J2000	17.4	V	32	4	14	phot	1.1	
106	NGC 6563	18 12 02.75	-33 52 07.1	J2000	17.49	V	36	4	14	phot	1.1	

Target Table for Run 4: CT-1.3m/ANDI + CCDIR

Obj ID	Object	α	δ	Epoch	Mag.	Filter	Exp. time	# of exp.	Lunar days	Sky	Seeing	Comment
107	**PHR1517-5751**	**15 17 31.2**	**-57 51 10**	**J2000**	**17.5**	**V**	**36**	**4**	**14**	**phot**	**1.1**	
108	**M 3-39**	**17 21 11.51**	**-27 11 38.1**	**J2000**	**17.5**	**V**	**36**	**4**	**14**	**phot**	**1.1**	

D.3 Service-mode SSO 4m proposal

Here we present a proposal for the observation of our sample in the J and H-bands in service mode. The time has been granted but due to technical issues and the need for photometric weather, we foresee that only a handful of objects will be added to the sample. The data have not been analysed yet.

```
AAO IRIS2 Service Proposal Application Form
Thank you for filling out the AAO service proposal form. This is what you submitted on Wednesd

Name: Dimitri Douchin
Email: dimitri.douchin@mq.edu.au
Institution: Macquarie University
Postal_address:

Room 322 Building E7A
Macquarie University
2122 Marsfield
NSW Australia

Collaborators: Orsola De Marco (Macquarie University) David Frew (Macquarie University) Gerard

Title: Estimating the binary fraction of central stars of planetary nebulae

Image: Yes

Imaging_configuration: f/8

Image_Broad_Filter: J, H

Image_Narrow_Filter: Not_used
```

```
Signal/Noise_imaging: 100, 100

Spectroscopy: No

Slit_Width: 1_arcsec

Grism: Sapphire

Source_list:

Name      RA   DEC       J magH magexp Jexp H
Abell 7  05 03 07.52-15 36 22.816.116.163539
PFP 1 07 22 17.75-06 21 46.416.6416.892122
Abell 31 08 54 13.16+08 53 53.015.8715.572414
FP0905-3033 09 05 05.34-30 33 12.017.0317.21184252
EGB 6 09 52 59.00+13 44 34.516.5215.957427
PHR1001-6152 10 01 18.75-61 52 03.616.6216.7189104
K 1-22 11 26 43.79-34 22 11.015.0314.4652
MeWe 2-4 14 01 15.42-50 40 09.517.2517.39270346
PHR1408-6106 14 08 48.07-61 06 33.816.8716.93137152
PHR1418-5144 14 18 25.83-51 44 39.017.4317.58370486
PHR1429-6003 14 29 43.9-60 03 1716.1816.074134
PHR1510-6754 15 10 22.05-67 54 24.015.1715.3179
FP1721-5654 17 21 09.0-56 54 2517.8417.97758967
FP1824-0319 18 24 40.88-03 19 59.615.515.61215
Sh 2-78  19 03 10.09+14 06 58.917.6417.74537644
WHTZ 1 19 40 43.83+02 30 3216.2916.395058
FS 11 04 52 58.92-00 14 41.611.3411.280.00940.0197
FS 14 07 24 14.40-00 33 04.114.1014.171.16933.7955
FS 18+ 08 53 35.51-00 36 41.710.8210.570.00380.0054
FS 19 10 33 42.75-11 41 38.313.5813.670.47191.5276
FS-20 11 08 00-05:09:26.113.4013.440.34231.0032
```

S273-E 14 56 52-44:49:14.011.3410.920.00940.0104

S279-F 17 48 23-45:25:45.012.4812.120.06860.0911

FS-35 18 27 14+04:03:09.412.1911.840.04140.0544

L547 18 51 16-04:16:02.011.759.890.01940.0016

total_time_hrs: 5.9

Last_date: 13/04/01

Worst_seeing: 0.75

Photometric_conditions: yes

Finding_charts: 10

Extra_information:

The target list is divided into 2: the science list and the standard list. For each target matches a standard (ex: the second target will have the second standard)

Each target has to be observed 3 times and framed with its associated standard . In other words, an image of the associated standard has to be taken before and after the target, for each target, each time, in each filter J and H.

AATAC: no

Justification:

We currently understand planetary nebulae (PN) as the ejected envelopes of intermediate mass stars before they become white dwarfs. Eighty percent of all PN are non spherical: they show multipolar structures, jets and bubbles.

Stellar rotation and magnetic fields of the giant star during the ejection of the nebula could generate these shapes. However, rotation and magnetic fields cannot be sustained by single giant stars for a sufficiently long time to impose the observed axi-symmetric PN shapes (Nordhaus et al. 2006, Soker 2006). The most plausible hypothesis that can account for these shapes is the presence of a nearby stellar or even substellar companion to the giant star (for a review see De Marco 2009). If binarity is a necessary pre-requisite for the formation of non spherical PN, the close and intermediate binary fraction of central stars of PN should be larger than it is predicted for the current scenario. As a result, the overall binary fraction for unresolved binary central stars of PN should be larger (close to 80%) than ~45% (Duquennoy & Mayor 1991).

So far, all binary central stars of PN have been discovered thanks to flux variability due to irradiation effects, ellipsoidal deformations and eclipses, a technique that discovers only binaries with periods less than 1-3 days (Miszalski et al. 2009). A method is needed to detect companions at larger separations.

Frew (2008) searched for a near IR excess using all currently-available data: 34 central stars have 2MASS and DENIS J-band data and of these at least 55% have excess consistent with a companion, but companions fainter than mid-to-late M would not have been detected because of the large errors of those surveys at the faint end. To enlarge the sample and increase the measurement precision, we have used the AAT/IRIS2, but the efficiency of our observations has been hampered by the need for photometric weather: only a handful of objects were observed in photometric conditions over three nights in June. To increase the efficiency of discovery we have undertaken a survey using the less sensitive I-band at the NOAO 2.1m telescope for which longer observing sessions are usually allocated. I-band excess were found around 25% central stars of 26 PN. However the I band was found to be insensitive to more than half of the companions expected to be around central stars of PN and

deemed non-viable.

To determine accurately the binary fraction, J band (and accompanying B and V) photometry is needed for the ~250 central stars in the 2-kpc volume-limited sample (Frew 2008). With this 6-hour service time request, we can complete J (and H, when possible, to obtain a colour) observations of an additional 20 objects. Since photometric conditions are required, service mode is optimal, even necessary if this project is to be completed in a timely manner. Single star, J and H magnitudes for our targets have been estimated from their intrinsic B-V colours fitted with Tlusty stellar atmospheres (Hubeny & Lanz 1995). Exposure times have been determined using the AAT exposure-time calculator for a SNR ~ 100. We estimate our J band excess error to be below ~0.1 mag, which allows us to detect an M8 companion to central stars with Mv>5.7 (see figure DeMarco_fig1.ps.gz). With ~50 well observed objects we will have solid, albeit still preliminary results which will form the basis of the next round of observations to complete the whole sample. (Complementary B and V photometry will be obtained once J photometry is secured). The determination of the binary fraction is a top priority in studies of planetary nebulae and results will be published in a timely manner even before the full sample if observed (e.g., De Marco et al. 2008, Hillwig et al. 2010).

Figures: 1

List of Publications

Douchin, D., De, M. O., Jacoby, G. H., et al. 2012a, in SF2A-2012: Proceedings of the Annual meeting of the French Society of Astronomy and Astrophysics, ed. S. Boissier, P. de Laverny, N. Nardetto, R. Samadi, D. Valls-Gabaud, & H. Wozniak, 325–327

Douchin, D., De Marco, O., Jacoby, G. H., et al. 2013a, in Astronomical Society of the Pacific Conference Series, Vol. 469, 18th European White Dwarf Workshop., ed. Krzesiń, J. ski, G. Stachowski, P. Moskalik, & K. Bajan, 293

Douchin, D., De Marco, O., Jacoby, G. H., et al. 2013b, Central European Astrophysical Bulletin, 37, 391

Douchin, D., Jacoby, G. H., De Marco, O., Howell, S. B., & Kronberger, M. 2012b, in IAU Symposium, Vol. 283, IAU Symposium, 344–345

Douchin, D., De Marco, O., Frew, D. J., et al. 2012c, in IAU Symposium, Vol. 283, IAU Symposium, 346–347 115

Douchin, D., De Marco, O., Frew, D. J., et al. 2014, in Asymmetrical Planetary Nebulae VI conference, Proceedings of the conference held 4-8 November, 2013. Edited by C. Morisset, G. Delgado-Inglada and S. Torres-Peimbert. Online at http://www.astroscu.unam.mx/apn6/PROCEEDINGS, id.18

These publications are conference proceedings.

Douchin et al. (2014) has been submitted to the Monthly Notices of the Royal Astronomical Society and is awaiting for the referee's report. It includes approximately the content of Sections 2.1, 2.2, 3.1 and Chapter 6.

References

Abazajian, K. N., Adelman-McCarthy, J. K., Agüeros, M. A., et al. 2009, ApJS, 182, 543 86

Abt, H. A., & Levy, S. G. 1976, ApJS, 30, 273 16

Acker, A., Gorny, S. K., & Cuisinier, F. 1996, A&A, 305, 944 72

Afšar, M., & Bond, H. E. 2005, Mem. Soc. Astron. Italiana, 76, 608 20, 122

Agüeros, M. A., Anderson, S. F., Covey, K. R., et al. 2009, ApJS, 181, 444 58

Ali, A., Sabin, L., Snaid, S., & Basurah, H. M. 2012, A&A, 541, A98 58, 75

Allen, D. A. 1973, The Observatory, 93, 28 158

Annunziatella, M., Mercurio, A., Brescia, M., Cavuoti, S., & Longo, G. 2013, PASP, 125, 68 45, 46

Balick, B., & Frank, A. 2002, ARAA, 40, 439 58

Becker, A. C., Silvestri, N. M., Owen, R. E., Ivezić, Ž., & Lupton, R. H. 2007, PASP, 119, 1462 44, 45

Bertin, E. 2011, in Astronomical Society of the Pacific Conference Series, Vol. 442, Astronomical Data Analysis Software and Systems XX, ed. I. N. Evans, A. Accomazzi, D. J. Mink, & A. H. Rots, 435 44

Bertin, E., & Arnouts, S. 1996, A&AS, 117, 393 44

Bessell, M. S. 1979, PASP, 91, 589 27

Bilíková, J., Chu, Y.-H., Gruendl, R. A., Su, K. Y. L., & De Marco, O. 2012, ApJS, 200, 3 26, 29, 75, 93, 159

Blackman, E. G. 2004, Plasma Physics and Controlled Fusion, 46, 423 9

Blackman, E. G., Frank, A., Markiel, J. A., Thomas, J. H., & Van Horn, H. M. 2001, Nature, 409, 485 9

Boissay, R., Parker, Q. A., Frew, D. J., & Bojicic, I. 2012, in IAU Symposium, Vol. 283, IAU Symposium, 316–317 34

Bond, H. E. 1979, in IAU Colloq. 53: White Dwarfs and Variable Degenerate Stars, ed. H. M. van Horn & V. Weidemann, 266–268 20

Bond, H. E. 1990, in IUE Proposal, 3648 20, 110

Bond, H. E. 1995, in Annals of the Israel Physical Society, Vol. 11, Asymmetrical Planetary Nebulae, ed. A. Harpaz & N. Soker, 61 20

Bond, H. E. 2000, in Astronomical Society of the Pacific Conference Series, Vol. 199, Asymmetrical Planetary Nebulae II: From Origins to Microstructures, ed. J. H. Kastner, N. Soker, & S. Rappaport, 115 20, 109, 110

Bond, H. E., Ciardullo, R., & Meakes, M. G. 1992, in IAU Symposium, Vol. 151, Evolutionary Processes in Interacting Binary Stars, ed. Y. Kondo, R. Sistero, & R. S. Polidan, 517 20

Brown, L. D., Cai, T. T., & DasGupta, A. 2001, Statistical Science, 16, 101 136

Cardelli, J. A., Clayton, G. C., & Mathis, J. S. 1989, ApJ, 345, 245 28, 165

Chu, Y.-H., Gruendl, R. A., Guerrero, M. A., et al. 2009, AJ, 138, 691 106

Chu, Y.-H., Su, K. Y. L., Bilikova, J., et al. 2011, The Astronomical Journal, 142, 75 81, 82

Ciardullo, R., Bond, H. E., Sipior, M. S., et al. 1999, AJ, 118, 488 19, 75, 81, 82, 94, 152

Clayton, G. C., De Marco, O., Nordhaus, J., et al. 2014, AJ, 147, 142 29

Cohen, M., Parker, Q. A., Green, A. J., et al. 2011, MNRAS, 413, 514 75

Corradi, R. L. M., Schönberner, D., Steffen, M., & Perinotto, M. 2003, MNRAS, 340, 417 106

Corradi, R. L. M., & Schwarz, H. E. 1995, A&A, 293, 871 33, 75

Corwin, H. G. 2004, VizieR Online Data Catalog, 7239, 0 96

Covey, K. R., Ivezić, Ž., Schlegel, D., et al. 2007, AJ, 134, 2398 86, 87, 91

Danehkar, A., Frew, D. J., Parker, Q. A., & De Marco, O. 2012, in IAU Symposium, Vol. 283, IAU Symposium, 340–341 68

De Marco, O. 2009, PASP, 121, 316 14, 19, 106, 116, 122

De Marco, O., Bond, H. E., Harmer, D., & Fleming, A. J. 2003, in Bulletin of the American Astronomical Society, Vol. 35, American Astronomical Society Meeting Abstracts, 127.03 159

De Marco, O., Bond, H. E., Harmer, D., & Fleming, A. J. 2004, ApJ, 602, L93 20, 21, 121, 122

De Marco, O., Hillwig, T. C., & Smith, A. J. 2008, AJ, 136, 323 20, 109, 111

De Marco, O., Passy, J.-C., Frew, D. J., Moe, M., & Jacoby, G. H. 2013, MNRAS, 428, 2118 xvii, xix, 18, 21, 22, 26, 28, 29, 30, 31, 40, 45, 55, 56, 58, 60, 61, 62, 64, 65, 66, 67, 68, 69, 71, 84, 87, 101, 105, 106, 126, 128, 135, 136, 140, 141, 143, 149, 167, 168, 174

De Marco, O., Wortel, S., Bond, H. E., & Harmer, D. 2007, in Asymmetrical Planetary Nebulae IV 21, 159

Debes, J. H., Hoard, D. W., Wachter, S., Leisawitz, D. T., & Cohen, M. 2011, ApJS, 197, 38 137, 138

Dekker, H., D'Odorico, S., Kaufer, A., Delabre, B., & Kotzlowski, H. 2000, in Society of Photo-Optical Instrumentation Engineers (SPIE) Conference Series, Vol. 4008, Optical and IR Telescope Instrumentation and Detectors, ed. M. Iye & A. F. Moorwood, 534–545 123

Delfosse, X., Kahane, C., & Forveille, T. 1997, A&A, 320, 249 6

Douchin, D., De Marco, O., Frew, D. J., et al. 2012, in IAU Symposium, Vol. 283, IAU Symposium, 346–347 115

Dreizler, S., Werner, K., Jordan, S., & Hagen, H. 1994, A&A, 286, 463 126

Drew, J. E., Greimel, R., Irwin, M. J., et al. 2005, MNRAS, 362, 753 71

Drew, J. E., Gonzalez-Solares, E., Greimel, R., et al. 2014, MNRAS, 440, 2036 75, 81

Duquennoy, A., & Mayor, M. 1991, A&A, 248, 485 16

Durand, S., Acker, A., & Zijlstra, A. 1998, A&AS, 132, 13 129

Dwarkadas, V. V., Chevalier, R. A., & Blondin, J. M. 1996, ApJ, 457, 773 8

Edelmann, H., Altmann, M., & Heber, U. 2006, Baltic Astronomy, 15, 191 105, 151

Ellis, G. L., Grayson, E. T., & Bond, H. E. 1984, PASP, 96, 283 69

Etoka, S., & Diamond, P. 2004, MNRAS, 348, 34 9

Farihi, J., Becklin, E. E., & Zuckerman, B. 2005, ApJS, 161, 394 26, 137, 138, 139

Feibelman, W. A. 1987, PASP, 99, 270 159

Feibelman, W. A., & Bruhweiler, F. C. 1989, ApJ, 347, 901 58, 159

Feibelman, W. A., & Kaler, J. B. 1983, ApJ, 269, 592 94

Feibelman, W. A., & Kondo, Y. 2001, ApJS, 136, 735 106

Ferguson, D. H., & James, T. A. 1994, ApJS, 94, 723 71

Ferguson, D. H., Liebert, J., Cutri, R., et al. 1987, ApJ, 316, 399 71

Ferguson, D. H., Liebert, J., Haas, S., Napiwotzki, R., & James, T. A. 1999, ApJ, 518, 866 71

Fitzpatrick, E. L. 1999, PASP, 111, 63 28

Frank, A., & Mellema, G. 1994, A&A, 289, 937 8

Frankowski, A. 2003, A&A, 406, 265 6, 127

Frew, D., & Parker, Q. 2007, in APN IV Conference Proceedings, 475 21, 26, 31, 95, 96, 97

Frew, D. J. 2008, PhD thesis, Department of Physics, Macquarie University, NSW 2109, Australia xviii, xx, 21, 25, 26, 32, 33, 34, 57, 58, 69, 71, 75, 85, 86, 89, 91, 92, 95, 96, 97, 98, 99, 100, 101, 102, 103, 104, 105, 107, 111, 147, 157, 166, 169, 170, 171, 172

Frew, D. J., Bojičić, I. S., & Parker, Q. A. 2013, MNRAS, 431, 2 33, 69, 78

Frew, D. J., Madsen, G. J., O'Toole, S. J., & A., P. Q. 2010, PASA, 27, 203 69

Frew, D. J., & Parker, Q. A. 2010, PASA, 27, 129 34, 67, 96

Frew, D. J., & Parker, Q. A. 2011, in Asymmetric Planetary Nebulae 5 Conference 34

Frew, D. J., Parker, Q. A., & Russeil, D. 2006, MNRAS, 372, 1081 75, 83

Frew, D. J., Bojičić, I. S., Parker, Q. A., et al. 2014a, MNRAS, 440, 1345 32

—. 2014b, MNRAS75, 79, 81

Fulbright, M. S., & Liebert, J. 1993, ApJ, 410, 275 69

Gabler, R., Kudritzki, R. P., & Mendez, R. H. 1991, A&A, 245, 587 58

García-Segura, G., Langer, N., Różyczka, M., & Franco, J. 1999, ApJ, 517, 767 6, 8, 9

García-Segura, G., López, J. A., & Franco, J. 2005, ApJ, 618, 919 6

Gaustad, J. E., McCullough, P. R., Rosing, W., & Van Buren, D. 2001, PASP, 113, 1326 69

Gianninas, A., Bergeron, P., Dupuis, J., & Ruiz, M. T. 2010, ApJ, 720, 581 106

Girven, J., Gänsicke, B. T., Steeghs, D., & Koester, D. 2011, MNRAS, 417, 1210 58

Guerrero, M. A., & Manchado, A. 1999, ApJ, 522, 378 106

Hajduk, M., Zijlstra, A. A., & Gesicki, K. 2010, MNRAS, 406, 626 81

Hambly, N. C., MacGillivray, H. T., Read, M. A., et al. 2001, MNRAS, 326, 1279 92

Han, Z., Podsiadlowski, P., & Eggleton, P. P. 1995, MNRAS, 272, 800 18, 19

Handler, G., Prinja, R. K., Urbaneja, M. A., et al. 2013, MNRAS, 430, 2923 116

Harrington, J. P., & Feibelman, W. A. 1983, ApJ, 265, 258 159

Harris, H. C., Dahn, C. C., Canzian, B., et al. 2007, AJ, 133, 631 58

Herald, J. E., & Bianchi, L. 2011, MNRAS, 417, 2440 58, 159

Herwig, F. 2005, ARA&A, 43, 435 3, 4, 5

Hillwig, T. 2014, in Asymmetrical Planetary Nebulae VI conference, Proceedings of the conference held 4-8 November, 2013. Edited by C. Morisset, G. Delgado-Inglada and S. Torres-Peimbert. Online at ¡A href="http://www.astroscu.unam.mx/apn6/PROCEEDINGS/"¿http://www.astroscu.unam.mx/apn6/ id.38 111, 116

Hillwig, T. C. 2004, in Astronomical Society of the Pacific Conference Series, Vol. 313, Asymmetrical Planetary Nebulae III: Winds, Structure and the Thunderbird, ed. M. Meixner, J. H. Kastner, B. Balick, & N. Soker, 529 111

Hillwig, T. C. 2011, in Bulletin of the American Astronomical Society, Vol. 43, American Astronomical Society Meeting Abstracts 217, 256.10 111

Hillwig, T. C., Bond, H. E., Afşar, M., & De Marco, O. 2010, AJ, 140, 319 110

Hoessel, J. G., Saha, A., & Danielson, G. E. 1988, PASP, 100, 680 69

Holberg, J. B., & Magargal, K. 2005, in Astronomical Society of the Pacific Conference Series, Vol. 334, 14th European Workshop on White Dwarfs, ed. D. Koester & S. Moehler, 419 26

Howell, S. B. 1989, PASP, 101, 616 51

Howell, S. B., Sobeck, C., Haas, M., et al. 2014, PASP, 126, 398 115

Hrivnak, B. J. 2012, Journal of Astronomy and Space Sciences, 29, 57 12

Iben, Jr., I. 1991, ApJS, 76, 55 1, 2

Iben, Jr., I. 1993, in IAU Symposium, Vol. 155, Planetary Nebulae, ed. R. Weinberger & A. Acker, 587 1

—. 1995, Phys. Rep., 250, 2 1

Icke, V. 1988, A&A, 202, 177 8

Icke, V., Balick, B., & Frank, A. 1992, A&A, 253, 224 8

Icke, V., Preston, H. L., & Balick, B. 1989, AJ, 97, 462 6, 8

Jacoby, G. H. 1980, ApJS, 42, 1 19

Jacoby, G. H., Ferland, G. J., & Korista, K. T. 2001, ApJ, 560, 272 68

Jacoby, G. H., & Kaler, J. B. 1989, AJ, 98, 1662 34

Jacoby, G. H., & van de Steene, G. 1995, AJ, 110, 1285 58, 70

Jacoby, G. H., Kronberger, M., Patchick, D., et al. 2010, PASA, 27, 156 8, 70

Jasniewicz, G., Thevenin, F., Monier, R., & Skiff, B. A. 1996, A&A, 307, 200 94

Jones, D. H., Read, M. A., Saunders, W., et al. 2009, MNRAS, 399, 683 158

Jordan, S., Bagnulo, S., Werner, K., & O'Toole, S. J. 2012, A&A, 542, A64 10

Jordan, S., Werner, K., & O'Toole, S. J. 2005, in Astronomical Society of the Pacific Conference Series, Vol. 334, 14th European Workshop on White Dwarfs, ed. D. Koester & S. Moehler, 257 9

Kaler, J. B. 1983, ApJ, 264, 594 158

Karachentseva, V. E., Karachentsev, I. D., & Richter, G. M. 1999, A&AS, 135, 221 72

Kastner, J. H., & Montez, J. 2012, AJ, 144, 58 94

Kerber, F., Furlan, E., Roth, M., Galaz, G., & Chanamé, J. C. 2000, PASP, 112, 542 69

Kerber, F., Guglielmetti, F., Mignani, R., & Roth, M. 2003, in IAU Symposium, Vol. 209, Planetary Nebulae: Their Evolution and Role in the Universe, ed. S. Kwok, M. Dopita, & R. Sutherland, 525 71

Kerber, F., Mignani, R. P., Pauli, E.-M., Wicenec, A., & Guglielmetti, F. 2004, A&A, 420, 207 72

Knapp, G. R., & Morris, M. 1985, ApJ, 292, 640 6

Kohoutek, L. 1983, in IAU Symposium, Vol. 103, Planetary Nebulae, ed. D. R. Flower, 17–29 34

Kurucz, R. L. 1979, ApJS, 40, 1 30

Kwok, S. 1994, PASP, 106, 344 1

Kwok, S. 2005, in American Institute of Physics Conference Series, Vol. 804, Planetary Nebulae as Astronomical Tools, ed. R. Szczerba, G. Stasińska, & S. K. Gorny, 187–196 1

Kwok, S., Purton, C. R., & Fitzgerald, P. M. 1978, ApJ, 219, L125 6

Lagadec, E., & Zijlstra, A. A. 2008, MNRAS, 390, L59 6

Landolt, A. U. 1992, AJ, 104, 340 58

Lanz, T., & Hubeny, I. 2003, ApJS, 146, 417 30

Lawrence, A., Warren, S. J., Almaini, O., et al. 2012, VizieR Online Data Catalog, 2314, 0 29

Lèbre, A., Aurière, M., Fabas, N., et al. 2014, in IAU Symposium, Vol. 302, IAU Symposium, 385–388 9

Leone, F., Corradi, R. L. M., Martínez González, M. J., Asensio Ramos, A., & Manso Sainz, R. 2014, ArXiv e-prints 10

Liebert, J., Bond, H. E., Dufour, P., et al. 2013, ApJ, 769, 32 69, 151

Liebert, J., Tweedy, R. W., Napiwotzki, R., & Fulbright, M. S. 1995, ApJ, 441, 424 58, 71

Long, J., Jacoby, G., De Marco, O., et al. 2013, in American Astronomical Society Meeting Abstracts, Vol. 221, American Astronomical Society Meeting Abstracts 115

Lutz, J. H., & Kaler, J. B. 1987, in Bulletin of the American Astronomical Society, Vol. 19, Bulletin of the American Astronomical Society, 1090 127

Lutz, J. H., Kaler, J. B., Shaw, R. A., et al. 1989, in Bulletin of the American Astronomical Society, Vol. 21, Bulletin of the American Astronomical Society, 1200 106, 111

Makarov, D. I., Karachentsev, I. D., & Burenkov, A. N. 2003, A&A, 405, 951 72

Marcolino, W. L. F., & de Araújo, F. X. 2003, AJ, 126, 887 102

Matt, S., Balick, B., Winglee, R., & Goodson, A. 2000, ApJ, 545, 965 8

Mellema, G., Eulderink, F., & Icke, V. 1991, A&A, 252, 718 8

Mellema, G., & Frank, A. 1995, MNRAS, 273, 401 6

Méndez, R. H. 1989, in IAU Symposium, Vol. 131, Planetary Nebulae, ed. S. Torres-Peimbert, 261–272 20, 121

Mendez, R. H., Herrero, A., & Manchado, A. 1990, A&A, 229, 152 159

Mendez, R. H., Kudritzki, R. P., & Herrero, A. 1992, A&A, 260, 329 159

Mendez, R. H., Niemela, V. S., & Lee, P. 1978, MNRAS, 184, 351 106

Mikulášek, Z., Kohoutek, L., Zejda, M., & Pejcha, O. 2005, Ap&SS, 296, 465 75

Miszalski, B., Acker, A., Moffat, A. F. J., Parker, Q. A., & Udalski, A. 2009, AA, 496, 813 20, 110, 150

Miszalski, B., Parker, Q. A., Acker, A., et al. 2008, MNRAS, 384, 525 34

Moe, M., & De Marco, O. 2006, ApJ, 650, 916 18, 19, 141

Montez, Jr., R., De Marco, O., Kastner, J. H., & Chu, Y.-H. 2010, ApJ, 721, 1820 94

Napiwotzki, R. 1999, A&A, 350, 101 58

Nordhaus, J. 2014, in Asymmetrical Planetary Nebulae VI conference, Proceedings of the conference held 4-8 November, 2013. Edited by C. Morisset, G. Delgado-Inglada and S. Torres-Peimbert. Online at ¡A href="http://www.astroscu.unam.mx/apn6/PROCEEDINGS/"¿http://www.astroscu.unam.mx/apn6/ id.64 116

Nordhaus, J., Blackman, E. G., & Frank, A. 2007, MNRAS, 376, 599 9, 12

Otsuka, M., Tamura, S., Yadoumaru, Y., & Tajitsu, A. 2003, PASP, 115, 67 158

Parker, Q. A., Acker, A., Frew, D. J., et al. 2006, MNRAS, 373, 79 8, 33, 34, 58, 69, 73, 106

Pascoli, G. 1997, ApJ, 489, 946 9

Peimbert, M. 1978, in IAU Symposium, Vol. 76, Planetary Nebulae, ed. Y. Terzian, 215–223 5

Peimbert, M. 1990, Rev. Mexicana Astron. Astrofis., 20, 119 19

Peimbert, M. 1993, in IAU Symposium, Vol. 155, Planetary Nebulae, ed. R. Weinberger & A. Acker, 523 19

Perinotto, M. 1989, in IAU Symposium, Vol. 131, Planetary Nebulae, ed. S. Torres-Peimbert, 293–300 6

Phillips, J. P. 2003, MNRAS, 344, 501 58, 75, 89, 94

—. 2004, MNRAS, 353, 589 58

—. 2005, MNRAS, 361, 283 5

Phillips, J. P., Cuesta, L., & Kemp, S. N. 2005, MNRAS, 357, 548 126

Pottasch, S. R. 1984, Planetary nebulae : a study of late stages of stellar evolution (Dordrecht ; Boston : Hingham, MA: Kluwer Academic) 33

Preite-Martinez, A., Acker, A., Koeppen, J., & Stenholm, B. 1989, A&AS, 81, 309 75

Raghavan, D., McAlister, H. A., Henry, T. J., et al. 2010, ApJS, 190, 1 xvii, 16, 17, 18, 137, 138, 139, 141, 145

Rauch, T., & Deetjen, J. L. 2003, in Astronomical Society of the Pacific Conference Series, Vol. 288, Stellar Atmosphere Modeling, ed. I. Hubeny, D. Mihalas, & K. Werner, 103 29

Rauch, T., Rudkowski, A., Kampka, D., et al. 2014, A&A, 566, A3 30

Rauch, T., Werner, K., Bohlin, R., & Kruk, J. W. 2013, A&A, 560, A106 30

Rauch, T., Ziegler, M., Werner, K., et al. 2007, A&A, 470, 317 58

Rebassa-Mansergas, A., Nebot Gómez-Morán, A., Schreiber, M. R., et al. 2012, MNRAS, 419, 806 137

Ruediger, G. 1989, Differential rotation and stellar convection. Sun and the solar stars 9

Ruediger, G., & Hollerbach, R. 2004, The magnetic universe : geophysical and astrophysical dynamo theory 9

Sahai, R., Morris, M. R., & Villar, G. G. 2011, AJ, 141, 134 106

Salpeter, E. E. 1974, ApJ, 193, 585 6

Sanduleak, N. 1975, PASP, 87, 705 106

—. 1983, PASP, 95, 619 159

Schaller, G., Schaerer, D., Meynet, G., & Maeder, A. 1992, A&AS, 96, 269 128

Schechter, P. L., Mateo, M., & Saha, A. 1993, PASP, 105 44

Schlafly, E. F., & Finkbeiner, D. P. 2011, ApJ, 737, 103 xviii, 28, 99, 100

Schlafly, E. F., Finkbeiner, D. P., Schlegel, D. J., et al. 2010, ApJ, 725, 1175 58, 61

Schombert, J. M., Bothun, G. D., Schneider, S. E., & McGaugh, S. S. 1992, AJ, 103, 1107 72

Schwarz, H. E., & Monteiro, H. 2006, ApJ, 648, 430 58

Shimanskii, V. V., Borisov, N. V., Pozdnyakova, S. A., et al. 2008, Astronomy Reports, 52, 558 61, 71

Skrutskie, M. F., Cutri, R. M., Stiening, R., et al. 2006, AJ, 131, 1163 26, 140

Soker, N. 1997, ApJS, 112, 487 10

—. 2006, PASP, 118, 260 9, 12, 13

Soker, N., & Livio, M. 1989, ApJ, 339, 268 6

Soker, N., & Subag, E. 2005, AJ, 130, 2717 14

Sorensen, P. M., & Pollacco, D. L. 2003, in Astronomical Society of the Pacific Conference Series, Vol. 303, Astronomical Society of the Pacific Conference Series, ed. R. L. M. Corradi, J. Mikolajewska, & T. J. Mahoney, 494 20, 122

Stetson, P. 2000, Software: Stellar Photometry, ed. P. Murdin 46, 47, 48

Stetson, P. B. 1987, PASP, 99, 191 44, 46, 47, 48

Todt, H., Kniazev, A. Y., Gvaramadze, V. V., et al. 2013, MNRAS, 430, 2302 75, 79

Tokovinin, A. 2008, in Multiple Stars Across the H-R Diagram, ed. S. Hubrig, M. Petr-Gotzens, & A. Tokovinin, 38 16

Tylenda, R., Acker, A., Stenholm, B., & Koeppen, J. 1992, A&AS, 95, 337 28, 75

Van Winckel, H. 1999, in IAU Symposium, Vol. 191, Asymptotic Giant Branch Stars, ed. T. Le Bertre, A. Lebre, & C. Waelkens, 465 12

van Winckel, H. 2003, in Astronomical Society of the Pacific Conference Series, Vol. 303, Symbiotic Stars Probing Stellar Evolution, ed. R. L. M. Corradi, J. Mikolajewska, & T. J. Mahoney, 294 12

Van Winckel, H., Jorissen, A., Exter, K., et al. 2014, ArXiv e-prints 21, 68, 94

Vázquez, R., Miranda, L. F., Olguín, L., et al. 2008, A&A, 481, 107 93

Vlemmings, W. 2012, in IAU Symposium, Vol. 283, IAU Symposium, 176–179 9

Vlemmings, W. H. T. 2014, in IAU Symposium, Vol. 302, IAU Symposium, 389–397 9

Vlemmings, W. H. T., & van Langevelde, H. J. 2005, A&A, 434, 1021 9

Vogt, N., Barrera, L. H., & Navarro, M. 1990, Ap&SS, 173, 145 127

Wachter, A., Schröder, K.-P., Winters, J. M., Arndt, T. U., & Sedlmayr, E. 2002, A&A, 384, 452 6

Weidmann, W. A., & Gamen, R. 2011, A&A, 526, A6 58, 75

Weinberger, R., & Kerber, F. 1997, Science, 276, 1382 1

Werner, K., Deetjen, J. L., Dreizler, S., et al. 2003, in Astronomical Society of the Pacific Conference Series, Vol. 288, Stellar Atmosphere Modeling, ed. I. Hubeny, D. Mihalas, & K. Werner, 31 29

Werner, K., & Dreizler, S. 1999, Journal of Computational and Applied Mathematics, 109, 65 29

Werner, K., Dreizler, S., Heber, U., & Rauch, T. 1996, in Astronomical Society of the Pacific Conference Series, Vol. 96, Hydrogen Deficient Stars, ed. C. S. Jeffery & U. Heber, 267 126

Werner, K., & Herwig, F. 2006, PASP, 118, 183 5, 126

Werner, K., Rauch, T., & Kruk, J. W. 2007, A&A, 474, 591 126

Wright, E. L., Eisenhardt, P. R. M., Mainzer, A. K., et al. 2010, AJ, 140, 1868 68, 137

Yungelson, L. R., Tutukov, A. V., & Livio, M. 1993, ApJ, 418, 794 19

Zacharias, N., Finch, C. T., Girard, T. M., et al. 2012, VizieR Online Data Catalog, 1322, 0 97

Zuckerman, B., Becklin, E. E., & McLean, I. S. 1991, in Astronomical Society of the Pacific Conference Series, Vol. 14, Astronomical Society of the Pacific Conference Series, ed. R. Elston, 161–166 25

Zwitter, T., & Munari, U. 1994, A&AS, 107, 503 159